Interacting Quantum Gases of Lithium and Ytterbium

Anders H. Hansen

A dissertation
submitted in partial fulfillment of the
requirements for the degree of

Doctor of Philosophy

University of Washington
2013

Reading commmittee
Subhadeep Gupta, Chair
Boris Blinov
Alejandro Garcia

Program Authorized to Offer Degree:
Physics

©Copyright 2013

Anders H. Hansen

University of Washington

Abstract

Interacting Quantum Gases of Lithium and Ytterbium

Anders H Hansen

Chair of the Supervisory Committee:
Subhadeep Gupta, Assistant professor
Physics

This dissertation describes the development of a scientific apparatus for trapping ultracold quantum gases of atomic lithium and ytterbium, and discusses the studies of interactions between such particles under a range of experimental conditions. The atoms are sequentially magneto-optically trapped and cooled, and subsequently transferred to an optical dipole trap. It is shown that, due to the details of the electronic structure of the constituent species, as well as the large atomic mass of ytterbium, the system is well-suited for cooling to temperatures well below a microkelvin, and for subsequent studies of quantum few- and many-body physics. The dynamical behavior of the ultracold samples is studied at a wide range of interaction strengths. These are controlled by means of externally applied magnetic fields, or by optical transfer of atoms to long-lived, metastable orbitals.

The work described in this paper paves the way for a large number of future experiments, including studies of quantum few-body physics in highly mass-mismatched systems and studies of dipolar matter using ultracold LiYb molecules.

To Mom, Dad,

Martin and Even

Acknowledgments

What could be a more daunting experience than committing to a 6-year PhD program in physics? To agree to spend so many years of one's life dedicated to a single research project? And yet, we walk light-hearted through the doors of the department on the first day, confident that we have plenty of time to figure things out as we go along. Well, looking back on those first days, and the intervening years, the myth of the a lone student "figuring out" graduate school is long dead. Instead, I now see a large group of people – friends, family, and mentors – who have all shaped my academic and professional development at the UW, and without whom my experience here would be far less fulfilling.

Of these, I must naturally begin by acknowledging my advisor, Subhadeep "Deep" Gupta, who took me in as a researcher during my first few months in Seattle. Deep, aside from being a highly competent scientist, is also a great mentor, with a true dedication toward education in the lab setting, always putting the academic experience of his students first. I cannot count the incidents I have caused around the lab that he has been willing to chalk up as a "learning experience," nor the times he has had to explain some concept to me three times or more without ever breaking his characteristic patience and cheerfulness. Indeed, Deep possesses an ardent and infectuous enthusiasm toward even the most minute details of his research; an enthusiasm that affects everyone he works with. While many professors opt to leave the day-to-day affairs of the lab to the graduate students, Deep takes a hands-on approach to his research that I have found highly motivating: frequently stopping by the lab to learn about progress, offer advice, or invite us out for a pint on a Friday afternoon.

Of the other "Deeple," (as we are affectionately called by denizens of neighboring labs) there are a few people with whom I have had the pleasure of working most closely during my time here, and who deserve a great deal more recognition than I can afford them on these few pages.

Alex Khramov also joined the lab very early on, and has since become one of my closest friends in Seattle. The tone of our collegial interactions was set already during orientation week, when I got lost on the *Blair Outing* hike and he came along and got me out of the pickle that I had caused myself. In the lab Alex appears to have an encyclopedic knowledge of what knobs need to be turned when the experiment stops working – a skill perhaps rivaled only by his ability to learn new languages. (He still greets me in Indonesian every morning, and expects the correct reply in Georgian.) Alex is a competent physicist, a dedicated experimentalist, and an endless source of interesting conversation topics, be it about stand-up comedy, mountaineering, or the history of professional tennis.

Alan Jamison was in the same incoming year as me and Alex, and found his way to our lab

after some time as a wayward particle theorist. Few physicists rise to the level of true genius in both theory and experiment; Alan, with his strange but refreshing perspectives,[1] has mastered both, being at once a confident tamer of misbehaving lasers and a gifted theorist, whether he is studying ultracold atomic interactions or superfluidity in neutron stars. He is also a skilled athlete, mathlete, history buff, and a connoisseur of just about every genre of music.

Will Dowd was also an early recruit on our experiment, and has contributed almost as much to our research with his unquenchable high spirits and optimism as he has with his competent hands. Will has taught us on more than one occasion that just because something *shouldn't* work it is not a given that it *won't*. Will also shares my personal affinity for board games, collecting very large data sets, and digging up interesting things on the Web while those data sets are being collected.

Beyond these major influences in my research career, there are many others that deserve acknowledgment for their contributions and comradery, though I have known less than half of them half as long as I would like. I will address a few of these in (roughly) chronological order.

Ryan Weh was one of two undergraduates who joined the lab in the early building phase. Ryan quickly proved himself to be as competent and industrious as any graduate student. He ended up providing the lab with a large fraction of our electronics circuitry during his short time here, and taught me much of what I now know about soldering and circuit design. He also created the first version of our group website, where he put his delightfully off-kilter sense of humor to good use, writing short blurbs about each lab member.

Vlad Ivanov was a post-doc in our lab for two years. During a time when Deep's presence in the lab was gradually giving way to other department (and family) commitments, Vlad took over much of the leadership of the experiment, and became the driving force behind our experimental progress toward achieving double-degeneracy. I will remember Vlad for his characteristic dry wit, loud Russian expletives around the lab, and the board game nights he would frequently host on weekends.

Ben Plotkin-Swing came to work with us on the two-species experiment, but has since moved on to the new interferometry lab. I know few people with hobbies as esoteric as Ben's: slacklining, mountain unicycling, and night-time mountain climbing to name a few. (He also deserves credit for bringing a hang-board into the lab, for communal recreation and exercise.) Despite his modest disposition, Ben is always ready to tell a good story about his adventures the previous weekend.

Ricky Roy is one of the most recent members of the group. In the face of two senior graduate students preparing to leave, he has shown an exceptional ability to internalize all

the details of the experiment in a short amount of time. Beyond being a hard-working and dependable colleague, Ricky is also a fellow college football enthusiast and homebrewer, and benefits the lab atmosphere with is excellent taste in music. As we, the first generation of grad students on the Li-Yb project, prepare to move on, we leave with confidence that Will and Ricky will continue to move the experiment forward with skill and dedication.

Last, but not at all least, I must thank my family for all their support and encouragement during my many years abroad, both as an undergraduate at the University of Oregon, and as a graduate student here at the UW. Deserving particular mention are my parents, Per and Rande Hansen, who have been dedicated in their support, and have remained a strong presence through all these years despite the distances and time zones. My grandmother "Mormor" Rose Helgesen was also instrumental in arranging many of my financial minutae when I first moved abroad. My grandparents, and aunt (Tante) Eli have in the past decade filled an entire box with their frequent and thoughtful cards and letters. Finally, my brothers Martin and Even, who were still young children when I left home, have always been a positive and motivating force in my education, and it delights me to see that they too have evolved into young, but competent scientists.

Contents

List of Figures

List of Tables

1 Introduction

When I began my research at the University of Washington, the field of ultracold quantum gases had been in rapid progress for over a decade. The first Bose-Einstein Condensates (BECs) had been demonstrated twelve years prior,[2, 3] (I recall reading about the discovery in Science Illustrated as a child) and the field of ultracold atoms had subsequently expanded in many directions. Perhaps most notably, there had been a widespread shift of interest toward fermionic systems [4, 5] and studies of Bardeen-Cooper-Schieffer-like (BCS) superfluids.[6, 7] Several groups had already delved into the physics that govern the fascinating BEC-BCS crossover,[8, 9] and magnetic Feshbach resonances had been used to synthesize molecules, some of which were showing remarkable in-trap stability and longevity.

1.1 One electron, two electron, red electron, blue electron

Most of the attention of ultracold atomic physicists was initially directed toward the alkali group of elements, due to the simplicity of its hydrogen-like structure. After the first BECs were produced in rubidium in 1995 [2] it did not take long before quantum degeneracy was achieved in sodium, [3] lithium,[10] and hydrogen.[11] Quantum degeneracy of fermionic potassium followed in 1999 [4] and cesium finally in 2003.[12]

For comparison, the first non-alkali species to be brought to quantum degeneracy was ytterbium in 2003.[13] (Helium degeneracy was achieved in 2001, using the alkali-like, metastable $^3S_1$ state.[14]) Due to its closed f-shell of electrons, ytterbium is structurally equivalent to a group-II atom, and it has since been joined by the "true" alkaline-earth species calcium [15] and strontium[16] in the society of Bose-condensed species. At the time of writing, only three species with open core shells – chromium, dysprosium and erbium – have been brought to degeneracy,[17, 18, 19] while direct laser cooling of even more structurally complex systems such as molecules is still in the early stages of development.[20]

As I joined my group at the UW 2007, the field of ultracold atoms was in the middle of a shift away from the now mature field of of single-alkali systems. With the growing availability of high-quality commercial lasers at almost any wavelength, two new directions were being explored.

The first of these was a growing interest in laser-cooling and trapping alkaline-earth and rare-earth atoms. Such two-electron atoms differ from alkali atoms in several important respects: the availability of narrow intercombination transitions for efficient laser cooling, wide ranges of stable isotopes with small isotope shifts, and large overall atomic mass, to mention a few. Whereas the alkalis all have electronic spin S=1/2 in the ground state, non-alkali elements range from S=0 (Yb, Sr) all the way up to to S=5. (Dy [18]) Finally,

the availability of metastable states and ultranarrow "clock" transitions provide additional experimental tools not available in one-electron species. For these reasons and others, a large number of groups were starting up new experiments with alkaline-earth-like atoms.

The second direction was toward production of stable, ground-state molecules of alkali atoms. Although direct cooling of molecules was a yet-inaccessible route, other experimental techniques involving magnetic Feshbach resonances had been demonstrated in single-species experiments.[21, 22] Several groups had already taken the step of adding a second atomic species to their experiments, and were exploring experimental pathways to ultracold, heteronuclear molecules.[23, 24] The principal motivation in trapping heteronuclear molecules is their intrinsic, permanent electric dipole moment. Interactions in ultracold gases are typically short-range, $(1/r^6)$ isotropic, and modeled simply as delta-function contact potentials, whereas polar molecules exhibit dipole-dipole interactions that are both long-range $(1/r^3)$ and anisotropic.

1.2 Why not both?

Our ambition from the outset was to combine these two directions into a single research project: to trap and cool mixtures of alkali and spin-singlet atoms, for production of heteronuclear molecules, and studies of strongly interacting mixtures. Such an experiment, while tapping into the most salient features of both of the above research areas, would also present unique opportunities. For instance, ground state molecules from two such species would have an odd number of valence electrons, leading to a net magnetic moment. Furthermore, differences in electronic structure could be exploited with spin-selective manipulation not typically available in bi-alkali systems.

Our species of choice were 6-lithium, a fermionic alkali atom with well-known properties, and ytterbium, which has several bosonic and fermionic isotopes available. In fact, laser-cooling of Ytterbium had previously been explored by Norval Fortson in the very same lab where we set up shop in 2007. Aside from the PI's first- and second-hand familiarity with these elements, Li and Yb were chosen for a number of reasons. Firstly, they constitute a mixture of alkali and spin-singlet species. Secondly, their very large mass ratio, $m_{Yb}/m_{Li} \approx 30$, opens up various studies of strongly mass-mismatched systems. Thirdly, the availability of a broad magnetic Feshbach resonance in ^{6}Li allows for studies of strongly interacting systems. And finally, because ytterbium has a large selection of naturally occurring fermionic and bosonic isotopes, with widely varying scattering properties.

The Li-Yb experiment started out with two long-term goals: to study thermodynamic properties of Li using Yb as a probe, and to synthesize LiYb molecules.

The former of these goals was largely inspired by a 2006 experiment at MIT, in which a superfluid of ^{6}Li was interrogated using a moving perturbation in the trapping potential.[25] This experiment succeeded in demonstrating Landau's prediction of a critical velocity in superfluids, but left several technical questions unanswered. These questions could be circumvented by replacing the perturbation with a heavy, ballistic, and microscopic probe such as an Yb atom. Our goal thus was (and still is) to study the structure of collective excitations in the BEC-BCS crossover regime using Yb as a perturbative or ballistic probe.

One of the initial inspirations for the second goal – to synthesize molecules – came from a range of experiments that have been carried out by various groups to search for a permant electric dipole moment (EDM) of the electron, as a test of fundamental symmetries in nature.[26] Such experiments have been carried out in atomic beams of ThO, PbO or YbF: heavy, paramagnetic, and polar molecules supporting a single unpaired electron. The LiYb molecule, due to its alkali-spin-singlet configuration, has such an unpaired electron, and may be used as a novel electron EDM probe. The advantage of our experimental proposal over existing ones was the possibility of very long interrogation times of several seconds: much greater than the millisecond timescales available in beamline experiments. Although this aspiration has since been tempered by theoretical predictions, suggesting that the LiYb dipole moment is significantly smaller than initially supposed, there is still a possibility that such an experiment could be carried out, either with ground-state LiYb molecules or with the metastable LiYb* system.

However, even beyond such an EDM search, paramagnetic, polar molecules such as LiYb offer a marvellously wide range of interesting experiments. The long- and short-range interactions between such molecules may be studied in a smooth trap, or in an optical lattice. In the latter, they may be used to simulate lattice spin models, and study exotic condensed matter phases. Chemical reactions could be studied, and controlled with externally applied electric and magnetic fields. Their multiple degrees of freedom also make them an attractive candidate for scalable quantum computing schemes.

Aside from these experimental paths in the Li-Yb system, our apparatus has also formed the starting point for a single-species experiment with ytterbium In this experiment a three-arm atom interferometry scheme, controlled by laser pulses, will be used to accurately measure the fine structure constant α. At the time of writing, this project has completed its data collection in the Li-Yb machine, and moved on to a separate trapping apparatus.

1.3 *The Machine* awakens

I was fortunate enough to join the PhD program almost concurrently with our PI arriving at the University of Washington, and was able to join the experiment at its outset. Our very first group meeting was held in the lab, which consisted of two empty tables and some scattered remnants of the previous experiment: an old wavemeter, two Titanium-Sapphire ring lasers, some RF electronics, and the venerable "Norvalator" vacuum chamber.

Since then a complex machine has been erected over several years. Our complex system of vacuum chambers was baked out and brought to UHV just in time for the holidays in 2008, after a year of careful planning and numerous design revisions. The first lithium atoms were trapped in a magneto-optical trap (MOT) during Spring Break in 2009, and successfully transferred to an optical dipole trap (ODT) in December of the same year. Meanwhile, with the competent aid of our first post-doc Vlad, we succeeded in laser-trapping ytterbium on the narrow intercombination line in September 2009 and had it co-trapped with lithium in the ODT just in time for the 2010 March Meeting in Portland. Over the next year we studied the stability of the mixture, and developed a scheme for cooling the two species together, culminating with the observation of simultaneous quantum degeneracy in April 2011. Our experiment had thus come to full maturity, and was ready to start chipping away at the boundaries of human knowledge!

The machine, now fully operational, has since been generating a steady stream of scientific research, which shows no sign of stagnating. I consider myself lucky to have participated in the building stages of the experiment, which I enjoyed immensely, and to have been around to partake in the first fruits of this large project.

Part I

Quantum Gases of Atoms & Molecules

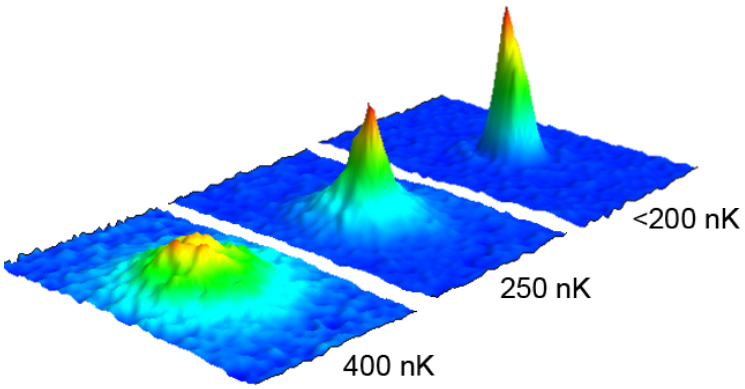

2 Bose & Fermi Physics

The study of quantum many-body physics in atomic traps has existed for almost 20 years, and has unquestionably become a mature field. Many references already exist detailing the behavior of trapped Bose and Fermi gases,[27, 28, 29, 30] and only a brief outline will be given here.

2.1 Bosons & fermions in harmonic traps

In classical statistical mechanics, the phase space density of particles in a non-interacting gas subject to an external potential is given by the Boltzmann distribution

$$f(\vec{p},\vec{x}) = e^{-\beta\epsilon} \tag{2.1}$$

where $\beta = 1/(k_B T)$, and $\epsilon = \epsilon(\vec{p},\vec{x})$ is the energy of a single particle with position $\vec{x}$ and momentum $\vec{p}$. In quantum statistics, however, the classical distribution is replaced by the occupancy function

$$f = \frac{1}{e^{-\beta(\epsilon-\mu)} \mp 1} \tag{2.2}$$

which gives the expected number of particles found in a quantum state with energy ϵ. The new parameter μ is the chemical potential of the system. We use the convention of the upper sign (-) pertaining to bosons, and the lower sign (+) to fermions.

The local density approximation (LDA)[1] prescribes the consideration of a small unit cell, across which the potential can be taken to be constant, and modeling the particles within this volume as a homogeneous quantum gas. The density of particles within that cell can then be found by adding up all the possible momenta.

$$n(\vec{x}) = \int \frac{1}{e^{-\beta\left(\frac{p^2}{2m}+U(\vec{x})-\mu\right)} \mp 1} \frac{d^3p}{h^3} \tag{2.3}$$

$$= \pm\frac{1}{\lambda_{TdB}^3} \mathrm{Li}_{3/2}\left(\pm\xi e^{-\beta U(\vec{x})}\right) \tag{2.4}$$

[1]The LDA is held to be valid in systems in the thermodynamic limit, where the chemical potential is much greater than the energy level separation. In such cases, f can be treated as a smooth function, sums over quantum states can be replaced with integrals.

Previous Page: Formation of a Bose-Einstein condensate in a gas of ^{174}Yb atoms. Each plot shows a 2D projection of the momentum distribution of the atoms.

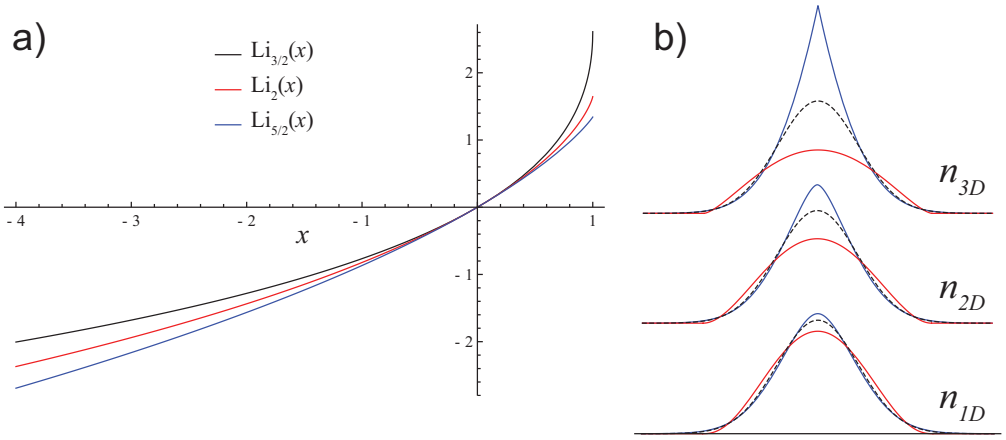

Figure 2.1: Effects of Bose and Fermi statistics. a) The polylog function $\mathrm{Li}_{3/2}(x)$, plotted on the domain [-3,1] b) Density distributions of three gases with equal mean particle energy: a Fermi gas at $T = 0$ (red line), a Bose gas at $T = T_C$ (blue line), and a classical Boltzmann gas (dashed, black line). The same gases are plotted with one and two dimensions integrated out. Note that the contrast becomes less pronounced in reduced dimensions.

Here λ_{TdB} is the thermal de Broglie wavelength, and $\xi = e^{\beta\mu}$ is the fugacity of the system. The function $\mathrm{Li}_n(x)$ is the n-th order polylogarithm of x, which can be expressed as

$$\mathrm{Li}_n(x) = \sum_{k=1}^{\infty} \frac{x^k}{k^n} \tag{2.5}$$

The polylogarithm for relevant values of n is plotted in Figure 2.1a. Note how the functions curve away from the x-axis on the positive side, and toward the x-axis on the negative side. This causes the density of a Bose gas to tend to build sharp peaks, whereas the Fermi density tends to form broad, flat peaks. This, of course, is just a consequence of the propensity of bosons to lump together and fermions to repel one another, often referred to as "Fermi pressure." This behavior emerges only at low temperatures, where the fugacity approaches unity. At higher temperatures, where $\xi \ll 1$, the gas probes only the region of the polylogarithm very close to zero, where it is approximately linear, and the Boltzmann distribution is recovered.

The form of the polylogarithm given in equation (2.5) can be used to analytically integrate the polylog function. This is useful for deriving the lower-dimensional distributions, where one or more dimensions are integrated out. In the common case of a harmonic trap, $U(\vec{x}) = \sum \frac{1}{2} m\omega_i^2 x_i^2$,

$$n_{3D}(x,y) = \pm\frac{1}{\lambda_{TdB}^3}\mathrm{Li}_2\left(\pm\xi e^{-\beta\frac{1}{2}m\left(\omega_x^2x^2+\omega_y^2y^2+\omega_z^2z^2\right)}\right) \tag{2.6}$$

$$n_{2D}(x,y) = \pm\frac{1}{\lambda_{TdB}^2}\left(\frac{k_BT}{\hbar\omega_z}\right)\mathrm{Li}_2\left(\pm\xi e^{-\beta\frac{1}{2}m\left(\omega_x^2x^2+\omega_y^2y^2\right)}\right) \tag{2.7}$$

$$n_{1D}(x,y) = \pm\frac{1}{\lambda_{TdB}}\left(\frac{k_BT}{\hbar\sqrt{\omega_y\omega_z}}\right)^2\mathrm{Li}_{5/2}\left(\pm\xi e^{-\beta\frac{1}{2}m\omega_x^2x^2}\right) \tag{2.8}$$

$$N = \pm\left(\frac{k_BT}{\hbar\bar{\omega}}\right)^3\mathrm{Li}_3\left(\pm\xi\right) \tag{2.9}$$

Here $\bar{\omega} = (\omega_x\omega_y\omega_z)^{1/3}$ is the geometric mean of the trap frequencies. Note that the order of the polylog increases by $1/2$ each time we reduce the dimensionality. By inspecting equation (2.5), one can see that this corresponds to an attenuation of the non-linear terms in the series expansion of $\mathrm{Li}_n(x)$. Since the first term corresponds to the classical limit, this means that the quantum characteristics become less pronounced in lower-dimensional projections. (See Figure 2.1b.)

The 2D and 1D distributions are of particular experimental interest, since techniques for imaging atom clouds do not return the full, 3-dimensional distribution, but only the projection (column density) along some axis.

It is also of experimental interest that the density distributions maintain their functional form after release from the trap. To calculate the distribution after some time of flight τ, one simply applies equations (2.6)-(2.8) with a rescaled set of trap frequencies

$$\omega_i \to \frac{\omega_i}{\sqrt{1+\omega^2\tau^2}} \tag{2.10}$$

and divides by an overall factor $(1+\omega^2\tau^2)^{3/2}$ to maintain normalization.

In the zero-temperature limit, the Fermi distribution function becomes a step function with a sharp cutoff at $\epsilon = \mu$. Thus, the integral in equation (2.3) evaluates trivially to yield the zero-temperature Fermi density distribution,

$$n_{T=0}(\vec{x}) = \int\limits_{p<\sqrt{2m(\mu-U(\vec{x}))}}\frac{d^3p}{h^3} \tag{2.11}$$

$$= \mathrm{Max}\left\{\frac{1}{6\pi^2}\left[\frac{2m}{\hbar}\left(\mu-U(\vec{x})\right)\right]^{3/2},0\right\} \tag{2.12}$$

Note that the density distribution goes sharply to zero at the point where $\mu = U(\vec{x})$. In

a harmonic trap, one obtains the Fermi radius

$$R_F = \sqrt{\frac{2E_F}{m\omega^2}} \tag{2.13}$$

where E_F is the Fermi energy – the highest particle energy in the system at zero temperature – which, by construction, is equal to the zero-temperature chemical potential. By integrating equation (2.12) over all space, we derive a useful expression for the Fermi energy.

$$E_F = (6N)^{1/3}\hbar\bar{\omega} \tag{2.14}$$

This energy can furthermore be converted to a characteristic temperature, $T_F = E_F/k_B$. The Fermi temperature marks the regime where the quantum behavior of the system begins to emerge, and allows the experimenter to report temperatures in terms of the system-independent dimensionless parameter T/T_F. For homogeneous systems, or when working in the LDA, it is also common to assign a Fermi wavevector k_F such that $E_F = \frac{\hbar^2 k_F^2}{2m}$.

In the case of bosons, the occupancy function f becomes non-analytical at $\mu = 0$, where it predicts an infinite number of atoms in the ground state. This, of course, marks the onset of Bose-Einstein condensation (BEC). Below this point, equation (2.9) does not account for the condensed atoms, but only the thermal component N_{th}. It is then instructive to rewrite equation (2.9) as

$$N_{th} \;=\; N\left(\frac{T}{T_C}\right)^3, T \leq T_C \tag{2.15}$$

where the subscript "th" indicates the thermal component of the gas, N is the total number of atoms, and the critical temperature

$$T_C = \left(\frac{N}{\zeta(3)}\right)^{1/3}\hbar\bar{\omega} \tag{2.16}$$

is the temperature of the BEC phase transition. The expression includes the Riemann zeta function $\zeta(3) = \mathrm{Li}_3(1) \approx 1.202$. It may come as a surprise that the critical temperature for Bose condensation has exactly the same scaling behavior as the Fermi temperature, (differing only by a factor ≈ 1.7 for equal particle number and trap frequencies) given the very different derivations used above. This is, however, a straightforward consequence of quantum statistics emerging when the phase space density (PSD) – the probability of a given quantum state being occupied – approaches unity. At temperatures above degeneracy, the PSD takes the approximate (classical) form $\rho = n\lambda_{TdB}^3$.

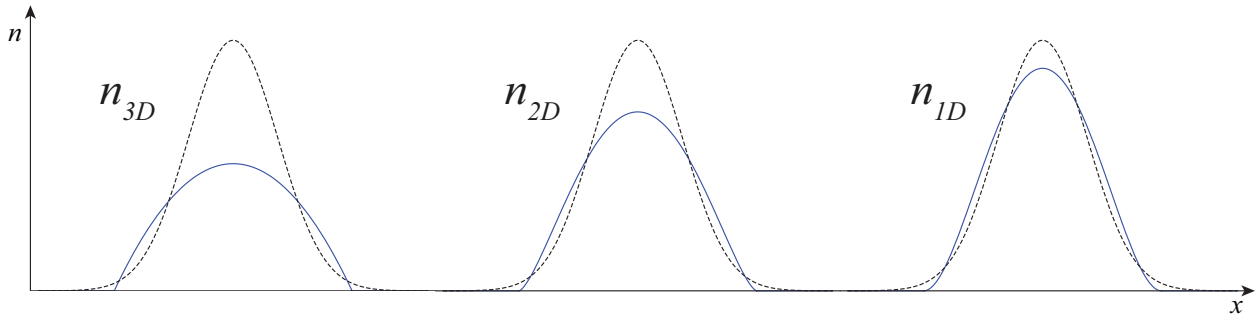

Figure 2.2: Density profile of a BEC, with 0, 1, and 2 dimensions projected out. As with the thermal distributions in Figure 2.1, the sharp features are increasingly washed out in higher dimensions.

We may also manipulate equation (2.15) to yield the fraction of atoms in the condensate.

$$\frac{N_0}{N} = 1 - \left(\frac{T}{T_C}\right)^3, \; T \leq T_C \tag{2.17}$$

In practice, although the ground state occupancy number of equation (2.2) diverges as $\mu \to 0^-$, one nonetheless ends up with $\mu > 0$ after the onset of condensation, since repulsive interparticle interactions within the condensate raise the energy of the ground state. Solving the nonlinear Schrödinger equation (Gross-Pitaevskii equation) in the Thomas-Fermi limit, we derive a functional form for the condensate density distribution.

$$n_C(\vec{x}) = \text{Max}\left\{\frac{m}{4\pi\hbar^2 a}\left(\mu - U(\vec{x})\right), 0\right\} \tag{2.18}$$

Here a is the s-wave scattering length.[2] For a harmonic potential, the projected distributions in reduced dimensions (plotted in Figure 2.2) have the form

$$n_{C,2D} \propto \left(\mu - \frac{1}{2}m\omega_y^2 y^2 - \frac{1}{2}m\omega_x^2 x^2\right)^{3/2} \tag{2.19}$$

$$n_{C,1D} \propto \left(\mu - \frac{1}{2}m\omega_x^2 x^2\right)^2 \tag{2.20}$$

[2]The s-wave scattering length a is an interaction parameter that is independent of the finer details of the scattering potential. Its validity as a one-stop-shop for modeling interactions is limited to dilute gases, where 2-body interactions dominate, at temperatures below the s-wave limit. This is the regime where typical scattering momenta $k \ll 1/r_{eff}$, where r_{eff} is the effective range of the scattering potential. Given the diluteness and low temperature involved in quantum fluid experiments, it is usually safe to talk about interactions simply in terms of a.

2.2 Feshbach resonances

An area of atomic physics that has been the subject of intense theoretical and experimental scrutiny in recent years is the studies of dilute, strongly interacting gases. With the use of Feshbach resonances, we are now able to access a highly idealized regime that is both dilute and strongly interacting; i.e. the scattering length a is greater than the interparticle spacing, while the effective range r_{eff} of the interaction potential remains much smaller than other length scales in the system.

$$r_{eff} \ll n^{-1/3} \lesssim a \tag{2.21}$$

Broadly speaking, a quantum scattering resonance occurs when a bound or quasi-bound state of the interatomic potential has nearly the same energy as the scattering state. Scattering events with nearly zero energy are then greatly enhanced by their proximity to the bound state, and such particles experience an amplified scattering cross-section.

A specific type of resonance, known as a Feshbach resonance, may occur in systems in which there are multiple, weakly coupled internal states. One example is two alkali atoms with nonzero nuclear spin. Two such atoms, when they collide, may be in the singlet state of their total electronic spin, $S = 0$, or in a triplet state $S = 1$. Mediated by their hyperfine structure, the atoms may "flip" from one such electronic configuration to the other, if it is energetically permitted. In the event that a bound state of one spin state (called the "closed channel") is within some energy range δ of a scattering state of the other, (the "open channel") a Feshbach resonance exists, and the scattering length of the system diverges. Quantum perturbation theory tells us that the width δ of such a resonance is determined by the strength of the hyperfine coupling Hamiltonian that drives the spin-exchange.

A degeneracy such as in the above example may be induced using an external magnetic field, which adds a selective bias to the energy of the $S = 1$ state. This sort of magnetic Feshbach resonance is a tool used by a large number of research groups to access various interaction regimes.

One remarkable feature of Feshbach resonances is that the coherent coupling between the open and closed channel gives rise to a bound state of the dressed system. The binding energy of this bound state decreases as one approaches resonance from one side, and reaches zero at resonance, where the bound state dissolves into the free particle continuum. Such Feshbach states constitute very weakly bound molecules, with internuclear separation of order a, and binding energy $\hbar^2/(ma^2)$. The molecules may subsequently be adiabatically brought away from the resonance, where the open and closed channels are decoupled and the molecules remain permanently bound.

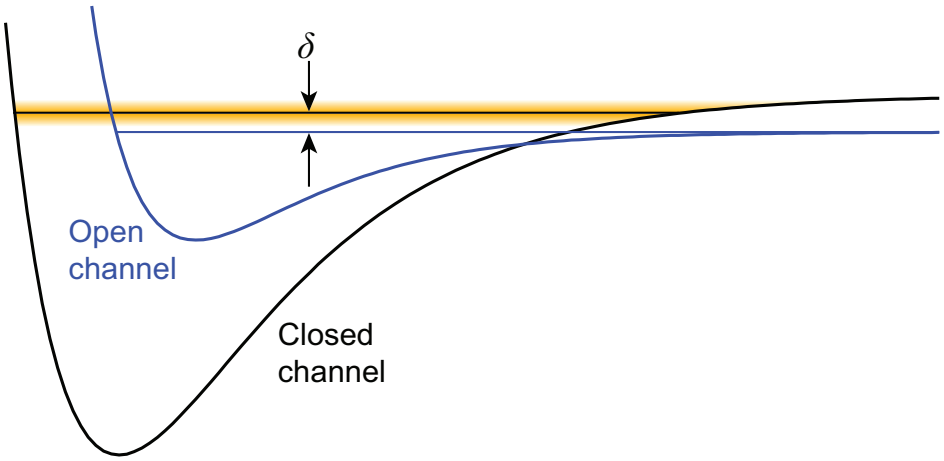

Figure 2.3: A Feshbach resonance occurs when, in a system with two or more internal configurations the bound state of one configuration couples strongly to the scattering state of another. Here, the open channel potential is shown in blue, the closed channel potential in black, and the width of the coupling Hamiltonian in yellow.

The vanishing of the bound state is, of course, related to the resonant scattering behavior, as hinted earlier in section. In fact, at the resonance point the scattering length flips sign, from positive to negative infinity, causing the interactions to go from repulsive to attractive. This gives the experimenter access to a vast range of interaction regimes, and the crossing from attractive to repulsive interactions has been one of considerable recent interest, although, as we shall see, this transition is not as abrupt as one might believe from fig. 2.4.

2.3 Strongly interacting fermions

With the availability of widely tunable interactions offered by Feshbach resonances, atomic physicists have been able to conduct a fascinating array of studies on the few- and many-body physics of strongly interacting particles. In such studies, fermions are frequently chosen over bosons, as the physics involved is applicable to many "real-world" problems in nuclear physics (structure of heavy nuclei, neutron star crusts) and condensed matter physics, (superconductivity, ferromagnetism) all of which involves spin-$1/2$ particles. Furthermore, a degenerate Fermi gas, by virtue of its repulsive Fermi pressure, is far more dilute than a BEC, and thus better satisfies the condition of equation (2.21). Finally, the Pauli-suppression of s-wave interactions between identical particles strongly suppresses many-body processes in a two-component Fermi gas.

Very close to resonance, where the 2-body scattering length overtakes the interparticle spacing, $a \gtrsim n^{-1/3}$, the notion of a scattering length becomes vague, as the individual scattering events can no longer be considered as independent, or evaluated in the canonical

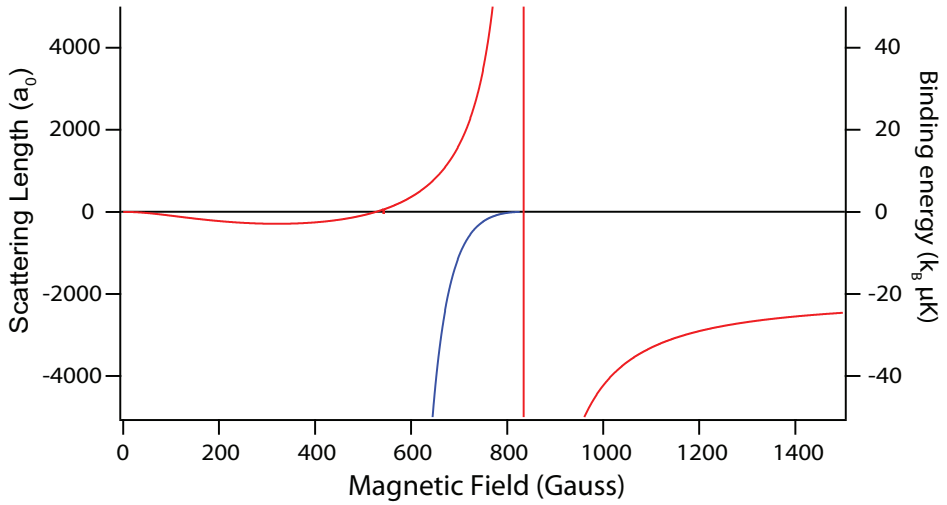

Figure 2.4: The ^{6}Li Feshbach resonance at 834G. By tuning the magnetic field, one may access a wide range of interactions, (red line) from strongly repulsive ($a \gg 0$) to strongly attractive ($a \ll 0$), as well as interaction-free regions at the zero-crossing at 528G. A bound state of the Li_2 molecule (blue line) dissolves into the free-particle continuum at the resonance point, giving rise to the divergent scattering behavior.

"far-field" picture $r \gg a$. Furthermore, as the de Broglie wavelength of typical scattering partners (which is of the order $1/k_F$ for a degenerate gas) becomes comparable to a, we expect the scattering cross-section to develop an energy dependence. We can see this quantitatively by studying the s-wave scattering amplitude

$$f_0 = \frac{1}{2ik}\left(e^{2i\delta_0} - 1\right) \tag{2.22}$$

where the phase shift δ_0 relates to the scattering length as $\tan \delta_0 = -ka$. In the low-energy limit, or weak interaction limit, $f_0 \approx -a$, whereas in the limit $\pm ka \gg 1$ – often called the unitary limit – the scattering amplitude saturates at $f_0 = \pm i/k$. The scattering length has then vanished from the scattering Hamiltonian, and all interaction effects in the system must be universal – that is independent of a.

If one wishes to quantify this behavior, one might consider a zero-temperature Fermi gas in a homogeneous potential. The chemical potential, which for a non-interacting gas is equal to E_F at zero temperature, may then be modeled as

$$\mu = E_F + U_{int} \tag{2.23}$$

The interaction term U_{int} is typically a function of the scattering length. However, in the unitary limit the scattering length is no longer a valid parameter: In fact, the only length scale left to choose from is the Fermi wavelength $1/k_F$, and the only energy scale the Fermi

energy $\frac{\hbar^2 k_F^2}{2m}$. U_{int} must therefore be some multiple of the Fermi energy, and we write

$$\mu = (1+\beta)E_F \tag{2.24}$$

where β is the so-called Bertsch parameter, which is yet to be determined. Its notational overlap with the reciprocal temperature is an unfortunate, but well-established convention. In some cases the parameter $\xi = (1+\beta)$ is given instead.

Using the LDA, we may treat an inhomogeneous Fermi gas in any smooth potential as a distribution of homogeneous systems with local chemical potential μ_{loc} and local Fermi energy ϵ_F. We may then extract all the other parameters of interest for the *global* system. For a harmonic trapping potential, we compute

$$\mu \rightarrow (1+\beta)^{1/2}\mu \tag{2.25}$$
$$E_F \rightarrow (1+\beta)^{-1/2}E_F \tag{2.26}$$
$$R_F \rightarrow (1+\beta)^{1/4}R_F \tag{2.27}$$
$$c \rightarrow (1+\beta)^{1/4}c \tag{2.28}$$

where μ is now the global chemical potential, and c is the speed of sound in the gas. The arrows indicate the mapping of a parameter in the interaction-free case to the unitary regime. These are just a few examples of how every measure of the system ends up scaling as some power of $(1+\beta)$.

The only problem is that the constant β is really hard to calculate or measure! Great effort, both theoretical and experimental has gone into pinning down the value of this universal parameter, and it is now generally agreed that $\beta \approx -0.6$. The negative value means that universal interactions are intrinsically attractive, whereas the condition $\beta > -1$ guarantees that unitary Fermi gases are thermodynamically stable: in the opposite case, where $(1+\beta) < 0$, the interactions would overcome the Fermi pressure, causing the gas to collapse.

2.3.1 The BEC-BCS crossover

Let us now briefly turn to the case of fermions with *weak* attractive interactions. It is known from Bardeen-Cooper-Schrieffer (BCS) theory that such a system exhibits a superfluid phase transition at a critical temperature, which is of order $T_C \sim T_F \exp(-\pi/k_F|a|)$ when $k_F|a| \ll 1$. In condensed matter systems, where typical Fermi temperatures are several times 10^4K, this temperature is usually a few Kelvin. In atomic systems, due to their extreme diluteness, such transition temperatures are unattainably low, and one is forced to

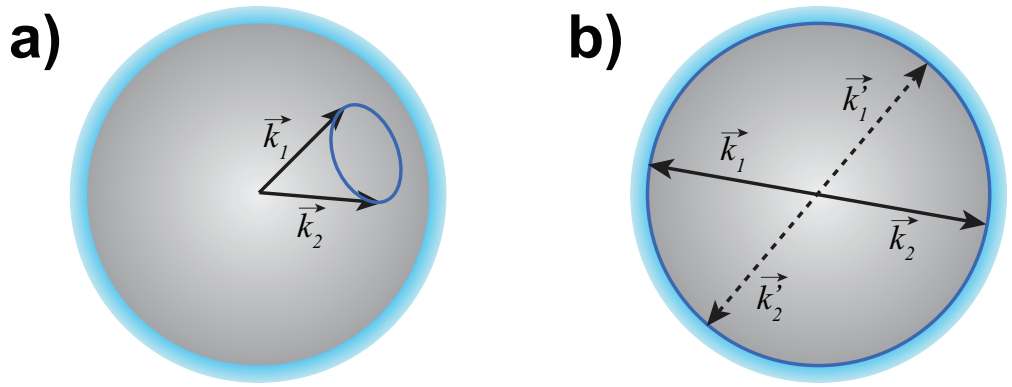

Figure 2.5: Cooper pairing in a two-component Fermi gas. a) Only particles near the Fermi energy, where unoccupied outgoing channels exist, may undergo scattering, and the final momentum states must also lie on the Fermi surface. Two particles with a net momentum are therefore constrained to scatter into the 1-dimensional circle shown. b) Particles with zero net momentum, however, may scatter into any other point on the Fermi surface, and thus will interact far more strongly.

seek a non-idealized superfluid regime where $1/k_F a$ is of order unity.

Such Fermi superfluidity is a consequence of the formation of so-called Cooper pairs near the Fermi surface of the particles' momentum distribution. Since identical, ultracold fermions do not undergo s-wave scattering, a balanced mixture of two distinguishable components (ents (e.g. different spin sta.g. different spin states) is required. The Cooper pairing effect is, roughly speaking, a consequence of Pauli exclusion: any scattering event between two particles is going to have its outgoing channel constrained to momentum states that are not already occupied. At very low temperatures, the only states that are both Pauli-allowed and energetically allowed are in the narrow band of partially occupied states near the Fermi surface. This effectively reduces the scattering problem to two dimensions, as shown in Figure 2.5. Now, according to quantum mechanics, bound states of weak attractive potentials that are forbidden in 3D may still exist in a 2D system, and this is the mechanism that allows the formation of Cooper pairs. The constituents of the Cooper pairs always have equal and opposite momentum, and retain momentum and phase entanglement over large interparticle separations. A fully paired Fermi gas, as predicted by the BCS model, will therefore exhibit long-range quantum phase coherence, a hallmark of superfluidity. Superfluidity in ultracold atomic systems was first demonstrated in 2005.[6]

In the opposite regime, where interactions are repulsive, such Cooper pairing cannot exist, since a repulsive potential will support no bound state in any dimensionality. However, a superfluid system may still exist on the repulsive side of the Feshbach resonance. This is due to the emergence of the weakly bound Feshbach state, which binds atoms pairwise into

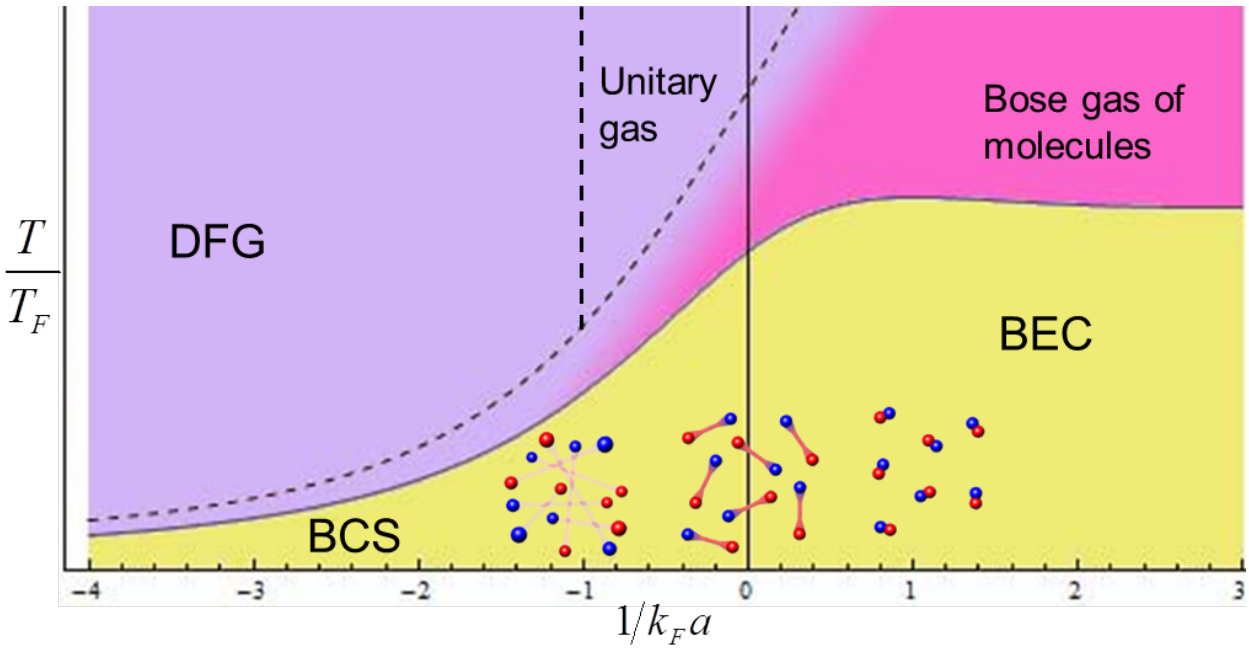

Figure 2.6: Phase diagram of a gas of fermionic atoms near the BEC-BCS crossover. The x-axis is the interaction parameter $1/k_F a$, which has a linear relationship to the magnetic field near resonance. Note that the repulsive (BEC) side of resonance is on the right hand side of the plot, in contrast to Figure 2.4. The curved, dashed line is an extrapolation of the (exponential) behavior of the transition temperature in the deep BCS regime. The area between the dashed and solid line is the pseudogap, in which the fluid is partially Cooper-paired. The inset figure, showing the transition from long-range Cooper pairs to tightly bound molecules, is courtesy of [28].

molecules. Such molecules are necessarily composite bosons, and may therefore form a BEC. Unlike Fermi superfluidity, the critical temperature for Bose condensation remains relatively large even as the interaction strength diminishes. A BEC of molecules was first demonstrated experimentally in 2003.[22, 31]

The interesting question is then what happens in the region close to resonance, on the interface between the BEC and BCS superfluids. As it turns out, there is no quantum phase transition as the interactions go from repulsive to attractive. Instead, there is a smooth "crossover" region in the regime of universal interactions, where the unitarity condition $|k_F a| \gtrsim 1$ is satisified. In the crossover regime the size of the Feshbach molecules becomes comparable to the interparticle spacing, and the molecular bonds gradually transform into long-range Cooper pairs.

There are various interesting questions that are still at least partially unanswered regarding the detailed nature of the BEC-BCS crossover. For instance, how does the critical temperature vary with the interaction parameter in the crossover region? How do the collective

and single-particle excitation spectrums (which determines the robustness of the superfluid) behave in the unitary limit? And is there other interesting behavior in the unitary regime near the transition temperature?

The shape of the phase surface in Figure 2.6 is one answer to the first question, based on theoretical estimates using a relatively naïve Landau-Ginzburg model.[32] Several groups have since achieved consistent theoretical results, using fixed-node Monte Carlo methods,[33, 34] and the critical temperature has also been carefully measured at resonance in one experiment.[35] The second question was the subject of a cursory experimental study, in which the dispersion relation of the lowest excitation modes were estimated through measurements of the critical velocity.[25] The third question ties in with the notion of a "pseudogap," believed to exist above the transition point, where the Fermi gas is partially Cooper paired, but not yet in a superfluid state.[36, 37]

2.3.2 Imbalanced superfluids

As mentioned in the previous section, a Fermi superfluid requires the presence of two distinguishable components, which we denote $\uparrow$ and $\downarrow$. Furthermore, the components must exist in equal abundance for superfluid to exist. In an imbalanced mixture, the respective Fermi momenta of the two components would be different, and the Fermi surfaces would not align. Figure 2.5 shows the importance of the Cooper partners having equal and opposite momenta. We should therefore expect superfluidity to be strongly suppressed in a mixture with a spin imbalance such that $E_F(\uparrow) - E_F(\downarrow) > k_B T$. In a harmonically trapped gas in the limit $T \ll T_F$, we therefore expect superfluidity to be quenched when the polarization of the mixture

$$P = \left| \frac{N_\uparrow - N_\downarrow}{N} \right| > \frac{3}{2} \frac{T}{T_F} \tag{2.29}$$

The numbers $N_{\uparrow(\downarrow)}$ are related to the Fermi energy of each spin state by equation (2.14).

This quenching mechanism has been tested by two groups [38, 7] both of whom discovered, remarkably, that superfluidity persists in the polarized mixture. This is due to the so-called pairing gap Δ, the binding energy of a single Cooper pair. When this binding energy is greater than the chemical potential difference $\mu_\uparrow - \mu_\downarrow$ the minority component will spontaneously undergo spatial contraction, increasing its local density at the center region of the trap to match that of the majority component, thus aligning the Fermi surfaces and enabling Cooper pairing. The true ground state of the system is thus a phase-separated system, consisting of a superfluid "core" surrounded by a halo of unpaired atoms. In the strongly interacting BCS regime, where these experiments were conducted, superfluidity was observed

all the way up to $P \approx 0.5$, much greater than the normalized temperature $T/T_F \lesssim 0.1$. The onset of phase separation was observed at $P \approx 0.1$, consistent with equation (2.29).

An interesting extention to the studies of such physical phenomena is what would happen if the imbalance was not due to unequal numbers of the two components, but (for instance) unequal mass. There is no *a priori* reason why Cooper pairing could not exist between mass-mismatched components; however, the functional form of the local Fermi energy scales inversely with mass, so the components would necessarily have mismatched Fermis surfaces, unless compensated by an appropriate number imbalance. Moreover, there are theoretical predictions suggesting the existence of a critical mass ratio 13.6, above which superfluids become highly unstable to collapse through many-body recombination channels.[39] Needless to say, there is a lot of work to be done, both theoretically and experimentally, in this class of physical systems.

3 Molecules & Dipolar Quantum Gases

In recent years, the field of quantum gases has enjoyed considerable experimental progress in developing and studying molecules. Although some groups have developed tools for slowing and trapping molecules directly from "hot" sources of a few kelvin,[20, 40, 41, 42] the largest strides toward ultracold molecules have come from controlled synthesis in pre-cooled gases of atoms.[21, 24]

Ultracold molecules offer many interesting features not present in atomic quantum gases. For instance, the density of states near the absolute ground state is far greater, leading to strong perturbative couplings; electric dipole-dipole interactions are available in heteronuclear systems; ultracold, controlled chemical reactions offer a wide range of interesting experiments; and various combinations of atomic species with different mass and electronic structure provides a far wider range of available systems to study.[43, 44]

Although our lab has only taken preliminatry steps toward synthesizing ultracold molecules at the time of writing, the motivation of building heteronuclear LiYb dimers has been a constant force behind our research. I will therefore in this chapter outline some of the properties of cold molecules, as well as experimental techniques and results that have shaped the research in our lab.

3.1 Molecular Notation and Structure

Molecular structure can be broken down into two components: electronic and rotational-vibrational. The former is similar to the atomic case; the latter is due to relative motion of the constituent nuclei. The Born-Oppenheimer approximation prescribes that the electronic and nuclear degrees of freedom may be separated and treated independently.[45] This is because the motion of the electrons is much faster than that of the nuclei, and can be treated at each point in time as though the nuclei were fixed in space. The slow nuclear motion is then treated independently, with the electronic Hamiltonian providing a potential energy $U(r)$, where r is the internuclear separation. (See Figures 3.1-3.2.)

As is well-known to any young physicsist who has studied for the GRE exam, atomic energy levels are denoted by three operators, $\mathbf{S}$, $\mathbf{L}$ and $\mathbf{J}$. The corresponding quantum numbers are typically grouped into a *term symbol* of the form ${}^{2S+1}L_J$. In the absence of spin-orbit coupling, these quantum numbers – and their projections m_s, m_l and m_j – all commute with the system Hamiltonian. However, when we introduce spin-orbit coupling the magnetic quantum numbers m_s and m_l cease to be good quantum numbers, and the system is entirely determined by s, l, j, m_j. In most atomic species, hyperfine coupling due to the nuclear spin $\mathbf{I}$ further changes the useful quantum numbers in a similar fashion.

3.1.1 The molecular term symbol

In diatomic molecules, similar arguments are used to derive the angular momentum spectrum.[46] One of the key differences from the single-atom case is the lack of spherical symmetry in a molecule. (Even in absence of spin-orbit coupling.) In the coordinate frame of the internuclear axis, the Hamiltonian is no longer spherically symmetric; thus, $[H, \mathbf{L}^2] \neq 0$ and l is no longer a good quantum number. One might intuitively imagine an orbiting valence electron acting as a gyroscope, which would necessarily be disturbed were one to attempt to rotate the rest of the molecule.

Instead, the electronic structure is determined by the quantum numbers s, m_s, m_l and m_j, where the quantization axis is understood to be the internuclear axis. The corresponding molecular term symbol has the form

$$^{2S+1}\Lambda_{\Omega} \tag{3.1}$$

where $\Lambda = |m_l|$ gives the electronic orbital angular momentum about the internuclear axis of the molecule. The absolute value is chosen to avoid degenerate values of Λ, and also to fall in line with the atomic notation, which permits only non-negative values of L. In further analogy to the atomic term symbol, which uses the letters S,P,D,F... to denote orbital angular momentum value, the corresponding greek capital letters are used to represent Λ:

$$\Lambda = \Sigma, \Pi, \Delta, \Phi, ... \tag{3.2}$$

With the introduction of the spin-orbit coupling Hamiltonian $H_{SO} = AS_zL_z$, the degeneracy of the spin eigenstates is broken. The energy then depends on the total angular momentum $\Omega = m_s + m_l$ along the quantization axis. To prevent degenerate values of Ω we assume the direction of the quantization axis to be parallel to the orbital angular momentum, i.e. $m_l \geq 0$. Nonetheless, in contrast to the analogous atomic symbol J, Ω is allowed to take both positive and negative values whenever the electronic spin is greater than the orbital angular momentum.

The attentive reader will notice that, with the exception of the $^1\Sigma_0$ level, all spectroscopic levels have a degeneracy factor of exactly 2, (neglecting hyperfine structure) corresponding to the forward and time-reversed copies of the molecule. This degeneracy can be recast into the eigenbasis of an arbitrary reflection through any plane that contains the internuclear axis, from which it is trivial to build one symmetric and one antisymmetric wavefunction: $\Lambda^{\pm}$ from the forward and reverse wavefunctions $e^{\pm im_\Omega \phi}$. This distinction is of little spectroscopic interest, except in the special case of $\Lambda = 0$, where only one orbital state exists. The symmetry of this state depends on symmetries of the internal electronic structure, and the

resulting pure state is denoted Σ^+ or Σ^-.

3.1.2 Rovibrational states

In addition to the electronic orbitals, molecules exhibit rotational and vibrational degrees of freedom, which show up as substructure of the electronic energy levels. The corresponding quantum numbers are N and ν. This molecular motion adds a large number of additional states to the physical system.

One might worry that molecular rotation would complicate the above discussion, as the internuclear axis, which we used as a quantization axis, is no longer an inertial reference frame. However, as discussed, the molecular rotation couples strongly to the electronic orbital angular momentum, which in turn couples to the electronic spin. This, along with the Born-Oppenheimer approximation, justifies the use of the internuclear axis for quantization of electronic structure: in a rotating molecule, the electronic orbitals will adiabatically follow the motion of the nuclei.

The energy of molecular rotation, by analogy to the classical rigid rotor, is $H_R = \mathbf{J}^2/(2\mu r^2)$, where $\mathbf{J}$ is the angular momentum operator, μ is the reduced mass of the system, and r is the internuclear separation. The eigenstates of H_R,

$$E_N = \frac{\hbar^2 N(N+1)}{2\mu r^2},\ N = 0, 1, 2, ... \tag{3.3}$$

have much higher density than the electronic orbital energies, which have structure of order $\hbar^2/(m_e r^2)$. We therefore expect to find a very large number of rotational levels between any two electronic states.

The structure of vibrational levels is far more complicated, as the molecular potential depends on a large number of mutual interactions between electronic orbitals. It can, however, be roughly estimated from a model in which the molecular potential is a harmonic oscillator of depth U and width r. A typical molecular potential depth is somewhat smaller than the electronic binding energy: $U \sim \hbar^2/(2m_e r^2)$. Thus, at the boundary of the model potential,

$$\frac{1}{2}\mu\omega_{osc}^2 r^2 = \frac{\hbar}{2m_e r^2} \tag{3.4}$$

Solving for the harmonic oscillator frequency ω_{osc}, we estimate

$$E_\nu = \hbar\omega_{osc} \sim \frac{\hbar^2}{\sqrt{m_e\mu}r^2} \tag{3.5}$$

Comparing this to the above expressions, we see that the vibrational level spacing is approximately the geometric mean of the rotational and electronic spacings, and that the

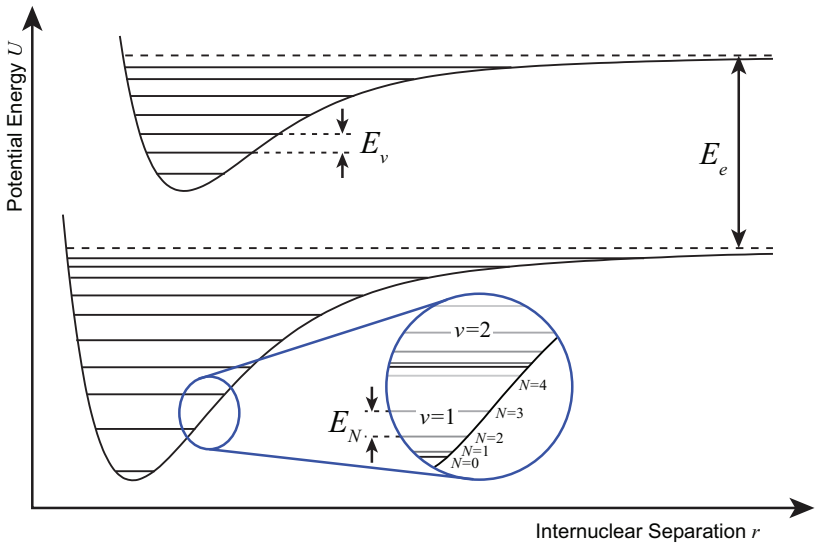

Figure 3.1: Schematic of rotational, vibrational and electronic structure. The vibrational and rotational level splittings, E_ν and E_N have been greatly exaggerated for clarity. A molecular potential typically has $\mathcal{O}(100)$ vibrational levels, each with a manifold of rotational sublevels.

three Hamiltonians differ in strength by an order parameter $\sqrt{\mu/m_e} \sim 100$.[3]

3.1.3 Too much of a good thing?

While the large density of rovibrational levels provides many unique experimental opprotunities, it is also the largest obstacle for experimental control of such systems. The large number of closely spaced energy levels means that optical cycling transitions (i.e. transitions to excited states with a single spontaneous decay channel) are very hard to find. Additional fine and hyperfine structure exacerbates the challenge.[20]

There are, however, mitigating effects that make optical manipulation of molecules possible.[49, 20] Firstly, conservation of angular momentum requires that only decays of the form $N' \to N, N \pm 1$ are allowed, which greatly reduces the number of rotational states that need to be addressed.

Secondly, transition strengths between vibrational states are governed by so-called Franck-Condon factors, (FCFs) which represent the spatial wavefunction overlap integrals between initial and final states. In general, the decay probability from a given vibrational level is microscopic for all but a small number of lower-lying vibrational levels. This is because the vibrational wavefunctions are sharply peaked near the classical turning points, and only states with nearby turning points will have significant overlap.

[3]This simple scaling factor of molecular structure has inspired some researchers to use molecules (typically from astrophysical sources) as a test system for searches for time-variation of the proton-electron mass ratio m_p/m_e.[47, 48]

3.2 Pathways toward stable, ultracold molecules

Despite the benefits of rotational selection rules and FCFs, branching of decay channels remains a problem in schemes that rely on incoherent scattering, and for this reason only a few research groups are currently pursuing laser cooling of molecules. The more common technique by far is to build the molecules from pre-cooled atoms, usually in an optical trap or lattice.

3.2.1 1-photon photoassociation

A straightforward way of producing molecules is through the process of photoassociation (PA).[50] This technique involves the coupling of a free particle state of two colliding atoms to a bound level of the electronically excited molecule The excited molecule is then free to spontaneously decay into any one of the ground state vibrational levels (Figure 3.2a). Beyond being a pathway to ground state molecules, PA spectroscopy – in which the transfer rate is monitored as a function of laser frequency – is also a common tool for probing molecular structure.[51, 52, 53] Furthermore, PA lasers have been demonstrated in homonuclear systems as a tool for weakly coupling rovibrational states to scattering states, which lead to *optical* Feshbach resonances,[54, 55, 56, 57] through a physical process similar to that of section 2.2.

Although this technique is conceptually straightforward, the potentially large number of populated final states may pose a problem if the experiment requires further manipulation of the electronic ground-state molecules. If the molecule is polar the vibrational states couple to ambient blackbody and virtual radiation, and will relax to the ground state over time; however, such decay rates are typically longer than the average graduate student's patience.[58]

One way to deal with this problem is to carefully select an excited level with a single large FCF to the ground state manifold – ideally a level that decays into the vibrational ground state with high probability.[59, 24] In this way, relatively large fractions (up to 25%) of the initial sample may be brought to the electronic and vibrational ground state; however, rotational and hyperfine branching may still pose a problem.

Another potential issue is the lack of temporal resolution of the PA process. Except in special cases where the atoms have strongly overlapping wavefunctions (such as in a BEC, or in an optical lattice) atomic collisions will occur stochastically, and the PA laser has to run continuously to achieve good transfer. This becomes a problem when the in-trap lifetime of the molecules is shorter than the transfer time, in which case it may be impossible to achieve large numbers of trapped molecules.

For an experimenter eager to populate the absolute ground state of the system, more

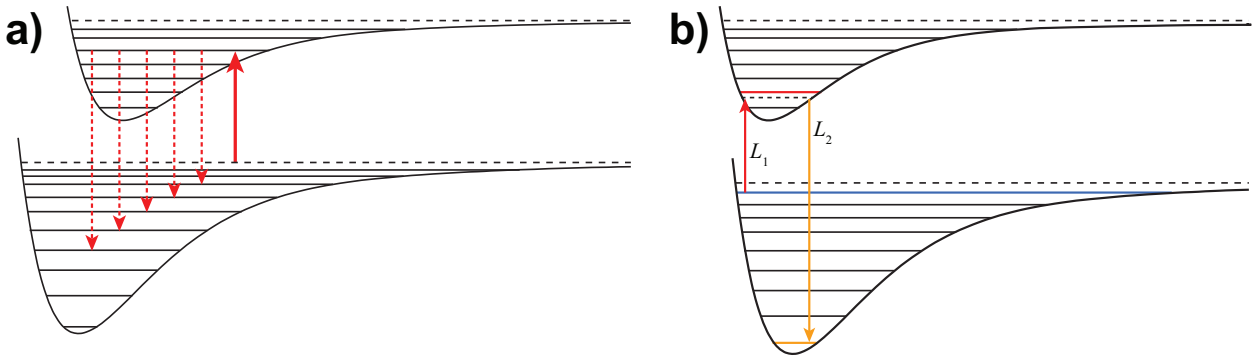

Figure 3.2: a) 1-photon photoassociation of a pair of atoms. A single photon transfers the atom-atom system from a free-particle eigenstate of the ground-state molecular potential to a bound state of the excited potential. Subsequently, the system may spontaneously decay into any of the ground state vibrational levels. b) 2-photon STIRAP scheme for transfer to a vibronic ground state. Adiabatic passage across a Feshbach resonance creates highly vibrationally excited molecules (blue). A pair of Raman lasers L_1, L_2 then transfer the system to the ground state (yellow) via an intermediate, electronically excited state (red). The Raman lasers are detuned from the intermediate state (dashed line) to maintain a coherent transfer, in which the intermediate state amplitude is zero at all times. The intermediate state is chosen for its classical turning points coinciding with those of the initial and final states, which is an important factor in achieving large FCFs.

precise tools therefore need to be developed.

3.2.2 Magnetoassociation and 2-photon schemes

One such tool, which is now in common use, is magnetoassociation using Feshbach resonances. This technique takes advantage of the emergence of a bound state from the scattering continuum at some magnetic field, as described in section 2.2. By ramping a superfluid adiabatically from the negative to the positive scattering length side of the resonance, or by holding a thermal cloud on the positive side and waiting for chemical equilibrium, one can convert atoms to highly vibrationally excited Feshbach molecules with high efficiency.[60, 61] Such dimers were first observed in rubidium in 2002,[62] and by the end of 2003 they had been demonstrated in every alkali species except francium.[31, 21, 22, 63, 64]

This technique may also be extended to heteronuclear systems, provided that an interspecies Feshbach resonance can be found. Although the progress on this front has been less explosive than the homonuclear development, a large number of weakly bound, heteronuclear dimers have recently been demonstrated, including KRb,[65] LiK,[66] NaLi,[67] NaK,[68] and RbCs,[69] and others are being developed at the time of writing.[70, 71]

A common feature of these Feshbach molecules is their remarkable stability to inelastic, vibrationally relaxing collisions, and corresponding long lifetimes. This is a consequence

of the large size of the Feshbach molecules, which is of the same order as the scattering length a – typically several thousand Bohr radii near resonance. Thus, the relevant FCFs to the rest of the vibrational manifold become vanishingly small, and all such decay channels strongly suppressed.[72] However, if the magnetic field is ramped far from resonance the molecules become more tightly bound, and inelastic channels become stronger. Since the typical vibrational spacing of several hundred GHz is many orders of magnitude greater than the optical trap depths used in experiments, these inelastic collisions invariably lead to the constituents leaving the trap.

The advantage of magnetoassociation over photoassociation, besides the typically higher transfer efficiency, is that the molecules are gathered in a single internal quantum state, making them far easier to manipulate and study systematically. One disadvantage is their inherent instability to vibrational decay. Another is their weak DC polarizability, compared to that of lower vibrational levels, which make them unsuitable for studies of dipolar matter. For all of these reasons, it is desirable to follow the magnetoassociation with a secondary transfer scheme, ideally to reach the rovibrational ground state.

The currently most successful experimental technique is to use a pair of lasers to coherently transfer the molecules using a stimulated Raman adiabatic passage (STIRAP) scheme:[73] a pulsed two photon transition via an intermediate, electronically excited state (Figure 3.2b). An ideal STIRAP scheme involves laser pulses whose frequency and amplitude are both carefully controlled. By detuning the lasers away from the intermediate level by equal amounts, one can achieve a fully coherent transfer, in which the intermediate state – often called a "dark state" – is never actually populated, i.e. its quantum amplitude is zero throughout the transfer. This prevents spontaneous decay from occurring during the transfer and allows, in principle, for 100% transfer efficiency. On the other hand, if the dark state is sufficiently long-lived (i.e. its lifetime is much longer than the Rabi frequency of either transfer beam), a simpler, incoherent 2-photon process may also be applied, albeit with somewhat lower transfer rates, and additional parasitic heating from photon recoils.[59]

The STIRAP technique is conceptually similar to the 1-photon PA scheme previously described. One of its main advantages is that the molecules are kept in a single, common internal state, which may then be systematically manipulated, interrogated, or even brought to quantum degeneracy. Another is the high temporal control achieved, which offers convenience to experiments that rely on a precisely timed duty cycle and also aids in diagnosing residual inelastic effects.

When developing such a 2-photon scheme, care must be taken to identify a dark state that has good FC overlap with both the intial and final states. In some cases, if such a state cannot be found, multiple STIRAPs may be required to reach the rovibrational ground

state.[74, 23, 75]

3.3 Interactions in dipolar matter

Ultimately, the goal of most heteronuclear molecule experiments is to exploit the dipolar nature of these systems, either through studies of dipole-dipole interactions[76] or utilization of the internal structure of the molecules to create strongly perturbed physical systems.[43]

3.3.1 Polarizability of heteronuclear molecules

It is important to note that polar molecues do not, in fact, have a net dipole moment in their rovibrational ground state. This is because their rotational wavefunction is spherically symmetric, and the expectation value of the dipole operator is zero. In order to make them behave as dipoles, it is necessary to apply an external field, which mixes in odd-parity states and leads to a net dipole moment.

Studies of magnetically dipolar matter have been performed in an atomic gas,[77] and in principle electrically dipolar matter could also be studied in atomic systems. Single atoms have some nonzero polarizability, as evidenced by the trapping force in optical dipole traps. By applying a DC electric field, one should expect weak dipole-dipole interactions between the polarized atoms in the trap.

Unfortunately, atomic polarizabilities are far too weak for experimental observation of such interactions to be realistic, even at the strongest achievable electric fields. For instance, lithium has a DC polarizability $\alpha \sim 10^{-37}\mathrm{ms}^2$, giving a dipole moment of order 10^{-4}Debye at a field of 10kV/cm. (At higher fields, dielectric breakdown becomes a significant experimental concern.) The problem here is that the Stark effect is a second-order perturbation on the atomic Hamiltonian, and therefore, according to basic quantum perturbation theory, leads to effects of order

$$\lambda^2 = \frac{e\vec{E} \cdot \langle i| \vec{x} |g\rangle}{E_g - E_i} \tag{3.6}$$

where $\vec{E}$ is the applied electric field, and $E_{i(g)}$ is the energy of the excited(ground) state that is subject to the Stark coupling. In this light, the advantage of using molecules should be quite transparent. In a heteronuclear molecule the rotational states have vastly higher density than the electronic states. As seen in section 3.1, the gain in density of states is of order $\frac{\mu}{m_e} \sim 10^5$. (Vibrational level structure does not contribute, since the dipole operator couples only the angular component of the molecular wavefunction.)

This does not mean that we actually gain a factor of 10^5 in polarizability: we also need

to take the dipole matrix element $D_{ig} = \langle i| x |g\rangle$ into account. This matrix element, which describes the degree of charge imbalance in the molecule, is typically somewhat smaller for molecular rotational states than for electronic ones. In the end, it is possible to achieve dipole moments of ~ 1 debye, using electric fields of a few kV/cm.[78]

3.3.2 Dipole-dipole interactions

By applying an electric field, as described above, one may turn on dipole-dipole forces between particles, and control their strength in a smooth fashion. The dipole interaction energy has the familiar form

$$E_{dip} = \frac{1}{r^3}\left(\vec{d}_1 \cdot \vec{d}_2 - 3\left(\hat{r}\cdot\vec{d}_1\right)\left(\hat{r}\cdot\vec{d}_2\right)\right) \tag{3.7}$$

where $\hat{r}$ is the unit vector in the direction of the interparticle separation $\vec{r}$. Such interactions are of great interest, both because of their long-range nature, and their inherent anisotropy. Dipole-dipole interactions may be explored in two principal regimes: in a smooth trap or in an optical lattice.

Studies of molecules in a smooth trap focus primarily on collisional interactions. Such experiments are particularly interesting for Fermionic molecules, which do not exhibit s-wave collisions. The centrifugal barrier blocks short-range p-wave collisions, which normally suppresses all interactions in the low-temperature limit; however dipole-dipole interactions may extend beyond the centrifugal barrier. The researcher thus has the ability to systematically study quantum gases whose only modes of interaction are dipole forces.

In a trap with three translational degrees of freedom, molecules that are all polarized along the same axis may experience either attractive or repulsive long-range interactions, depending on the direction along which they approach one another. In the attractive, "head-to-tail collision" case, the dipole force may overcome the centrifugal barrier entirely, and facilitate chemical processes between the scattering constituents.[78]

In an optical lattice of sufficiently large depth the motional degrees of freedom of the molecules are frozen out. Although this suppresses scattering processes, the molecules may still exhibit interactions between neighboring lattice sites due to the long-range dipole force. Such systems are also interesting because, in absence of intermolecular collisions, very long lifetimes can be achieved, allowing for interrogation of interaction energies on a very fine resolution.

In such systems it is conventional to rewrite the interaction Hamiltonian in the language of the Hubbard model. For instance, the Hamiltonian

$$H_{int} = \sum_{i,j} J \left(\sigma^x_{i,j} \sigma^x_{i+1,j} + \sigma^y_{i,j} \sigma^y_{i,j+1} \right) \tag{3.8}$$

where σ^i are the Pauli spin matrices, describes a 2D lattice in the x-y plane, with unit site occupancy and external field parallel to the z-axis.[76, 79]

Spin-lattices such as this are of significant theoretical and experimental interest, not least because of their applicability toward studies of ferromagnetism in condensed matter systems, where they may constitute a quantum simulation of the d-dimensional Ising model. Furthermore, a 2D Hamiltonian such as equation (3.8) may be used for studying topological ordered phenomena. Such lattice Hamiltonians are also of interest to quantum information research, where they may form the backbone of scalable quantum computing schemes.

4 Lithium and Ytterbium

The superstars of our experiment are the two atomic species lithium (atomic symbol Li) and ytterbium (Yb). The chief motivations for choosing these two elements is outlined in the introduction. Briefly, lithium and ytterbium were chosen to give an alkali-spin-singlet mixture, with a high constituent mass ratio, and with quantum degeneracy experimentally demonstrated in both species. Furthermore, we wished to have access to magnetically tunable interactions in at least one of our components, to access various types of interactions.

4.1 Basic properties and optical transitions

Some of the basic properties of lithium and ytterbium are summarized in table 4.1. Ytterbium has as many as seven stable isotopes, five of which have natural abundances above 10%. Of these, the even isotopes are Bosons, whereas the odd isotopes are Fermions. The most abundant isotope is the Bosonic ^{174}Yb (32%), whereas the most abundant Fermionic isotope is ^{173}Yb (16%).

Our lithium sample consists of purified ^{6}Li, which otherwise occurs in nature at 7.5% abundance.[4] ^{6}Li is a Fermion, and one of the most popular choices for studies of Fermi gases in atomic physics experiments.

The two species have a significant mass ratio of 28-29, depending on the isotope of Yb.

It is also worth noting from table 4.1 that although lithium and ytterbium have similar vapor pressures at 400°C – the temperature at which we run our atomic ovens – lithium is a liquid at this temperature, whereas ytterbium remains a solid. This became a problem for us in the early stages of the experiment, when we discovered that our supplier had accidentally shipped ^{7}Li instead of ^{6}Li. By then the wayward lithium had already melted and grafted to the walls of our lithium sample cup, and had to be removed with great labor, and a great deal of highly exothermic chemical reactions.

Also of note is that although the vapor pressure of ytterbium is three times greater than that of lithium at 400°C, the rate of extraction from the atomic oven is only half as great, as flux scales inversely with the square root of mass: $\Phi \propto P/\sqrt{mk_BT}$. For some time we operated the Yb at a higher temperature to compensate for this, but we have since reverted to heating the two species to the same temperature.

The most interesting numbers, on a day-to-day basis, are those pertaining to the optical properties of the two species. The principal structure and main laser cooling transitions of

[4] On a side note, compared to other isotopically purified elements ^{6}Li is relatively cheap to acquire. This is evidently because large amounts of ^{6}Li were produced during the Cold War, as a neutron absorber for hydrogen bombs. Although it is no longer used for this purpose, the US still maintains a large stockpile.

	^{6}Lithium	Ytterbium
Atomic Mass (amu)	6.015	173.94 (^{174}Yb)
Melting Point (°C)	181	824
Vapor Pressure at 400°C (Torr)	9.1×10^{-5}	3.8×10^{-4}
Wavelength in vacuum λ (nm)	670.992	398.911 555.798
Wave number k (cm^{-1})	14903.3	25068.2 17992.1
Transition width $\Gamma/(2\pi)$ (MHz)	5.87	28.9 0.182
Saturation intensity I_{sat} (mW/cm^2)	2.53	59.2 0.138
Polarizability α at 1064nm ($k_B\,\mu$K/(mWcm^{-2}))	6.04×10^{-7}	2.69×10^{-7}
Doppler temperature T_{Dop} (μK)	140	4.4

Table 4.1: Properties of ^{6}Li and Yb. Where more than one number occurs for Yb, the first number pertains to the $^1S_0 \rightarrow {}^1P_1$ transition, and the second number to the$^1S_0 \rightarrow {}^3P_1$ intercombination transition. The saturation intensity I_{sat} is defined in equation (4.14). Atomic mass is given for the most abundant isotope, ^{174}Yb. All other numbers are common to all isotopes. All number derived from [80, 81].

Lithium and Ytterbium are shown in Figure 4.1.

Ytterbium, with its two valence electrons, has two dipole-allowed optical transitions: one to a *para* (spin-singlet) state, $^1P_1$, and one to an *ortho* (spin-triplet) state, $^3P_1$. The ground state is spin-singlet, and ground-state ytterbium is therefore magnetically neutral. The spin-changing transition (called an intercombination transition) is a factor of 160 narrower than the other; this is because optical fields interact almost exclusively with orbital angular momentum, and any electron-spin-changing process must therefore be mediated via the fine structure of the atom.

The triplet state is one of three states in the ^3P manifold. The other two are metastable states, not suitable for laser cooling.

Bosonic isotopes of ytterbium have zero nuclear spin, and therefore no hyperfine structure, whereas the Fermionic isotopes have hyperfine splittings of order 1GHz in the excited states.

Lithium, like all alkali elements, has a $^2S_{1/2}$ ground state, which couples to the nuclear spin ($I = 1$) to give two hyperfine substates. The ground state hyperfine splitting in ^{6}Li is a modest 228MHz, and we may use a single laser source and acousto-optic modulators (AOMs [82]) to address both of these states. We use the optical transition to the $^2P_{3/2}$ state, which has hyperfine splittings smaller than the natural linewidth of the transition, which are thus not resolved in our experiment. (Figure 4.1b.)

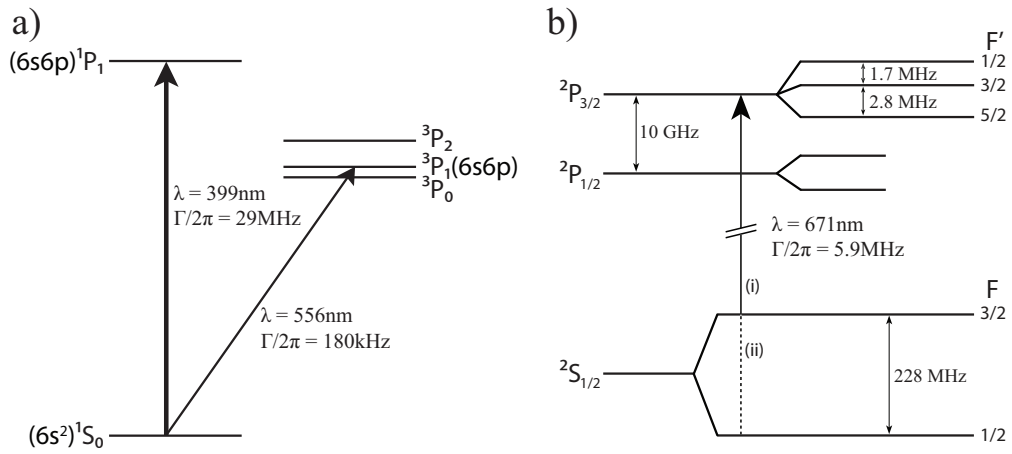

Figure 4.1: Lowest-lying energy levels for ytterbium and 6-lithium, with transitions used for slowing and cooling. For Yb we use the 399nm transition for Zeeman slowing, and the 556nm transition for trapping in the MOT. For Li the 671nm transition is used for both slowing and trapping. We use a set of AOMs to achieve the frequencies needed for the cycling (i) and repumping (ii) transitions.

4.2 Spectroscopy and laser locks

We lock all of our trapping and cooling lasers using saturated-absorbtion spectroscopy schemes. Such schemes involve two laser beams counter-propagating through a vapor cell containing an atomic sample. In the broad range of velocities present in the thermal sample, each laser beam interacts only with a narrow Doppler class of atoms. Only when the laser is precisely tuned to the atomic resonance do they see the same velocity class – those atoms with $v = 0$ – and a "saturation" feature appears. This is typically due to the stronger (pump) laser transferring the atoms to another, dark hyperfine state, making the sample partially transparent to the probe beam. In addition, because the ground state hyperfine splitting in lithium is far smaller than its Doppler width, an inverted crossover peak appears between the two hyperfine states. This is due to the pump and probe interacting with different hyperfine levels within a single velocity class, with the pump beam increasing the population of atoms that interact with the probe.

Our 671nm and 556nm spectroscopy setups employ a pair of home-built stainless steel vapor cells. The 399nm setup uses a commercial hollow-cathode lamp (HCL) vapor cell. Although the 399 and 556 spectroscopy lasers are both locked to ytterbium samples, we are unable to use a single vapor cell for both lasers. The narrow linewidth of the 556 laser, allows it to only interact with a very narrow velocity class. To boost the population of this narrow class enough to achieve a signal, the vapor pressure has to be turned up substantially, rendering the sample completely opaque to the much broader 399nm laser.

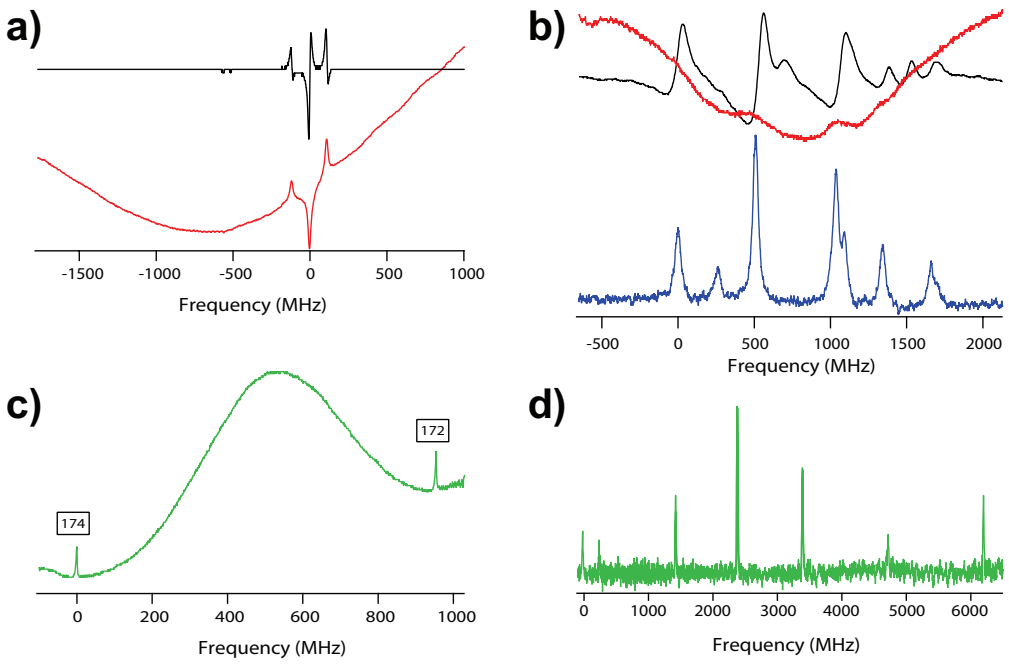

Figure 4.2: Saturated absorption spectroscopy signals for our main lasers. a) Lithium signal at 671nm (red), showing the broad Doppler signal, two saturation peaks, and the inverted crossover peak. Also shown is the derived error signal (black). b) Ytterbium signal at 399nm (red). The saturation peaks are barely visible against the Doppler profile, but show up strongly in the error signal (black). The blue trace is a fluorescence signal from crossed-beam spectroscopy in the Yb intermediate chamber. (See section 5.3.) c) Ytterbium signal at 556nm. Unlike the 399nm signal, the isotope shift is greater than the Doppler width, leading to multiple Doppler-broadened signals. d) Crossed-beam fluorescence spectroscopy at 556nm.

We derive an error signal (derivative of spectroscopy signal) from our 671nm and 399nm setups by modulating the frequency of the pump light at a few tens of kHz using an acousto-optical modulator. In the 556nm setup we modulate both the pump and probe by equal amounts. The error signals are used to achieve a stable feedback lock, which we achieve using electronic PID circuits that feed back to the piezo transducer on the external cavity of the master diode laser.

4.3 Laser cooling and trapping Li and Yb.

The functionality of the Zeeman slower and MOT are well-documented by now (see e.g. [83]) and only a very brief introduction should be warranted.

The Zeeman slower relies on the time-averaged recoil force experienced by an atom as it scatters photons from a single laser beam, which is aligned anti-parallel to the velocity of the atom in the lab frame. As the atom decelerates, the Doppler effect shifts it out of resonance with the laser. To compensate for this, a spatially varying magnetic field is applied, to create a Zeeman shift equal and opposite to the Doppler shift. In general, one seeks to minimize the effective detuning

$$\delta_{eff} = \delta_{laser} - \vec{k} \cdot \vec{v} + \Delta\vec{\mu} \cdot \vec{B}/\hbar \tag{4.1}$$

at each point in the trajectory of the atom. δ_{eff} describes the frequency offset of the laser, in the atom's frame of reference ($\omega_{laser} - \vec{k} \cdot \vec{v}$), from the Zeeman-shifted resonance frequency ($\omega_0 - \Delta\vec{\mu} \cdot \vec{B}/\hbar$). Here $\delta_{laser} = \omega_{laser} - \omega_0$ is the native detuning of the laser beam from atomic resonance, in the stationary lab frame and at zero magnetic field; k is the wavevector of the laser, and $\Delta\vec{\mu}$ is the change in magnetic moment induced by laser excitation. Proper polarization of the slowing light needs to be maintained in order to achieve the value of $\Delta\mu$ that will lead to the correct Zeeman shift.

A schematic of the spatial confinement functionality of the magneto-optical trap (MOT) is given in Figure 4.3. The trap relies on a spatially inhomogeneous quadrupole field, established by two counterpropagating current loops. As long as the atom remains in the center of the trap, where the magnetic field is zero, the magnetic sublevels are degenerate in the ground and excited state, respectively. When the atom enters a region with a nonzero field, however, the energies of the levels are perturbed according to their magnetic projection. By subjecting the atom to counterpropagating, red-detuned lasers with opposite helicity, we can selectively bring the atom into resonance with a restoring scattering force. The magnetic quadrupole provides a field gradient in all directions, so the scheme can be used to achieve 3-dimensional trapping.

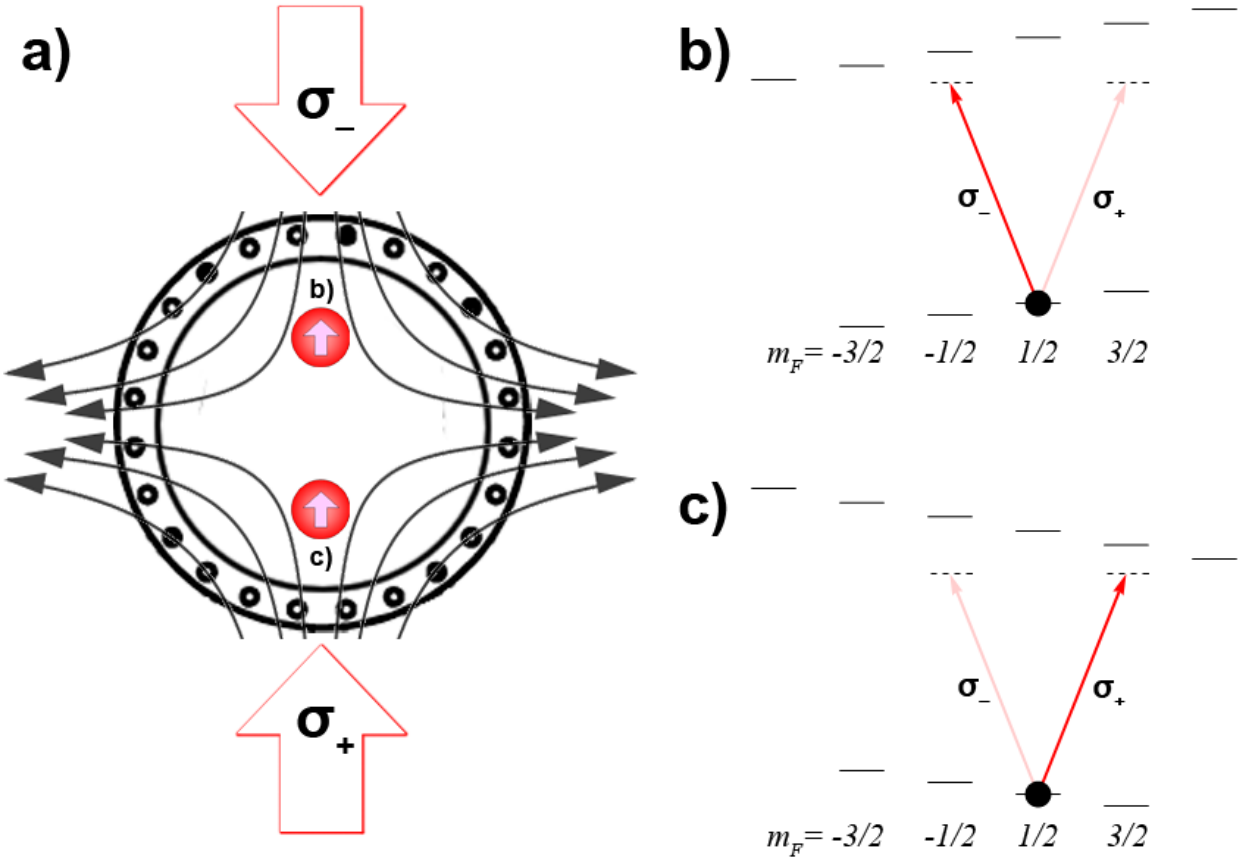

Figure 4.3: Basic confinement functionality of a MOT. a) Basic geometry, including quadrupole field lines, vertical laser beams, and two "test atoms," each with magnetic moment pointing up. Circularly polarized light $\sigma_{\pm}$ is used to selectively address $\Delta m_F = \pm 1$ transitions. b) The upper test atom has its magnetic moment anti-aligned with the local magnetic field. The resulting Zeeman shift of the excited-state levels brings the σ_- laser close to resonance, and shifts the σ_+ resonance away. This causes a downward-biased scattering force. c) The lower test atom has its magnetic moment aligned parallel to the local field, and is Zeeman-shifted into resonance with the σ_+ laser.

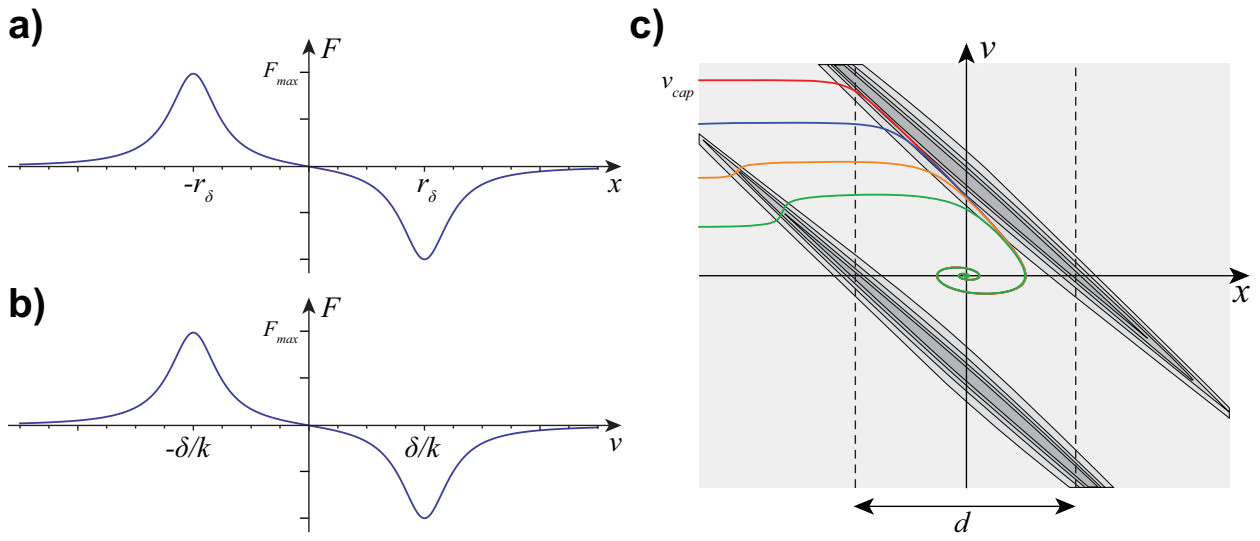

Figure 4.4: Trapping force in a MOT. In the frequency domain, the scattering force from each laser has the shape of a Lorenzian with FWHM= Γ_s . a) In the spatial domain the trapping lasers provide a restoring force that is linear at the center, and peaked at a distance $r_\delta = \frac{\hbar|\delta_L|}{\mu B'}$. b) In the velocity domain the lasers provide a restoring force that is peaked at δ_L/k. c) Phase portrait of a MOT, operating at $s = 10$. The shaded area is the interaction region, where $\delta_{eff} \leq \Gamma_s$ for either laser. The vertical dashed lines give the diameter d of the MOT beam, which we take to be Gaussian with waist $w_0 = d$. Figures (a) and (b) represent cross-sections along the horizontal and vertical axis, respectively. The colored lines are simulated phase space trajectories of atoms with $v/v_{cap} = 1/4,\ 1/2,\ 3/4$, and 1, respectively.

We can examine the function of the MOT more quantitatively by considering the scattering force from each laser beam

$$F_{scat} = \hbar k \frac{\Gamma}{2} \frac{s}{1 + s + 4\delta_{eff}^2/\Gamma} = \hbar k \frac{\Gamma}{2} \left(\frac{s}{1+s} \right) \frac{1}{1 + 4\delta_{eff}^2/\Gamma_s^2} \tag{4.2}$$

Here k is the laser wavevector and $s = I/I_{sat}$ is the saturation parameter. Table 4.1 contains values of I_{sat} for the lithium and ytterbium cooling transitions. $\Gamma_s = \Gamma\sqrt{1+s}$ is the effective, saturation broadened linewidth. The effective detuning δ_{eff} is given in equation (4.1).

Figure 4.4a-b shows the scattering force from counterpropagating MOT beams with detuning $\delta_{laser} < 0$, in a magnetic gradient $B(z) = B'z$. The beams operate on opposite velocity classes, because they have opposite wavevector k, and also on opposite displacements because, by virtue of the $\sigma_\pm$ configuration shown in Figure 4.3, $\Delta\mu$ is opposite for the two beams.

We can inspect the phase portrait in Figure 4.4c to extract some quantities of interest. The interaction regions (the two diagonal bands) are the loci that satisfy $\delta_{eff} < \Gamma/2$, for

beams of equal laser detuning, and equal and opposite k, $\Delta\mu$.

As an atom passes through this region, its path through the diagram is governed by the differential equation

$$\frac{\partial v}{\partial x} = \frac{\partial v}{\partial t}\frac{\partial t}{\partial x} = \frac{F}{m}\frac{1}{v} \tag{4.3}$$

The capture velocity of the trap,v_{cap} – i.e. the highest velocity class that the trap can capture – is that for which the slope $\partial v/\partial x$ equals the slope of the interaction bands.

$$\frac{F}{m}\frac{1}{v_{cap}} = \frac{\mu B'}{\hbar k} \tag{4.4}$$

$\mu = g_{F'}\mu_B$ is usually a good approximation for $|\Delta\mu|$, where $g_{F'}$ is the appropriate g-factor of the excited state.

Most MOTs operate at high saturation parameters, $I \gg I_{sat}$, for which, according to equation (4.2), $F \simeq \hbar k\Gamma/2$ on resonance (i.e. $\delta_{eff} = 0$). Thus, we can derive

$$v_{cap} = \frac{\hbar^2 k^2}{2m}\frac{\Gamma}{\mu B'} \tag{4.5}$$

Now, in order to collect every velocity class up to v_{cap}, we require that the slope of the interaction bands in Figure 4.4c is sufficiently great that they vertically span the range $[0, v_{cap}]$ within the finite spatial extent of the MOT beams, i.e.

$$\frac{\mu B'}{\hbar k} \geq \frac{v_{cap}}{d} \tag{4.6}$$

where d is the MOT beam diameter. We can combine the above equations to obtain an expression for v_{cap} that is independent of the magnetic gradient

$$\frac{1}{2}mv_{cap}^2 \leq \frac{1}{2}\hbar k\frac{\Gamma}{2}d \tag{4.7}$$

In other words, the work-energy theorem holds in a MOT: the kinetic energy of the highest trappable velocity class is no greater than the maximum scattering force times the distance over which it acts. The overall factor-of-2 is due to the interaction region being a straight line, whereas the path corresponding to constant force is a parabola.

From the capture velocity, we can compute some target parameters for the MOT, including the magnetic gradient that maximizes v_{cap}, which follows directly from equation (4.6).

$$B' = \frac{\hbar k}{\mu d}v_{cap} \tag{4.8}$$

Next, the optimal (red-)detuning, which by simple inspection of the phase portrait must be

$$\delta_{laser} = -\frac{kv_{cap}}{2} \tag{4.9}$$

If we plug in numbers for lithium and ytterbium: $d = 1\text{cm}$, $g_{F'} = {}^3\!/_2(1)$ for Li(Yb), and other physical values from Table 4.1, we find that for a lithium MOT $v_{cap} = 130\text{m/s}$, $B' = 100\text{G/cm}$, and $\delta_{laser} = 17\Gamma$. For an intercombination-line ytterbium MOT, $v_{cap} = 4.8\text{m/s}$, $B' = 6\text{G/cm}$, $\delta_{laser} = 24\Gamma$.

As we shall see in chapter 7, these figures differ substantially from the experimentally optimized values. This discrepancy is due to several practical considerations. Firstly, while large detunings are good for obtaining high load rates, the damping (cooling) force at the center of the trap rapidly weakens as $\delta_{laser} \gg \Gamma$. Secondly, large magnetic gradients cause strong spatial confinement, and high atomic densities, which tend to precipitate various loss mechanisms.[84] Finally, in lithium (but not ytterbium) the existence of "dark" hyperfine states leads to reduced photon scattering rates, even when repumping light is present.

4.4 Optical dipole trapping of Li, Yb

With easily maintained, high-power lasers now commercially available, the optical dipole trap (ODT) has become an increasingly popular option for the secondary trap. The ODT relies on the high-field-seeking nature of ground-state atoms. When placed in some external electric field $\vec{E}$ an atom will tend to polarize, acquiring a dipole moment $\vec{p} = \alpha c\epsilon_0 \vec{E}$. Here, ϵ_0 is the permittivity of free space, and α is the polarizability of the atom. The force on the atom by the electric field is

$$\vec{F} = \left(\vec{p} \cdot \vec{\nabla}\right) \vec{E} \tag{4.10}$$

Plugging in the above form of $\vec{p}$, and applying the appropriate vector identity, we find that the dipole force is a conservative force, i.e. it has the form $\vec{F} = -\vec{\nabla} U$

$$\vec{F} = -\vec{\nabla}\left(-\frac{\alpha c\epsilon_0}{2}\left|\vec{E}\right|^2\right) - \alpha c\epsilon_0 \vec{E} \times \left(\vec{\nabla} \times \vec{E}\right) \tag{4.11}$$

The second term on the right-hand-side can be rewritten as $\alpha c\epsilon_0 \vec{E} \times \partial\vec{B}/\partial t$. In the case of a traveling electromagnetic wave, this term averages to zero, whereas the first term does not. Recalling that the intensity of an electromagnetic wave is given by $I = \frac{1}{2} c\epsilon_0 \left|\vec{E}\right|^2$, we find that the dipole trap potential is simply

$$U = -\alpha I \tag{4.12}$$

Thus, the trapping potential of an ODT has the same functional form as the beam intensity profile, up to an overall polarization factor. One can show, using semi-classical time-dependent perturbation theory, that this factor is a function of the laser frequency ω_L and the natural transition frequency ω_0 of the atom. This is known as the AC Stark effect, and gives a polarizability of the form

$$\alpha = -\frac{\hbar\Gamma^2}{8}\left(\frac{1}{\omega_0 - \omega_L} + \frac{1}{\omega_0 + \omega_L}\right)\frac{1}{I_{sat}} \tag{4.13}$$

where the saturation intensity I_{sat} is given by

$$I_{sat} = \frac{\hbar\omega_0^3\Gamma}{12\pi c^2} \tag{4.14}$$

Knowing only the basic characteristics, ω_0 and Γ, of the dominant transitions for lithium and ytterbium, we may thus compute their polarizability in the ODT. Using the data from table 4.1, we find that in an optical trap driven by a 1064nm laser,

$$\alpha_{Li} = 8.34 \times 10^{-37} m^2 s \tag{4.15}$$

$$\alpha_{Yb} = 3.71 \times 10^{-37} m^2 s \tag{4.16}$$

in SI units. (Table 4.1 provides the same numbers, converted to experimentally applicable units.) The positive sign of both numbers shows that the trap is attractive to both species, as we should expect, since the ODT laser is red-detuned from the dominant transitions of both Li and Yb, at 671nm and 399nm, respectively. Using the numbers above, we find that a modest laser power of 1.6W is sufficient to produce a 100μK trap depth for lithium in an ODT beam with 25μm waist.

The ratio of 2.2 between the two polarizabilities is an important property of our system, as we will see later on. Some groups with two-species experiments have chosen to avoid such experimental conditions by using multiple ODT lasers of different wavelengths;[85] however, we have found that a single-frequency ODT is sufficient for our experimental needs.

4.5 Absorption imaging

We study our trapped clouds using an absorption imaging scheme. A small amount of light from the 671nm laser (for lithium) and the 399nm laser (for ytterbium) is separated, and

frequency-shifted onto resonance using AOMs. The AOMs also allow fast ($< 1\mu$s) switching of the probe light. Each probe is then sent through a single-mode fiber to extract a pure $\mathrm{TEM}_{0,0}$ mode. The beams are combined immediately after the fiber, and expanded in a telescope before entering the chamber. Inside the chamber a deterministic amount of light is absorbed by the atoms, according to Beer's law,

$$I(z) = I_0 e^{-\int_{-\infty}^{z} n(z)dz} \tag{4.17}$$

A system of lenses further magnifies the beam after the chamber, and refocuses the atomic cloud images onto the camera CCD plane. To image the atoms, we use a 3-shot sequence: first an absorption image I_1 with the atoms present, then an image I_2 of the probe beam, without the atoms, and finally a background shot I_3 without the probe. The fraction of light transmitted through the atomic cloud is then

$$p(x,y) = \frac{I_1 - I_3}{I_2 - I_3} \tag{4.18}$$

where I_n is the intensity of the n-th image at position x,y. This fraction may be converted to column density of atoms using equation (4.17)

$$n(x,y) = -\frac{1}{\sigma} \ln p(x,y) \tag{4.19}$$

The atom-photon cross-section is $\sigma = \frac{3}{2\pi^2}\lambda^2 \times f$ for resonant light. The factor f is the so-called Clebsch-Gordan factor,[5] which accounts for the angular matrix element of the transition.

4.5.1 Dual-species imaging

In order to image both species simultaneously, we use dichroic mirrors to separate the two imaging beams, and allow them to reconverge at the camera with a slight offset. This setup gives us independent control of the position of the two images on the CCD. However, it also leads to the shadow of each species being washed out by the imaging light of its companion species, and for this reason we can no longer use equation (4.18) to normalize the image. Instead, we use a 4-shot imaging sequence:

1. An image with both species and both imaging beams present

[5]This variable, which is used to account for corrections in the atom-photon interaction matrix elements due to angular wavefunction overlap, is directly related to the Wigner 3-J and 6-J symbols. These corrective terms are a function of the atom's initial quantum numbers, including magnetic quantum number (an ensemble average is used for unpolarized samples), and the helicity (polarization) of the scattering photon, in a common eigenbasis.

2. Lithium imaging beam only

3. Ytterbium imaging beam only

4. Background (no imaging light)

To extract the transmitted fraction for Li(Yb) we then use the formula

$$p_{Li(Yb)} = \frac{I_1 - I_{3(2)}}{I_{2(3)} - I_4} \tag{4.20}$$

This scheme is an efficient way of imaging both species, but gives a somewhat reduced signal-to-noise ratio. This is because, rather than subtracting only the background in the numerator, one has to correct for an imaging beam, which necessarily is accompanied by far greater shot noise per CCD pixel. To combat this problem, we have on several occasions placed sharp-edged beam blocks in the section of the imaging path where the beams are separated, in an effort to prevent each beam from overlapping with the locus of its companion image. For single-species imaging, however, we still use the 3-frame scheme.

4.5.2 Field-dependent imaging

Ytterbium imaging is always carried out at zero magnetic field. This is because two of the magnetic substates of the excited state $^1P_1$ will Zeeman shift out of resonance, creating an environment where the Clebsch-Gordan factor is strongly dependent on the polarization of the Yb imaging light. Rather than attempt to accurately quantify this, we simply shut off the bias field before imaging. (As we shall see in chapter 13 this can be done even when lithium requires a strong magnetic field during imaging.

Lithium, too, experiences a polarization-dependence of f in a bias field. However, for this species there are often significant advantages to imaging at high magnetic fields. One of these is that we may achieve state-dependent imaging, and thus measure the spin-composition of our sample. This is typically a mixture of the two lowest hyperfine levels, traditionally labeled $|1\rangle$ and $|2\rangle$, which are the scattering constituents in the broad Feshbach resonance. Another benefit is that a high-quality cycling transition may be achieved in the strong Zeeman limit, which removes the necessity for a repumping laser, and also the systematic number errors that accompany a finite time spent by the atoms in the non-imaged hyperfine state.

Our high-field imaging scheme is set up to be resonant with $|2\rangle$ at 528G. This is because the s-wave scattering length between $|1\rangle$ and $|2\rangle$ vanishes at this field, and so we may use the imaging beam to "blast" away the population in $|2\rangle$ without causing heating of the atoms in $|1\rangle$ through inter-state collisions. In this way we achive a pure spin mixture, which may in turn be brought into resonance with imaging at 475G, and probed at this field.

High-field imaging is also used to calibrate the magnetic field response of our bias coils. (And the MOT coils, run in bias configuration.) The field-dependence of the ^{6}Li energy levels are known to very high accuracy from the theoretical Breit-Rabi solution, which has been sensitively tested by various groups using RF spectroscopy. By observing the dependence of the resonance frequency on the electromagnet current, we may numerically extract the proportionality constant of magnetic fiels at the atoms vs current.

4.6 Metastable extensions for Yb

The energy level diagram for ytterbium in Figure 4.1 includes the triplet manifold of ^3P levels, only one of which is used for laser cooling. The other two levels are so-called metastable states, which have very long lifetimes against spontaneous decay. The $^3P_0$ state has a lifetime of several minutes in the Fermionic isotopes, and far longer in the Bosonic ones. The $^3P_2$ state has a more modest, but still impressive, lifetime of 15s.[86]

4.6.1 Strategies for accessing the metastable state

The vanishing width of these states means that exciting to them directly is extremely challenging: the lasers need to be stabilized to a few mHz to drive a coherent π-transfer. A far easier way of reaching these levels is shown in Figure 4.5, and consists in exciting the atoms to a higher-lying energy level, and allowing them to spontaneously decay. The $^3P_2$ level may be accessed in this way using the comparatively broad $^3D_2$ state as an intermediate point. The decay time from this state is $\approx 0.5\mu$s.

The drawback of this transfer technique is that, with a branching ratio of 1:7:0 into the $^3P_{2:1:0}$ manifold, it takes a large number of attempts to get an atom into the $^3P_2$ state this way, with each unsuccessful attempt leading to a decay to the ground state via the MOT transition. Each transfer involves multiple photon recoils, which deposit thermal energy in the sample. In experiments requiring very low temperatures or quantum degeneracy, this heating may be unacceptable.

A third method for populating the metastable $^3P_2$ state has also been demonstrated, whereby which the $^3S_1$ state is populated by a two-photon transfer via the $^3P_1$ level.[87] This method also relies on spontaneous decay, but benefits from a favorable branching ratio into the desired state.

To return the metastable atoms to the ground state, the short-lived ($\Gamma = 2\pi \times 12$MHz) $(6s7s)^3S_1$ state may be utilized. This state may be optically accessed from the metastable state, and decays into the entire $^3P_{2:1:0}$ manifold with a branching ratio of 0.51:0.36:0.13.[86] Again, some of the atoms return to the ground state via the MOT transition; of the remainder

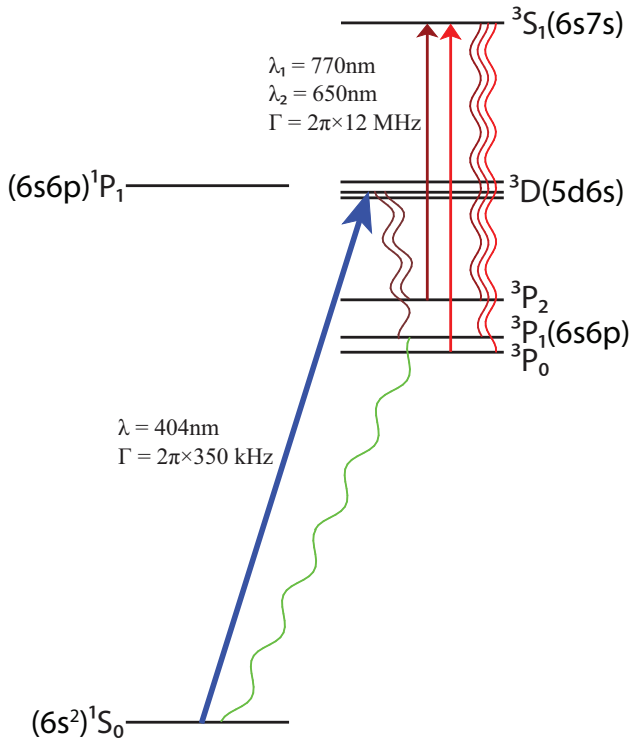

Figure 4.5: Relevant levels and transitions for studying metastable $^3P_2$ ytterbium. Arrows represent laser-driven transitions, and wavy lines denote spontaneous decay channels. Rather than exciting the atom directly, a 404nm laser is used to transfer the atoms to the $^3D_2$ state, from which they spontaneously decay to the ^3P manifold in $< 1\mu$s. To return the atoms from the metastable state, a 770nm laser excites the atoms to the $^3S_1$ state, from which they may decay to the ground state via $^3P_1$. A 650nm repump laser is used to recycle atoms from the other metastable state $^3P_0$.

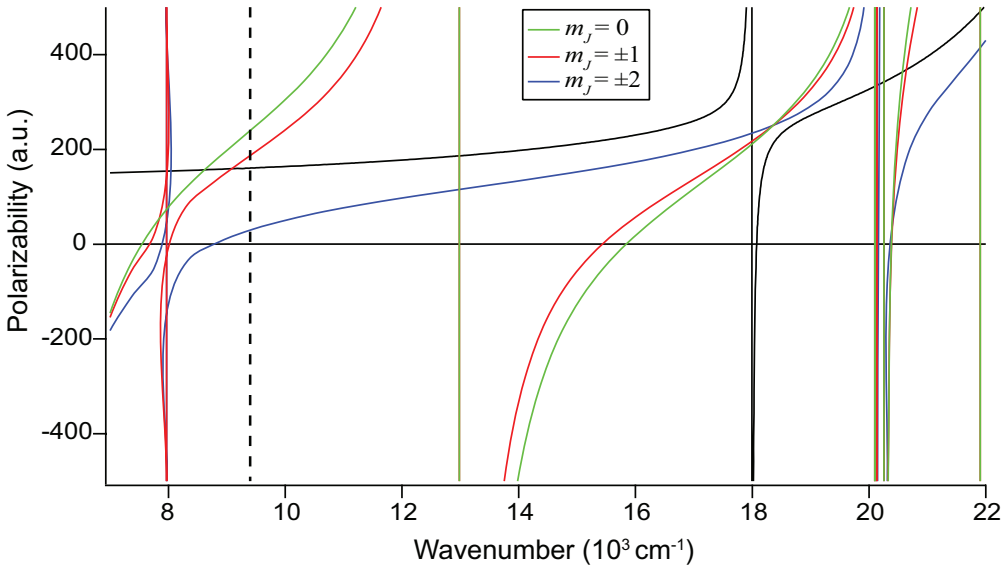

Figure 4.6: Calculated polarizability of the magnetic sublevels, $m = 0, \pm 1, \pm 2$ as a function of ODT frequency, with trap polarization parallel to the magnetic field. The black trace is the ground state polarizability. The vertical dashed line marks our ODT wavenumber, $(1064\text{nm})^{-1}$. Data courtesy of Svetlana Kotochigova.

most return to the $^3P_2$ level. After many cycles, most of the atoms will be in the ground state, but with a 27% fraction of the population stuck in the $^3P_0$ state. To return the entire population to the ground state, a second laser must be present to repump these atoms back via the $^3S_1$ state.

4.6.2 Optical trapping of Yb*

It was not immediately obvious that the $^3P_2$ state of ytterbium should be optically trappable in our 1064nm ODT. Indeed, the laser frequency of our trap lies between several transitions. Some of these contribute an attractive trapping potential, whereas others contribute a repulsive potential.

As it turns out, the polarizability of Yb* is dependent on the magnetic sublevel under consideration. For π-polarized light (i.e. the ODT polarization perpendicular to the magnetic basis) the $m = 0, \pm 1$ substates have allowed transitions to the $^3S_1$ state (which yield an attractive potential), whereas the $m = \pm 2$ substates do not. Although the complexity of the problem increases as we include additional energy levels to the problem, the prediction remains valid that the $m = 0, \pm 1$ states are significantly more strongly trapped than the $m = \pm 2$ states.

The situation changes, however, when the ODT polarization is rotated 90°. In this case, the $m = \pm 2$ states are the most strongly trapped ones. We can see this from the form of the

SU(5) rotation matrix, which has the form

$$\mathcal{D}_y\left(\frac{\pi}{2}\right) = \frac{1}{4}\begin{pmatrix} 1 & 2 & \sqrt{6} & 2 & 1 \\ -2 & -2 & 0 & 2 & 2 \\ \sqrt{6} & 0 & -2 & 0 & \sqrt{6} \\ -2 & 2 & 0 & -2 & -2 \\ 1 & -2 & \sqrt{6} & -2 & 1 \end{pmatrix} \tag{4.21}$$

In particular, a $m = \pm 2$ state in one eigenbasis is equal to a superposition in a perpendicular basis, which is strongly weighted toward the $m = 0, \pm 1$ substates. Thus, the polarizability of the $m = \pm 2$ states in the perpendicular polarization case is similar to that of the $m = \pm 1$ states in the parallel case. By controlling the polarization of the ODT, we may thus control the balance of trap depths experienced by each substate.

Part II

The Red-Green Science Machine

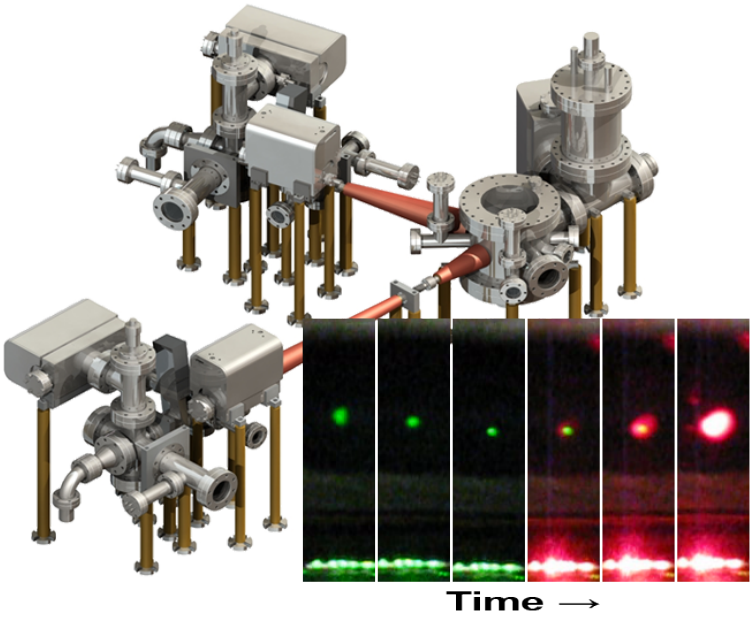

5 Vacuum System

The vacuum system, once it is built and brought to target pressure, is perhaps the aspect of an atomic physics experiment that requires the least amount of maintenance. Yet, the design and careful assembly of this structure is absolutely vital to even the most basic experiments. Our ultra-high vacuum (UHV) system took almost 1 1/2 years to complete, from the early planning stages to the end of the bakeout. As such, it was by far the most extended single project in the development of the machine. This chapter, provides an overview of the main features of our vacuum system.

5.1 Overall structure

The vacuum system used in our experiment is of considerable complexity. From the outset we decided to use an all-stainless-steel setup, using exclusively conflat (CF) seals, with two independent oven assemblies for lithium and ytterbium, respectively. There were several reasons for choosing such a layout. Firstly, we wished to have access to single-species experiments, and to be able to run experiments even with one of the ovens being serviced. Secondly, we wished to avoid any unwanted chemical reactions that may arise in a single oven with two species. Finally, we wanted to be able to independently optimize the Zeeman slowers during simultaneous MOT loading. We have since found that simultaneous loading is not an optimal scheme in our machine. However, as we moved to sequential loading, the option of independent beam line switching has been a valuable feature of our dual-slower setup.

The oven assemblies may be sealed off from the main chamber by gate valves, which maintain UHV even when one of the ovens is at atmospheric pressure. Angle valves on each oven assembly may be connected to a high-capacity pump to evacuate the oven after servicing, e.g. to replenish an atomic sample.

The entire vacuum system is mounted on a set of brass pillars. These were cut to the appropriate length on the student shop lathes, and fitted with screw holes in either end.

All parts of the vacuum chamber are made from type 304 stainless steel, except the oven parts. These are built from type 316 stainless steel, which was chosen over type 304 for its corrosion resistance. The viewports are BK7 glass, and all main chamber viewports have a broadband AR coat, manufactured for visible light and with an additional AR band around 1064nm. The exceptions are the viewports opposite the Zeeman slowers. (I.e. the slower

---

Previous Page: Graphical rendering of vacuum chambers, and time-lapse photographs of magneto-optically trapped atoms of ytterbium (green) and lithium (red).

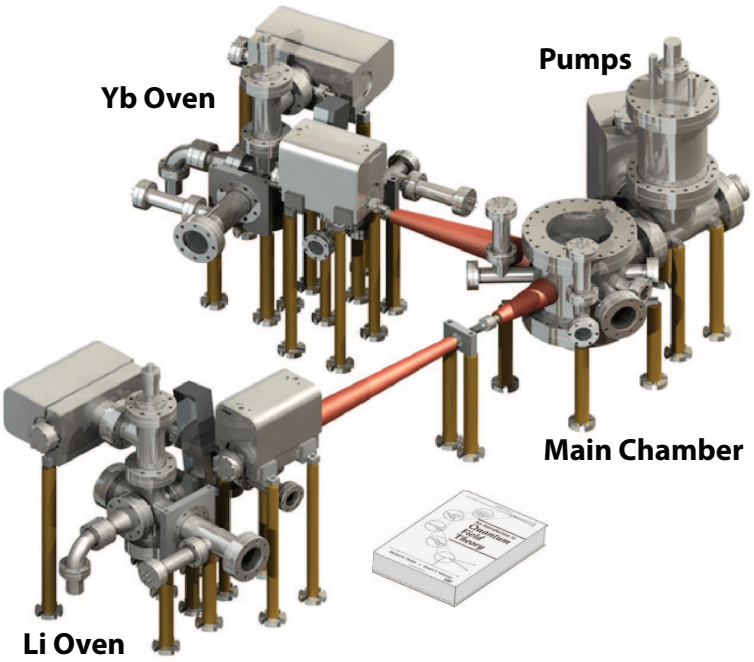

Figure 5.1: Fully rendered SolidWorks schematic of vacuum chambers. The separate oven assemblies are connected to the main chamber by Zeeman slower tubes. (Solenoids shown in red.) The main chamber connects to the pump assembly via a wide 8" tube to maximize conductance and maintain high-quality vacuum at the atoms. Physics textbook shown for scale.

beam entry viewports.) These are made from sapphire glass, which has a high temperature rating and can be permanently heated to bake off any depositions that might form from the incident atomic beam. We maintain the Yb(Li) viewport at 200(250)°C for this reason. Nonetheless, we have in the past seen a gradual degradation of viewport transmission, due to the atomic beams. This process may be reversed by increasing the temperature of the viewport over a period of a few days. Unfortunately, to achive this we have to cover the viewport entirely with aluminum foil, which prevents us from maintaining this high a temperature on a permanent basis.

An early graduate student on the project, Lee Willcockson, stood for most of the design work for the vacuum system, using a SolidWorks model to estimate the size and shape of the finished product, and avoid any geometric impossibilities.

5.2 The main chamber

The main chamber was one of the major design challenges of the vacuum apparatus. Our experiment demanded a large number of features to be incorporated:

- Two Zeeman slower tubes, with space on either side for the coils.
- Viewport flanges opposite the slowers, for slowing beam access.
- 6 viewport flanges for orthogonally aligned MOT beams.
- Additional viewport flanges for imaging beams and crossed ODT beams.
- Two additional access points for ion gauges
- Space for two concentric sets of magnet coils, for the MOT and bias fields respectively.
- A large tube to connect the chamber to the pump assembly with good conductance.
- Electric feedthrough for access to internal RF coils.
- A large (4½") flange to increase the numerical aperture of our imaging, and for possible future extensions to the vacuum system.

Needless to say, there are no commercially available products that would satisfy all these requirements. Instead, a custom chamber needed to be designed and submitted to UHV manufacturers for construction, even before the overall vacuum system design was complete.

The final design, shown in Figure 5.2, and built by Sharon Vacuum, was inspired by similar vacuum chambers at MIT and Berkeley. The chamber consists of an 8" OD and 8"

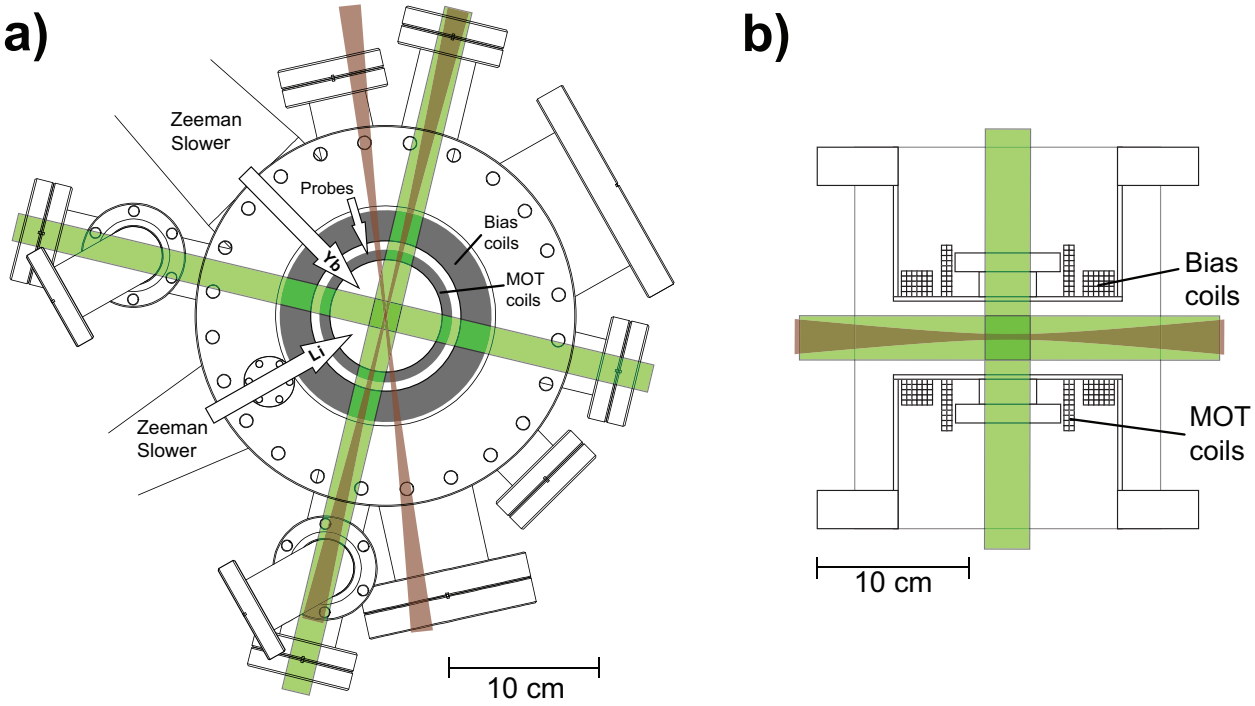

Figure 5.2: a) Overhead blueprint of main chamber, with trapping laser beams and atomic beams shown. MOT beams are shown in green, (vertical beam omitted for clarity) and ODT beams in brown. The recessed electromagnets are shown in gray. The large, open flange on the upper-right connects the main chamber to the pump assembly, whereas the open flanges pointing down and left connect to a pair of ion gauges. The mini-flange for the electric (RF) feedthrough is visible underneath the Li atomic beam arrow. b) Cross-sectional side view of the main chamber, with horizontal viewports removed for clarity. The re-entrant buckets, are shown with electromagnets in place

long vertical tube, terminated by a 10" CF flange on either end. The viewports are attached to smaller tubes welded to the side of the chamber. The slower tubes are terminated by rotatable CF mini-flanges, but were delivered (per our instruction) with the rotating part (receiver) separate. This is because, when they were slipped onto the vacuum tubes, the Zeeman slower solenoids would not fit over the receivers. Instead, the receivers were cut in half on a band saw, and put in place after the solenoids had been installed. The viewport tubes were delivered with non-rotatable CF flanges.

A pair of re-entrant "buckets," built into 10" CF blanks, are recessed into the chamber to provide access for the electromagnets. (See figure 5.2b.) In addition, each bucket is equipped with a viewport flange and tube, for vertical optical access. The bucket lids are also equipped with electric feedthroughs and external BNC connectors. Finally, a set of screw holes (not shown in Figure) provide anchor points for a set of π-shaped structures that hold the electromagnets in place within the buckets.

In addition to the chamber and buckets, a custom 4-way cross was custom-built, to connect the main chamber to the pump assembly. The most noticeable feature of this part is the angle of the ion pump section, which is slanted at a $\approx 45^\circ$ angle away from the main chamber. This design was chosen to allow access to a nearby main chamber viewport, but it also has the benefit of improving the conductance of background gas atoms from the main chamber to the pump. The assembly also includes a titanium sublimation pump (TSP, from Thermionics Northwest Inc.) to reduce the hydrogen background. This pump is equipped with a shroud through which liquid nitrogen may be passed for improved gettering efficiency, but this has not yet been deemed necessary for our experiments.

5.3 The ovens

Our atomic gases are prepared from metallic samples, each placed in a vertically oriented cup and heated to 400°C. The atomic vapor effusively leaves the heated region, and is further skimmed and collimated before the Zeeman slower.

Each of our oven assemblies consists of two sections: a main oven assembly, and an "intermediate" chamber. Each section is provided with an individual ion pump and ion gauge. The two assemblies are separated by a gate valve, and also by a short "differential pumping tube" (11cm long, inner diameter 5mm) that maintains differential pressure between the sections. With the Zeeman slower providing an extra stage of differential pumping, we achieve excellent diffential pressure between the ovens (which read $P \sim 10^{-7}$ Torr during operation) and the main chamber ($P \lesssim 1 \times 10^{-10}$ Torr with gate valve open, and $\approx 5 \times 10^{-11}$ Torr otherwise).

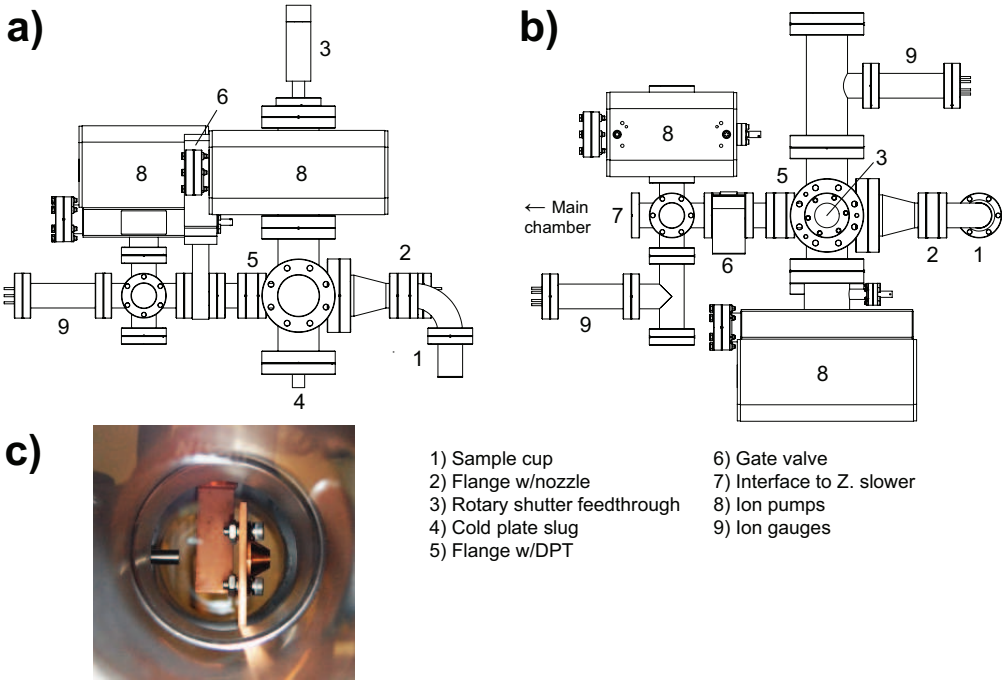

Figure 5.3: a) Side view of Li oven assembly, showing both the main oven and intermediate chamber. The metallic Li and Yb samples are stored in a vertical cup (1). The atomic beam is skimmed and collimated by a ⌀4mm nozzle (2), a tapered cold plate skimmer, and an 11cm×⌀5mm differential pumping tube (5). The main and intermediate sections may be mutually sealed off by a gate valve (6). The intermediate section is provided with a 6-way-cross, for diagnostics, and possible future improvements to our atomic beam collimation. b) Top view of chamber. The separate ion pumps and gauges are clearly visible. c) Photograph of the inside of the oven 6-way cross, showing the cold plate skimmer, atomic beam shutter, and differential pumping tube.

The differential pressure is of course due to the collimating effect of the tube, as only a small unit solid angle of velocities are allowed to pass through the tube without interacting with the walls. We achieve additional collimation with two other elements within the main oven assembly. The first is a 4mm diameter nozzle – an aperture bored directly into a CF flat – that separates the heated atomic samples from the rest of the chamber. The nozzle is maintained at 450°C to prevent metallic deposition and congestion.

The second element is a tapered skimmer, built into a "cold plate." This copper plate is connected to a high-thermal-conductance copper "slug" fed through the stainless steel assembly, and cooled by an array of thermoelectric coolers. In this way, even though it is in close proximity to the 450°C nozzle, we maintain it at a permanent low temperature of −7°C. This is to facilitate gettering of wayward atoms that might otherwise contaminate the main chamber background pressure. A keen eye will be able to see the silver-y deposition on the front of the skimmer, whereas the back has retained its copper hue.

Finally, our oven is equipped with a rotary feedthrough, (Thermionics Inc.) attached to an atomic beam shutter. The shutter design is simply a small copper plate that is slightly offset from the axis of rotation. The actuator above the oven assembly may be toggled by hand, or electronically using a home-built rig with two solenoids to rotate the shaft.

Whereas the rest of the vacuum system uses copper CF gaskets, we chose to use nickel gaskets instead in the heated sections of the oven. This decision was based on experience from prior experiments with lithium, in which copper was observed to corrode and "seize" to the stainless steel after long periods of heating. The nickel gaskets have so far been trouble-free for lithium, but caused an unexpected problem in the ytterbium oven, as the Yb vapor reacted chemically with the nickel, causing the gasket to fail twice, each time after approximately one year of running. The leaks that followed required us to bake out the chamber once more, and also have the knife edges on the CF components re-sharpened by the machine shop staff. After this, we decided to switch to copper gaskets for the ytterbium oven, and these have maintained vacuum for many years now. Other commercially available gasket types, such as silver-plated copper, have not yet been examined.

5.4 Evacuation and Bakeout

The entire vacuum system consists of a large number of sections, held together by no less than 83 CF seals. The construction of the vacuum system was a nontrivial task, not least because of the difficulty in aligning the oven assemblies to accurately deliver the atomic beams. (Short bellows near the Zeeman slowers allowed for very small adjustments without stressing the stainless steel.) After several months' worth of elbow grease we had a complete

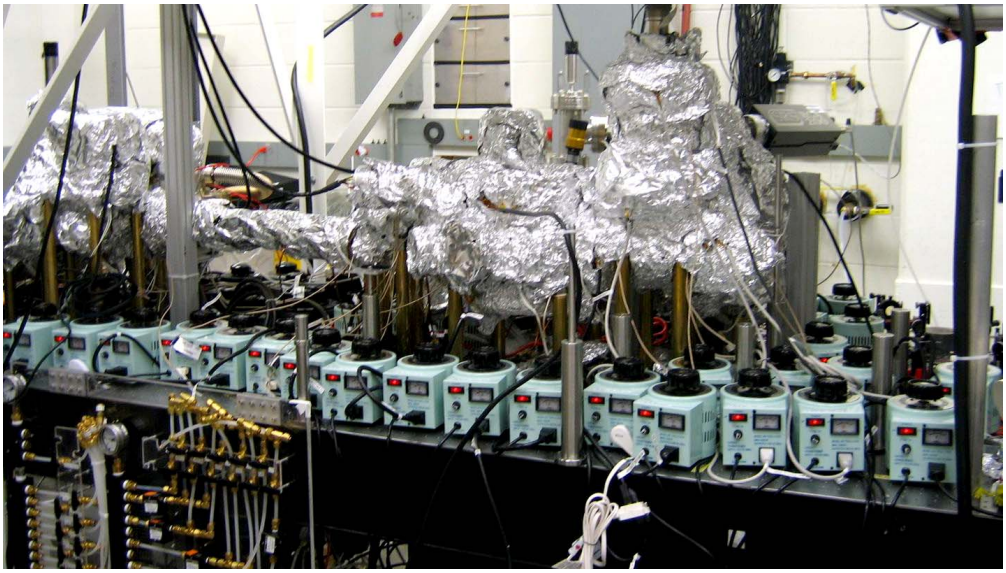

Figure 5.4: Photograph of the vacuum chamber before bakeout, covered in tin foil, and surrounded by Variacs.

system without any detectable faults, and began pumping the main chamber in November 2008.

5.4.1 Baking once...

Due to the very large number of components that required heating, the bakeout was carried out in two stages. The first, and by far the largest, involved the main chamber, the pumps, the intermediate chambers, and the lithium oven, while the ytterbium oven was sealed off. To achieve this, we used 50 variable AC supplies (Variacs), most of which were purchased on eBay, but many others were borrowed from neighboring labs. 13 of these variacs were required to perform double-duty, with multiple heater elements connected. In total, 40 band heaters and 19 lengths of fiberglass heater tape were used, along with the internal heaters of four ion pump magnets, and an unknown quantity of aluminum foil.

62 probe points were designated for monitoring the temperature, and had to be checked every few hours throughout the bakeout. These points consisted of little holes poked in the alumnium foil, into which a thermocouple probe could be inserted. One then had to wait 1-2 minutes for the probe temperature to thermalize with the stainless steel. An entire cycle of reading therefore took over an hour to perform, after which the poor graduate student had only a short time to rest his weary "poking" arm before beginning a new round of measurements.

The initial bakeout had a target temperature of 200°C, with a few sensitive elements

(such as the gate valves and beam shutter feedthroughs) maintained below 150°C. Target temperatures were reached after a few days of carefully cranking up the Variacs, and adding more aluminum foil as needed. After 24 hours at target temperatures, during which the ion gauges were degassed, the ion pumps were turned on to draw out the last bits of contaminants, and the chambers were gently brought back to room temperature over the course of the next day.

Of course, a few snags were encountered along the way. (Other than the inevitable electric shocks and burned fingers!) One problem that arose during the bakeout was an unexpected heating in the main chamber buckets, where the temperature reached 250°C in the course of a night, higher than the maximum rating of the viewport AR coating. Furthermore, we found that the foil that was stretched over the top bucket had started corroding, with fallen flakes lying in the bucket and on the viewport surface. The temperature here was brought down as swiftly as possible; however, there is evidence that some permanent damage was done to the viewports, which now exhibit a significant glare when illuminated by the MOT beams, even after thorough cleaning with methanol. This is also one of the reasons why we have chosen to do the majority of our absorption imaging from the side instead of top-down.

Another surprise came early on during the bake, when the thermocouple that was regulating the thermostat for the lithium cup failed, sending the temperature out of control. We discovered this after noticing that the oven temperature readout was surprisingly low. After a quick "defoiling" of the cup, we found it glowing dull red – at 550°C, according to the hand-held thermocouple.

5.4.2 ...baking twice...

During the cooldown from the first bake we discovered an unsettling discontinuity in the main chamber pressure. We surmised that a minor leak, on the 10^{-7} Torr-scale, had occurred due to our activities. After some "sniffing," using the attached residual gas analyser (Ametek Instruments *Dycor* series) and a cannister of helium, we determined that the leak had arisen in a filament feedthrough on one of the ion gauges.

The ion gauge was quickly replaced, with the chambers pressurized with argon to prevent contamination. However, we still worried that some contamination had occurred, which might cause problems down the road, when re-baking would be far more troublesome. We therefore settled on conducting a second, shorter bake at a lower target temperature. This bakeout went quite a bit smoother than the first, partly due to experience, and partly because the lithium oven (which had been sealed off at the time of the leak) could be left out of the routine. At the end of the second bake, after the TSP had been fired, the ion gauges were measuring pressures $< 10^{-10}$ Torr, and the bakeout was declared a success.

5.4.3 ...and third time is the charm

After clearing out the Variacs and heater elements, as we were preparing to set up optics for the MOT beams, we found it necessary to move a clamp that was holding down one of the brass legs of the vacuum chamber. This immediately caused a rapid rise in the ion gauge pressure reading. Attempts to re-fasten the clamp only exacerbated the problem, and we were forced to shut down the pumps and gauges and re-connect the turbo pump. This time, the leak was found in the 6" flange connecting the main chamber to the pump assembly. Fortunately, we were able to close the leak with some judicious cranking at the vacuum bolts. (The alternative would have been pulling apart the entire pump assembly to replace the gasket.) But meanwhile, another problem had arisen.

After attaching the turbo pump and beginning to open the connecting angle valve (VAT Inc.), the valve appeared to attain a life of its own, and quickly spun open on its own accord. This behavior was entirely unknown to all of us, and we worried that something might be wrong with the valve. Since another bake was required anyway because of the leak, it was decided to replace the suspicious angle valve with a new one. This, however, led to a new problem: one of the bolts holding it in place was utterly stuck!

A makeshift clean room, consisting of hanging lab coats, was fashioned, and I descended upon the troubled bolt with a Dremel tool. After hours of grinding away, the bolt head finally came off. Triumphantly holding the angle valve aloft, I then witnessed the screw – which until recently no force of nature could undo – spontaneously slide off, and gracefully tumble into the open ion pump. At that moment, my advisor's forehead received the biggest palm print it has even known.

The only solution was to undo the ion pump from the assembly, and shake it until the screw came out.

For the third round of baking, we decided to make things more efficient by attaching adhesive thermocouples (Omega SA-series) to various points on the chamber instead of using the hand-held probe. The leads from these probes were bundled at a handful of "stations" where they could be rapidly connected, one by one, to the reader. This innovation dramatically reduced the time required to measure all temperatures, and consequently both improved the accuracy of temperature control and the anxiety levels of all the grad students involved.

Finally, nearly two months after the first variac had been turned on, the third and final bakeout of the main chamber was complete. Since then, it has been well-behaved, and maintaining a consistent pressure at or below 10^{-10}Torr.

5.4.4 The Yb oven

Once the lithium oven and main chamber were stabilized at UHV, much of the equipment used for the first bakeouts was transfered to the Yb oven. This much smaller operation was carried out with relative ease. For this bakeout, we were able to fit all the required variacs into a portable equipment rack, which was placed next to the oven assembly, and subsequently rolled off to storage. This proved to be fortunate, as we were required to do a second bake one year later, when the nickel gaskets failed, and were able to simply roll in the rack again and hook things back up.

6 Magnetic Fields

In any atomic physics experiment, control of the magnetic fields inside the vacuum chamber is one of the most important aspects. These fields are almost always controlled by electromagnets, which typically need to be "home-built" by the researchers. More complex experiments may employ more than a dozen individual components, many of which also need to be cooled to prevent resistive heating from warping or damaging the coil structure.

6.1 Zeeman slower construction

Our Zeeman slowers were the first electromagnets to be built in our lab, and were completed in the first year of operation. A total of three Zeeman slower solenoids were designed and built: one for the ytterbium slower, and two for the lithium slower, which was designed in a two-stage "spin-flip" configuration consisting of a long, decreasing-field slower followed by a short, increasing-field stage. The ytterbium slower was built in an increasing-field configuration.

Each slower was wound from a special copper wire with a square cross-section and a hollow core to allow internal water cooling (S&W Wire). The wire has an outer dimension of $1/8$", and comes with an insulating Kapton coat that adds $1/100$" to its overall size. The hollow core also has a square cross-section, with a dimension of $1/16$".

The geometry of the Zeeman slowers was carefully computed before winding the solenoids, to closely approximate the ideal, square-root form for the internal magnetic field. The square wire was to be tightly wound, one layer at a time, with some region of each layer wound in a double-spaced manner. The "fattest" slower coil would have a total of 8 layers. Each coil was to consist of two separate lengths of wire, connected in series electrically, but with internal coolant water run in parallel through the two channels. This was chosen not only to increase the total water flow through each solenoid, but also to ensure that a blockage somewhere in one of the wire cores would not be catastrophic.

The winding of the Zeeman slowers was performed in the student machine shop. A length of brass tube (1" OD) with an insulating Kapton coat was placed in a lathe, and the engine was set to neutral so the chuck could be rotated by hand. The copper wire was then fed by hand from the large spool on which it arrived, which was mounted on a "hi-tech" rig consisting of two bar stools and a broom shaft. To keep the wire steady, and to prevent twisting or "pinching" the wire was fed through a home-built wooden guide, and onto the brass tube as it was slowly rotated. The guide was designed so it could be mounted on the tool holder of the lathe, which was then set up with the lathe's feed-forward mechanism to translate $1/8$" axially per revolution. For the longer coils, we found it necessary to manually

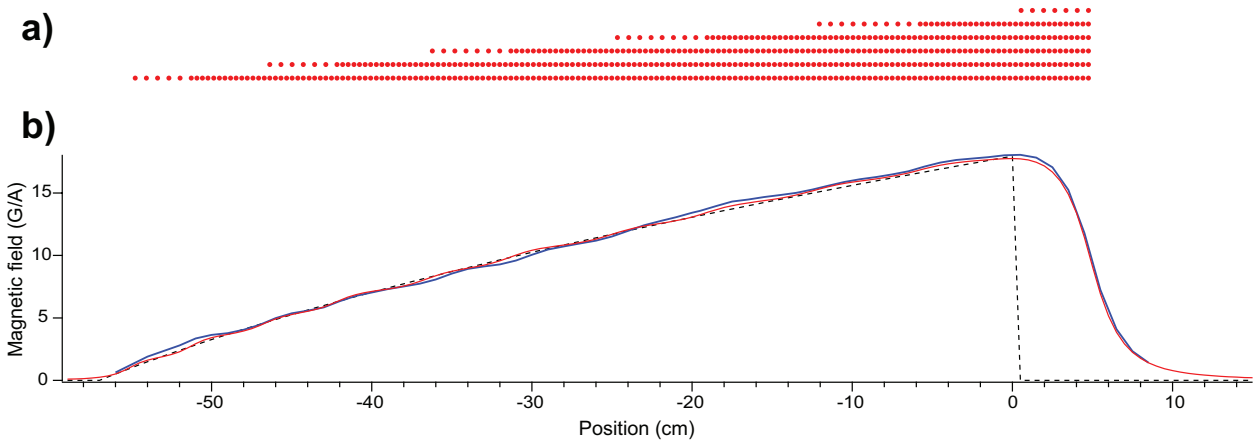

Figure 6.1: a) Cross-sectional winding diagram for the long section of the lithium Zeeman slower, showing the number of coils, and the spacing. Our atomic beam travels from right to left. The innermost 2 layers were wound from one length of wire, and the outermost 4 layers from another length. b) Comparison of idealized magnetic field profile of the Zeeman slower in Figure a (black, dashed line) with numerical estimate of the field strength, based on the winding model in Figure a (red line) and the actual internal field, as measured with a hall probe (blue line). Note that on the high-field side, accuracy near the cutoff is prioritized over fringe field reduction; hence the additional magnetic coils at $z > 0$.

adjust the axial position of the guide every few revolutions to account for the extra wire thickness due to the insulation.

During winding, the endpoint segment of the outer layers showed a troublesome penchant for slipping off the end of the solenoid. We therefore placed a disk, with a hole punched through the center, at the end of the slower, and secured it in place with a C-clamp. Even with this device in place, great care needed to be taken to keep the final coil of each solenoid from coming dislodged.

After all the layers of each solenoid were fully wound, before it was removed from the lathe, the entire solenoid was covered in a thick layer of high-temperature epoxy. The epoxy, which had an unpleasant odor of rotten shrimp before setting, was applied to prevent the coils from shifting during transport to the lab, or from warping during the bakeout. The slowers thus had to be wound one-per-day, as they could not be moved from the lathe until the epoxy had hardened overnight.

After the coils were all complete, we tested the internal magnetic field of each slower against our theoretical estimates. This was done by scratching off some kapton on each lead, and connecting a current supply to feed 3-5A through the solenoid. A Hall probe was mounted on a long shaft, and placed in a cork-like device to keep it centered in the tube. The probe was then passed through the slower tube, with readings taken every cm or half-cm. In this way we learned that the actual field profile of each slower was in excellent agreement

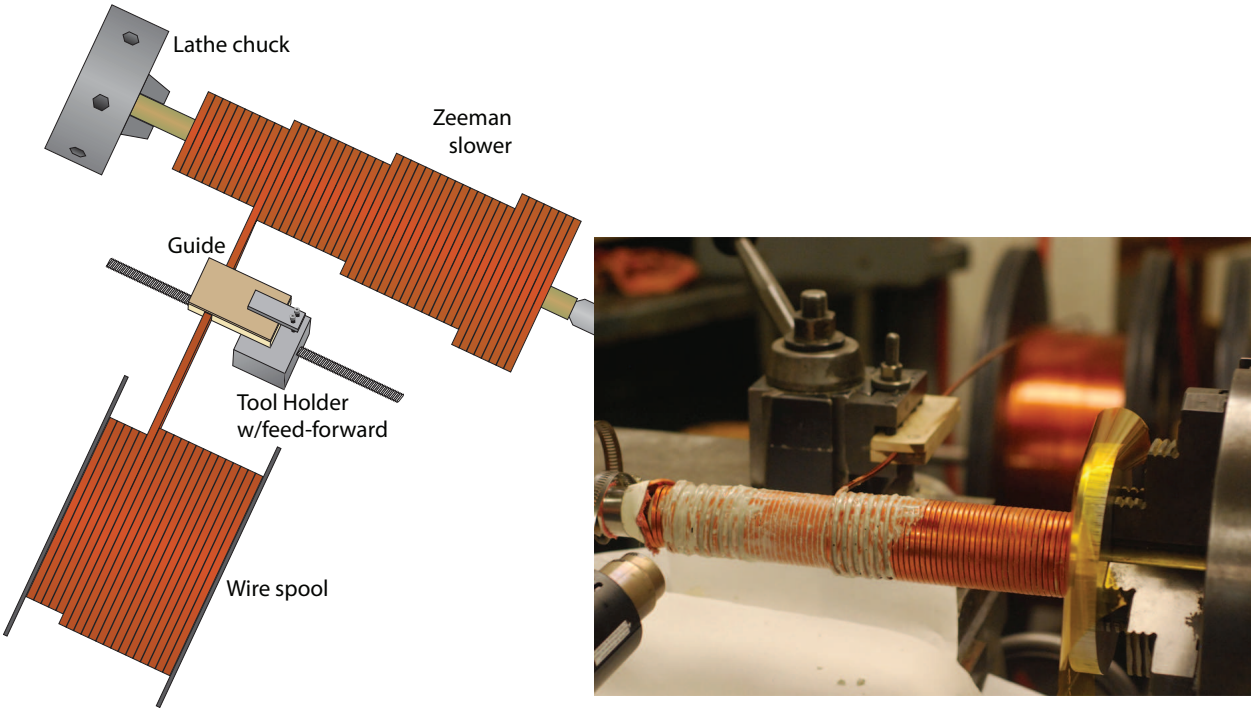

Figure 6.2: Schematic of slower coil winding. The wire is extracted directly from the spool To guide the wire accurately on to the copper tube core, a wooden feedthrough is mounted on the tool holder, and smoothly translated 1/8" per revolution. The lathe chuck (upper left) is rotated by hand, to achieve maximum control over the winding process. The inset shows the winding of a Zeeman slower for a different experiment, using the same techniques. The wooden guide and spool are visible in the background. The solenoid is partially covered in high-temperature epoxy (light gray).

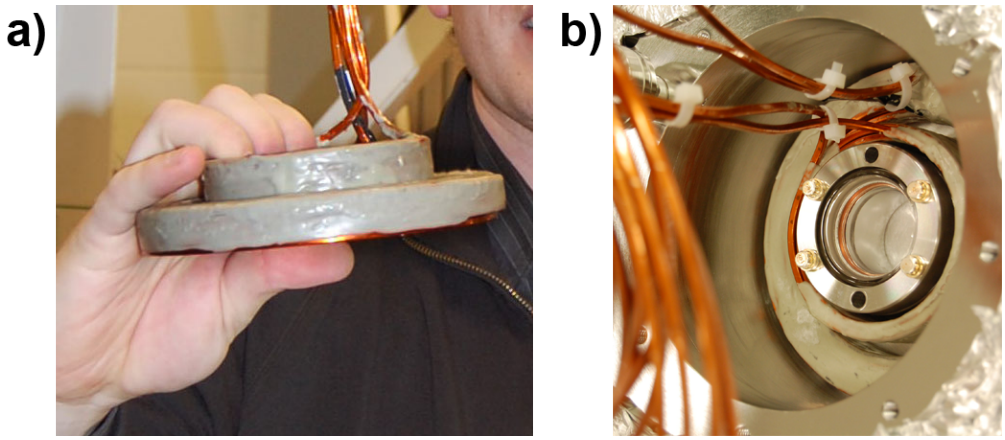

Figure 6.3: The main chamber coils. a) Photograph of one set of coils (MOT and bias), epoxied together. b) Photograph of upper main chamber coils recessed into main chamber buckets, and enclosing the viewport for vertical MOT beams.

with the theoretical estimate (Figure 6.1b).

The Zeeman slowers were finally slipped over long vacuum tubes, which were incorporated into the vacuum system.

6.2 The main chamber coils

With the experience gained from winding the Zeeman slowers, we now felt confident in our next challenge, to build the electromagnets for the main chamber. For this, a total of four coils would have to be built: two MOT coils, to be run in anti-parallel configuration, and two bias coils, to be built and run in Helmholtz configuration.[6]

The main chamber coils – sometimes affectionately referred to as the "Nolan coils" – were designed and built by a 2008 REU student, Nolan Maloney, as his main project for the summer, with myself and another graduate student, Lee Willcockson, for technical guidance. The design and winding process was mostly the same as for the Zeeman slowers, but with a more sophisticated mount, with a retaining plate on either end, onto which the coils could be wound without slipping off. After the winding process was complete, the mount was carefully removed, and the coils covered with high-temperature epoxy on the top, inner, and outer surfaces. The bottom surface, which would be facing the vacuum chamber, was instead secured by a single sheet of kapton, held in place around the edges by the epoxy. Finally, a large volume of epoxy was poured between the inner (MOT) and outer (bias) coils to keep them flush and concentric.

[6]The Helmholtz condition is satisfied for two wire loops carrying parallel currents when the diameter of each loop is twice their vertical separation. In such a configuration the curvature of the magnetic field at the center vanishes, yielding optimal field uniformity.

	MOT Coils	Bias Coils
Bias field strength (G/A)	2.4	4.2
Field gradient strength (G/cm/A)	1.0	≈ 0.1
Self-inductance (μH)	13 (quadrupole) 23 (bias)	105
Resistance (mΩ)	10.8	20.0

Table 6.1: Properties of MOT and Bias coils. The MOT coils have two current configurations (see section 6.4.2), whereas the bias coil fields are both measured for parallel currents.

As with the Zeeman slowers, the main chamber coils had their theoretical characteristics tested with a Hall probe, while mounted on a "dummy mount" to simulate their configuration in the vacuum chamber. It was found that the MOT coils, when run in anti-parallel configuration, produced an axial magnetic gradient of 0.84G/cm/A. The bias coil field was measured at 4.37G/A, with excellent flatness of field at the trap center. Small corrections to these field responses have since been found, by measuring Zeeman-shifts of ^{6}Li optical resonances at high magnetic fields, and observing the free-fall acceleration of ^{6}Li with a magnetic gradient present. These corrections may be due to systematic errors in the Hall probe measurements, or subtle differences in coil alignment between the dummy mount and main chamber. Our current best estimates of the main chamber coil properties are summarized in Table 6.1.

6.3 Water cooling of electromagnets

Long before the electromagnets were installed, work had already begun on a distribution system to deliver cooling water to each segment of the magnets. The high currents used in each of our magnets makes water cooling an absolute necessity, and the flow in each magnet had to be independently controlled to allow for diagnostics, and to permit the rest of the machine to run even when one of the coils was being serviced. Furthermore, a flow monitoring system needed to be in place, to shut down the current supplies in the event of a disruption of flow.

6.3.1 Calculating flow rates and coil temperatures

The flow through each of the coils was estimated using the Hagen-Poiseuille equation, which is a special case of Navier-Stokes theory. The Hagen-Poiseuille formula relates differential pressure to flow rate, assuming laminar (non-turbulent) flow through a straight, cylindrical pipe:

$$\Delta P = \frac{8\eta}{\pi}\frac{L}{R^4}\Phi \tag{6.1}$$

Here, η is the dynamic viscosity of water (which has a surprisingly strong temperature dependence), L and R are the length and radius of the tube, and Φ is the total flow through the tube, in units of volume over time. Note in particular the strong dependence on the size of the tube, which scales inversely with R^4. This simplifies calculations somewhat, since we can assume the pressure drop through the 1/4" delivery tubes to be negligible compared to that in the wire cores. The length of each coil was never measured directly, but was estimated by counting the number of revolutions and coil radius of each wire segment.

Of course, none of the above idealizations (non-turbulent, straight tube, circular cross-section) are strictly true in our case, but are reasonable approximations. The most important deviation is the square cross-section of the wire core. Although the exact analogous flow equation could presumably be derived for a square pipe using series expansion techniques, we went with the more straightforward approach of setting reasonable bounds on the theoretical flow. We take our lower bound to correspond to a flow restricted to the cylinder with radius $a/2$ inscribed within a square pipe with dimension a. Our upper bound assumes a cylinder with cross-sectional area a^2, equal to that of the wire core.

$$\frac{\pi}{128}\frac{a^4\Delta P}{\eta L} \leq \Phi \leq \frac{1}{8\pi}\frac{a^4\Delta P}{\eta L} \tag{6.2}$$

The two bounds differ only by a factor of 1.6, which at any rate is less than our safety margin.

The flows in each of the coils was measured experimentally after they were installed. Although flowmeters were later installed, the first measurements were done simply with a measuring beaker and a stopwatch. It was found that all the experimental flows were slightly lower than theoretical predictions by a fixed amount, which was independent of wire length. This is likely due to a small pressure drop between the gauge on the entry line and the beginning of the coil, perhaps because of resistance in the delivery lines, but more likely due to turbulent flow near the interface to the wire core. The experimental flows are well-modele by an equation o fthe form $\Phi = \Phi_0/(L - L_0)$, where the "virtual length" L_0 accounts for boundary effects.

The goal of the flow calculation was to ensure that, for a given delivery pressure and electrical current in the coil, the flow was sufficient to prevent the magnets from overheating. If we make the assumption that the cooling water fully thermalizes with the coils as it passes through, it carries away heat at a rate

$$Q = \Phi c_{H_2O}\left(T_{coil} - T_{wall}\right) \tag{6.3}$$

where c_{H_2O} is the volumetric heat capacity of water, and T_{wall} is the ambient temperature

of the water in the walls of the physics building, typically about 15°C. At steady state, this will be equal to the heat deposited in the coil by electrical work, $Q = I^2R$. Combining these equations, we find

$$T_{coil} = T_{wall} + \frac{I^2R}{\Phi c_{H_2O}} \tag{6.4}$$

Computing the flow rate for each coil, it was found that all of the Zeeman slowers were within a factor-of-3 tolerance of reaching 100°C. (Beyond this temperature, Very Bad Things are prone to happen.) However, the bias coils were found to reach dangerously high temperatures of above 80°C when ramped to the currents needed to access the ^{6}Li Feshbach resonance at 834G. This concern led us to set up the MOT switching circuitry (described below) and eventually to acquire the rowdy "Webtrol" booster pump.

6.3.2 Water distribution & wire connectors

To distribute cooling water to the many wire segments – there are 10 in total – a water distribution system was built. Colloquially dubbed "the water panel," (and later, in reference to concurrent political events, renamed "the waterboard") the distribution system consists of a single 1/2" plexiglass sheet supporting two manifolds, entry and return valves for each of the lines, and a set of flowmeters. The entire project was carried out with $3000 worth of hardware from Swagelok, with the flowmeters coming from the McMillan Corp.

In addition to the electromagnets, several other items are cooled by the waterboard. These include a set of thermoelectric coolers (TECs) under each of the vacuum chamber ovens, as described in section 5.3. Furthermore, two high-power beam dumps for the ODT laser receive water cooling. Finally, the "IGBT box" (described below) has two sets of water-cooled components: the switching IGBTs, and the forward high-current diodes.

Water and electrical current both need to be interfaced with the electromagnets. The water interface was a bit of a challenge, since there are no commercially available fittings for square tubing. Our solution was to order up a set of compression fitting caps, and have the physics department machine shop staff etch 1/8" square holes in them with their electrical discharge machine. These caps were then brazed onto the end of the square wire, using standard electrical solder, generous amounts of flux, and a small blowtorch.

Electrical interface was achieved with a home-built connector block, which was clamped onto the wire approximately 1" above the compression fitting cap. 25 identical connector blocks were tediously machined from copper, cutting them on a dull bandsaw, grinding them to shape, milling out a gutter for the squarewire, and drilling holes for clamp screws and wire entry. The blocks were built for No. 4 AWG wire, which was originally used for all

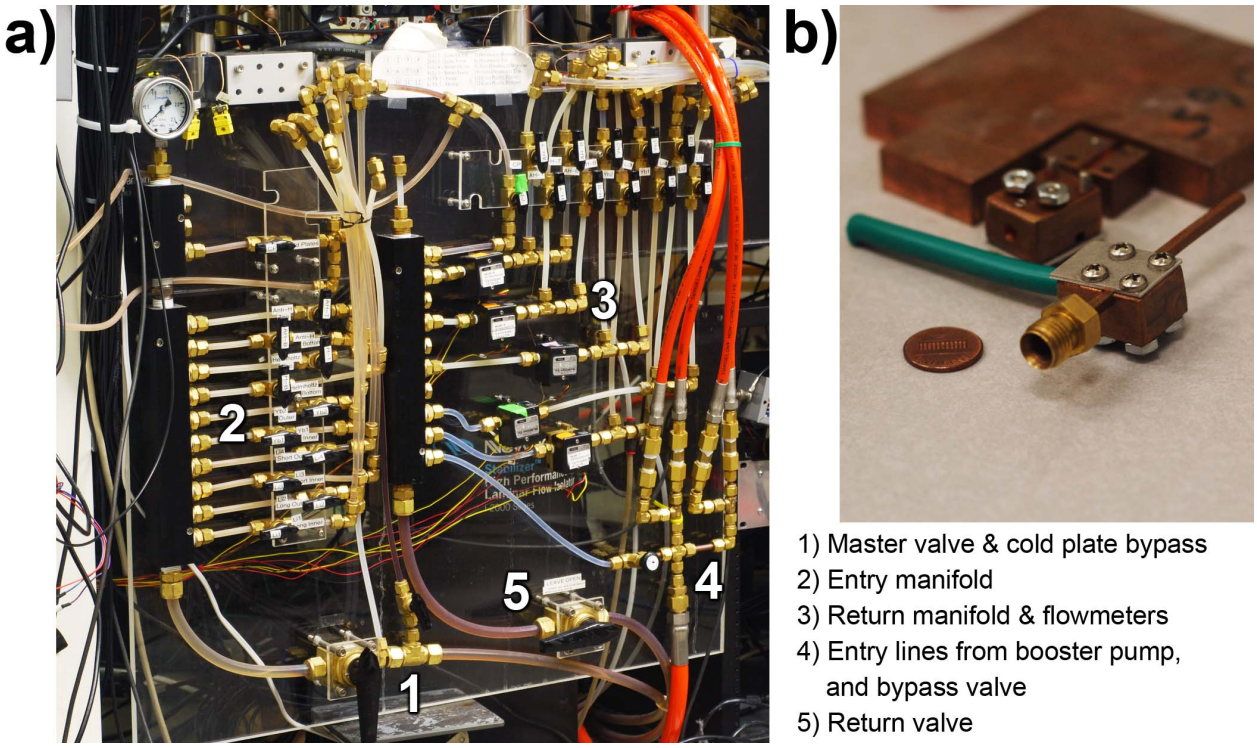

Figure 6.4: a) Photograph of water distribution panel. b) Photograph of a square wire interface. The compression fitting cap has been equipped with a square hole, and is brazed onto the square wire.

high-current applications. However, once our experiments required currents in excess of 40A a heavier-gauge wire was required. Only a few of the connector blocks have been modified to handle this larger wire, but so far no major issues have been detected in the somewhat awkwardly mismatched interface.

It should be noted that, once current has been switched on, the compression fittings on the squarewire are floated at some voltage above that of the optical table. Care therefore must be taken that these are properly insulated, so current intended for the magnets does not instead escape through the table surface.

6.3.3 The "Webtrol" booster pump

In the summer of 2011 we began a search for narrow Feshbach resonances in the ground state Li-Yb system. These were predicted to exist at either 1100G or 1600G.[88] After a cursory but fruitless search around the lower of these fields it was decided that an upgrade to the water cooling of the bias coils was necessary, so that we could safely bring the field above 1600G. We decided to boost the cooling water flow not only in the bias coils, but also the MOT coils. Although the MOT coils can run safely at the power supply's maximum output, we chose to include them in the upgrade, in anticipation of possible future experimental requirements.

By recommendation from colleagues at MIT, we purchased a 300PSI booster pump from Weber Industries' "Webtrol" division. Like other sorts of trolls, the Webtrol is particularly loud and obnoxious, and for this reason it is placed in the equipment storage alley behind the lab, with a switchbox installed in one of the portholes between the lab and the alley. A nylon-fiber-reinforced hose, rated to 2000PSI, runs from the pump to the waterboard, where a homebuilt manifold divides the high-pressure water into 4 components.

It is worth noting that most high-pressure tubing is reinforced by an internal metal mesh. Since our magnet wire interfaces are electically charged, such tubing would have carried dangerous voltages and currents to the booster pump, and presumably onward to other places they absolutely do not belong. We were therefrore careful to select non-conductive tubing.

Finally, a bypass valve was installed between the high-pressure entry manifold and the return manifold. This was implemented because the Webtrol is not designed to pump on highly resistive systems. In order to prevent damaging pressures from building up within the pump some minimum flow needs to be maintained. We adjust this flow with a needle nose valve on the bypass line to maintain a gauge pressure of 400PSI at the pump.

Figure 6.5b shows the performance enhancement gained from the Webtrol. Equation (6.4) predicts the coil temperature to be a quadratic function of the current, with a pref-

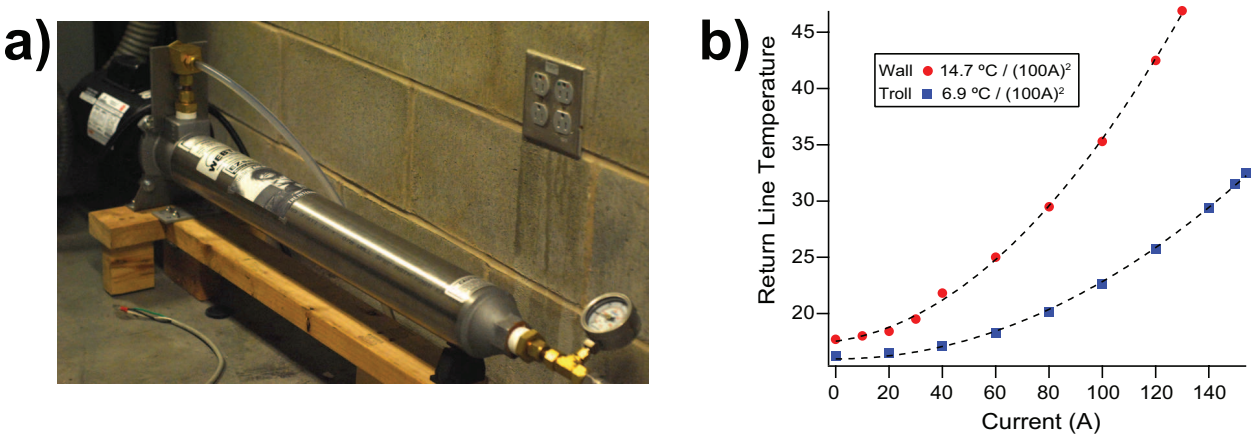

Figure 6.5: The Webtrol booster pump. a) The pump, set up for operation. The inset shows the safety warning label and power switch. b) Temperature of water exiting the bias coils, with the pump active, and with wall pressure only. With the pump in place, significantly higher currents can be achieved at safe temperatures.

actor inversely proportional to the flow Φ. (This assumes that the resistivity of the coil has negligible temperature dependence.) The experimental temperatures do indeed follow a square law; however, the curvature decreases only by a factor of ≈ 2, while the flow quadruples when the Webtrol is active. Although the booster pump raises the pressure by a factor of 3.5 (from 100PSI to 350PSI), the flow increases only by a factor of ≈ 2. This may be due to the auxiliary water filters that are installed in each of the coil entry lines to prevent corrosion debris from the Webtrol from clogging the wire cores.

The enhanced flow levels raise the safety ceiling of our bias coil current by 50%, or approximately 400G, barely sufficient to reach the target field of 1600G.

Unfortunately, although the Webtrol improves the performance of our electromagnets, it also introduces a lot of acoustical noise to the optics table, which destabilizes our lithium laser lock. This, we believe, is due to 120Hz modulations in the water pressure resulting from the 60Hz single-phase power used to drive the pump. The MIT group uses a model that runs on 3-phase power, and they have not noticed any significant vibrations resulting from their Webtrol.

6.3.4 Interlock system

Given the importance of our electromagnets, and the immense difficulty of replacing any one of them, we have an interlock circuit in place, to shut down the currents in the event of a failure in the cooling water. The interlock consists of three main components. The first is the set of flowmeters on the water panel, which output a DC voltage proportional to the detected flow. These voltages feed into a Keithley 2700-series multi-channel voltmeter,

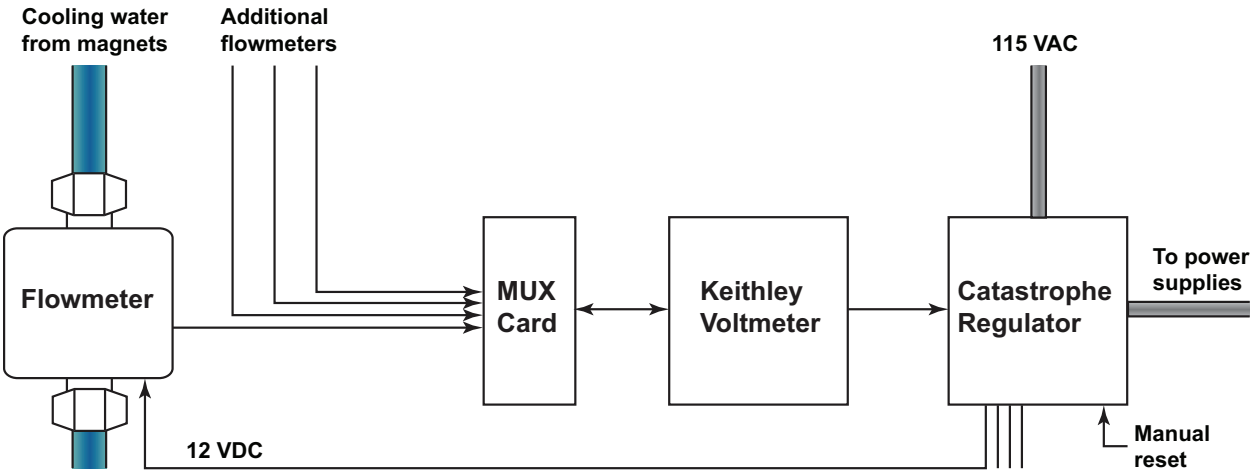

Figure 6.6: Schematic of the interlock system. The flowmeters report the water flow, and are sequentially interrogated by the Keithley voltmeter through an onboard multiplexer (MUX) card. The catastrophe regulator receives a TTL signal when any flow reading is below threshold, and shuts down the electromagnet power supplies until manually reset.

which may be programmed to sequentially and cyclically scan up to 20 channels.[7] Each of the 5 channels that we use in our scan is programmed with a lower voltage limit, typically set to $\approx 90\%$ of its normal value. If any channel is found to drop below this threshold, a TTL signal on the back panel of the Keithley unit goes to its low value. This is then detected by a home-built "catastrophe regulator box," which then latches and switches off the AC power to the Zeeman slower power supplies, and also the IGBT switches that control MOT and bias currents. (The MOT and bias power supplies run on 3-phase power, which the regulator box is not built to manage.) The regulator box may subsequently be reset with a push button, once the flow issue has been resolved.

It is a persistent fact in our lab that the flowmeter readings tend to degrade over time. We believe that this is not an issue with the water flow degrading over time, but rather with the flowmeter. The flowmeters measure the water flow using a paddle wheel with black-and-white "spokes," and a photodiode and detector to measure the revolution rate of the wheel. The paddle wheels have been found to jam if there are sudden changes in the flow level, or if large air bubbles pass through at high speed. We therefore believe that the slow reduction of flow reading is due to friction in the paddle wheel. This hypothesis is further supported by the observation of a "slow" flowmeter reverting to full reading after having water run through it in reverse for a short time, which presumably helped dislodge the paddlewheel. For this reason, when the interlock spontaneously trips, the solution is usually to simply lower the

[7] The Keithley voltmeter may also be programmed to read thermocouple probes. We currently have such probes fixed to a handful of areas, for manual diagnositcs. In the future, these may be incorporated into the interlock, if this were deemed necessary for a high-duty experiment.

threshold. Nonetheless, a detailed log is maintained of such changes, to prevent the threshold value from wandering too far from its original setting without some investigation into the cause.

6.4 Current supplies & control

Once the water delivery system to the electromagnets was fully built, it was time to hook up the current supplies. Our experiment has a total of 8 independently controlled supplies: one for each of the Zeeman slower segments, two for the main chamber coils, and one for each of the three "compensation coils." The latter three coils, which provide small, orthogonal bias fields, are not water-cooled due to the low current (10-15A) they carry.

6.4.1 Fast current switching

The Zeeman slowers and compensation coils are all switched by a set of solid-state relays, which are rated to 40A. In order to switch the much larger currents used in the MOT and bias coils, a pair of high-current IGBTs (insulated-gate bipolar transistors) are employed. These huge switching devices may carry currents up to 300A, with 1kV isolation when in the "open" state.[8] Each transistor is gated by an 18V signal, the cathode terminal of which is common to the source terminal. The control circuitry thus needs to be isolated from the rest of the lab, and floated at whatever voltage the IGBT source happens to hold. We achieve this by using individual, isolated power supplies for the MOT and bias switches, and analog isolators to maintain a floating offset from the computer control output. (Digital isolators would also work for simple switching, but, as we shall see, there are cases where we want analog control of the gate voltage.)

In addition to the IGBTs, several layers of protective circuitry are required for such high-current applications. When running, the electromagnets store a significant amount of internal energy, by virtue of their inductance. When the magnets are subsequently switched off, this energy needs to be safely dissipated somewhere. If the inductor current has nowhere to go, tremenedous voltages will build up at the terminals, often on a megavolt-scale, until something breaks down and provides a discharge path. Needless to say, such events are not conducive to a safe and happy lab environment.

To prevent damage to lab hardware (and any inquisitive grad students) a flyback path is installed in each circuit. The flyback path consists of a reverse-biased diode and a resistor.

[8] An IGBT may be modeled as two transistors: an n-channel MOSFET, which provides an insulated gate; and an npn bipolar transistor, the base of which is supplied by the MOSFET source. The high current flows through the bipolar transistor only. The need for very large junctions gives these devices their characteristic wide, flat shape.

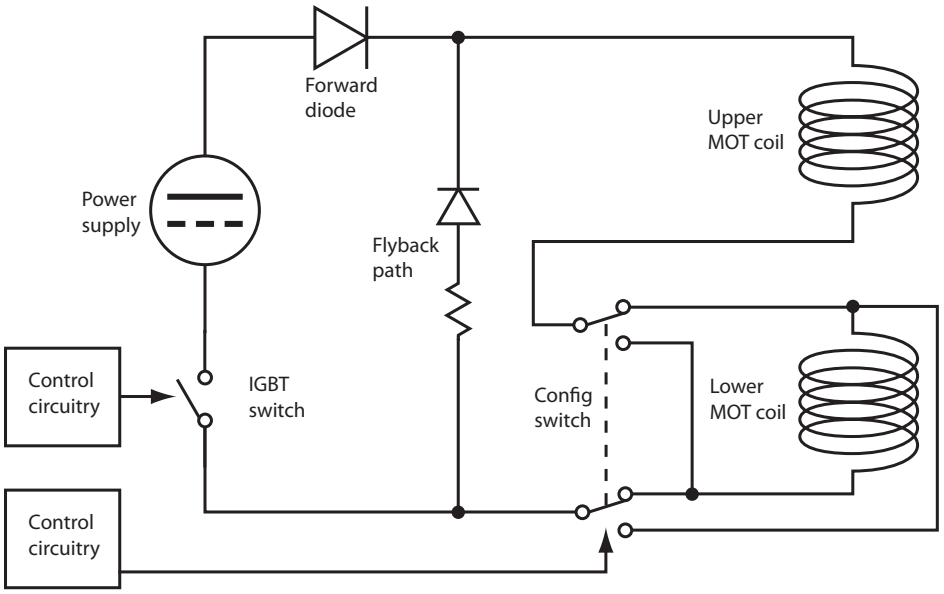

Figure 6.7: Schematic of high-current circuit used for MOT coils. Control circuitry needs to be floated, using isolated power supplies and analog isolators. The flyback diode dissipates the self-inductance energy of the coils, whereas the forward diodes protect the power supplies from mutually induced voltage spikes from the bias coils. The bias coil setup is identical, but with the omission of the configuration switch.

During operation, this path carries no current; however once the IGBT is switched off it provides a path for the inductor current to dissipate. The value of the resistor (typically a few Ohm) is chosen low enough that the resultant voltage during ringdown is within safe limits, but high enough to provide a fast field shutoff for the experiment.

Another problem, which we discovered during preparation for our Feshbach molecule paper, arises when both the MOT and bias coils are run simultaneously at high currents. If one supply is shut off, with the other one still running, mutual inductance effects will produce a large current spike in the still-running coil, which may travel through the power supply. We found that when both coils were run in parallel configuration the current spike was in the forward direction (as anticipated), and could be handled by the flyback circuit. However, when the MOT coils were in quadrupole configuration the spike was reverse, and it is believed that such a voltage spike was responsible for the tragic death of one of our expensive Lambda-EMS power supplies. To prevent future problems of this sort, a forward diode was installed near the anode terminal of each power supply.

As a final layer of protection, varistors were placed across the terminals of each power supply. A varistor behaves as two diodes connected back-to-back in series, providing a high level of isolation up to some breakdown voltage, V_{th}, beyond which their resistance drops precipitously. They thus act as protection against voltage spikes above V_{th}, and can be

purchased with a wide range of thresholds, according to hardware requirements.

6.4.2 MOT coil configuration switching

We discovered early on that the bias coils had a current limit, set by both water cooling capacity and the resistance of the bias coils, which yielded a magnetic field limit below the regime of greatest interest to us, near the Feshbach resonance at 834G. To solve this problem, we developed a switching system for the MOT coils, by which they could be alternated between anti-parallel (quadrupole) configuration, and parallel (bias) configuration. The scheme was to use two SPDT switches that toggle together to reverse the current in the bottom coil, as shown in Figure 6.7.

The original version of this circuit was built using four IGBTs, each of which would act as an SPST switch. In implementing this setup, several frustrating obstacles were encountered, most of them related to the commonality of the gate cathode and source. To account for all the different floating voltages and different possible configurations that resulted, the control circuitry had to be built with extreme care to avoid current leakage paths. Even a small fraction of the current passing through the control circuit instead of the coil would significantly alter the quadrupole field for the MOT in an unpredictable way, leading to persistent troubles with spatial alignment of the atoms. In the end, no less than four independent voltage supplies were required to drive the final version of the control circuitry.

The eventual choice to dispose of the IGBT scheme was, however, not due to issues with the control circuit, but with the voltage drop that is native to the IGBTs. Each transistor carries a persistent drain-source voltage of ≈ 2V. In the MOT coil circuit this led to a 6V parasitic drop due to all the IGBTs, which left the power supply unable to produce sufficiently high currents for our purposes. The solid-state scheme was therefore replaced with a pair of physical SPDT contact relays (Stancor 586-series). These devices are rated for up to 100A in the "low" state, and 200A in the "high" state. The main drawbacks to these relays is that they make some amount of acoustic noise when toggling, and that there is a brief moment, during switching, when all terminals are open. The latter means that the relays may only be toggled when the current is shut off entirely, to prevent inductive voltage spikes.

6.4.3 Current feedback option

All of our computer-controlled power supplies come with two external control options: current-mode and voltage-mode. The current mode maintains a stable current by means of an internal duty cycle in the 1-10kHz range, which is controlled by a feedback circuit to maintain constant current. Although the current supplies we have used for the main chamber

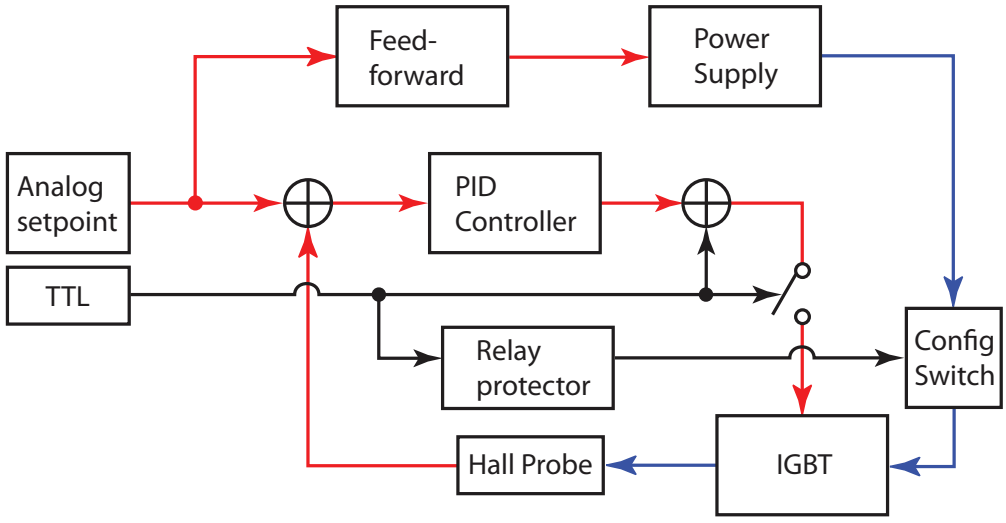

Figure 6.8: Block diagram of homebuilt current feedback system. Analog signals are shown in red, digital signals in black, and high-current leads in blue. The feed-forward circuit controls the power supply output voltage, whereas the PID controller provides fast control of the IGBT drain-source voltage. The TTL input adds a bias to the PID output to bring the IGBT gate voltage near threshold, and also controls a solid-state switch to secure the gate to ground when off.

coils have proven to be stable and repeatable enough for our purposes so far, we also have a home-built current stabilization system with the same purpose.

A block diagram of the homebuilt feedback system is shown in Figure 6.8. Briefly, the current supply is set to voltage mode, and a feed-forward circuit ensures that the voltage limit is set slightly above that required for the set point current. A feedback circuit then reduces the current to the appropriate level by modifying the gate voltage on the IGBT. The FET characeristics of the IGBT cause the parasitic drain-source voltage to increase at gate voltages close to threshold, and we use this feature to accurately control the current. The current in monitored by the feedback circuit via a Hall current meter. Additionally, the feedback signal is mixed with an external TTL signal, to preserve the original IGBT functionality of fast current switching.

Finally, the feedback box has a built-in delay generator to prevent switching of the MOT coil configuration relays while the current is on, or whithin 10ms of the IGBT being shut off.

The homebuilt feedback system has a few advantages over the internal one that is built into the current supplies, and is likely to find use in the future. For one, it allows for downward current ramps much faster than those afforded by the internal mechanism, which are typically limited to $\sim$ 20ms settling time. Secondly, it does not suffer from the problem with transient current overshoots durign switching that the internal current control has, which is due to the internal feedback railing high when the IGBT is switched off. Finally, the

external feedback may prove to dampen out the current ripples that are endemic to variable high-current supplies. These ripples, which come from the internal current-switching duty cycle of a few kHz, may be measured by the Hall meters, but the readout signal is currently below the noise level of our oscilloscopes. Nonetheless, the feedback circuit may be able to respond to them and dampen them out, or the Hall meter circuit could be modified if these current ripples are found to be a problem.

7 Two-Species Magneto-Optical Trapping

When we started our experiment, there was very little available information on trapping two species from different groups of the periodic table. The ins and outs of trapping lithium with another alkali were well-studied, as were those of trapping ytterbium alone, but there was a very real chance that the two species would not behave well when trapped together. In chapter 11 we shall look at the stability of this mixture in an ODT. Here, we explore the experimental details of loading the dual-species MOT, and efficiently transferring the atoms to the ODT.

7.1 Single-species trapping methods.

Before exploring simultaneous trapping schemes, we consider the techniques used in single-species experiments, which are generally transferrable to the dual-species schemes.

7.1.1 Lithium MOT

The lithium MOT was the first one we achived, shortly after the successful bakeout of the main chamber. Initially, we were puzzled to find extremely high MOT temperatures of $\gtrsim$ 4mK. It was subsequently discovered that this was due to the high power offered by our lithium laser. By doubling our cycling transition detuning from 3Γ to 6Γ we got temperatures $\lesssim$ 1mK, with greatly enhanced atom numbers, up to 4×10^8, due to the 8-fold increase in capture volume.

Nonetheless, further improvements were required to reach sufficiently low temperatures and high densities, to transfer efficiently to the ODT. In particular, the temperature of the loading MOT is still much greater than the theoretical lower limit: the Doppler temperature $k_B T_{Dop} = \hbar\Gamma/2 = 140\mu$K. To cool and compress the MOT further we employ a transitional scheme in which the laser power and detuning are both reduced over the course of 50ms. Such compression schemes are not at all a novelty, but are used by almost all ultracold atom experiments. With the final compression settings finely tuned, we are able to reach temperatures as low as 300μK in lithium. Although this is still a factor of 2 above the Doppler temperature, lower temperatures are almost impossible to achieve, due to the excited state hyperfine manifold in ^{6}Li, (see Figure 4.1) which causes an apparent broadening of the transition linewidth.

Finally, in the 100μs after transfer to the ODT we optically transfer the atoms to the $F = 1/2$ hyperfine state. We do this by quickly ramping up the power in the cycling laser, after the repump laser has been switched off. This transfer to the absolute ground state is

		^{6}Li F=3/2	^{6}Li F=1/2	^{174}Yb	^{173}Yb
Load	I	$60I_{\rm sat}$	$55I_{\rm sat}$	$750I_{\rm sat}$	$750I_{\rm sat}$
	δ	6Γ	3.5Γ	$(55\pm20)\Gamma$	$(40\pm20)\Gamma$
	B'	20G/cm		3G/cm	3G/cm
Final	I	$0.07I_{\rm sat}$	$0.08I_{\rm sat}$	$0.8I_{\rm sat}$	$2I_{\rm sat}$
	δ	1.5Γ	3Γ	2Γ	4Γ
	B'	60G/cm		18G/cm	25G/cm

Table 7.1: Typical experimental parameters for loading of ^{6}Li, ^{6}Li repumper, ^{174}Yb, and ^{173}Yb. The key parameters that require optimizing are laser intensity I, laser detuning δ, and magnetic field gradient B'. Two sets of numbers are provided for each isotope, reflecting the parameters for MOT loading and for the end point of compression. I refers to the total laser intensity in all three retro-reflected beams. B' refers to vertical gradient; for horizontal gradients divide the figures by 2. Γ and $I_{\rm sat}$ for Yb refer to the properties of the intercombination transition.

necessary to prevent inelastic, spin-relaxing collisions in the ODT, and also to obtain the states $|1\rangle$ and $|2\rangle$ in the high magnetic field regime, which form the constituents of the broad Feshbach resonance.

7.1.2 Ytterbium MOT

Compared to the lithium MOT, and other alkali MOTs by other research groups, our ytterbium MOT requires a surprisingly long time to load. Even with our best loading rates, the time required for the number to saturate is similar to our vacuum-limited lifetime, suggesting that our peak numbers are limited by background collisions, and not by internal inelastic processes, as is common in alkali MOTs.[84] We attribute this low load rate to the mismatched linewidths of the slowing and trapping lasers. The narrow width of the intercombination line leads to a low capture velocity, much smaller than the width of the velocity distribution coming out of the Zeeman slower. The accuracy with which we can control the speed of the atoms at the end of the slower is limited by the width of the slowing transition, which is 160 times broader than the MOT (intercombination) transition, and additionally power broadened by the intense slowing beam.

Although this has not yet been experimentally tested, it is likely that we have optimized our Zeeman slower parameters – the solenoid current and laser detuning – such that almost half of the atoms actually fully stop and turn back before the end of the slower tube. In this way, the peak of the velocity distribution will be within the capture range of the MOT, but a disappointingly large fraction of the atoms are lost.

In an effort to improve our capture velocity, and also increase the capture volume of the

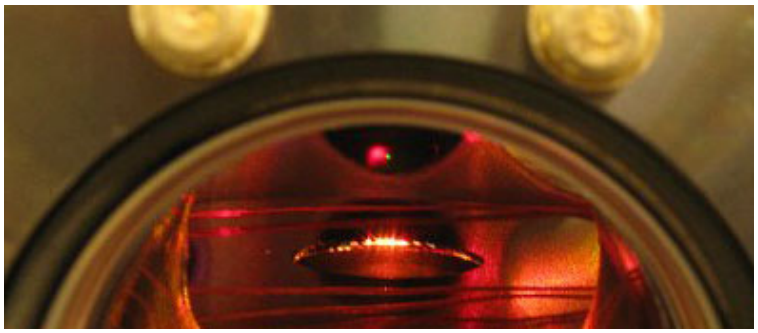

Figure 7.1: Photograph of simultaneously magneto-optically trapped lithium and ytterbium. The ytterbium atoms are visible as a tiny, green dot, to the right of the much more diffuse lithium cloud.

Yb MOT, we modulate the detuning of the trapping laser. We find the best results with a modulation frequency of $\approx$ 150kHz. This is much faster than the trap motion $\sim$ 1kHz, of a trapped atom, so the effect of the modulation is to artificially broaden the trapping light. Overall, we find a factor-of-2 improvement in our CMOT number with a modulation amplitude of 20 linewidths, sufficient to trap 2×10^7 atoms in 10s of loading. Furthermore, the modulation reduces the effects of stochastic frequency drift in the trapping light.

The Yb MOT, like its counterpart, is compressed before transfer to the ODT. We find that the time required for compression is significantly longer for ytterbium: 200ms instead of 50ms. During the compression step we also ramp down the modulation amplitude to zero. A short (5ms) hold step at the end of compression is sometimes found to improve transfer to the ODT.

7.2 Dual-species techniques

To accommodate dual-species experiments, the MOT light for lithium and ytterbium is overlapped using a dichroic mirror. The combined beam is then split into the three (retroreflected) MOT beams using broadband polarizing beam splitters, and wavelength-selective $\lambda/2$ waveplates. Circular polarization is established using dual-wavelength $\lambda/4$ waveplates.[9]

Our original plan for the two-species MOT was to load lithium and ytterbium simultaneously, using the same quadrupole field strength. This technique had previously been successfully implemented with lithium and sodium.[89] However, after achieving single-species MOTs in both lithium and ytterbium, some very obvious problems were identified.

[9]These custom waveplates were produced by the Chinese manufacturer Foctek, which will forever be remembered in the lab for their ability to ship the wrong items halfway around the world, and forgetting to process our credit card payment until prompted by us. Our lab books contain at least one exasperated instance of "what the Foctek" jotted in the margin.

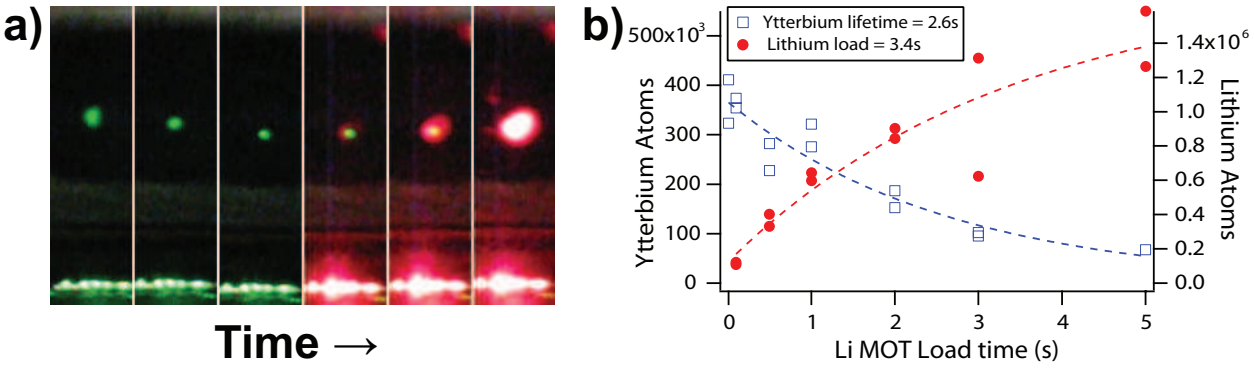

Figure 7.2: Dynamic two-species trapping. a) Time-laphoweverse photographs of loading atoms. The fully loaded Yb MOT is compressed as the magnetic field is ramped up. The Li MOT is then loaded over the course of 2s, before both species are transferred to the ODT. In the last frame, the Yb atoms are entirely blotted out by the much stronger Li fluorescence. b) Number of atoms loaded into the ODT as a function of Li loading time. As Li numbers increase, Yb is quickly ejected from the trap.

Due to its narrow trapping linewidth of 180kHz, the ytterbium MOT operates at a very low detuning, and requires correspondingly weak magnetic gradients in order to achieve reasonable capture volumes. At the gradients at which ytterbium is optimized, however, the lithium trapping force is very weak, leading to low atom numbers. Furthermore, as one can see from Figure 7.1, the two species proved to be almost entirely spatially separated when coexisting. This separation was due partly to the weak confinement force on lithium, which made it sensitive to small power differences in each pair of counter-propagating MOT beams, and partly (we believe) to inelastic processes which lead to trap loss of both species in the overlap region. All of these issues raised serious doubts about the viability of the simultaneous trapping scheme.

Our second idea for a MOT loading scheme was a dynamic, simultaneous loading technique. This was inspired by our method for compressing the Yb MOT, which involved ramping up the magnetic quadrupole to achieve a high density of atoms before transfer to the ODT. The dynamic scheme involved compressing ytterbium, and then loading lithium at this higher magnetic field, where high atom numbers of lithium could be achieved in $\sim$ 2s. The magnetic gradient was then further ramped up during compression of lithium, before both species were simultaneously transferred to the ODT.

The choice of loading ytterbium first came naturally, as the required MOT load time for this species was 30s or more, whereas lithium could be loaded much faster. We have since reduced the required ytterbium load time to $\sim$ 10s, but still use a scheme where the Yb MOT loads first, for this reason and others described below.

The dynamic simultaneous loading method was the technique with which we first achieved

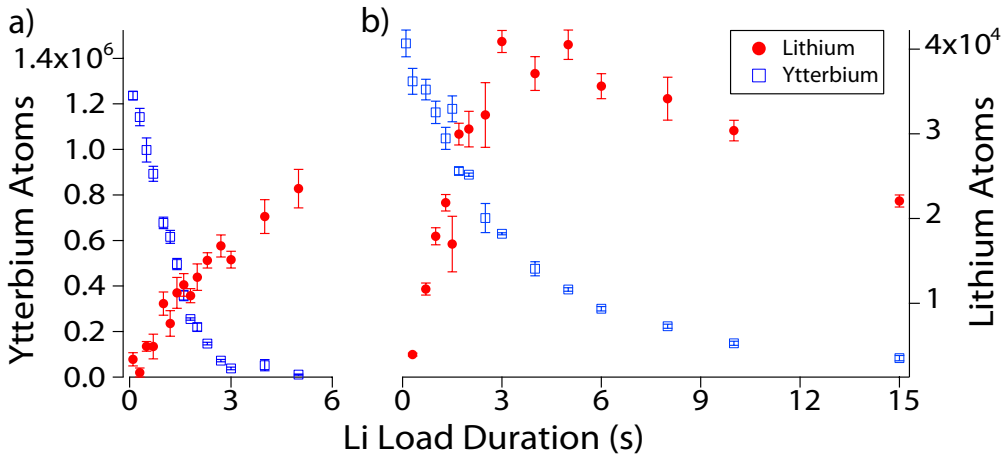

Figure 7.3: Loading curves for the sequential MOT loading scheme. The data is taken 1s after transfer to the ODT, after some thermalization and spontaneous evaporation has taken place. Note that, unlike in Figure 7.2b, the axes for the two species are different. a) The Li load still has a strong adverse effect on Yb numbers when the MOT and ODT are collocated. b) The lifetime of Yb during Li load may however be drastically enhanced in the sequential scheme, by displacing the Li MOT from the loaded Yb atoms.

simultaneous optical trapping. By counting the atoms of each species in the ODT, we observed the effect of the loading Li MOT on the ytterbium atom number. Our finding was, not surprisingly, that the lifetime of ytterbium was strongly reduced during the lithium load step. The technique was nonetheless considered a success, as it provided up to 5×10^5 atoms of either species in the ODT, or a mixture of the two with similar total atom number. By varying the duration of the Li MOT load step, we could accurately control the ratio N_{Yb}/N_{Li}.

The dynamic simultaneous loading scheme was nonetheless eventually abandoned, in favor of the technique that we are still using today. This is the sequential loading scheme, in which ytterbium is fully loaded, compressed, and transferred to the ODT before the Li MOT load begins. On the surface, this should not lead to a significant improvement in atom numbers, as the same inelastic channels exist whether ytterbium is in a MOT or ODT during lithium load. Indeed, Figure 7.3a shows a lifetime of ytterbium similar to that in the dynamic scheme. (The much greater initial ytterbium number in this figure is not a result of the loading scheme, but comes from the data being collected at a later date than that in Figure 7.3b, after major improvements had been made to ytterbium loading techniques.) However, the sequential scheme does have a distinct advantage in that it allows the two species to be displaced from one another during the sensitive period during Li MOT load.

Our sequential technique therefore involves a small vertical bias field that shifts the center of the MOT quadrupole upward by a modest 1mm, similar to the diameter of the Li MOT itself. This bias field is then removed during lithium compression, in order to overlap the Li

MOT with the ODT in the last milliseconds before transfer.

In this way we reduce the density overlap of the two atomic clouds, and, as shown in Figure 7.3b, greatly suppress the inelastic processes that lead to loss of ytterbium. Furthermore, since lithium is also affected by these inelastics, the displacement leads to a doubling of the Li MOT loading rate, leading to larger numbers of both species. For most current experiments, we are interested in a $\sim$ 10:1 ratio of Yb:Li, and therefore choose lithium loading times of 1-2s.

An interesting feature in Figure 7.3b is the turnover of lithium number for long load times. Apparently, loading the Li MOT for too long may actually reduce the number of atoms captured. The reason for this rolloff is that the data shown was taken after a 1s hold in the ODT after lithium transfer. During this time, it is typical for the most energetic lithium atoms to escape the trap through spontaneous evaporation. Through the presence of a thermal bath of (much colder) ytterbium atoms, this evaporation quickly reduces as the lithium atoms cool through thermal contact with the bath. By loading lithium for too long, this thermal bath is destroyed, and there is nothing to prevent lithium from evaporating off.

The observation of such thermalization effects are also a good sign that, with the Li MOT displaced, the ytterbium atoms are allowed to remain at a low temperature. Indeed the losses observed when the Li MOT is overlapped with the ODT are not only due to inelastic processes, but also elastic collisions, through which the ytterbium is heated up until it escapes from the ODT.

8 The ODT

Although our dual MOT collects a large number of atoms in an ultracold environment, it is unsuitable for most of the experiments of interest to us. For one, the temperature is still several orders of magnitude too high, and the density too low to study quantum phenomena. Secondly, the atoms in the MOT interact far more strongly with the trapping beams than with one another, making studies of interparticle collisions highly impractical. Finally, the specific magnetic field configuration demanded by the MOT excludes any experiment that requires a magnetic bias field. For all these reasons, a second type of trap is required by most atomic experiments.

8.1 Potential form and trap frequencies

Our ODT is comprised of one or two tightly focused Gaussian beams, (depending on experimental requirements) with a wavelength of 1064nm. Each beam has a $\mathrm{TEM}_{0,0}$ intensity distribution near the focal point, which has the form

$$I(x,y,z) = \frac{2P}{\pi w(z)^2} e^{-\frac{2r^2}{w(z)^2}} \tag{8.1}$$

where $r^2 = x^2 + y^2$, and the beam width

$$w(z) = w_0\sqrt{1+(z/z_R)^2},\ z_R = \frac{\pi w_0^2}{\lambda} \tag{8.2}$$

The focused waist w_0 is typically a few tens of microns, whereas the Rayleigh length z_R is on the order of a millimeter.

More generally, we may expect our beam to exhibit some ellipticity, such that the focus

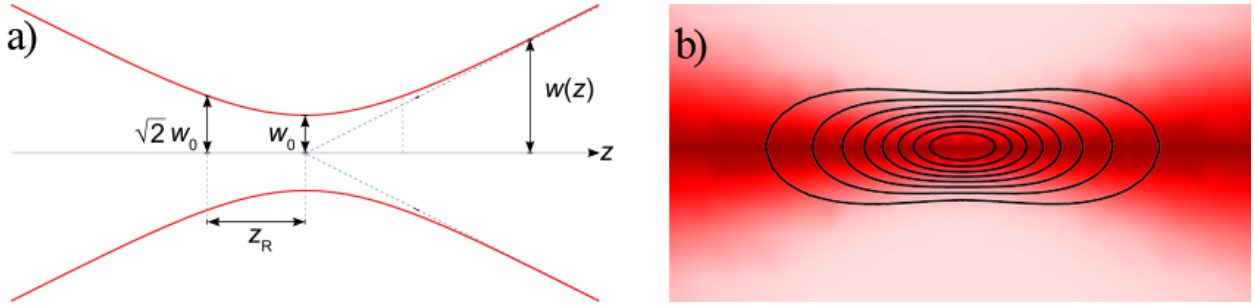

Figure 8.1: A lowest-transverse-order ($\mathrm{TEM}_{0,0}$) Gaussian laser beam. a) Geometry of beam, showing the hyperbolic form of the beam near the focus. Beam waist w_0, beam width $w(z)$, and Rayleigh length z_R are shown. b) Intensity distribution of beam near focus, with equipotential lines.

has a major and minor axis, with respective waists w_x and w_y, and corresponding separate Rayleigh lengths. Thankfully, the Maxwell wave equation is separable in Cartesian coordinates, so we can treat the two principal transverse axes independently, according to the above equations. The form of the intensity distribution near the focus then becomes

$$I(x,y,z) = \frac{2P}{\pi w_x(z) w_y(z)} e^{-\frac{2x^2}{w_x(z)^2} - \frac{2y^2}{w_y(z)^2}} \tag{8.3}$$

Defining the trap depth $U_0 = \alpha I(0,0,0)$, in accordance with the discussion in section 4.4, the dipole potential experienced by the atoms becomes

$$U(x,y,z) = \frac{-U_0}{\sqrt{1+(z/z_{Rx})^2}\sqrt{1+(z/z_{Ry})^2}} e^{-\frac{2x^2}{w_1(z)^2} - \frac{2y^2}{w_2(z)^2}} \tag{8.4}$$

Since the cold atoms typically probe only the region close to the trap center, we may expand this function to second order about the origin. Comparing with the traditional, functional form of a harmonic oscillator potential,

$$U(x,y,z) = \frac{1}{2}m\omega_x^2 x^2 + \frac{1}{2}m\omega_y^2 y + \frac{1}{2}m\omega_z^2 z^2 \tag{8.5}$$

we can straightforwardly extract a functional form of the radial trap frequencies,

$$\omega_x^2 = \frac{4U_0}{m w_x^2},\ \omega_y^2 = \frac{4U_0}{m w_y^2} \tag{8.6}$$

and by expanding to first order in z^2 we get the axial frequency

$$\omega_z^2 = \frac{U_0}{m}\left(\frac{1}{z_{Rx}^2} + \frac{1}{z_{Ry}^2}\right) \tag{8.7}$$

Notice that the radial-to-axial aspect ratio of the trap, given by ω_x/ω_z, is of the order w_0/z_R, leading to highly elongated trap geometries, and low rates of interparticle interactions. One way to combat this problem is by using very long-wavelength (CO_2) lasers, which yield short Rayleigh lengths. However, we instead chose to use a crossed-beam ODT (XODT), consisting of two beams with collocated foci, crossed as an angle. To compute the local geometry of such a trap, it is useful to rewrite equation (8.5) in the form

$$U(\vec{x}) = \frac{1}{2}\vec{x}^T \Omega \vec{x} \tag{8.8}$$

where $\vec{x}$ is the vector (x,y,z), and the omega-matrix has the form

$$\Omega = \begin{pmatrix} \omega_x^2 & 0 & 0 \\ 0 & \omega_y^2 & 0 \\ 0 & 0 & \omega_z^2 \end{pmatrix} \tag{8.9}$$

We can then superimpose multiple beams with various crossing angles using standard rotation matrices, e.g.

$$U(\vec{x}) = \frac{1}{2}\vec{x}^T \left(\Omega_1 + R\left(\vec{\theta}\right)\Omega_2 R^T\left(\vec{\theta}\right)\right)\vec{x} \tag{8.10}$$

where Ω_1, Ω_2 represent the omega matrices for the respective beams. Additional rotations may be implemented to account e.g. for beam ellipticity outside the XODT plane. The resulting trap frequencies of the combined potential are then simply the square roots of the eigenvalues of the resultant omega-matrix.

The above matrix technique is an efficient way of extracting the potential of multiple ODT beams, but may yield inaccurate results if the foci are not perfectly collocated. Fortunately, corrections to the trap frequencies are quadratic in the displacement: $\mathcal{O}(d/w_0)^2$ for offsets perpendicular to the crossing plane (mis-crossing), and $\mathcal{O}(d/z_R)^2$ for displacement along one beam axis (focal shift). Such effects can generally be mitigated through zealous tuning-up of optical alignment.

8.2 Experimental layout

We derive our ODT beam from a 1064nm Yb fiber laser, which gives up to 100W of linearly polarized light. To minimize thermal lensing effects in our optics, we run the laser at a significantly lower power of 30W, which is near the lasing threshold of 20W. This power is nonetheless sufficient to trap large numbers of ytterbium atoms. The Li atoms, being released from the MOT at a higher temperature, are trapped in far greater numbers at higher powers.

Our ODT setup consists of two beams with similar waists, crossed at a shallow ($\approx 20°$) angle. Both beams are horizontally aligned, as shown in Figure 5.2. The small crossing angle differs from the configuration used by many other groups, in which the beams are perpendicular or nearly perpendicular. We chose this configuration in order to mitigate the effects of Raman scattering, in which a photon is coherently absorbed from one beam and emitted into the other, imparting a momentum kick $\vec{k}_2 - \vec{k}_1$ on the mediating atom. With a smaller angle, we reduce the magnitude of this momentum kick, thus improving the longevity of the atoms in the trap. Further improvement is achived by ensuring that the two beams have orthogonal polarization, and thus couple to different magnetic substates. The effect of

Raman scattering was tested with Lithum, whose background lifetime exhibited a significant dependence on the relative polatization angle. Other groups, e.g. the Takahashi group in Kyoto, have instead opted to suppress this effect by maintaining different frequencies in the two beams. [13]

In the early stages of the experiment, in order to maximize the power in each beam, we employed a rather clumsy setup in which the first beam was brought, via a series of awkwardly placed mirrors, around the chamber to enter a second time through the same viewport. Aside from being hard to align, this configuration suffered from thermal lensing causing the beams to come un-crossed. Since the return mirrors were mounted on various breadboards and posts around the main chamber, ambient temperature drifts and vibrations were also a problem for this setup. As it became clear that less power was needed to trap ytterbium and lithium together, we switched to the current setup, in which the beams are split before the chamber, and independently enter through different viewports. A waveplate before the polarizer allows us to easily switch between one- and two-beam trap geometries. A single AOM before the beam splitter controls the total power at the atoms.

The trapping region is located not at the center of the chamber, but a few mm below the center of the MOT quadrupole field. This was implemented after we started loading the two species sequentially, for reasons described in section 7.2.

8.3 Cooling to degeneracy

After our atoms are loaded into the ODT from the MOT, a rapid drop in temperature is observed in the first few hundred milliseconds. This is due to "spontaneous" evaporation from the trap, as the atoms collide with one another and form a thermal (Maxwell-Boltzmann) distribution. In the process, some atoms are ejected from the trap, as they populate the high-energy tail of the distribution and escape. This leads to a net cooling effect. A parameter of interest here is $\eta = U_0/k_B T$, describing how deeply trapped the atoms are. Once η reaches a critical value – typically 12-14 – spontaneous evaporation is quickly suppressed.

To reach lower temperatures, we impose a *forced* evaporation scheme. This is done by ramping down the trap depth U_0 over a period of several seconds. The atoms scramble to maintain a constant η, continuously ejecting the highest-energy atoms and re-thermalizing at a lower temperature. This process may be sustained to reach arbitrarily low temperatures, or until all the atoms have evaporated from the trap.

A more in-depth analysis of forced evaporation may be found in [90]. The simple scaling laws presented in that paper have been used with great success in our group, to simulate and predict the effects of both spontaneous and forced evaporative cooling.

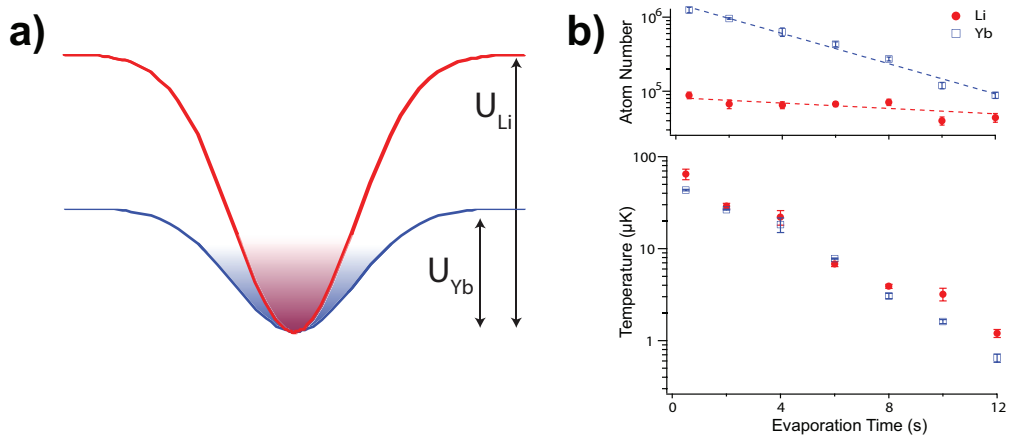

Figure 8.2: a) ODT potential for lithium (red) and ytterbium (blue). The greater polarizability of Li leads to the two species seeing different potential depths. When at thermal equilibrium, evaporation of Li is greatly reduced. b) Evidence of sympathetic cooling in the Li-Yb mixture. Thermal equilibrium is maintained throughout evaporation, while the relatively slow loss of Li atoms from the trap suggests that Yb is performing the bulk of evaporation. The small temperature deviation toward the end of evaporation is probably due to the low number of coolant atoms, as well as separation of the clouds due to gravitational sag.

Additional effects need to be taken into consideration when performing evaporative cooling on multiple species. One such effect is that different types of atoms generally have different polarizabilities, and thus experience different trap strengths. Figure 8.2a shows this effect for lithium and ytterbium, whose polarizabilities differ by a factor of 2.2 in our 1064nm ODT. If left to evaporate independently, with similar η, the two species would maintain very different temperatures.

Of course, the trapped species do not evolve entirely independently. Interspecies collisions lead to thermalization between lithium and ytteribium over time scales of $\sim$ 1s, roughly the same as the time constant of our evaporation ramp. This leads to a situation in which lithium maintains a similar temperature to ytterbium throughout the evaporation period, thus maintaining a far greater value of η. As a consequence, ytterbium alone experiences evaporation, while lithium cools sympathetically through thermal contact with ytterbium.

This interspecies thermalization, and its application toward sympathetic cooling, was the subject of study for our first publication. During this work it was found that a 10:1 ratio of ytterbium to lithium led to a balanced number of both species at temperatures near quantum degeneracy, which inspired us to subsequently optimize the system for loading large numbers of Yb.

8.4 Measuring trap frequencies

A wide range of experiments require accurate knowledge of the geometry of the trap in which the atoms are confined. Studies of interactions between atoms rely on understanding the in-trap density distribution of the atomic cloud, which is not directly observable in most experiments; accurate time-of-flight thermometry of thermal gases often requires knowledge of the cloud size upon release; and studies of degenerate Fermi gases require an understanding of the density of quantum states near the bottom of the trap.

Each of the publications from our lab has included analysis that relies on knowledge of trap frequencies. Most notably, the "Feshbach molecule" paper involved studies of 3-body collision rates that scale as density to the third power, and thus necessitated highly accurate frequency measurements. Fortunately, a number of tools are available for measuring or calculating the trapping frequencies of an ODT. The techniques described below have all been used in the lab at some point.

8.4.1 Measurement of trap waist

From section 8.1, we see that knowledge of the power of our beam(s), as well as the beam waists is sufficient to compute the trap frequencies of the system. Measuring the power is of course straightforward: all you need is a power meter that can handle the power in the ODT beam. (Typically a few Watts at trap depths of $\sim 100\mu$K.) Measuring the waist, however, can be tricky, since the region of interest is inside the vacuum chamber. The waist can, however, be estimated in a straightforward way, using one or more carefully positioned lenses to project the focus inside the chamber (the object) onto an image focus on the outside. The object waist is then equal to the image waist divided by the intrinsic magnification of the lens setup.

Figure 8.3 shows a schematic of the setup used in our lab to measure the waist of our ODT beams. The first lens is carefully placed to collimate the expanding ODT beam, and the second lens re-focuses the beam onto a CCD camera. The magnification of this setup is the ratio of the focal lengths f_2/f_1, and these focal lengths need to be measured for the specific ODT wavelength in order to get an accurate measurement.

Our portable CCD camera software automatically computes beam widths, and these can be quickly recorded while either the camera itself or one of the lenses is translated. The resulting plot then describes the longitudinal shape of the beam near the focal plane, which should be in good agreement with equation (8.2). The theoretical model may then be fit to the data to get an accurate estimate of the image waist, which yields the object waist after magnification is accounted for. Naturally, this technique also captures any ellipticity

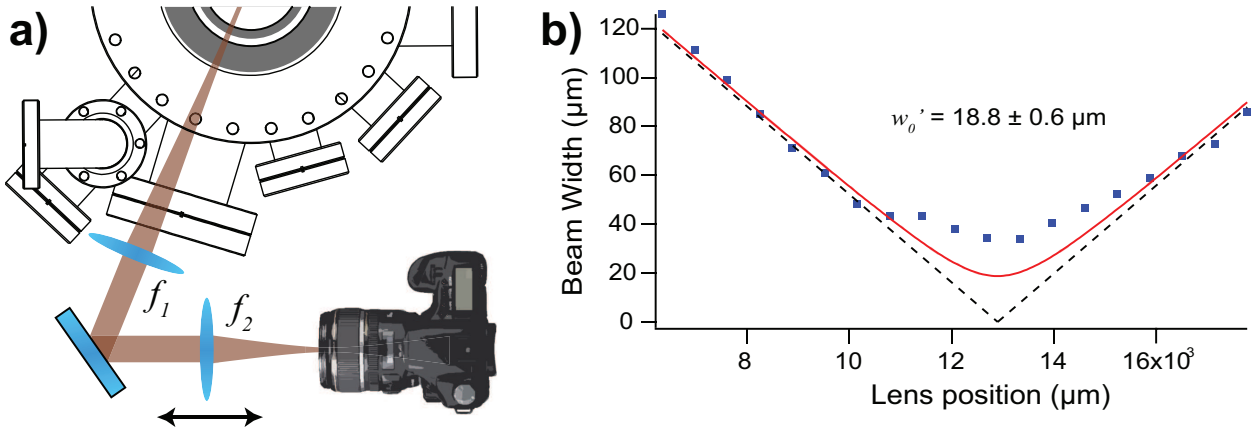

Figure 8.3: Measuring ODT beam waist. a) Experimental setup, using two lenses and a CCD camera. One of the lenses is placed on a translation stage to tune the focus about the camera plane. b) Measured beam size on camera as a function of translation stage setting. Fitting the functional form of the waist, $w(z) = w_0\sqrt{1+(z/z_R)^2}$, to the plot yields an image waist $w_0' = 18.8\mu$m, corresponding to object waist $w_0 = 38\mu$m. At the narrowest waists, the camera image is broadened due to saturation effects. For this reason, only the data points far from the center are used for fitting.

of the ODT focus, and may be applied separately to the two principal axes without further modification.

Finally, the technique may be used to detect astigmatism in the ODT beam. Beam astigmatism is characterized by the beam waists w_x and w_y being centered at different longitudinal locations, and may arise due to bad and/or damaged optics, off-center alignment through lenses, or from thermal lensing effects. Due to the high power of our ODT beams, the latter effect has proven the most worrisome, and has led to our keeping the laser power below 1/3 of its maximum capacity. A thorough measurement of astigmatism at various laser powers was carried out before the publication of our first paper, using the setup described above. The resulting data, shown in Figure 8.4, clearly shows a strong beam astigmatism, which at the highest powers is as large as the Rayleigh range. ($\approx$ 3mm) The laser is now maintained at an output power 30W, which has also been observed to yield the best experimental performance at low trap depths.

8.4.2 Direct measurement of trap frequencies

We have found that, despite our best efforts, the above technique to measure the waist of our ODT beams yields trap frequencies that differ from more reliable measurements by 10% or more. This discrepancy may be due to beam astigmatism, systematic errors in our estimate of magnification, or errors in the waist measurements of the CCD camera (e.g.

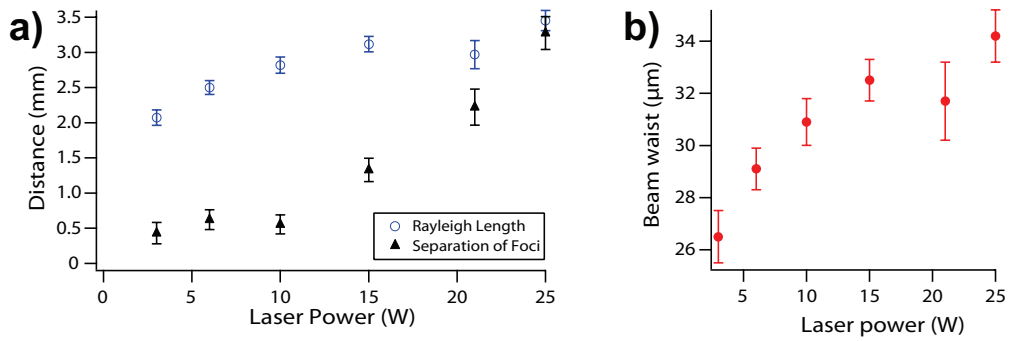

Figure 8.4: a) Measurement of beam astigmatism in our ODT beam. The plot shows the axial separation of the horizontal and vertical foci for various laser powers. At very low powers, where we expect no thermal lensing. some residual astigmatism persists. This is probably due to imperfections in alignment. b) In addition to shifting the focus of each beam, thermal lensing may increase the beam waist.

due to electronic and optical "halo" effects at small beam sizes), or some combination of the above. Furthermore, in an XODT geometry there are additional trap frequency modifications related to imperfect overlap of foci. For these reasons, we require additional techniques to measure trap frequencies in a more direct fashion.

The most conceptually straightforward way of measuring trap frequencies would be to directly observe the atoms oscillating back and forth in the trap. Although we can neither resolve motion on such a small scale nor detect single atoms, there are simple extensions to this idea that may be employed.

By displacing the center-of-mass of an entire cloud of atoms and then releasing it, we create dipole oscillations: a bulk sloshing motion of the entire cloud in the trap, at a frequency $f = \omega/(2\pi)$. By switching off the trap after some variable sloshing time τ, and allowing the cloud to expand for some time before imaging, we effectively measure the in-trap center-of-mass velocity, which may be plotted as a function of τ. A typical resulting data set is shown in Figure 8.5a. This data was obtained with ytterbium atoms by lowering the trap depth a factor of 5 below the target depth, and then rapidly (< 1ms) ramping up the ODT laser power. At the low trap depth, the atoms are displaced from the trap center due to gravitational sag, and are subsequently drawn back to the center after recompression.

The clear damping of the dipole oscillations after a few cycles in the trap may appear to be at odds with notions of the ODT being a conservative potential. Where does the momentum go? The answer lies in the deviation of the Gaussian trap profile from a harmonic potential, which produces an energy-dependent correction to the (idealized) trap frequency ω. Thus, in the thermal ensemble of trapped atoms, different energy classes oscillate at slightly different frequencies, leading to a washing-out of the center-of-mass motion after several oscillation

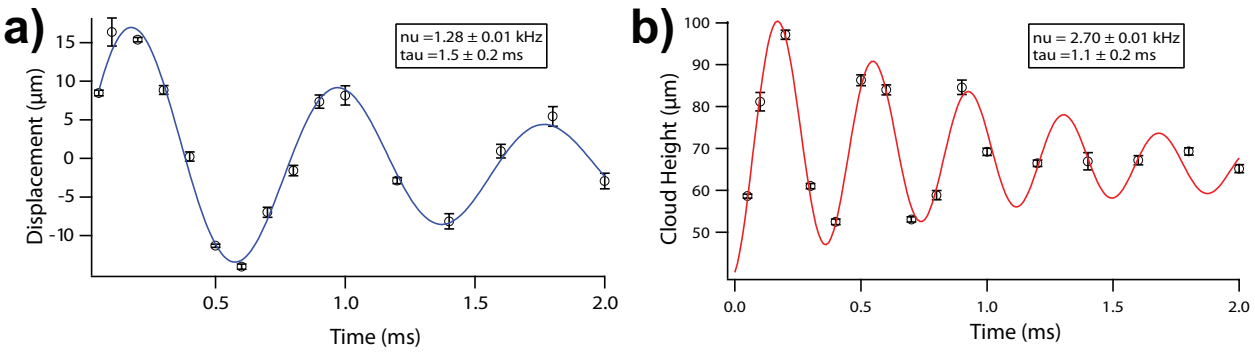

Figure 8.5: Measurements of different bulk modes of an out-of-equilibrium atomic sample in a single-beam ODT. a) Dipole oscillations, corresponding to center-of-mass sloshing motion of the atoms. b) Quadrupole oscillations ("breathing" mode) corresponding to periodic expansion and contraction of the atoms. As expected, the breathing frequency is twice as great as the dipole frequency, whereas the damping times are approximately equal.

periods.

In addition to the dipole oscillations, the atomic cloud may exhibit a second, quadrupole mode in the trap, colloquially referred to as the "breathing" mode. In this mode there is no center-of-mass motion, but instead a series of expansions and contractions of the cloud. The concept can be visualized by imagining each atom pairing up with an atom with equal and opposite position and momentum. Each pair then oscillates 180° out of phase, the magnitude of their separation changing at a frequency $2f$. As with the dipole mode, the dephasing of different energy classes leads to an apparent damping of the breathing mode over a similar time scale.

Figure 8.5b shows breathing mode data extracted from the same data set as Figure 8.5a. Although the recompression technique described above provides both dipole and breathing excitations, the overall broadening of the cloud at low depths is typically greater than the displacement due to gravity. This, along with the greater number of observed oscillations before motion is damped out, is responsible for the lower fractional error on the breathing mode calculation.

8.4.3 Parametric excitations

Generally, the most successful method for measuring trap frequencies is through so-called parametric excitations. To motivate this technique, we note that the oscillation patterns from the previous section resemble those of a damped harmonic oscillator. Thus, we should expect that by applying a driving force to such a mode, the responding amplitude of oscillation will be peaked when the driving frequency is near the natural frequency of the mode. By measuring the amplitude of the system after some period, we should thus be able to map

out the location of the resonance, and hence compute the corresponding trap frequency.

Of course, the damping of the system is somewhat of an illusion: the energy that dissipates from the bulk motion remains in the system as thermal motion. Thus, instead of looking for oscillations in the system, we simply measure its temperature, by studying the size of the cloud after some expansion time from the trap. Furthermore, the heat deposited in the trap will tend to induce spontaneous evaporation of atoms, which may be detected as a frequency-dependent decrease in remaining atoms at the end of modulation. Interestingly enough, these two diagnostics typically give slightly different estimates of trap frequencies. This is because the atoms, in order to completely leave the trap, require a sustained near-resonant drive, even when they are hot enough to probe the anharmonic regions of the trap. These energetic atoms have a lower oscillation frequency, and so the loss features tend to be red-shifted from true resonance.

As in the previous section, the breathing modes of the trap are easier to work with than the dipole oscillations, due to the number of cycles per coherence time and because of experimental convenience. Although we are able to dither the vertical position of the trap to excite dipole modes, we choose instead to modulate the trap depth to access the quadrupole modes. This also allows us to access all three trap frequencies, and has the added benefit that power modulations are easier to quantify than subtle displacement.

Figure 8.6 shows typical data from a trap frequency measurement in ytterbium. Notice that in addition to the main features at $f_0 = 2\omega/(2\pi)$ there are sub-harmonics at $f_0/2$. In principle we should expect a whole family of such sub-harmonics at f_0/n. However, our signal-to-noise is not yet sufficient to resolve features beyond $n = 2$.

8.5 Effects of gravity

An effect in our ODT that we initially underestimated, is that of the Earth's gravitational gradient. Given the large atomic mass ratio of ytterbium to lithium, there is a significant differential force between the two species. In addition, the lower polarizability of Yb makes the heavier species even more susceptible to sagging in the trap. The net result of these effects is a differential displacement of the center-of-mass of the two clouds, which reduces interspecies interactions. In most cases, this is an effect that we would prefer to mitigage.

To quantify the effects of gravity it is useful to re-define the trap depth in terms of a dimensionless parameter

$$u_0 = U_0/(mgw_0) \tag{8.11}$$

where U_0 is the "nominal trap depth," i.e. the trap depth in absence of gravitational effects,

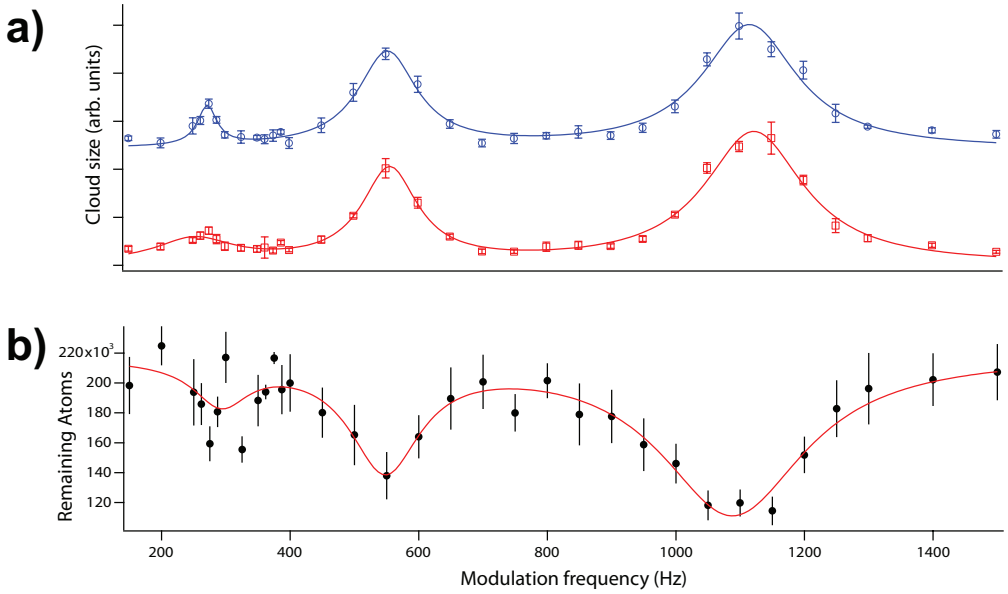

Figure 8.6: Trap frequency measurement through parametric excitations of radial breathing modes of Yb. Due to beam ellipticity, the trap has two distinct breathing modes, at $\omega/(2\pi) =$ 540, 1120 Hz. a) Size of cloud some time after release from the trap provides a measure of the energy deposited by the modulation. Blue circles denote the vertical extent of the cloud, and red data points denote horizontal size. The system response to the driving force is peaked at $f_{mod} = 2 \times \omega/(2\pi)$, with a weaker resonance at $f_{mod} = \omega/(2\pi)$. The sub-harmonic of the 1120Hz resonance is obscured by the much stronger primary harmonic of the 540Hz mode. b) Remaining atoms in trap after modulation. Atoms evaporate from the trap due to parametric heating. As expected, these peaks are slightly offset from the cloud size peaks.

or, equivalently, the AC Stark shift at the trap center. The actual ("effective") trap depth is significantly reduced by the presence of gravity. The reduced depth u_0 is given in terms of intrinsic units related to the geometry of the tilted trap.

At relatively large values of u the atoms remain within the harmonic region of the trap, and we can compute the sag by finding the minimum of the offset parabola

$$U(x) = \frac{1}{2}m\omega^2 x^2 - mgx \tag{8.12}$$

which gives a displacement $s = g/\omega^2$ from the center of the ODT beam. Combining this with equations (8.11) and (8.6), we derive $s = w_0/(4u_0)$, which shows that the sag is inversely proportional to the laser power when the harmonic approximation is valid. For a typical beam waist of 25μm the fundamental energy unit of the system, mgw_0 is 5μK for Yb, so assuming $\eta = U_0/k_BT \sim 10$ we should expect to see significant sag effects at temperatures approaching 1μK.

The sag effects are further strengthened, however, by the anharmonicity of the Gaussian beam. The next-leading order, quartic term in the Taylor expansion of the trap potential is of opposite sign to the quadratic term, which further weakens the trap when the sag is on the same scale as the beam waist. A more complete version of equation (8.12) can be written using the proper form of the trap

$$U(x) = U_0 e^{-\frac{2x^2}{w_0^2}} - mgx \tag{8.13}$$

which we can rewrite in dimensionless units

$$u(x) = u_0 e^{-2\xi^2} - \xi \tag{8.14}$$

where $\xi = x/w_0$. We compute the displaced trap minimum by differentiating the above equation, giving us the transcendental equation

$$\xi e^{-2\xi^2} = \frac{1}{4u_0} \tag{8.15}$$

We can use equations (8.14) and (8.15) to numerically extract all interesting information about the tilted trap, e.g. the displacement of the local potential minimum, the effective trap depth, and the modified trap frequency. These are plotted in Figure 8.7. Of these, the trap depth modification is the most pronounced effect at a large range of trap depths. At the spilling point $u_0 = 0.82$ the depth goes to zero, as the potential no longer supports a local minimum. On the other hand, the trap frequency correction is significant only at trap depths very close to the spilling point.

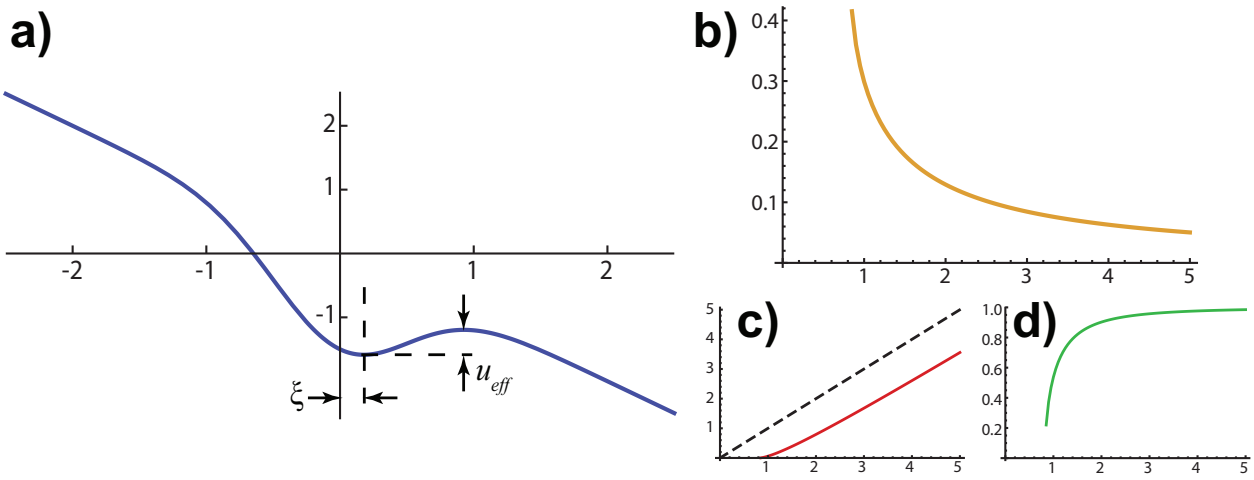

Figure 8.7: Properties of the tilted trap, computed using numerical software, and plotted vs the reduced nominal trap depth u_0. a) Schematic of the tilted Gaussian 1D potential. b) Displacement ξ of the trap minimum from the center of the ODT beam. (I.e. sag distance) c) Effective trap depth u_{eff}. The dashed line shows the nominal trap depth u_0 for comparison. d) Modified trap frequency, in units of the frequency of an un-tilted trap of equal depth and waist.

The rapid reduction in trap depth near the spilling point carries some interesting implications. For one, it leads to a region of very rapid evaporation. If care is not taken to slow down the ODT power ramp, this can lead to large atom losses, as the evaporating species is unable to maintain a large η. Exacerbating this effect, atoms in the tilted trap are able only to evaporate in one direction: downward, where the potential barrier is lowest. This leads to a factor-of-3 reduction in the evaporation rate, since only one of the three motional degrees of freedom is being utilized toward evaporation.

When working with Fermionic isotopes, the tilting of the trap may also have the effect of removing atoms near the surface of the Fermi sea, leading to significant trap losses. This effect has been seen in lithium, using a magnetic gradient to simulate gravity, but not yet in Fermionic ytterbium. This effect may also be used to the experimenter's advantage in this case, as it allows for "skimming" of thermally excited atoms above the Fermi surface, after which the trap may be adiabatically un-tilted to preserve a deeply degenerate Fermi gas.

A more in-depth study of evaporation in tilted optical trap potentials was carried out at the University of Chicago.[91] The results show that when the experimenter may control the gradient such traps have evaporative cooling characteristics far superior to un-tilted traps. The reason for this is that, except very near the spilling point, the trap depth may be decreased without significant reduction of trap frequencies. This is the key criterion for so-called runaway evaporation, in which the rate of interparticle collisions increases with time, despite the total atom number decreasing. Although it would be much to hope for runaway

evaporation in our experiment, where the potential gradient is rather inconveniently fixed by the Earth's mass, it is likely that the gravitational tilt does already play an enhancing role in achieving degeneracy in ytterbium.

9 Metastable Ytterbium

The basic structure of the ytterbium metastable states (typically denoted Yb*) was described in section 4.6. The level diagram with the relevant transitions discussed in this section is shown in Figure 4.5. In this chapter, we explore the experimental buildup of the laser systems relevant to the metastable states, and discuss the motivation and experimental details of these experiments.

9.1 Planned studies with Yb*

A large part of atomic physics involves the studies of strongly interacting gases. We chose ^{6}Li as one of our experimental constituents largely because of the availability of widely tunable interactions, and have already published one paper about a 3-component mixture (ytterbium, and states $|1\rangle$ and $|2\rangle$ of lithium) where the equal-mass components exhibit strong pairwise interactions. It would be a natural extension to such studies to explore systems where the strong interactions were in a mass-mismatched pair, or where there is more than one adjustable pairing channel.

In order to access such studies, however, an experimental pathway to strong, interspecies interactions must be found. Groups that operate with bi-alkali systems have already been using interspecies Feshbach resonances for years.[92, 61] However, the magnetic Feshbach resonances used by such groups are not available to experiments such as ours, where one component has a spin-singlet electronic structure. This is because, as discussed in section 2.2, magnetic Feshbach resonances arise from coupled multiplets of the total electronic angular momentum. With Li-Yb, only the $S = 1/2$ state exists, and no Feshbach resonances can arise.[10]

One may, however, circumvent this issue by endowing the ytterbium atoms with some amount of angular momentum. The metastable $^3P_2$ state has a lifetime of 15s, much longer than the interrogation time scale of such experiments, and forms $S = 3/2, 1/2$ spin doublets with lithium, thus potentially exhibiting interspecies Feshbach resonances. In addition, so-called anisotropic-interaction-induced resonances have been observed in the Yb-Yb* system.[93] Indeed, theorists with whom we have recently collaborated give us good reason to believe that several LiYb* resonances exist in the range 0-100G. Such a resonance, if it is broad enough to be accurately utilized, would open up a set of very interesting experiments

[10] In fact, magnetically induced scattering resonances may still exist in such systems, as predicted by Brue and Hutson.[88] Such resonances use different, much weaker, coupling mechanisms, and are therefore extremely narrow. ($\sim$ 1mG or less) Our lab has performed searches for these resonances, but without success. Such narrow resonances, although they would be interesting to discover, are of little use for accurately tuning interspecies interactions.

	404nm	770nm	650nm
Vacuum wavelength λ (nm)	404.0086	770.1607	649.0871
Wave number k (cm^{-1})	24751.95	12984.30	15406.25
Linewidth $\Gamma/(2\pi)$ (MHz)	0.346	12	12
Saturation intensity I_{sat} (mW/cm^2)	N/A	3.4	5.7

Table 9.1: Characteristics of the metastable lasers.

involving strongly interacting mass-mismatched systems, including mass-imbalanced Cooper pairing and exotic Efimov-like few-body resonances.[39]

Furthermore, interspecies Feshbach resonances are already a well-established pathway toward syntesizing stable, heteronuclear molecules. A LiYb* Feshbach resonance might considerably enhance our ability to create molecules of lithium and ytterbium. The interest in, and experimental potential of such molecules was outlined in chapter 3. There is also theoretical and experimental interest in the stability of such molecules, given the additional decay channels not present in electronic ground state molecules. Whether the metastable state continues to be "metastable" when strongly distorted by the presence of a second, covalently bonded atom is unknown.

9.2 The lasers

To access the $^3P_2$ state of ytterbium, and to interrogate the metastable atoms, several new lasers are needed. We have chosen to use the scheme outlined in section 4.6, in which the metastable state is pupulated via spontaneous emission from the $^3D_2$ state (the transfer state). This state is reached directly from the $^1S_0$ ground state, using the electric quadrupole transition at 404nm. Rather than imaging the Yb* atoms directly, we transfer ("flash") them back to the ground state using a 770nm laser that couples $^3P_2$ to the highly excited $^3S_1$ state. A repump laser at 650nm may be employed to optically pump stray atoms out of the $^3P_0$ state.

9.2.1 The 404nm laser

We derive our 404nm transfer light from a home-built external-cavity diode laser (ECDL).[11] This laser has a linewidth of a few MHz, much broader than the transition linewidth of

[11]Laser diodes at 405nm have recently become widely commercially available, due to their use in Blu-Ray and HD DVD readers. To reach 404nm, it was originally sufficient to buy a few such diodes, and select the lowest-wavelength specimen. However, improvements in manufacturing techniques are now, somewhat ironically, threatening to undermine this technique, as newer diodes exhibit less variation in center wavelength. New sources of 404nm light may have to be sought for future experiments.

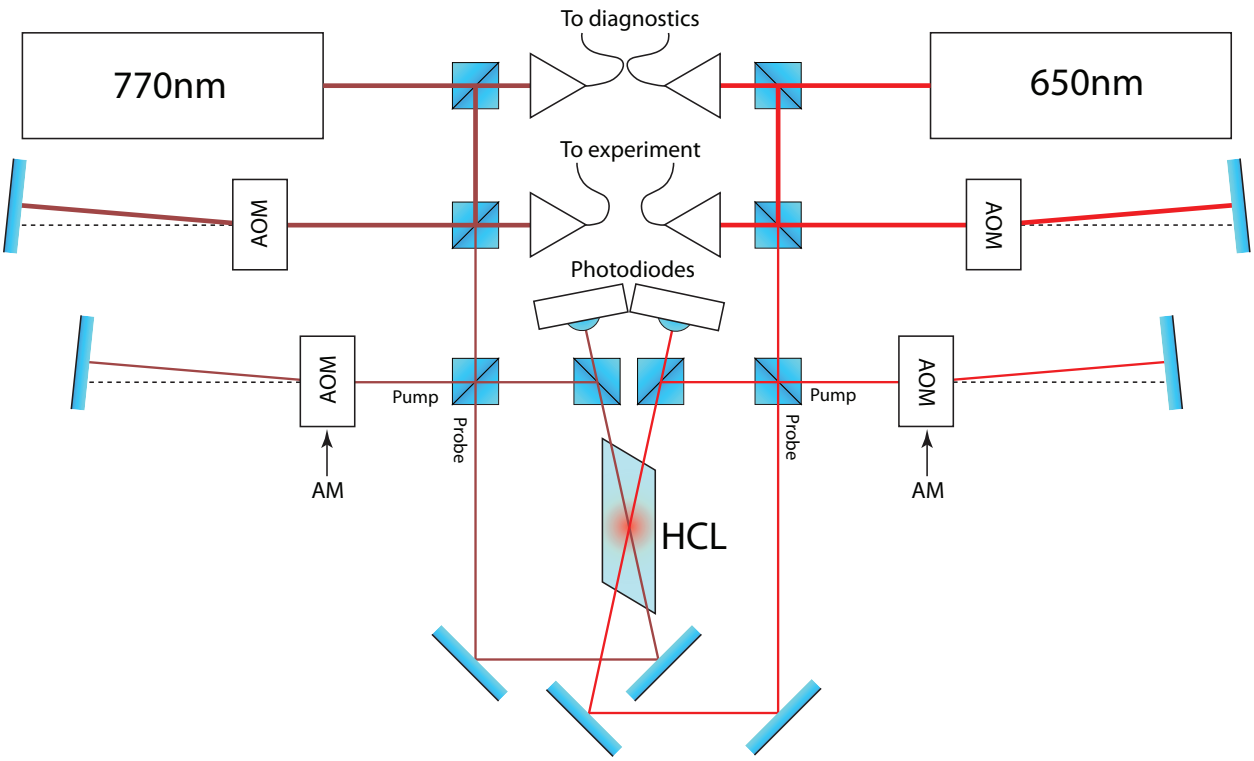

Figure 9.1: Layout for flashback lasers at 770nm and 650nm. Each laser is split into three parts: one part passes through an AOM and goes to the experiment via a single-mode optical fiber; one part goes to spectroscopy, with the pump passing through an AOM for modulation; and a small amount is directed into a second optical fiber for diagnosics purposes.

350kHz or the typical Doppler width of the atoms, but still narrow enough to achieve transfer times of a few milliseconds.

We lock this laser to a Fabry-Perot cavity, the length of which in turn is stabilized using the 399nm laser. This transfer lock scheme has proven to be robust over long time scales, but suffers from some amount of noise, or "jitter," with frequencies around 100Hz. This appears to cause the laser frequency to jump around within a $\sim$ 10MHz range, which needs to be taken into consideration when developing the experimental sequence.

A more detailed overview of this laser system can be found in [94].

9.2.2 The 770nm & 650nm lasers

The flashback lasers at 770 and 650nm were established on a separate optics table. The lasers are each derived from a Toptica TA100 ECDL assembly, operated from a common laser controller unit. The rig suffers from some inexplicable cross-talk between the two piezo driver modules, which causes some difficulty in locating both spectroscopy lines at once.

The laser setup for the flashback lasers is shown in Figure 9.1. The greater part of the

power of each laser is sent to the experiment through a common, single-mode optical fiber. A double-pass AOM for each wavelength provides the required frequency offset. With good alignment, we achieve up to 4(0.25)mW of power at 770(650)nm at the atoms, more than enough to achieve flashback times of $\ll$ 1ms. An auxiliary optical fiber for each wavelength is used to carry a small amount of light to a wavemeter, when needed for coarse tuning or various diagnostics.

We derive our spectroscopy signal for each wavelength from a common hollow cathode lamp (HCL, Hamamatsu Photonics) vapor cell, operating at 170VDC. The vapor in these commercial cells is produced by a high-voltage discharge, which is sufficiently energetic to populate a large number of lower-lying energy levels, including the metastable ^3P states. Collisions with the Neon buffer gas at 10Torr do not seem to lead to significant inelastic decays to the ground state, and we thus have a sufficient population of metastable atoms to perform saturated-absorption spectroscopy.

The term "saturated-absorption spectroscopy" is used somewhat loosely in this sense. In traditional schemes, such as the ones used in our lab for the trapping and cooling lasers, the pump laser saturates a closed transition, effectively removing some of the population from the ground state. For the metastable states, however, the transition is far from closed: after a few photon scatters, the atom decays into the ground state. Although the net result is the same – a depletion of the lower-lying state under scrutiny – far less power is required from the pump beam to achieve a "saturation" signal. Furthermore, unlike in traditional schemes, the atoms in the HCL do not return to their original state once the pump laser is swept away from resonance. Instead, one must wait for the atoms to be replenished from the discharge region. Meanwhile, Boltzmann transport, induced by collisions with the buffer gas, may broaden the depleted velocity class, leading to greatly broadened saturation peaks in the spectroscopy signal. Indeed, as one can see in Figure 9.2, the peak width in our spectroscopy setup is several hundred MHz.

We find that for 770 a probe power of 30μW (corresponding to a saturation parameter $s \approx 1/4$) and a pump power of 50μW ($s \approx 1/2$) leads to the optimal signal. At these settings, and at 3mA HCL current, we see a peak absorption of 4.5%. For 650nm, we use a probe power of 45μW ($s \approx 1/4$) and a pump power of 65μW ($s \approx 1/3$), for a peak absorption of 1.2%. The large difference in absorption is due to a large population imbalance in the two states, presumably because higher-lying energy levels tend to decay more strongly into the $^3P_2$ state. Indeed, an HCL current of 2mA is more than sufficient to see a strong signal at 770nm, whereas even at 3mA, where the vapor density is more than twice as great, the 650nm signal remains quite weak.

The large widths of the spectroscopy peaks make it inconvenient to derive an error signal

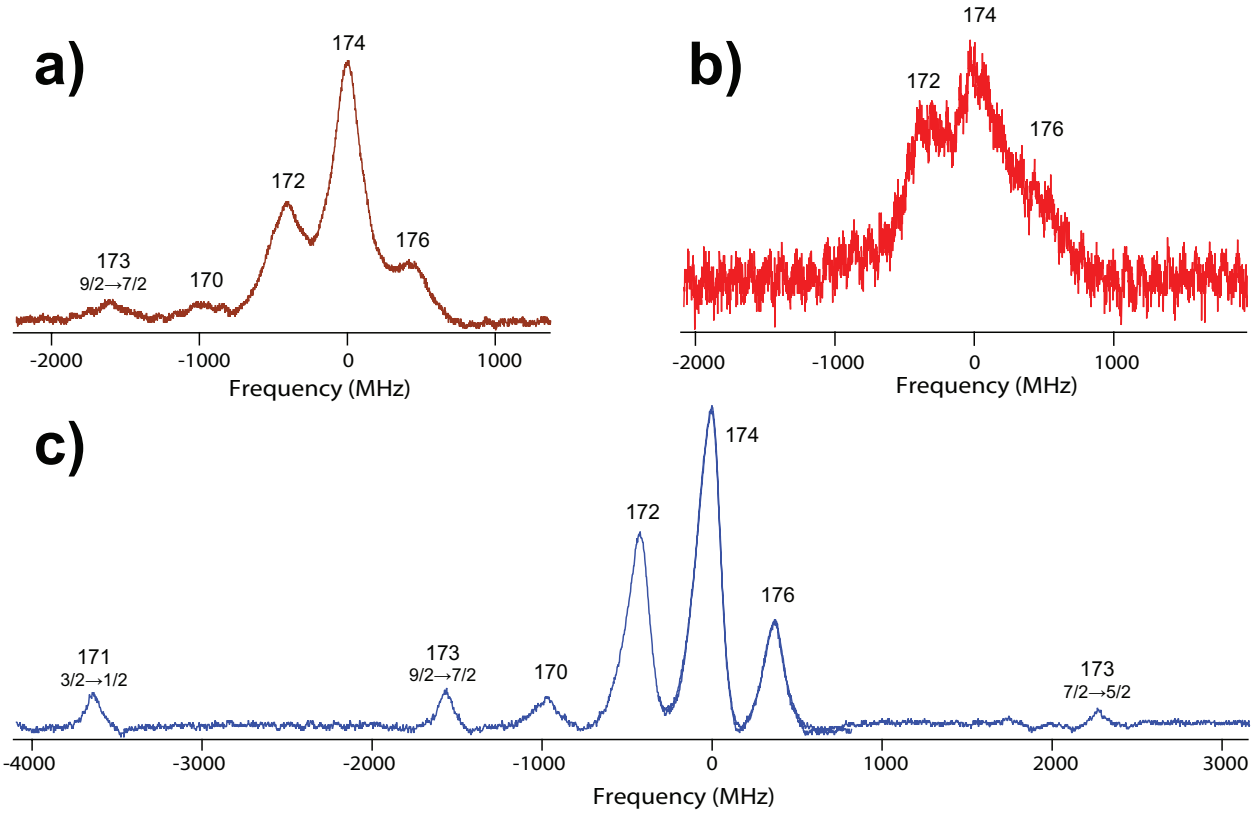

Figure 9.2: Saturated-absorption spectroscopy signal for the flashback transitions, obtained with 3mA HCL current. a) Typical saturation signal at 770nm. b) Typical saturation signal at 650nm. Note the difference in signal-to-noise between the two transitions, due to the large population ratio in the HCL of the respective states. c) Greatly narrowed signal at 770nm, taken at a modulation frequency of 110kHz. The FWHM of each peak is 135MHz.

by modulating the frequency of the pump or probe, as is common in most such schemes. The amplitude of frequency modulation on the AOM would have to be very large – greater than a double-pass AOM can typically handle without falling out of alignment. Strangely enough, when we attempted to frequency-modulate the pump beam, the signal we discovered was not a derivative of the absorption signal as one would expect, but rather a greatly enhanced view of the saturation peaks. (Similar to the profile in Figure 9.2b) It is unclear precisely why this happened. Most likely it was due to the pump beam alignment dithering due to the AOM frequency modulation, causing an oscillating pump-probe overlap.

It was, however, also found at this time that a very narrow modulation frequency band existed around 40kHz where the traditional error signal was recovered. However, this band tended to drift over time periods of several hours, leading to unreliable locks. On the other hand, we found that the width of the saturation peaks could be greatly reduced by increasing the modulation frequency, (Figure 9.2c) but at an unacceptable cost to signal strength. (The signal shown in the figure is an average over 16 frequency sweeps, to achieve good signal-to-noise.)

In the end, we decided to switch from frequency-modulating the AOM to amplitude-modulating. The AM signal, although it cannot replicate a true error signal, with a zero-crossing on resonance, reproduces the signal we saw with the FM scheme, but with improved signal-to-noise. The AM scheme was also successfully adopted for the 650nm laser, for which at the time no saturation signal had been observed at all. We now lock each laser to the center of the right-hand slope of the ^{174}Yb signal. We then use the AOMs to frequency-shift the light going toward the experiment to the atomic resonance. Fortunately, the lasers are sufficiently saturation-broadened at the atoms to achieve sub-millisecond flashbacks within a $\sim$ 100MHz frequency band, which takes some burden off the experimenter's locking the laser accurately.

9.3 Initial progress toward creating and studying Yb*

It was clear from a very early stage that the trapped Yb* atoms undergo inelastic collisions, which lead to considerable trap losses.[95] In the crossed ODT geometry these losses led to typical population half-lives of a few milliseconds – shorter than the time required to populate the metastable state. We therefore decided to shift to a single-beam geometry, where the atomic density would be lower, and inelastic collisions (which scale as density-squared) suppressed. In the single-beam geometry we see lifetimes of $\sim$ 100ms. Although other forms of interactions that we may wish to study are reduced by the same amount, making the lifetime longer than other relevant timescales of the experiment is a major overall

improvement. Furthermore, the single-beam geometry allows for straightforward control of the ODT polarization, using a single $\lambda/2$ waveplate.

Our experimental sequence for producing metastable atoms, in its present form, applies the following steps:

1. Load the ODT, and evaporate to a trap depth of 20μK. Apply a magnetic bias field of ~ 10G, and a weak gradient of 2G/cm.

2. Apply the 404nm transfer laser for ≈ 15ms.

3. Remove any remaining ground-state atoms with a 3ms pulse of the imaging beam.

4. Rapidly recompress the trap to a depth of 100μK.

5. Manipulate the atoms as required by the experimental details.

6. Release atoms from trap

7. Flash back atoms during expansion, $\sim 100\mu$s before imaging.

We apply the bias field in order to break degeneracy between the magnetic sublevels of $^3P_2$, thus maintaining the composition of our spin ensemble. Furthermore, by splitting the sublevels of the $^3D_2$ transfer state, and choosing which one to access with the 404nm laser, we may indirectly control the Yb* substates that are populated. The magnetic gradient selectively removes the weakly trapped $m = \pm 2$ atoms from the trap. By lowering the ODT laser power beyond its target value and recompressing after transfer, we cause the more weakly confined substate(s) to spill from the trap, leaving a pure spin ensemble.

As mentioned above, the 404 laser lock experiences jitter on ~ 10ms time scales. For this reason, although our on-resonance transfer time is much shorter, we are required to keep the 404nm light on for 15ms or more to achieve a repeatable Yb* population. Fortunately, we achieve much faster flashback times with the 770nm light. Fast flashback times allow us to keep the atoms in the metastable state during release and expansion. In this way, any residual heating due to the flashback will not affect the expansion rate, and we may therefore accurately estimate the temperature of the Yb* atoms.

9.3.1 404 laser geometry

Our initial scheme for the transfer beam was to deliver it to the chamber through the bottom MOT viewport. We did this by combining the beam with the MOT beams in a broadband polarizing beamsplitter.

This scheme, unfortunately, had several problems. The first was that it gave us little control of the polarization of the transfer light, as it had to pass through a $\lambda/4$ waveplate designed for another wavelength. Much worse, though, was that we were illuminating the atoms perpendicular to their axis of elongation, and thus creating a very low column density of atoms for the light to interact with. Finally, the focused transfer beam interacted only with the very center of the elongated cloud, and transfer times of 100ms or more were required to allow the atoms in the axial wings of the atomic distribution to oscillate into the beam for transfer.

For all of these reasons, we deemed it necessary to set up a horizontal path for the transfer light. By choosing to combine the 404nm beam with one of the ODT beams (using one of the dichroic IR mirrors, which are transparent to visible light) we had the added benefit that the ODT focusing lens also focused the transfer light onto the atoms. After aligning this path, we saw immediate improvements: transfer times on the order of 10ms, and vastly improved numbers of Yb*.

There was, however, one problem with the horizontal geometry. Each absorbed photon from the transfer beam imparts a momentum recoil $\hbar k$, and on average (because of the branching from $^3D_2$ into the ^3P manifold) it takes an average of 8 transfers to bring any given atom to the metastable state. As a consequence, the entire Yb* cloud began its existence in the trap with an initial velocity

$$8\frac{\hbar k}{m} = 5\text{cm/s} \tag{9.1}$$

The induced dipole oscillations were not only frustrating by their own merit, but also led to clear atom losses at the point of greatest displacement, where the beam width is greater, and the trapping potential much weaker against gravity. Furthermore, in a two-species experiment the displacement of the Yb* cloud would severely attenuate and complicate any interspecies processes that we might wish to induce and/or study.

For all of these reasons, we moved to a two-beam setup for the transfer light. The transfer beam was split into two parts using a polarizing beam splitter, with the second beam aligned into the chamber from the opposite side. By tuning the power ratio of the counterpropagating beams with a $\lambda/2$ waveplate, we succeeded in completely eliminating the sloshing motion of the atoms, improving in-trap lifetimes, and even making an incremental improvement to the transfer efficiency, since the second beam could be more tightly focused onto the atoms.

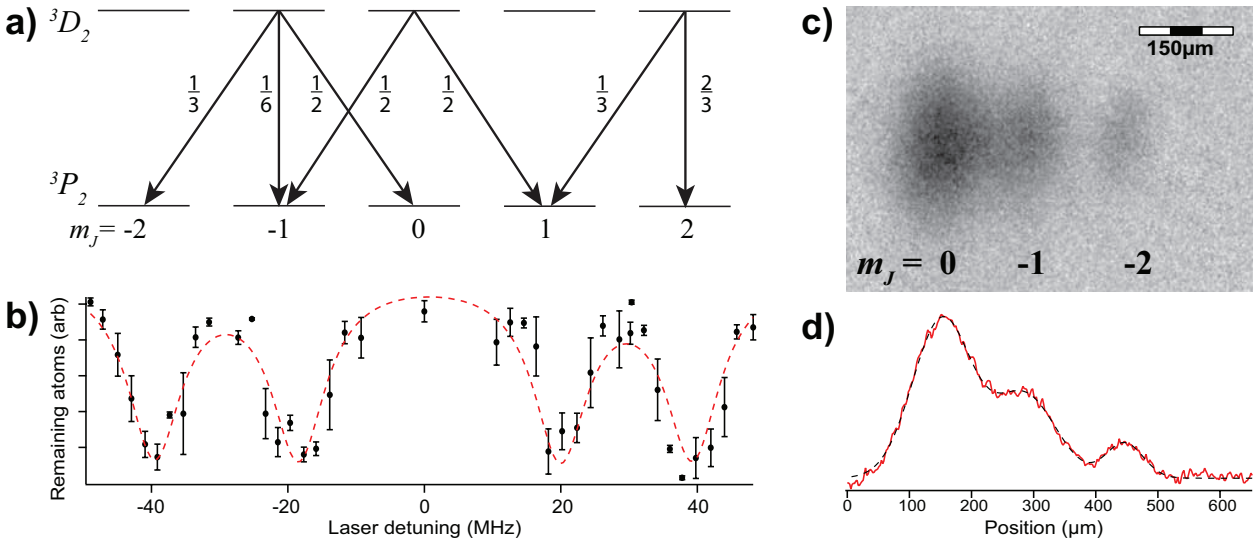

Figure 9.3: Substate-selective techniques. a) Branching ratios of the electric dipole transitions in $^3D_2 \rightarrow {}^3P_2$. b) Remaining ground-state atoms after 20ms of transfer at a bias field of 12G. The inverted peaks correspond to different magnetic sublevels of the transfer state. c) Absorption image after 2.5ms of expansion in a magnetic field gradient of $\sim$ 60G/cm. The three clouds are the Stern-Gerlach-separated sublevels $m = 0, -1, -2$, derived from the $m = -1$ transfer state. d) Integrated 1-D profile of the above image, with a fit to a triple Gaussian (dashed line). The population ratio here is 7:4:1; the disagreement with the branching ratios in Figure (a) is partly due to gravitational spilling of the weakly trapped $m = -2$ state.

9.3.2 Substate-selective techniques

As we have seen, the different magnetic substates of Yb* may have very different properties when exposed to a magnetic bias field. For this reason, it is of great interest for us to produce pure spin-ensembles, and to develop diagnostics to measure our spin composition.

Although we cannot directly control the way in which we populate the magnetic manifold of $^3P_2$, we may indirectly influence the population ratio by selecting the $^3D_2$ substate via which we transfer our atoms. Figure 9.3 shows the branching ratios from the transfer state, which govern the composition of the spin-ensemble of Yb*. For instance, by transfering to the $m = -2$ sublevel of the transfer state, we should expect a 1:2 ratio of $m = -1, -2$. In general, we prefer to work with the negative substates, as these have fewer inelastic spin-relaxation channels.

As shown in Figure 9.3b, we are able to selectively transfer to each of the transfer substates $m = \pm 1, \pm 2$ by applying a magnetic bias field and detuning our laser from resonance by the appropriate amount. The $m = 0$ sublevel is not accessible in this way because the Wigner factor (angular wavefunction overlap) in the matrix element for this transition is

identically zero.

We have also succeeded in spatially separating the magnetic substates with a Stern-Gerlach-style technique, which we use for diagnostics of spin composition. To do this, we add a gradient to the magnetic bias field, using our MOT coils. When released from the trap, the component substates experience a differential acceleration due to the gradient. After some time of flight, the atoms are flashed back to the ground state and imaged. This technique required some fine-tuning, as the gradient needs to be large enough that one achieves fully separated clouds within a reasonable time of flight, but cannot be so large while the atoms are still trapped that they are pulled out of the trap prematurely. The technique that we have found to work best is to quickly ramp up the field to a high value, and shut off the trap just as the gradient becomes strong enough to spill the atoms. In this way, the gradient still increases during time of flight, leading to enhanced separation. Figure 9.3c-d demonstrates how this technique may be used to accurately estimate the spin-composition of our Yb* samples.

10 Experimental Control & Analysis

Quantum gas experiments such as ours almost always operate on a duty cycle, with a new atomic sample being loaded, cooled, manipulated, and interrogated for each repetition. To control the timing of each step of this process, a computer control system is required, with capability of controlling the many elements of the machine with μs-level accuracy.

Furthermore, a wide range of analysis tools are required to extract useful data from our absorption images, and process the data collected over the course of many experimental cycles.

10.1 Cicero

At the heart of our experimental control system lies the program called Cicero – an open-source GUI client designed by Aviv Keshet, a former MIT graduate student in the Ketterle group,[96] and currently used by a large number of atomic physics groups worldwide. Cicero connects to a server utility, (named Atticus) which controls a series of digital and analog outputs on a National Instruments PC card.

Cicero provides a convenient and intuitive interface to the output channels. The experiment is divided up into a number of time steps, each with a variable duration. The time steps are given appropriate names, such as "Load Li MOT," "ODT Hold," or "Reduce Detuning." Each time step is given 32 color-coded indicator boxes, which may be toggled to set the digital channel configuration (called a "word") for that time step. In addition, each time step may be assigned an analog "group," which provides a waveform directive to each of our 16 analog output channels. A group may span several time steps, which is useful in situations where we require certain channels to trigger halfway through a smooth analog transition, e.g. while ramping of our ODT depth.

Cicero also provides a set of user-defined "variables," which provide a means of building "batch" runs. The variables are linked to user-defined lists of numbers, or they may be mathematical functions, and they may be assigned to numerical parameters in the time sequence, such as time step duration or analog output value. During a batch run the variables are incremented for each iteration of the experimental cycle, providing a "scan" of values for the assigned parameter. The batch run option is extremely valuable during collection of large data sets, as it allows the experimenter to focus on real-time data analysis, while the machine takes care of itself.

In order to protect the National Instruments card from any electrical back-action, and to provide a second level of user control, a set of isolator boxes were built to regulate the computer outputs. These boxes, which are shown in Figure 10.1b, are provided with a digital

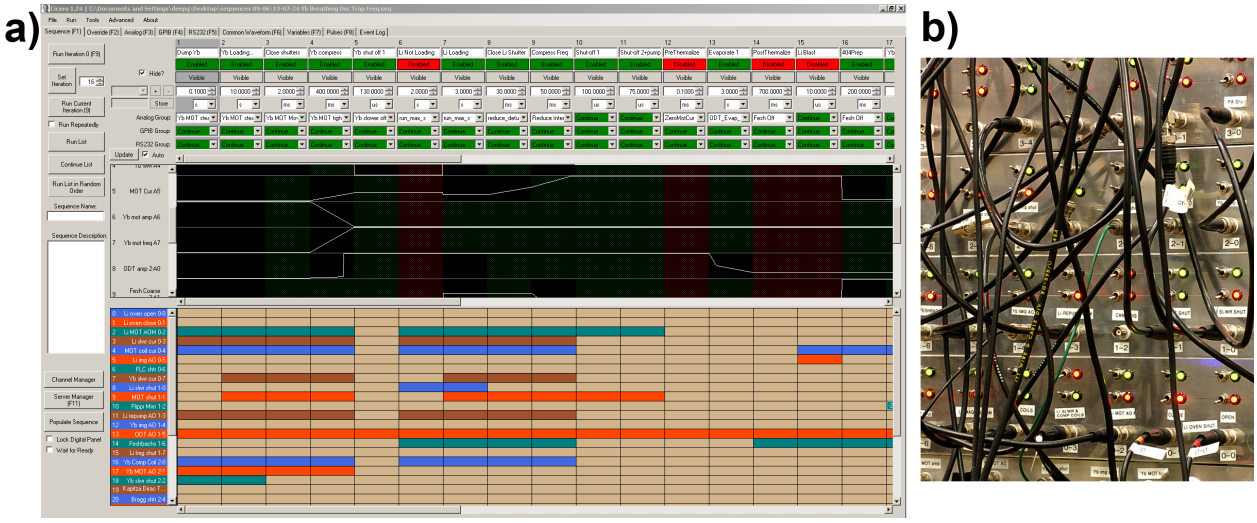

Figure 10.1: a) User interface of Cicero. Each column represents a single time step, of variable length. The upper set of rows shows plots of the analog channel waveforms, while the lower set of rows control the digital output channels. b) The digital switchboard. Each of our 32 digital channels has two indicator LEDs: one displaying the output state, and one toggling between manual and computer control.

isolator IC chip, and a handful of bipolar transistors to toggle between computer control and manual override. Each channel comes with two LEDs, to show the binary output state and the computer/manual state, and two toggle switches, to toggle the override and to flip the bit value.

Furthermore, we protect the analog channels with a set of isolator boxes. Each of these contains, for each channel, an analog isolator, a buffer op-amp, and a floating linear power supply to drive the output.

10.2 The camera & the image processor

During the first years of the experiment, we used a Princeton Instruments CCD camera that had been handed down to us from the previous inhabitants of the lab. The camera had all the required functionality, but suffered from a bothersome issue with interference fringes on the image. These were due to a viewport directly behind the camera shutter, leading into the evacuated chamber surrounding the CCD chip. Because this viewport was not AR coated, it was prone to etalon effects when illuminated by coherent light, which caused clearly visible fringes on the exposed image. These fringes were highly sensitive to alignment, and were impossible to reproduce perfectly in the normalization image. The net effect of these artifacts was a lower limit on the number of atoms we could resolve. As the optical density of the atomic cloud dropped below the fringe level, it became impossble to resolve.

For this reason, we eventually saw the need to purchase a new camera. We settled on a model from Andor (iXon3 885), with similar properties to the Princeton Instruments camera but with smaller (8μm) CCD pixel size, higher quantum efficiency, lower shot noise, and no bothersome interference fringes.

Rather than rewriting parts of the analysis code to accommodate the new image type output by the Andor camera, (both cameras store their pictures in a proprietary file format) we wrote a script in Numerical Python (NumPy) to convert the 3- or 4-frame images from the Andor camera into a single-frame, normalized OD plot, which is retrofitted to the Princeton Instruments .spe format around which our analysis was built. This script operates silently in the background, processing image files as they are generated by the Andor client, and re-triggering the camera for the next shot. Together with the batch processing function of Cicero, this program removes all sustained user-input from data collection, making it possible, in principle, to collect an entire experiment's worth of data with nobody present.

10.3 The *Igor Pro* data analysis system

To analyze the collected and normalized images, we use the data analysis program Igor Pro. For simple applications, Igor offers a spreadsheet-style user interface, with a large number of tools for graphically displaying the data in just about any manner. A command window allows more experienced users to bypass the built-in menus and dialog windows, and manipulate and display the data directly.

For more involved analysis, Igor offers its users a platform for writing custom procedures, which may then be called from a pull-down menu, or from the command line. The procedures are written in a C++-based language, with a set of built-in high-level functions, mostly for dealing with the intrinsically global spreadsheet entries. (Which are called "waves.") Although there are some kinks and annoyances in the way Igor incorporates these global objects into a runtime environment, the custom procedures are a terrific way of combining complex data analysis with a highly flexible graphics package. Using the built-in user control functions, such as prompt windows, buttons, and input boxes, it is possible to develop an entire GUI within Igor, to aid in logging, sorting, and analyzing data.

Our user interface for analyzing image data is shown in Figure 10.2. The functionality of the underlying procedures – including loading images into the program, studying the density plots, manipulating data, and plotting and computing various parameters – is all accessed via a control panel.

The images are loaded from .spe files, either piecemeal or an entire folder at once. The images may then be selected one-by-one from a pulldown menu on the control panel and

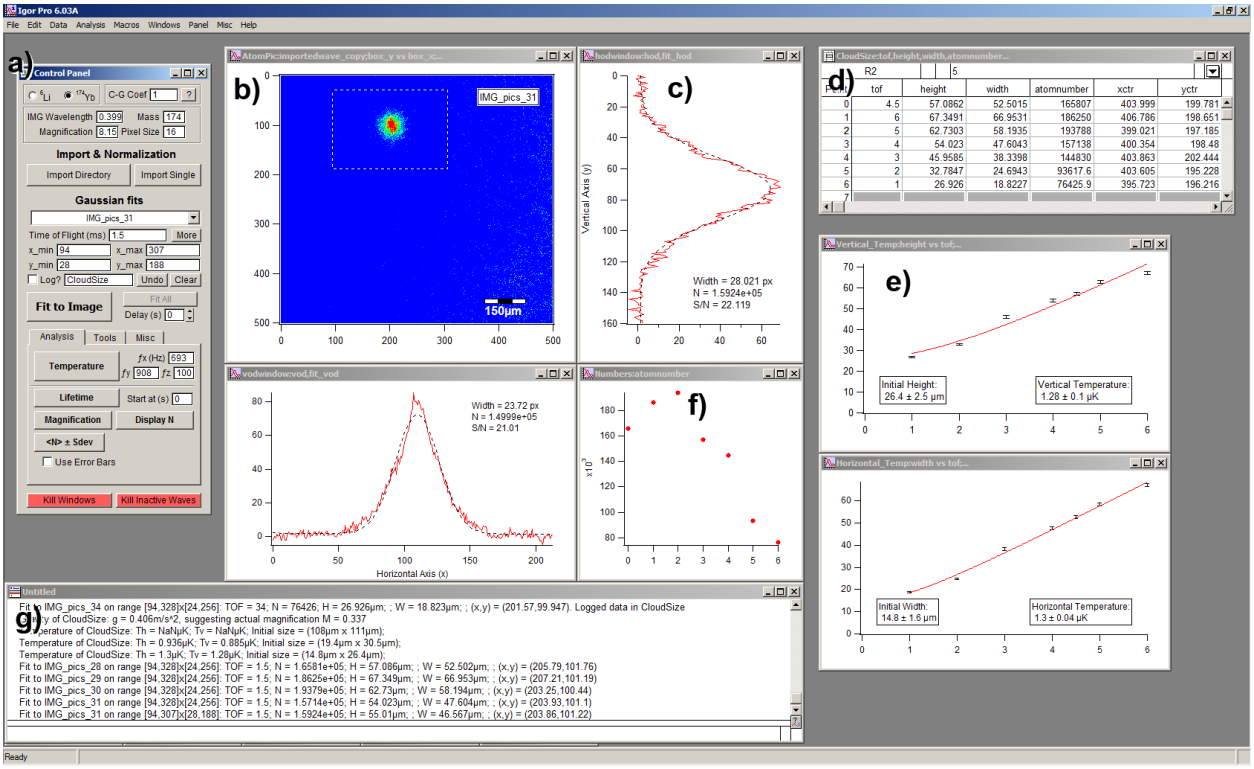

Figure 10.2: Our data analysis layout in Igor Pro. a) The control panel contains all of the commands needed to load image files, extract information, and log and manipulate the data collected from a batch of images. b) Density plots of images are displayed, and c) Gaussian best-fits to the integrated column density within the bounding box are estimated. d) Data from the Gaussian fits is logged, along with one or more independent variables. From the logging tables, numberous properties, e) e.g. temperature may be calculated. f) A scatterplot of atom number vs time provides information about long-term drifts in the stability of the machine during large experiments. g) The command window provides additional utility, and keeps a history log of the experiment.

analyzed, or a "fit all" function might be used to analyze all the loaded images. A variable time delay may be set, to give the researcher a chance to study each analyzed image before the next one runs.

The Igor GUI keeps track of both lithium and ytterbium when both are visible on screen. (When the double-imaging scheme is used.) The species toggle at the top of the control panel remembers the location of each species and moves the bounding box accordingly, sets variables such as imaging wavelength, Clebsch-Gordan coefficient, and atomic mass, and toggles between logging tables, to facilitate parallel data collection.

The default independent variable, used for bookkeeping or as x-values when plotting data, is called "tof." Up to two additional independent variables may be appended to the control panel at any time. These variables are treated on the same footing as tof, e.g. they are included in all logging tables, and are duplicated for lithium and ytterbium.

10.3.1 Basic analysis

The analysis of a single image begins with mapping the OD data in the images onto a density distribution using Beer's law. The density plot is displayed, along with a bounding box for cropping out uninteresting parts of the image. The area within the bounding box is then converted to two 1-D plots by integrating each row(column) to derive the vertical(horizontal) distribution of atoms. These 1-D distributions are then fit to Gaussian profiles to extract interesting parameters, such as atom number, cloud size, and center-of-mass position on screen. The fit function also includes an overall gradient, to account for imperfections in the image normalization. Finally, the extracted parameters are logged in a spreadsheet, if the logging option is selected.

Several options are available for pre-processing of images. For instance, the images may be rotated to align the principal axes of the cloud, as projected on the image, with the horizontal and vertical axes. There are two options for smoothing images: a Gaussian envelope-style blur to wash out point-like imaging artifacts, and a "Fourier" blur to remove intrusive wavelike patterns. (The latter of these is mostly obsolete after the switch to the Andor camera.) Finally, there is an option to average data across several images to reduce single-pixel shot noise.

10.3.2 Data processing & presentation

The Igor procedures provide lots of ways to manipulate and present data. The most important function is also the original one: computing temperature from cloud size data, taken at various times of flight. The built-in independent variable, which is now used to log a wide

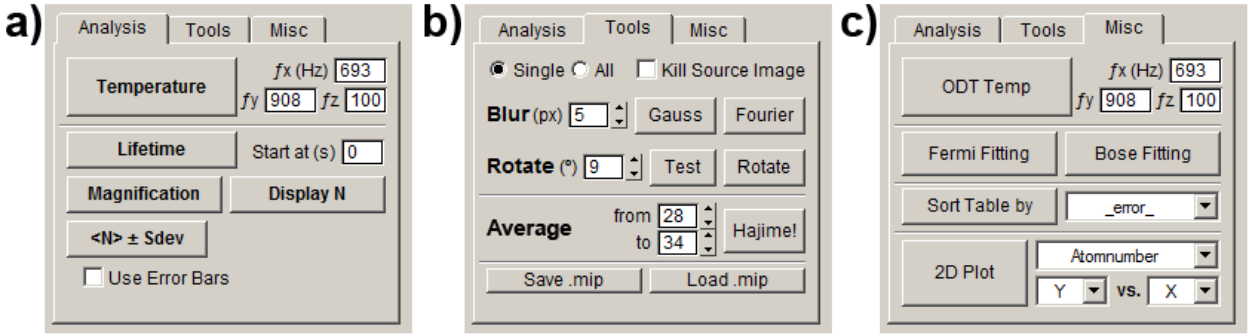

Figure 10.3: Detail of control panel, showing various functions. a) The basic analysis tab takes care of the most common functions, such as computing temperature or displaying the atom number vs the "ToF" variable. b) Pre-processing functions include rotating images, blurring them (to wash out unwanted artifacts) and averaging the density distribution over multiple images. c) Other options include sorting the table, or plotting data vs two variables. The "Bose" and "Fermi" buttons call the auxiliary control panels for analyzing quantum degenerate gases.

variety of parameters, is still named "tof" for this reason. The temperature is calculated twice, once from the $1/e$ height and once from the width of the atomic clouds, and is extracted from least-squares fits to hyperbolae of the form $y = \sqrt{y_0^2 + \frac{2k_BT}{m}t^2}$, with y_0 and T as free parameters.

The same data that gives the temperature of a sample may also provide us with the exact magnification of the imaging setup. This can be hard to estimate accurately from the lenses themselves, but may be calculated with a function that compares the acceleration of the center-of-mass of the cloud with the known value of 9.81m/s^2. The function also suggests the correct magnification value, and the user may opt to have all the logged data rescaled to reflect the new estimate. In units more appropriate to our experiment, $g = 9.81\mu\text{m/ms}^2$, so expansion times of several milliseconds are required to get a good estimate. In practice, such long times of flight are achievable only in ytterbium. To calibrate the magnification of lithium, we study their asympmtotic temperatures during interspecies thermalization.

Independent magnification calibration has been carried out on a few occasions with an USAF-style test pattern, placed in the object plane of the imaging setup. This also provides us with accurate information about the resolving power of our images.

Furthermore, the control panel includes options for displaying atom number versus the ToF wave, or to create a 2-D contour plot of any wave from the logging table vs any two independent variables.

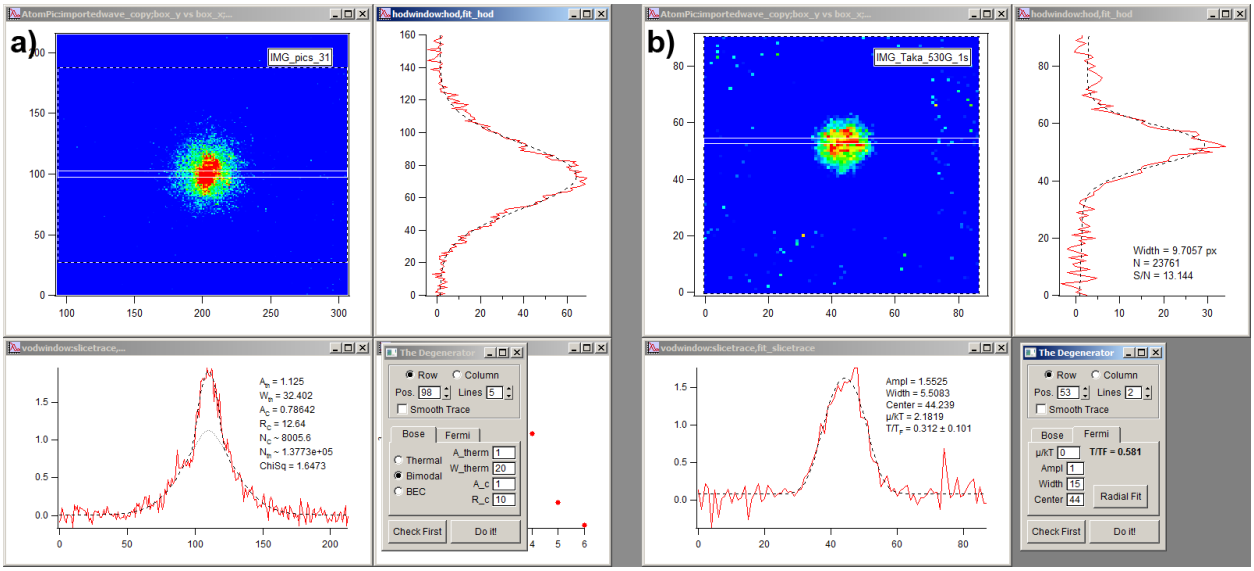

Figure 10.4: Bose and Fermi fitters in Igor. The auxiliary control panel opens in the lower right hand corner of the density plot. The density plot is rescaled to the size of the bounding box, and an indicator is added to show the location and width of the slice being evaluated. The slice is projected onto the appropriate 1-D plot, where the best-fit LDA model is overlaid. a) Fit to a bimodal distribution, consisting of a BEC and a Bose gas with $\mu = 0$. The dotted line indicates the boundary of the thermal and condensed components. b) Fit to a degenerate Fermi gas.

10.3.3 BEC/Fermi fitters

As we have seen in chapter 2, the density profile of a harmonically trapped cloud of atoms begins to deviate at low temperatures from the Boltzmann case of a Gaussian distribution. When this happens, the main fitting routine in Igor becomes unreliable, especially for estimating the temperature of the trapped gas. To probe quantum phenomena, a set of functions for dealing with degenerate gases was therefore devised.

"The Degenerator" is the name of the auxiliary control panel that takes care of such cases. When this panel is called, the currently loaded image is rescaled so that only the field within the bounding box is visible. The horizontal, integrated density distribution is replaced with a thin slice, probing only the density along a narrow line in the center of the cloud. The position of this slice is adjustable through the subpanel, as is its thickness – i.e. the number of pixel rows over which to average. A toggle on the subpanel allows for switching between horizontal and verical slices.

The reason for the switch from integrated densities to thin slices should be evident from the discussion in section 2.1, and in particular Figure 2.1. As the dimensionality of a degenerate gas is reduced by repeated integration, the profile, governed by the polylogarithm

functions, increasingly resembles a classical distribution. Although the signal-to-noise may be greatly improved by integrating over the entire image, this gain is typically not enough to offset the intrinsic weakening of the quantum degeneracy signal.

Since Igor does not offer support for polylogarithms, a pair of custom functions is built into the degenerate gas procedure. Each function is an 8th-order polynomial approximation $P(x)$ to either the positive or negative values of the $^5/_2$-order polylogarithm. The polynomial coefficients were chosen so as to minimize the integrated residual $\int \left[P(x) - Li_{5/2}(x)\right]^2 dx$ on the appropriate range. For the Bose fitter this range is [0,1], whereas for the Fermi fitter it was chosen so that the model would be accurate for temperatures down to $T = 0.2T_F$. For temperatures lower than this, the fit routine will fail, and a different approach is needed to estimate the temperature accurately.

For Bose gases, the subpanel offers three best-fit schemes: a purely thermal cloud at $T > T_C$, a pure condensate, and a bimodal distribution with a condensate component and a thermal Bose gas at $\mu = 0$. In either case, the user may enter manual guesses for the width and amplitude of each relevant component, and then perform a least-squares fit.

The output parameters may then be used to estimate the temperature, and condensate fraction. (These calculations are not yet automated by the Igor procedure.) In the case of a purely thermal gas, the temperature may be estimated either from the width of the cloud or from the chemical potential. For a bimodal distribution, the temperature is given by both the width of the thermal component, and the fraction of condensed atoms using equation 2.17. In the latter case, fits must be performed both vertically and horizontally, to account for the elongated aspect ratio of the condensate. The fitting function returns an estimate of the condensate number (as shown in Figure 10.4a) assuming a spherical distribution. The true number is the geometric mean of the horizontal and vertical values thus derived.

For Fermi gases (lithium, Fermionic ytterbium) recall that the apparent quantum behavior is entirely determined by the fugacity $\xi = e^{\mu/(k_B T)}$. The reduced chemical potential $\mu/(k_B T)$ is therefore included in the manual guess parameters, with a function that returns the corresponding value of T/T_F on the fly. The fitting routine also outputs the reduced temperature and its uncertainty, based on the formula

$$\mathrm{Li}_3(-\xi) = \frac{-1}{6\,(T/T_F)^3} \tag{10.1}$$

where the 3rd-order polylogarithm is also estimated by a high-order polynomial, accurate for $T/T_F \geq 0.2$.

An additional function was added to the set of Fermi routines, to estimate the reduced temperature based on the radial profile of the cloud. This is done by numerically performing

path integrals around the (estimated) elliptical contour lines of the distribution. In this way one gathers statistics from all the pixels in the image, but still maintains the quantum degeneracy signal of a 2-D distribution. Unfortunately, for reasons that are still unclear, the radial scheme consistently returns temperatures much higher than the thin slice scheme. This might be due to difficulties in estimating the center and ellipticity of the cloud, or it might be because it places low statistical significance on the region near the center of the cloud, where the deviation from classical behavior is most apparent.

Part III

Experimental Results

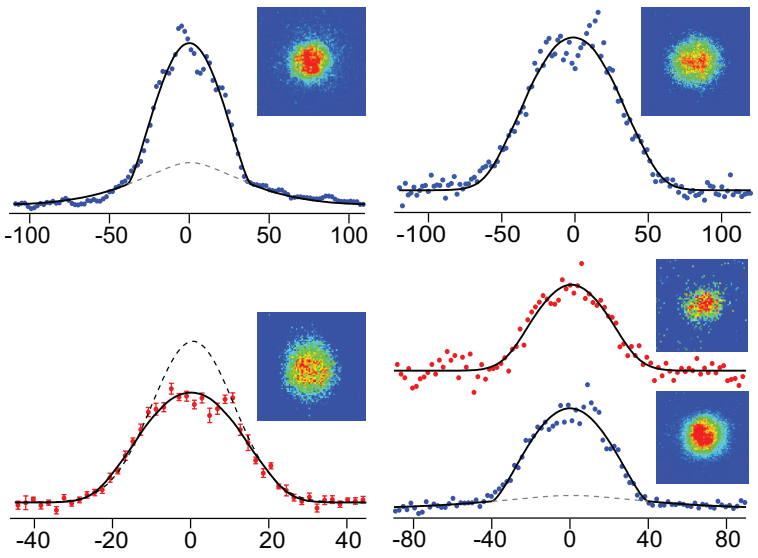

11 Interactions at Zero Magnetic field

This section provides details of the first experimental publication of our lab,[97] which is provided in Appendix A.

The data collection for our first publication was begun in the autumn of 2010. Simultaneous optical trapping of lithium and ytterbium (in a single-beam trap) had been observed in the spring of that year, and we spent the summer developing a crossed-beam ODT, and optimizing the number of atoms of each species transferred from the MOTs. The sequential loading scheme was developed at this time, as were many of our techniques for characterizing the shape of the trap.

The first baby-steps in our long-term mission to study interacting quantum gases of alkali and spin-singlet atoms involved understanding their basic characteristics at zero magnetic field. At this field the Li-Li scattering length is zero (to within uncertainty of all measurements and calculations [98]) which simplified our system and allowed us to focus on interspecies effects.

11.1 Measuring elastic interspecies interactions

Despite our prior efforts to implement an XODT, much of the work for the paper was done in a single-beam trap. We chose this because of observed thermal lensing effects, which, due to our complicated crossing scheme (described in section 8.2), were causing the two beams to become partially uncrossed at times and in ways that could not be accurately characterized. In order to extract quantitative data that required accurate knowledge of the trapping frequencies, we were therefore compelled to revert to a single beam.

As outlined in chapter 4, our lithium MOT has a significantly higher temperature than the ytterbium MOT. This, paired with the lower polarizability of ytterbium and our sequential loading scheme, leads to the lithium atoms entering the ODT with a significantly higher temperature than the extant ytterbium atoms. In a 50-50 mixture of the two species the subsequent thermalization process, which is driven by elastic interspecies collisions, will significantly heat the ytterbium, causing a large fraction of these atoms to evaporate from

---

Previous Page: Momentum distributions of quantum-degenerate ytterbium (blue) and lithium (red). Clockwise from upper left: BEC of ^{174}Yb. Degenerate Fermi gas of ^{173}Yb at $T = 0.3T_F$. Simultaneously degenerate ^{6}Li and ^{174}Yb. Deeply degenerate Fermi gas of ^{6}Li at $T = 0.06T_F$. Solid lines are fits to Bose and Fermi local-density models, while dashed lines are classical fits to the wings of the distributions.

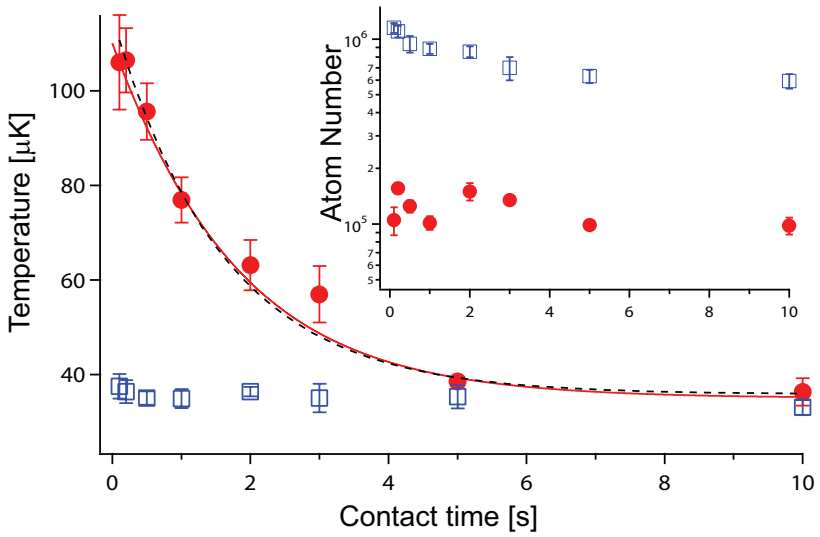

Figure 11.1: Temperature evolution of Li (red circles) immersed in a bath of Yb (blue squares). From the time scale of thermalization, the scattering length of the system can be calculated. The black dashed line is an exponential fit to the Li temperature, whereas the solid, red line is the best fit of a numerical model that accounts for evaporation and background lifetime effects. The inset displays the atom numbers during thermalization, which are almost an order of magnitude apart.

the trap before thermal equilibrium is reached.

However, a mixture biased heavily towards ytterbium will largely suppress such effects, as the cooling lithium sample imparts only a small amount of energy to each ytterbium atom. Figure 11.1 shows the evolution of such a system, with an atom number ratio of 10:1. Initially, the lithium temperature is almost twice that of ytterbium. During thermalization a small amount of ytterbium is lost (see inset to Figure 11.1) due to the aforementioned "sympathetic evaporation" effect, but the atom number quickly stabilizes, maintaining a favorable ratio.

This feature of our system was utilized to perform a measurement of the elastic interactions between our two species. An average of $\alpha = 2.7$ collisions are required for thermalization of an errant particle with a buffer gas of equal-mass particles. This number is derived from a set of Monte-Carlo simulations, and is independent of particle mass or scattering cross-section.[99, 100] For an unequal-mass buffer, the number of required collisions increases by a factor $1/\xi = 4(m_1 + m_2)^2/m_1 m_2$.[101] For lithium and ytterbium, $\xi = 0.13$. Using this model, the thermalization of a sample of lithium with a large bath of ytterbium is governed by

$$-\frac{1}{\Delta T}\frac{\partial(\Delta T)}{\partial t} = \frac{\xi}{\alpha}\langle n\rangle \bar{v}\sigma_{LiYb} \tag{11.1}$$

where $\Delta T = T_{Li} - T_{Yb}$, $\langle n \rangle = \left(\frac{1}{N_{Yb}} + \frac{1}{N_{Li}}\right) \int n_{Li} n_{Yb} d^3x$ is the density overlap, and $\bar{v} = \sqrt{\frac{8k_B}{\pi}\left(\frac{T_{Li}}{m_{Li}} + \frac{T_{Yb}}{m_{Yb}}\right)}$ is the mean relative velocity of interspecies scattering partners.

The temperature dependence of $\bar{v}$ and $\langle n \rangle$ means that the differential equation is not solved exactly by an exponential. For this reason, we used a numerical model to simulate the thermalization, with the scattering cross-section as a free parameter for least-squares fitting. In addition, the model included small corrections to account for evaporation of ytterbium and our finite vacuum lifetime of ≈ 30s. For comparison, a best exponential fit is shown on the figure, which differs from the numerical model by only a small amount.

From the above analysis, an s-wave scattering length with magnitude $|a_{LiYb}| = (13 \pm 3)\, a_0$ was derived. The relatively large error of $\approx 25\%$ was dominated by systematic uncertainties in trap frequencies, which affected our overlap density estimate. The validity of this calculation depends on the interspecies elastic scattering being s-wave dominated: i.e. the mean energy of collisions is far beneath the p-wave threshold, as defined in chapter 3. Calculations of the LiYb C_6 coefficient yield a threshold of 2.5mK, more than an order of magnitude above the highest temperatures used in the analysis.

11.2 Demonstrating sympathetic cooling

This paper also reported on our initial progress in sympathetically cooling lithium during forced evaporation of ytterbium. As discussed in section 8.3 the lower polarizability of ytterbium makes it necessary to impose an evaporation scheme in which ytterbium is the majority species and used as a coolant for lithium. For this experiment, since accurate characterization of the trap geometry was far less important than high density overlap, we used a crossed ODT geometry.

Figure 8.2 shows an early experiment, demonstrating that efficient two-species cooling is indeed possible. As in the thermalization measurement we introduced ytterbium and lithium in a roughly 10:1 ratio, and allowed for an initial thermalization at full trap depth. In subsequent evaporation the lithium temperature was seen to closely track that of ytterbium down to all but the lowest trap depths. In the published data, we demonstrated a factor-of-1000 increase in phase space density of lithium, with an estimated final temperature $T = 0.7T_F$. We had thus brought our lithium to the threshold of Fermi degeneracy; however, further cooling was hampered by dwindling numbers of coolant atoms and reduced thermalization rates due to gravitational sag. The latter effect, in particular, was a fundamental technical limitation of our system, which called for a tightening of our ODT beam waists, or the development of species-selective manipulation techniques to compensate.

Since further experimental improvements were needed to achieve true quantum degener-

acy in both species, the paper was submitted to PRL for publication in January 2011 without the final punch line,[97] but with the promise of a second publication down the road, once simultaneous degeneracy could be established.

11.3 Stability of the LiYb mixture

An important auxiliary result to come out of these studies was establishing of the stability and longevity of the Li-Yb mixture. Several mechanisms may lead to heating or ejection of atomic samples when multiple distinguishable species are brought together. For instance – and of chief concern to us – 3-body inelastic processes involving molecular decay channels are present in all ultracold atomic systems. In cases of particularly strong interactions, these can lead to conditions highly unsuitable for systematic studies of interspecies interactions.[102] It was therefore with some relief that we observed in-trap lifetimes of each atomic species that were almost entirely unperturbed by the introduction of the partner species.

12 Double-Degeneracy of ^{6}Li and ^{174}Yb

This section provides details of the second experimental publication of our lab,[103] which is provided in Appendix B.

Shortly after our first paper was published, it was clear that we were in an excellent position to push toward simultaneous quantum degeneracy of ^{6}Li and ^{174}Yb. The first ytterbium BEC had been observed in our lab in March, just as we were sending the paper out for review, and efforts were underway to optimize the system for trapping large numbers of both species. The large trap frequency ratio $\omega_{Li}/\omega_{Yb} \approx 8$ all but guaranteed that a two species sample with an ytterbium condensate would also be Fermi-degenerate in lithium. The only obstacles at the time were optimizing the evaporation scheme for sympathetic cooling and developing the tools to accurately quantify quantum degeneracy in each species.

Some improvements had already been made while the sympathetic cooling paper was in review for publication. Most notably, our antiquated 399nm source – consisting of an 18W Verdi laser pumping a Titanium-Sapphire ring cavity laser, which in turn was driving a homebuilt bow-tie cavity – was replaced with a commercial all-in-one system, (Toptica SHG Pro) which more than doubled the power available in the ytterbium Zeeman slower and greatly reduced routine maintenance demands. Beyond this, the ODT scheme had been altered from consisting of a single, recycled beam to two independent beams, as described in section 8.2. This not only improved stability of the XODT crossing, but also included a tightening of the waist of each beam from 30μm to 26μm, and an increase of the crossing angle from 10° to 19°. These improvements contributed to reducing the trap volume, thus increasing the collision rates needed for sympathetic cooling, and also raising the temperaturres of interest, T_C and T_F. On the eve of the last week of April 2011 we were prepared to see sure signs of simultaneous quantum degeneracy at any moment!

12.1 Fortunes and misfortunes

And then many things happened, almost all at once.

The first of these was the April 25 publication by the Kyoto group, demonstrating double degeneracy of both ^{174}Yb and ^{173}Yb with lithium.[104] This paper also offered a measurement of the interspecies scattering length ($|a_{LiYb}| = (19 \pm 4)\, a_0$ consistent with our measured value) and was in some sense a hybrid between the paper we had recently published and the one we were preparing to write. In the field of ultracold atoms, experiments are built on time scales of many years, and it is not uncommon for results achieved within months of one another to be considered as simultaneous. Nonetheless, the Kyoto publication imparted

a sense of urgency for us to to complete our project in a timely fashion.

The second event was the first sign of double degeneracy on April 27. Although we did not yet have the analysis functionality to make good quantitative estimates, it appeared that the 15-20 thousand ytterbium atoms and 10-15 thousand lithium atoms were both displaying signs of degeneracy. Over the next days, more images were taken, and it was established that there was indeed a measurable condensate fraction in ytterbium, whereas lithium had $T/T_F \approx 0.6$. Although this was a good achievement, we still wanted at least one picture that was conclusively below $0.55T_F$. This is where the sign of the chemical potential flips, and also where the classical phase space density $n\lambda_{TdB}^3 = 1$. For these reasons, it is commonly regarded as the threshold of Fermi degeneracy.

The third, and least fortunate, event was the failure of both of our ytterbium lasers. First, on the morning of May 4, the power supply for the 399nm laser controller failed spectacularly, with black smoke pouring out of the back of the chassis. The manufacturer had a replacement power supply shipped to us on short notice; however, in the mean time the fiber laser (an old Koheras Boostik) from which we got our green light had broken down. No more ytterbium data could be collected until it could be shipped off and repaired at the factory in Denmark.

Fortunately, before the 399nm laser failed a very promising pair of images had been taken, but not yet fully analyzed. It was, however, evident that these images were showing the strongest signatures yet of Fermi degeneracy in lithium, and it was agreed that we would carefully scrutinize them for potential publication merit.

12.2 Establishing quantum degeneracy

During the analysis of these two images from May 3rd, several of the tools that are now part of our routine procedures were developed. The quality of the images was not sufficient to conclusively establish quantum degeneracy in the 1-D integrated images, as had previously been done in single-species studies. Instead, for the first time, we extracted information from thin slices of pixels taken near the center of the clouds, where the quantum signal is the strongest. The model we used was that of equation (2.6), modified to use simplified and independent fit parameters.

$$n(x) = n_0 \frac{\mathrm{Li}_2\left(\pm\xi e^{-(x-x_0)^2/w^2}\right)}{\mathrm{Li}_2\left(\pm\xi\right)} \tag{12.1}$$

The most important parameters here are the fugacity ξ and the width w. For ytterbium a bimodal distribution was used, with two extra parameters for the condensate amplitude

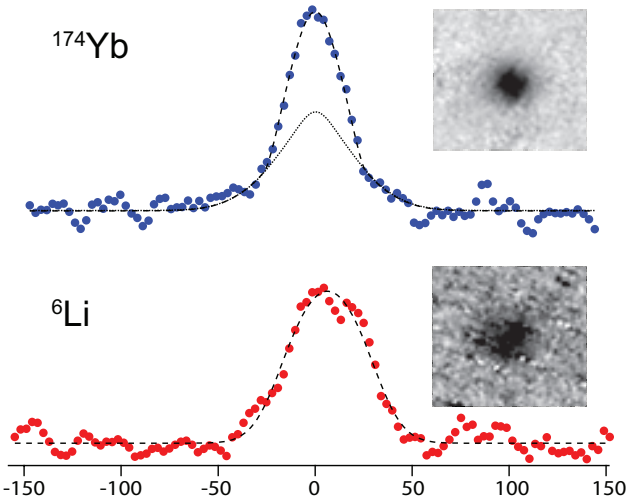

Figure 12.1: Density traces of simultaneously degenerate (bosonic) ytterbium and (fermionic) lithium. Atom numbers are $2.3(1.2)\times10^4$ for Yb(Li), with reduced temperatures $T/T_C = 0.8$, $T/T_F = 0.3$, respectively. The insets are cropped secitions from the absorption images from which the data was extracted.

and width.

Using this technique, we were able to establish quantum degeneracy in lithium with very high confidence. However, given our somewhat scant quantity of data, we chose to use an extended approach of several different techniques to consolidate the result, and to reduce our error bars.

For ytterbium, the temperature was extracted twice: first directly, by measuring the width of the thermal component of the 2-D density distribution; (extracted from a thin slice of the image) and then indirectly, by estimating the fraction of condensed atoms, extracting T/T_C using equation (2.17), and hence getting the temperature from equation (2.16). The two methods returned consistent temperatures, with a weighted mean $T = 100 \pm 10$nK, or $T/T_C = 0.8 \pm 0.1$.

For lithium, the temperature was estimated in three ways, firstly by using the thin-slice method. This method has the benefit of amplified quantum signal, but also suffers from high shot noise, as fewer camera pixels are used for the density trace. To combat this problem, a thick slice, averaging over many pixel rows, was initially used. The thickness was then gradually reduced, and the reduced temperature and its error recorded for each thickness. As expected, the apparent temperature decreased as the thickness was reduced, while the error bars increased. Finally, an exponential function was heuristically fit to the data, and the "zero-pixel" extrapolated value was used to estimate the reduced temperature.

Next, we estimated the temperature, again from the thin-slice data, using the cloud width. Using the transformation of equation (2.10), we may back out the temperature

$$k_B T = \frac{\frac{1}{2} m\omega^2 w^2}{1 + \omega^2 \tau^2} \tag{12.2}$$

Finally, we repeated this calculation, but using the entire cloud, and fitting a simplified model of the 1-D Fermi distribution of equation (2.8). Putting these results all together, we arrived at a weighted mean of $T = 320 \pm 36$nK, or $T/T_F = 0.27 \pm 0.03$. As we had hoped, the temperature was below $0.55 T_F$ by much more than the error bars, conclusively establishing that our sample was quantum-degenerate.

All of the calculations above were, of course, dependent on accurate knowledge of the trap frequencies. These had, by good fortune, been measured for two different powers shortly before the lasers failed. By extrapolating this data to the trap depths where the double degeneracy images were taken, and applying a small correction for gravitational effects, we had a confident estimate in the radial trap frequencies. The axial frequency was then estimated by taking further trap frequency measurements with lithium, and extracting a trap aspect ratio of 6.75.

We noted, while doing these computations, that the Kyoto group had observed a depletion of the ytterbium condensate number, when in the presence of lithium. Although they chose not to speculate on the origin of this observation in their paper, it is quite plausible that the effect is real, and due to collisions with energetic lithium atoms. (Which have energy $\sim E_F$, even when $T \ll T_F$) If this depletion were also present in our experiment, we should have expected the second method above to yield an artificially higher temperature than the first. It is unclear why this was not the case. It may be that our experimental sensitivity was insufficient to register the discrepancy, or perhaps the two clouds were significantly separated, due to gravitational sag.

The latter of these conjectures is consistent with our observation that the clouds were not fully thermalized. (Note the temperature difference in the above discussion.) To estimate the effects of gravitational sag, the numerical model described in section 8.5 was devised, which took into account the displacement of the trap center, change in trap frequencies, reduction of trap depth due to spilling, and the density distributions of the two species, including quantum statistics. This model predicted that the spatial overlap would have dropped off by a factor $1/e$ by the time the ytterbium temperature reached $\simeq$300nK, a number reassuringly consistent with the lithium temperature measurement of 320nK.

12.3 Wrapping up the paper

The writeup was submitted to PRA Rapids on May 27, one month after the first signs of simultaneous degeneracy were observed, and submitted with only minor corrections from our

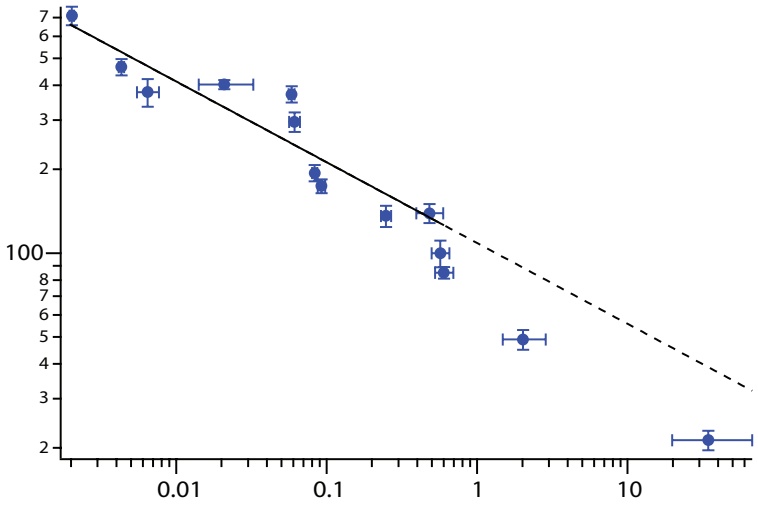

Figure 12.2: Atom number vs phase space density. The source data was taken before the double-degeneracy data, while we were working to optimize the evaporation ramp. The straight line fit to the data with $\rho < 1$ gives the evaporation efficiency $-\partial \ln \rho / \partial \ln N = 3.4$.

reviewers.[103]

In addition to presenting the double degeneracy, we added some experimental details to the paper, discussing our trapping scheme and geometry. In particular, we demonstrated that a shallow-angle XODT with beams of equal wavelength could be used to achieve efficient quantum degeneracy in ytterbium. The layout of our optical trap differs from many other groups, and it was not clear from the outset that efficient evaproation schemes could exist in such a trap. For this purpose, temperature and number data was collected at a number of points along our evaporation ramp, as shown in Figure 12.2. To characterize efficiency, we calculated the rate at which the phase space density $\rho = n\lambda_{TdB}^3$ increases as atom number decreases:

$$-\frac{\partial \ln \rho}{\partial \ln N} = 3.4 \pm 0.4 \tag{12.3}$$

which is very high for an all-optical evaporation scheme.[91] As discussed in section 8.5, the gravitational tilting may play a significant role in the evaporation process, even at higher trap depths.

13 Interspecies Interactions in Feshbach-Resonant Lithium

This section provides details of the third experimental publication of our lab,[105] which is provided in Appendix C.

With the achievement of double-degeneracy in our Li-Yb mixture, our machine had finally reached full maturity, and was ready for more advanced (and interesting) experiments. However, the breaking of our Koheras laser and subsequent loss of Yb MOT light put our experimental capacity on hold for many months. It was thus only in the summer of 2012 that we published our next paper, on the chemical dynamics of Li Feshbach molecules immersed in a bath of Yb.

13.1 Motivations

One of the more interesting features of the Fermionic ^{6}Li atom is the broad Feshbach resonance between the lowest hyperfine states $|1\rangle$ and $|2\rangle$. This resonance has been previously utilized by a number of groups, often as a means of building highly excited Li-Li dimers, bound in the Feshbach-molecular state. When these molecules were first produced at ENS, Paris and the University of Innsbruck [63, 106] the researchers were surprised to find that their in-trap lifetimes were extremely long when held at fields close to resonance. Naïvely, one would expect significant losses as the molecules collide with unbound atoms, or one another, and decay into one of the many lower rovibrational levels. The longevity was later intererpreted as a result of Fermi statistics.[107] The key idea is that a sufficiently weakly bound Feshbach molecule largely retains the statistical properties of two individual atoms. In a gas consisting of only two spin states, the third particle that is needed to mediate vibrational decay would necessarily be identical to one of the two components of the dimer, and thus Pauli exclusion would prevent collisions between atoms and molecules.

The goal of our study was to explore the detailed role of Fermi statistics in these processes. By introducing a third, non-indentical and non-resonant component, we expected to see a considerable reduction in molecule lifetime, as we introduced a large family of Pauli-allowed decay channels. Furthermore, we set out to study the nature of the inelastic rate coefficients in a quantitative manner, and to explore their scaling behavior near resonance.[72] Finally, we were motivated by the possibility of future Li-Yb experiments in the strongly interacting regime, and wished to explore the stability of the mixture at fields very close to resonance.

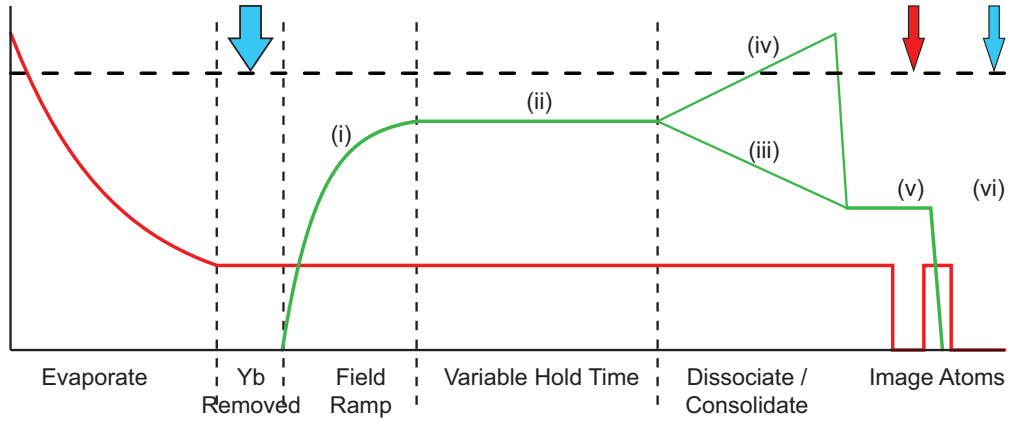

Figure 13.1: Experimental time sequence for the experiment. ODT laser power is shown in red, and magnetic bias field in green. After evaporation, Yb atoms are removed, if necessary, and the magnetic field is ramped to a target value. (i) After a variable hold time, (ii) the field is either ramped down to 530G (iii) or up across resonance and then back down. (iv) Li atoms are released from the ODT and imaged at this field, (v) while Yb atoms are recaptured and imaged a few ms later at zero field. (vi)

13.2 Experimental details

The experimental geometry was essentially the same as in the double-degeneracy paper.

After both species were loaded into the XODT we evaporated the sample down to approximately 5μK. This set point was chosen for being far below the p-wave threshold for elastic collisions, but still above quantum degeneracy for both species. ($T/T_F \approx 2$ for Li, and $T/T_C \approx 10$ for Yb) Once the atoms had thermalized, we quickly ramped up the field, using both the MOT and Feshbach coils, to a pre-determined point near resonance. Fast ramping was found to be crucial, as there exists a wide region of magnetic fields around 650G in which molecules are spontaneously formed, leading to premature chemical reactions. Even at our fastest ramp speeds, this led to a significant loss of Li atoms, and a corresponding heating of the sample.

The molecules were then held at the target field for a variable amount of time before interrogation. In order to characterize the mixture, we carried out one of two possible procedures: either the magnetic field was rapidly ramped down, or the field was ramped up across the resonance. In the former case, the Feshbach molecules were consolidated into more deeply-bound pairs. In the latter case, the Feshbach molecules were dissolved into unpaired atoms. Regardless of procedure, the field was then ramped to 530G, where the unbound Li atoms could be released from the trap and measured using the high-field imaging setup, as described in section 4.5. By counting the surplus of atoms in the second technique, where the dimers were dissociated before imaging, we estimated the number of molecules present

in the sample at the end of the variable hold time.

To count Yb atoms accurately, the magnetic field had to be ramped down to zero. Although the IGBTs allowed switching of the current from the power supplies in $\sim 1\mu s$, the ringdown of the current in the MOT and Feshbach coils would persist for several ms. We therefore found it necessary to switch the ODT back on immediately after imaging Li. Thanks to the large mass of Yb, and corresponding slow expansion, it was possible to recapture almost 100% of the Yb atoms in this way. The Yb cloud was subsequently released once more after the field turnoff was complete, and imaged within a few ms of the Li atoms: close enough in time to use the four-frame double imaging setup.

For calibration, half of our data was taken in the absence of Yb. To prepare a pure Li sample, we blasted away the Yb using a 1ms pulse of the imaging light. This blast could be carried out either before or after the field ramp, with no discernable difference. The calibration runs then proceeded in the same fashion as with Yb, except that single-species imaging was used.

In addition to varying the hold time and alternating field ramp configuration, we varied the expansion time of both species after release. This allowed us to also compute the temperature of each species from the data.

13.3 Observations

13.3.1 Inelastic losses near resonance

Before carrying out a detailed study of the dynamics of the system, we conducted an evaluation of the overall Feshbach spectrum of the system at a range of fields around resonance. This was carried out by taking two sets of images at each field, one at a hold time of 500ms, and one at a shorter hold time of 10ms for normalization purposes. Thus studying the fractional loss at each field, we quickly found the familiar loss feature centered near 650G. Of far greater interest to us, though, was the effect of the inclusion of ytterbium. With the second species added, the loss feature was broadened, but only, it seemed, on the right-hand (high-field) side.

To understand the origin of this one-sided broadening, we need to consider the nature of the chemical processes at play. The most evident process is the dynamic equilibrium of free atoms and Feshbach molecules.[60, 108] These dimers may be both formed and broken through collisions, but a simple entropy argument prescribes that the equilibrium fraction should favor free, unpaired atoms even when the binding energy $U \gtrsim k_B T$. Therefore, the formation of Feshbach dimers is not sufficient to explain the deep loss feature.

Consider, then, a second step, in which a Feshbach molecule collides with another particle

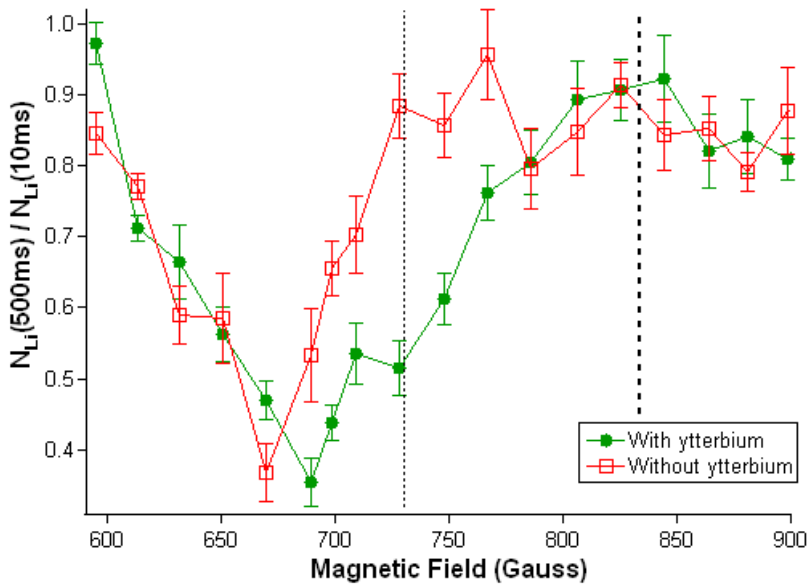

Figure 13.2: Atom loss near the Feshbach resonance. (Resonance indicated with thick, dashed line.) Data points show fraction of unpaired atoms remaining after a 500ms hold, normalized to samples after 10ms hold. In absence of Yb (open squares) there is a distinctive loss feature centered at 660G. When Yb is included (filled circles) the feature is broadened, and shifted toward resonance. The thin dashed line indicates where the interaction parameter $1/ka = 1$. The lines connecting data points are to guide the eye.

to form a deeply bound dimer. The vibrational level spacing of the Li dimers is far greater than the trap depth, so such a process invariably leads to both collision partners escaping the trap. Only when both of these steps are in place should we expect to see significant loss features like in Figure 13.2.

The first of these two steps occurs at a quickly increasing rate as one approaches resonance. This is because, as the bound state approaches the scattering continuum, the spatial overlap between the bound and free quantum wavefunctions approaches unity. On the other hand, the second step is suppressed close to resonance, where the overlap between the Feshbach wavefunction and the rest of the rovibrational manifold approaches zero. There are thus two regimes to consider: one far from resonance where the first step limits the trap loss rate, and one close to resonance where the second step is rate-limiting. From Figure 13.2 it thus appears that the inclusion of the ytterbium bath increases the rate of the second step, but leaves the first step unchanged.

13.3.2 Dynamics at intermediate interaction strength

We therefore decided to focus our more detailed study on fields near 700G, where neither step is strongly suppressed, and there is a clear contrast between the behavior with and without

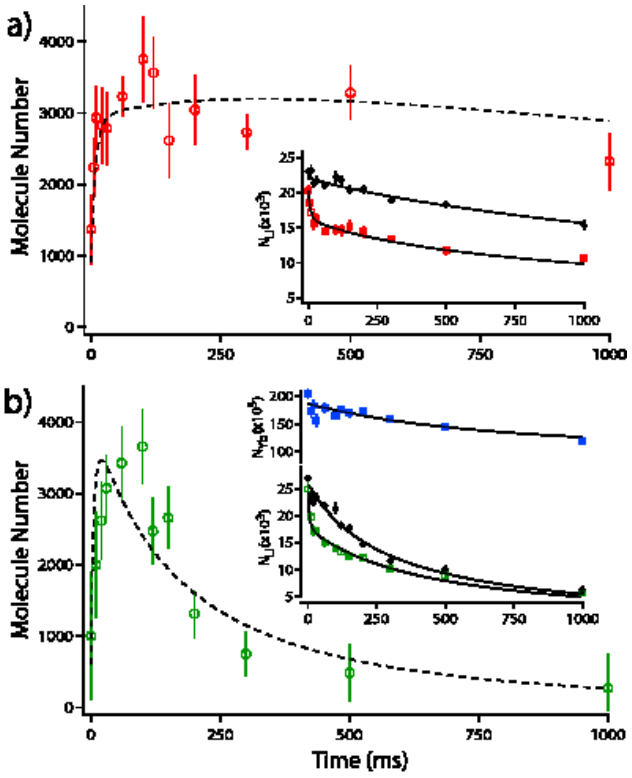

Figure 13.3: Dynamics of molecule formation and decay at 709G, a) without Yb, and b) immersed in a bath of Yb. The data points represent the contrast between the data in the insets, taken either with or without a molecule dissociating ramp across resonance. Also shown in inset of b is number of ytterbium atoms. The dashed and solid lines are results of the numerical simulation.

ytterbium. In our system, this is also the regime where the scattering length becomes comparable to the thermal de Broglie wavelength, and it can thus be characterized as a regime of "intermediate" interactions.

To our delight, we found that we were able to measure the chemical dynamics of the system with good resolution. Plots of molecule number vs hold time, such as Figure 13.3 were carried out for a range of magnetic fields. In the end, we settled on 710G as the ideal field, where we could resolve all the important features: the creation of dimers in the first few milliseconds, the subsequent decay of molecule number, and the contrast between the data with and without ytterbium. The data collected at this field is shown in Figure 13.3, and became the basis for extracting the inelastic rate coefficients in the analysis described below. As expected, the inclusion of ytterbium had only a small effect on the initial slope of molecule number vs time. However, the subsequent decay is strongly influenced by the presence of the second species, just as anticipated from the spectral data above.

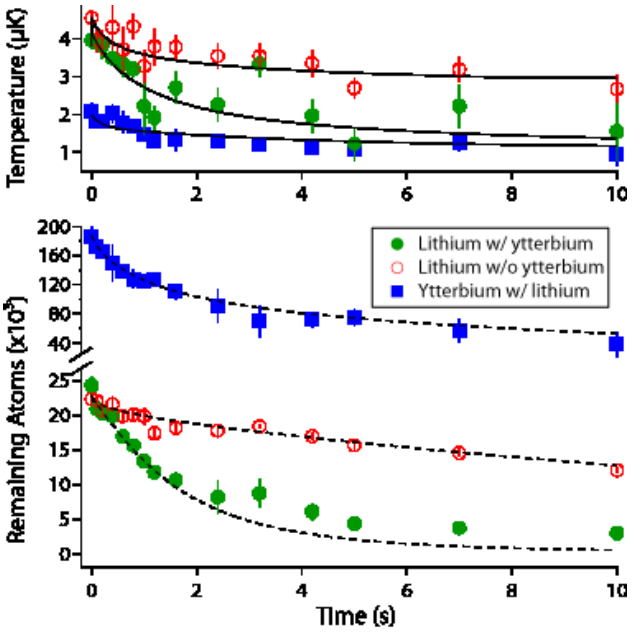

Figure 13.4: Dynamics at 810G. At this field, we can only count atom number; however, the simulation model still assumes a chemical equilibrium of atoms and molecules. Although there are still losses enhanced by the presence of Yb, the sample lifetime is now several seconds. Furthermore, there are clear signs of thermalization between Li and Yb.

13.3.3 Stability in the unitary limit

Finally, we conducted a study of the dynamics very close to resonance. For this we chose a field of 810G, where, as expected we found extremely long atomic lifetimes. At this field we did not attempt to count the molecules. This is because the molecules here have such low vibratonal frequencies that a field ramp away from resonance could not realistically be carried out in an adiabatic fashion. A non-adiabatic ramp would force the molecules into a superposition of a free and deeply bound state, with a preference for the unbound state, thus effectively dissociating the molecules. We therefore switched off the field rapidly with the IGBT, and assumed that all molecules were dissociated before imaging.

The key result of this study was the evident thermalization of lithium with the bath of ytterbium, as shown in Figure 13.4. Initially, the lithium atoms were at a higher temperature, due to heating during the field ramp. However, with Yb present the temperature of the Li atoms slowly decreased over a period of several seconds. This was an indication that, at these fields, elastic collisions were dominating over inelastic ones.

13.3.4 Toward superfluid ^{6}Li?

The stability of our mixture close to resonance raised the natural question of whether simultaneous degeneracy could be achieved in the unitary regime of Li-Li interactions. Such a system would be of great scientific interest, not least because it permits the use of ytterbium as a massive, microscopic probe of the lithium superfluid. This could be used, for instance, in studies of the Landau critical velocity across the BEC-BCS crossover.[25, 29]

A major obstacle, however, was the heating effects of ramping the magnetic field across the lossy region around 650G. Even when the system was brought to deep degeneracy before the field ramp, the lowest temperatures we achieved in lithium were $T = 0.25T_F$: degenerate, but significantly above the superfluid critical temperature. Furthermore, at these conditions, the ytterbium numbers were insufficient to sympathetically re-cool lithium after the field ramp.

A second approach of ramping the field to resonance before evaporation – or during an intermediate point – was attempted. However, the ytterbium-induced losses at this field were found to be too great, causing our lithium to vanish entirely before the end of the evaporation ramp.

Some improvement was achieved by selectively removing one of the lithium spin states before the bias field was brought near resonance. Since the strong interactions occur only between the $|1\rangle$ and $|2\rangle$ states of lithium, the removal of one of them greatly reduced losses. This state could subsequently be repopulated with an RF transfer of half of the remaining atoms. Unfortunately, the accompanying factor-of-2 reduction in overall lithium number proved to be more than we could afford, leading to hopelessly low-quality images of the < 5000 remaining atoms.

Unable to produce a sample of resonant, deeply degenerate lithium, we decided to put this project on ice until further experimental improvements could be made: either to the number of trapped atoms or to the speed of our magnetic field ramp.

13.4 Estimating the Chemical Dynamics

To interpret the data above in a quantitative way, a numerical simulation model was devised, and implemented using *Igor Pro*. The simulation modeled the dynamics of the co-trapped gases of Li, Li_2, and Yb using a coupled set of 5 nonlinear ordinary differential equations (ODEs). By evaluating the ODE repeatedly, with varying input parameters, we derived a least-squares fit to our data, and thus succeeded in extracting numerical estimates of the inelastic rate parameters. Of these, some had previously been measured,[106, 13] and could provide a test of our model, whereas others (especially those involving ytterbium) were new

measurements.

The following two sections provide an outline of the physical model that was used in the ODE, and a brief description of the modified forward-Euler scheme and least-squares search routine used for this experiment.

13.4.1 The Chemical Processes

To simulate molecular dynamics in or without the presence of Yb, we study the rates of the following reactions:

$$\begin{aligned}
\mathrm{Li} + \mathrm{Li} + \mathrm{Li} &\rightleftharpoons \mathrm{Li}_2 + \mathrm{Li} + E_b && (13.1)\\
\mathrm{Li} + \mathrm{Li} + \mathrm{Yb} &\rightleftharpoons \mathrm{Li}_2 + \mathrm{Yb} + E_b && (13.2)\\
\mathrm{Li}_2 + \mathrm{Li} &\rightarrow 0 && (13.3)\\
\mathrm{Li}_2 + \mathrm{Yb} &\rightarrow 0 && (13.4)
\end{aligned}$$

Note that reactions (13.1) and (13.2) may happen in reverse. The latter two reactions represent transitions to deeply bound molecules, which are ejected from the trap along with their collision partners.

13.4.2 Equations of Motion

Following the notation of Zhang and Ho,[108] we write down the differential equations for the local density of Li dimers (n_m), Li atoms (n_{Li}) and Yb atoms (n_{Yb}).

$$\begin{aligned}
\dot{n}_m &= \left(\frac{3}{4}L_3 n_{Li}^3 - qL_3 n_m n_{Li}\right) + \left(\frac{1}{2}L_3' n_{Li}^2 n_{Yb} - qL_3' n_m n_{Yb}\right)\\
&\quad -L_2 n_m n_{Li} - L_2' n_m n_{Yb} && (13.5)\\
\dot{n}_{Li} &= -2\left(\frac{3}{4}L_3 n_{Li}^3 - qL_3 n_m n_{Li}\right) - 2\left(\frac{1}{2}L_3' n_{Li}^2 n_{Yb} - \frac{2}{3}qL_3' n_m n_{Yb}\right) - L_2 n_m n_{Li} && (13.6)\\
\dot{n}_{Yb} &= -L_2' n_m n_{Yb} && (13.7)
\end{aligned}$$

The L-factors are related to the square of the matrix elements for each of the four reactions: L_3, L_3', L_2, L_2' respectively. (Note that the "prime" denotes the equivalent, unprimed reaction, but with Yb as the spectator particle instead of Li.) The prefactors of 3/4 and 1/2 inside the brackets are due to processes (13.1) and (13.2) involving two different spin states, each with population $n_{Li}/2$. (Throughout this section, factors of 2 will be popping

up due to the two states of Li. It is assumed throughout that the mixture is unpolarized, e.g. $N_\uparrow = N_\downarrow = N_{Li}/2$.) The q-factor is related to the equilibrium constant of the two-way chemical reaction $\mathrm{Li} + \mathrm{Li} \rightleftharpoons \mathrm{Li}_2$, and is a function of the bound state energy as well as the densities of Li and Li_2. When the dynamical time scales of the system are longer than the inverse mean trap frequency $1/\bar{\omega}$ we can take q to be a global parameter. In our experiment, chemical time scales were ~ 10ms, whereas $1/\bar{\omega} \sim 0.5$ms, so the global-q approximation was assumed to be valid.

Integrating over the atomic clouds, we get the global analogues of the above equations:

$$\dot{N}_m = L_3\left(\frac{3}{4}I_1 - qI_3\right) + L_3'(\frac{1}{2}I_2 - qI_4) - L_2 I_3 - L_2' I_4 \tag{13.8}$$

$$\dot{N}_{Li} = -2L_3\left(\frac{3}{4}I_1 - qI_3\right) - 2L_3'(\frac{1}{2}I_2 - qI_4) - L_2 I_3 \tag{13.9}$$

$$\dot{N}_{Yb} = -L_2' I_4 \tag{13.10}$$

In the above equations, the four I-factors are spatial integrals of the products of density terms that appear in the local equations of motion.

$$I_1 = \int n_{Li}^3 d^3x = \left(\frac{N_{Li}}{2\pi\sqrt{3}R_{Li}^2}\right)^3 \tag{13.11}$$

$$I_2 = \int n_{Li}^2 n_{Yb} d^3x = \frac{N_{Li}^2 N_{Yb}}{(2\pi\sqrt{2})^3}\frac{1}{(R_{Li}^2 R_{Yb}^2 + \frac{1}{2}R_{Li}^4)^{3/2}} \tag{13.12}$$

$$I_3 = \int n_m n_{Li} d^3x = \frac{N_{Li}N_m}{(3\pi R_{Li}^2)^{3/2}} \tag{13.13}$$

$$I_4 = \int n_m n_{Yb} d^3x = \frac{N_m N_{Yb}}{(2\pi)^{3/2}}\frac{1}{(R_{Yb}^2 + \frac{1}{2}R_{Li}^2)^{3/2}} \tag{13.14}$$

Here, we have defined the mean cloud radius of lithium (ytterbium) as

$$R_{Li(Yb)} = \sqrt{\frac{k_B T_{Li(Yb)}}{m_{Li(Yb)}\bar{\omega}_{Li(Yb)}^2}} \tag{13.15}$$

with $\bar{\omega} = (\omega_x\omega_y\omega_z)^{1/3}$. An important assumption behind the above equations is that each species is quasistatic, remains in internal thermal equilibrium throughout the process, and maintains a Boltzmann density distribution

$$n(\vec{x}) = \frac{1}{R^{3/2}} e^{-\sum_i \frac{x_i^2}{R_i^2}} \tag{13.16}$$

Furthermore the molecules and free Li atoms are assumed to remain in thermal equilibrium, and thus the size of the molecular cloud, $R_m^2 = R_{Li}^2/2$. Although this assumption was not tested experimentally, we assumed it to be valid due to the very large scattering length between Li atoms in the magnetic field regime of interest.

13.4.3 The q-Factor

When simulating the system, using equations (13.8-13.10), the L-factors are experimental "knobs" that can be tweaked to fit experimental data, whereas the I-factors are dynamic variables that depend on instantaneous numbers and temperatures. In addition, we have the thermodynamic "q-factor" to worry about.

In essence, q determines the quantitative balance of atoms and molecules in chemical equilibrium. Its value is such that when the free energy F of the system is minimized, the forward and backward reaction rates are equal. Take the free energy of the three-component (classical) gas to be

$$F = -k_B T \ln \left(\frac{Z_{Li}^{N_{Li}} Z_{Yb}^{N_{Yb}} (Z_m e^{-E_b/k_B T})^{N_m}}{N_{Yb}! N_m! \left((N_{Li}/2)! \right)^2} \right) \tag{13.17}$$

where the Zs are the single-particle partition functions. Note that q depends on the *instantaneous* properties of the system: numbers and temperatures. Since the Yb number & temperature does not depend on the molecular population, we are left with minimizing the reduced free energy

$$F = -k_B T \ln \left(\frac{Z_{Li}^{N_{Li}} (Z_m e^{-E_b/k_B T})^{(N_{Tot}-N_{Li})/2}}{\left(\frac{N_{Tot}-N_{Li}}{2}\right)! \left(\left(\frac{N_{Li}}{2}\right)! \right)^2} \right) \tag{13.18}$$

which gives us the equilibrium molecule fraction (see ref. [60])

$$\frac{N_{Tot}}{2N_m^{(eq)}} = 1 + \frac{1}{\phi_{Li}^{(eq)}} e^{-E_b/k_B T} \tag{13.19}$$

In the above equation, ϕ is the phase space density of Li atoms in the ground state of the harmonic trap

$$\phi_{Li} = \frac{N_{Li}}{2} \left(\frac{\hbar \bar{\omega}}{k_B T} \right)^3 \tag{13.20}$$

We can link this ratio to q by setting the Yb number to zero (this is ok, since q is independent of N_{Yb}), so that $I_2 = I_4 = 0$ in equations (13.8)-(13.9). We also set L_2 to zero, since the concept of chemical equilibrium assumes a lossless regime. The steady-state

solution then yields

$$\begin{aligned} q &= \frac{3I_1^{(eq)}}{4I_3^{(eq)}} \\ &= \frac{N_{Li}^{(eq)2}}{N_m^{(eq)}} \times \frac{3i_1}{4i_3} \end{aligned} \tag{13.21}$$

which we can combine with equation (13.19). The lowercase, reduced integral factors $i_1 = I_i/N_{Li}^3$, $i_3 = I_3/(N_{Li}N_m)$ are number-independent. To eliminate the *a priori* unknown equilibrium quantities $N_{Li}^{(eq)}$, $N_m^{(eq)}$ we write down equations (13.19), (13.21), plus a "conservation of mass" criterion. In simplified notation,

$$\frac{N^2}{2M} - A = x \tag{13.22}$$

$$n_q \frac{A^2}{M} = q \tag{13.23}$$

$$A + 2M = N \tag{13.24}$$

Where, $A = N_{Li}^{(eq)}$, $M = N_m^{(eq)}$, $n_q = 3i_1/4i_3$, and $x = 2(k_BT/\hbar\bar{\omega})^3 e^{-E_b/k_BT}$. Combining these equations to eliminate A and M, we get

$$q = 2xn_q = \frac{3}{(4\pi R_{Li}^2)^{3/2}} \left(\frac{k_BT}{\hbar\bar{\omega}}\right)^3 e^{-E_b/k_BT} \tag{13.25}$$

As expected, q depends sensitively on the temperature of Li atoms and molecules, so it needs to be reevaluated for each step of the simulation.

13.4.4 Thermal Equations of Motion

The conversion of an unbound atom pair to a bound molecule releases an amount of binding energy E_b, which adds to the temperature of the mixture. Since the I- and q-factors in the number equations are strongly temperature-dependent, the temperature of the mixture needs to be maintained as a dynamic parameter of the simulation. Process (13.1) dumps E_b of energy into Li, whereas process (13.2) distributes the same amount of energy between Li and Yb. However, conservation of momentum dictates that, in the center-of-mass frame, the ratio of energies absorbed by the two reactant particles $E_{Li_2}/E_{Yb} = m_{Yb}/m_{Li_2} \simeq 15$. In other words, both processes give nearly all the energy to Li, so rather than splitting hairs we simply assume

$$\dot{E}_{Li} = E_b \left(\dot{N}_m\right)_{3-body} \tag{13.26}$$

where $\left(\dot{N}_m\right)_{3-body}$ is simply the first term on the right-hand side of equation (13.8). To convert this to a temperature gradient, let $E_{Li} = 3(N_{Li} + N_m)k_B T_{Li}$. Differentiating this with respect to time, solving for $\dot{T}_{Li}$, and plugging in the 3-body terms from (13.8)-(13.9), we get

$$\begin{aligned} \dot{T}_{Li} &= \frac{1}{3Nk_B}\left(\dot{E}_{Li} - 3(\dot{N}_{Li} + \dot{N}_m)k_B T_{Li}\right) \\ &= \left(\frac{E_b}{3k_B} + T_{Li}\right)\frac{1}{N_{Li} + N_m}\left\{L_3\left(\frac{1}{4}I_1 - qI_3\right) + L_3'(\frac{1}{2}I_2 - qI_4)\right\} \end{aligned} \tag{13.27}$$

To evaluate the above equation, we used $\left(\dot{N}_{Li}\right)_{3-body} = -2\left(\dot{N}_m\right)_{3-body}$. Note that we are still considering only processes (13.1)-(13.2), since the others do not add kinetic energy to the sample. Since Yb is mostly unaffected by this heating ($\dot{E} = 0$), we let

$$\dot{T}_{Yb} = 0 \tag{13.28}$$

The additional term proportional to T_{Li} in equation (13.27) may come as a surprise to some. The physical explanation is that when atoms bond into molecules, there are fewer particles across which to spread the thermal energy of the sample. Thus, the mean energy per particle must increase. Equivalently, one could note that formation of molecules would spontaneously decrease the entropy of the sample, unless there is a rise in temperature to compensate for this.

13.4.5 Evaporation

Each species may cool itself, in order to dump released chemical energy, through spontaneous evaporation. The rate of evaporation of a Boltzmann gas with $\eta = k_B T/U_{trap} \gg 1$ can be found in [90].

$$\left(\dot{N}\right)_{evap} = -2(\eta - 4)e^{-\eta}\gamma N \tag{13.29}$$

Here γ is the rate of effective thermalizing collisions: $\gamma = \gamma_{intra} + \xi\gamma_{inter}$. A more detailed discussion of interspecies collisions and the mass correction factor ξ is provided in the next section. The intraspecies collision rate for each species is

$$\gamma_{intra} = \sigma\sqrt{\frac{8k_BT}{\pi m}}\int n^2 d^3x \tag{13.30}$$

where σ is the cross-section of elastic collisions. For ytterbium, we can use the low-energy formula for identical Bosons.

$$\sigma_{Yb} = 8\pi a_{Yb}^2 \tag{13.31}$$

For the case of Li-Li collisions, however, in which the scattering length is comparable to the thermal de Broglie wavelength $\lambda_{TdB} = \hbar/\sqrt{2\pi m k_B T}$, the cross-section is momentum-dependent of the form $4\pi a^2/(1+k^2a^2)$, and needs to be averaged over the distribution:

$$\gamma_{Li-Li} = \int \frac{4\pi a_{Li}^2}{1+k^2a_{Li}^2}\left(\frac{\hbar k}{m}\right)\left(\int n^2 d^3x\right)\left(e^{-\beta\frac{\hbar^2k^2}{2m}}\lambda_{TdB}^3\right)d^3k \tag{13.32}$$

$$= \sigma_{mean}\sqrt{\frac{8k_BT}{\pi m}}\int n^2 d^3x \tag{13.33}$$

Although I never succeeded in evaluating a closed-form of the integral that yields the mean cross-section σ_{mean}, its apparent functional form (according to my good friend *Mathematica*) is a rather straightforward function of the dimensionless parameter $\zeta^2 = a_{Li}^2/(\pi\lambda_{TdB}^2)$:

$$\sigma_{mean} \simeq 4\pi a_{Li}^2\left(1+\zeta^{3/2}\right)^{-4/3} \tag{13.34}$$

In addition to particle loss, the evaporation also (of course) adds a term to the temperature equations. (13.27-13.28) The form of this can also be found in [90].

$$\left(\dot{T}\right)_{evap} = \frac{T}{3N}\left(\dot{N}\right)_{evap}\left(\eta - 2 - \frac{1}{\eta-4}\right) \tag{13.35}$$

The number and time derivatives thus derived may then be appended as additional terms in the thermal equations of motion.

13.4.6 Interspecies Thermalization

The simulation includes a set of terms to account for interspecies thermalization:

$$\left(\dot{T}\right)_{therm} = \frac{\Delta T}{N}\left(\frac{\xi}{2.7}\gamma_{LiYb} + \frac{\xi_m}{2.7}\gamma_{Li_2Yb}\right) \tag{13.36}$$

where ΔT is the temperature of the evaluated species with respect to the other ($\Delta T = T_{other} - T_{this}$). The number 2.7 is the mean number of collisions required for thermalization

of equal-mass partners. $\xi(\xi_m)$ is a correction factor for collisions between Yb atoms and Li atoms(molecules), of the form $4m_{Li(Li_2)}m_{Yb}/(m_{Li(Li_2)}+m_{Yb})^2 = 0.13(0.24)$, that accounts for the greater number of collisions required to thermalize unequal mass partners. Finally, γ_{LiYb} is the (global) interspecies scattering rate.

$$\gamma_{LiYb} = (4\pi a_{LiYb}^2)\sqrt{\frac{8k_B}{\pi}\left(\frac{T_{Li}}{m_{Li}}+\frac{T_{Yb}}{m_{Yb}}\right)}\int n_{Li}n_{Yb}d^3x \tag{13.37}$$

$$\gamma_{Li_2Yb} = (4\pi a_{Li_2Yb}^2)\sqrt{\frac{8k_B}{\pi}\left(\frac{T_{Li}}{2m_{Li}}+\frac{T_{Yb}}{m_{Yb}}\right)}\int n_m n_{Yb}d^3x \tag{13.38}$$

The second density integral is just the previously calculated I_4. By analogy, we can write the first density integral as

$$\int n_{Li}n_{Yb}d^3x = \frac{N_{Li}N_{Yb}}{(2\pi)^{3/2}}\frac{1}{(R_{Li}^2+R_{Yb}^3)^{3/2}} \tag{13.39}$$

Although the Li-Yb cross-section a_{LiYb} has been measured in our lab, the atom-molecule cross-section a_{Li_2Yb} is unknown. For the simulation, I boldly assumed that for very large, weakly bound molecules, the constituent atoms would scatter independently, and thus $a_{Li_2Yb} = \sqrt{2}a_{LiYb}$. Since this effect was miniscule in our experiment, it was impossible to estimate the accuracy of this assumption, but, in corollary, any discrepancy from reality would have had a very small impact on the outcome of the simulation.

13.4.7 3-Body Direct Losses

In addition to processes (13.1-13.4) there are two others that may affect our results:

$$\mathrm{Li} + \mathrm{Li} + \mathrm{Yb} \rightarrow 0 \tag{13.40}$$

$$\mathrm{Yb} + \mathrm{Yb} + \mathrm{Yb} \rightarrow 0 \tag{13.41}$$

The first of these is essensially processes 13.2 and 13.4 combined, and represents three atoms forming a deeply bound Li-dimer in a single step, without going via a Feshbach molecule. The second one represents the formation of Yb-dimers. In either process more than enough kinetic energy (typically several K) is released to eject the collision partners from the trap. In order to estimate the strength of these effects, additional population dynamics data was taken at fields above the Feshbach resonance, where the scattering length has equal magnitude, but no bound Feshbach state exists. The results from this measurement were

then plugged into the molecule simulation. Except at fields very close to resonance, where the lifetimes were several seconds long, the effect of these processes was found to be miniscule.

13.4.8 Anti-evaporation

So far we have assumed that processes leading to deeply bound molecules simply cause the constituents to vanish from the trap. However, as described in [109], these losses impose an effective heating, by virtue of happening selectively to atoms near the trap minimum, where the density is greatest. This effective heating rate can be computed by working out the mean potential energy of the participating collision partners. For process 13.40, the mean energy lost by each Li atom is

$$\langle U \rangle = \int \frac{1}{2} m_{Li} \bar{\omega}_{Li}^2 x^2 \times \frac{1}{A} \exp\left\{ -\frac{1}{2} \left(\frac{1}{R_{Li}^2} + \frac{1}{R_{Li}^2} + \frac{1}{R_{Yb}^2} \right) x^2 \right\} d^3x \tag{13.42}$$

where A is the normalization constant

$$A = \int \exp\left\{ -\frac{1}{2} \left(\frac{1}{R_{Li}^2} + \frac{1}{R_{Li}^2} + \frac{1}{R_{Yb}^2} \right) x^2 \right\} d^3x = \left(\frac{2\pi R_{Li}^2 R_{Yb}^2}{R_{Li}^2 + 2R_{Yb}^2} \right)^{3/2} \tag{13.43}$$

which yields

$$\langle U \rangle = \frac{3}{4} k_B T_{Li} \left(\frac{2R_{Yb}^2}{R_{Li}^2 + 2R_{Yb}^2} \right) \tag{13.44}$$

Since the mean potential energy for all Li atoms in the trap is $\frac{3}{2} k_B T_{Li}$, this leaves an energy surplus for each lost Li atom, which is deposited to the remaining atoms:

$$E_{dep} = \frac{3}{2} k_B T_{Li} \left(\frac{R_{Li}^2 + R_{Yb}^2}{R_{Li}^2 + 2R_{Yb}^2} \right) \tag{13.45}$$

Note that this effect is maximized in the limit $R_{Li}^2 \gg R_{Yb}^2$. In that limit, Yb atoms are only available to react with Li at the center of the trap, and all atoms lost this way thus have zero potential energy. In the opposite limit, $R_{Li}^2 \ll R_{Yb}^2$, Yb is equally abundant throughout the Li cloud.

Using similar derivations, we can complete table 13.1, which provides the cloud size dependent multiplicative factor for each relevant loss process.

In addition to the location heating, one can imagine the constituents of these reactions depositing some energy through collisions as they leave the trap. Modeling such an effect would be beyond the scope of this analysis. However, we can assume that the collisional energy transfer scales linearly with the number of remaining atoms in the trap (i.e. the mean number of atoms that an ejected particle must pass on the way out), and that s-wave

Process	Li heating $\left(E_{dep}/\frac{3}{2}k_B T_{Li}\right)$	Yb heating $\left(E_{dep}/\frac{3}{2}k_B T_{Yb}\right)$
L_2 : $\mathrm{Li} + \mathrm{Li}_2$	1	N/A
L_2' : $\mathrm{Yb} + \mathrm{Li}_2$	$\left(\frac{R_{Li}^2}{R_{Li}^2+2R_{Yb}^2}\right)$	$\left(\frac{2R_{Yb}^2}{R_{Li}^2+2R_{Yb}^2}\right)$
L_{3D}' : $\mathrm{Li} + \mathrm{Li} + \mathrm{Yb}$	$2 \times \left(\frac{R_{Li}^2+R_{Yb}^2}{R_{Li}^2+2R_{Yb}^2}\right)$	$\left(\frac{2R_{Yb}^2}{R_{Li}^2+2R_{Yb}^2}\right)$
L_{Yb} : $\mathrm{Yb} + \mathrm{Yb} + \mathrm{Yb}$	N/A	2

Table 13.1: Heating due to potential-selective losses. Numbers are for a single reaction.

resonant behavior can be ignored (since the escaping particles have momenta far above the p-wave threshold.) Thus, we simply impose an additional heating term, proportional to number of escaping particles, and independent of remaining particle number. The net effect of both the anti-evaporation and collisions is

$$\begin{aligned}\left(\dot{T}_{Li}\right)_{inel} &= \frac{1}{2}\frac{T_{Li}}{N_{Li}+N_m}\left\{k_2 + \left(\frac{1}{1+2r^2}\right)k_2' + 2\left(\frac{1+r^2}{1+2r^2}\right)k_{3D}'\right\} \\ &\quad + \left(\dot{T}\right)_{coll}(2k_2 + 2k_2' + 2k_{3D}' + 2k_{Yb}) \qquad (13.46)\\ \left(\dot{T}_{Yb}\right)_{inel} &= \frac{1}{2}\frac{T_{Yb}}{N_{Yb}}\left\{\left(\frac{2r^2}{1+2r^2}\right)k_2' + \left(\frac{2r^2}{1+2r^2}\right)k_{3D}' + 2k_{Yb}\right\} \\ &\quad + \left(\dot{T}\right)_{coll}(2k_2 + 2k_2' + 2k_{3D}' + 2k_{Yb}) \qquad (13.47)\end{aligned}$$

where the k-factors are products of the corresponding L- and I-factors from section 13.4.2, and $r^2 = R_{Yb}^2/R_{Li}^2$. The deposition energy $\left(\dot{T}\right)_{coll}$ was treated as an empirical constant that can be roughly estimated to fit the data, but was not varied dynamically by the least-squares finder.

13.4.9 Background Lifetime

Even at very low densities, where chemical processes are suppressed, the samples have a finite, species-independent lifetime, τ, that can be measured and accounted for through an additional decay term

$$\left(\dot{N}\right)_{BG} = -N/\tau \qquad (13.48)$$

in each of equations (13.8-13.10).

13.5 Numerical techniques

In order to integrate the differential equations (13.8)-(13.10) at a wide range of conditions, and to extract quantitative estimates for the rate coefficients, a set of simple numerical techniques were used. Each of the following sections discusses a particular routine, which was designed to call upon a subroutine that incorporates all the physical effects discussed in section 13.4.

13.5.1 The adaptive forward-Euler scheme

In the above sections, we have described the considerations needed to estimate the equations of motion of the system, i.e. we have derived a functional form for

$$\left(\dot{N}, \dot{T}\right) = f\left(N, T, ...\right) \tag{13.49}$$

However, we have yet to determine a scheme to numerically integrate this differential equation. One such scheme is the forward-Euler method,

$$y_{n+1} = y_n + \Delta t \frac{\partial y}{\partial t} \tag{13.50}$$

where the time derivative of y is some known function of y, t. This method is straightforward, and requires minimal computing resources, but has the disadvantage of potentially suffering from unstable (divergent) behavior.

Dynamical systems in which one or more parameters are subject to dynamics much faster than the overall time scale of investigation are referred to as "stiff" systems. In solving such systems numerically, great care has to be taken to ensure a sufficiently small iteration size Δt to avoid diverging solutions.

Multi-step (e.g. Adams-Bashforth) or multi-stage (Runge-Kutta) methods may provide substantial improvements in computational accuracy, thus reducing the number of steps required for a stable solution. However, additional complications arise when the stiffness of the system varies over several orders of magnitude over the course of a single simulation. If the step size is sufficiently small to accommodate the stiffest regions of the simulation, computation will be needlessly slow in more relaxed areas. In such cases it is desirable to estimate the local truncation error (LTE) of the numerical scheme so that the iteration density can be varied "on the fly" as need dictates.

The molecule simulation proved to be just such a system. In the beginning of each experimental run at 710G there is a very rapid increase in molecule number, on time scales of $\sim$ 10ms. Evidently, the system is attracted to the (dynamically varying) equilibrium

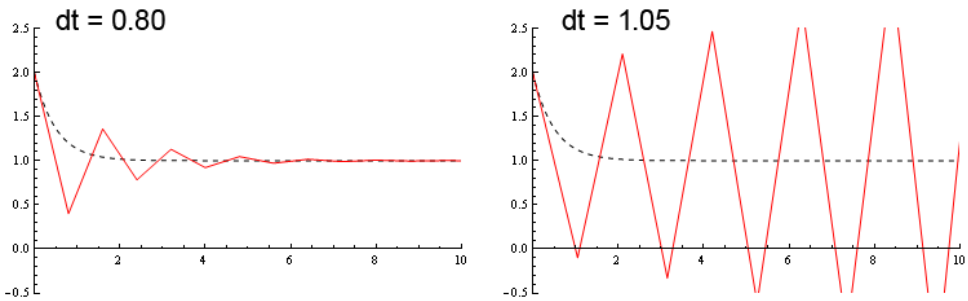

Figure 13.5: Solutions to the differential equation $y' + 2y - 2 = 0$, $y(0) = 2$, using the forward-Euler method, (red lines) shown together with the analytic solution (dashed line). If the step size of the iteration is chosen to be appropriately small the Euler method rapidly converges to the true steady-state solution. If the step size is too large, the numerical solution diverges.

fraction on this sort of time scale, and for the remainder of the simulation we need to maintain a sufficiently small Δt to prevent instabilities. A time step of 1ms was found to be sufficient to model the dynamics at this field. Matters were complicated, however, when extending the technique to other fields, as described in section 13.6. In particular, the L_3, L_3' and L_{3D}' coefficients all diverge close to resonance, leading to dynamics several orders of magnitude faster than at 710G. To accommodate such a range of systems, while allowing for "batch runs" of simulations, an adaptive numerical scheme was required.

The straightforward solution employed to deal with the above problem involves running the iteration two steps at a time, and estimating the LTE associated with the discretization for each pair of iterations. Essentially, we measure the significance of having simulated this region in two steps instead of one, and use the difference to determine if higher iteration density is warranted.

To put this idea into proper notation, we take the LTE of a single step, using forward-Euler and starting at $t = t_0$, to be

$$\begin{aligned} LTE &= \left| \frac{1}{2} y''(\Delta t)^2 \right| \\ &= \frac{1}{2} \left| y(t_0) - 2y(t_0 + \Delta t) + y(t_0 + 2\Delta t) \right| + \mathcal{O}(\Delta t)^3 \end{aligned} \tag{13.51}$$

where $y(t)$ is the simulated output value at time t. Note that three discrete points are needed to estimate the curvature y''.

Figure 13.6 shows an alternate interpretation of the LTE, as the local discrepancy between forward-Euler with step size Δt and step size $2\Delta t$. Here $LTE \approx \frac{1}{2}\epsilon$, where the error ϵ

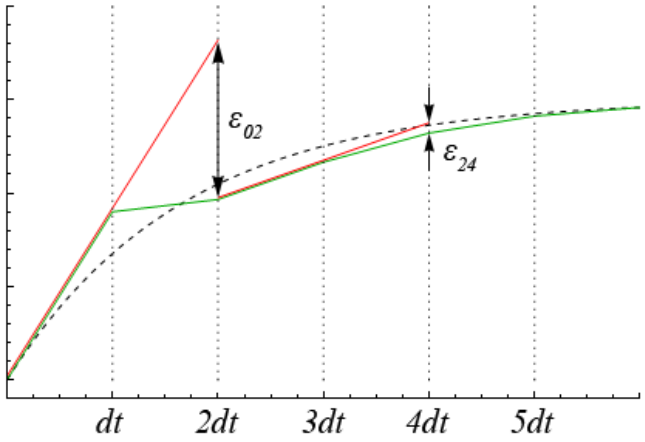

Figure 13.6: Numerical solution to a dynamical system (green line) together with the exact solution (black, dashed line). The red lines are extrapolations of the green line segments, used to estimate $\epsilon_{i(i+2)}$, the reduction in error from step size $2\Delta t$ to step size Δt. Depending on the desired tolerance, the first two steps may require further bifurcation, whereas steps 3-4 may not.

describes how much you "gain" from halving the step size.

If it is found that the LTE is greater than some user-defined tolerance on a region $[t_0, t_0 + 2\Delta t]$, the simulation doubles the iteration density, in this region only, and re-evaluates all time steps in the region. If either of the subdivisions still returns a higher-than-tolerance LTE, the bifurcation is repeated as necessary, until all steps are within tolerance, or until some storage limit is reached. The additional memory required for the additional iterations may be borrowed from unused, future time steps. The algorithm used for the molecule simulation may therefore produce errors very close to the end of the simulation, where sufficient unused data points may not be available. This trivial problem was circumvented by letting the simulation go slightly further than required to collect the 500ms data for the field dependence simulation.

Note that this algorithm does not guarantee that the simulation is stable everywhere. In a stiff system near equilibrium, the simulation may slowly begin to diverge until the instability exceeds the specified tolerance, at which point the algorithm temporarily decreases the step size and pushes the system back to equilibrium. In such cases it is common to see a "frayed" plot, with discrete, periodic outliers.

13.5.2 Least-Squares Fitting

In order to estimate the true value of the simulation input parameters, a least-squares fitting routine needed to be devised.

Assume that a measured observable of our physical system (e.g. molecule number, temperature...) follows some dynamical path f, which depends on a set of k initial, unknown physical parameters $\vec{a}$:

$$f \,:\, t \rightarrow f_{\vec{a}}(t) \tag{13.52}$$

In the molecule simulation, we considered $k = 9$ input parameters, in no particular order:

$$\vec{a} = (N_{Li},\, N_m,\, N_{Yb},\, T_{Li},\, T_{Yb},\, L_3,\, L_3',\, L_2,\, L_2') \tag{13.53}$$

where the numbers and temperatures represent the initial values at $t = 0$.

For a given data point, $\{t_i, y_i\}$ with error bars σ_i, the *a priori* probability of that point falling where it did is

$$P_i \propto e^{-\frac{(y_i - f_{\vec{a}}(t_i))^2}{2\sigma_i{}^2}} \tag{13.54}$$

If the errors are purely statistical, the corresponding probability for the entire set is thus

$$\begin{aligned} P_1 P_2 \ldots P_N &= \exp\left(-\frac{1}{2}\sum_{i=1}^{N}\frac{(y_i - f_{\vec{a}}(t_i))^2}{\sigma_i{}^2}\right) \\ &\equiv \exp\left(-\frac{1}{2}\chi^2(\vec{a})\right) \end{aligned} \tag{13.55}$$

The most likely set of physical parameters $\vec{a}$ are those that minimize the chi-square parameter $\chi^2(\vec{a})$: this is the set of parameters that yield the highest probability that we would measure what we did.

To find the minimum of χ^2, a decent-looking fit was found manually, by varying parameters by hand and monitoring the output channels, $N_{Li}(t)$, $N_m(t)$, $N_{Yb}(t)$, $T_{Li}(t)$, $T_{Yb}(t)$ plotted alongside the experimental data. The computer, too, was set to monitor all the output channels, and group their individual variances into a global χ^2. Once a reasonable fit was found, both by eye and through the χ^2, the computer took over, refining the fit using a basic gradient search.

The gradient search involves varying $\vec{a}$ by some small amount $\epsilon_i \sim \frac{1}{100}a_i$ in the i-th component, and recalculating χ^2. After doing this for each component of $\vec{a}$, the direction of the search is determined by the gradient

$$\vec{S} = -\vec{\nabla}_{\vec{a}}\chi^2 \simeq \sum_{i=1}^{k}\frac{\chi^2(\vec{a}) - \chi^2(\vec{a} + \epsilon_i\hat{i})}{\epsilon_i} \tag{13.56}$$

The search is then iterated with

$$\vec{a} \to \vec{a}\left(1 + \delta \frac{\vec{S}}{\left|\vec{S}\right|}\right) \tag{13.57}$$

The size of δ determines the speed of the search, but increasing δ also compromises the accuracy of the search, once an approximate local minimum is found. As a compromise, a "slow-down" function is built into the search algorithm: each time a step returns a greater χ^2 than the previous step, δ is halved, and the search is continued on this more refined scale.

To check for situations where the system gets stuck in a non-global minimum, the gradient search was run many times, starting from a variety of initial conditions. In the end, the search that returned the lowest χ^2 was assumed to have reached the global minimum, and these output values of $\vec{a}$ were chosen for publication.

13.5.3 Assigning Errors

The error bars associated with $\vec{a}$ depend on the local landscape of $\chi^2(\vec{a})$. In our chemical dynamics problem, where there are several processes that yield similar effects, we expect significant covariance of errors. It was therefore necessary to compute the full covariance matrix in order to estimate the true error bars.

In the spirit of equation (13.55), we take the error associated with of $\vec{a}$ to be the amount by which the input parameters must be changed (from their optimized values $\vec{a}_{best}$) to increase χ^2 by 1. This is the point at which the probability of getting the measured data has dropped off by $e^{-1/2}$. To find this value, we consider the second-order Taylor expansion

$$\chi^2(\vec{a}) \simeq \chi^2(\vec{a}_{best}) + \vec{v}^T \mathbf{M} \vec{v} \tag{13.58}$$

where $\vec{v} = \vec{a} - \vec{a}_{best}$. $\mathbf{M}$ is the $k \times k$ precision matrix – the inverse of the covariance matrix – given by

$$\mathbf{M}_{ij} = \frac{1}{2} \frac{\partial}{\partial a_i} \frac{\partial}{\partial a_j} \chi^2(\vec{a}) \tag{13.59}$$

Within the region of applicability of the second-order truncated expansion, $\mathbf{M}$ completely determines the $k+1$-dimensional landscape of χ^2 about its minimum. In particular, if one were to vary any one parameter a_i, χ^2 would increase by 1 when $a_i \to a_i + 1/\sqrt{\mathbf{M}_{ii}}$. If $\mathbf{M}$ were diagonal, we could therefore conclude that

$$\sigma_{a_i} = 1/\sqrt{\mathbf{M}_{ii}} \tag{13.60}$$

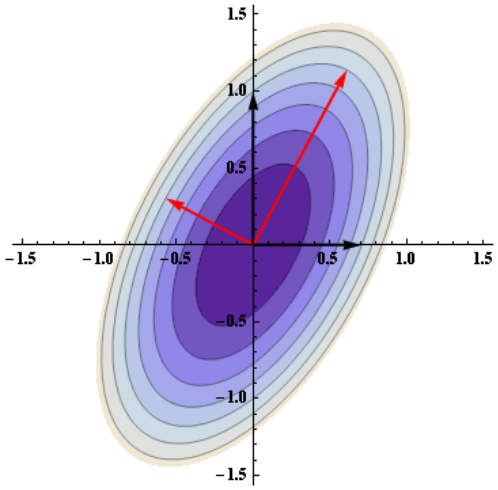

Figure 13.7: Example of landscape of χ^2 for two parameters, (x,y), with covariance matrix $\begin{pmatrix} 2 & -3/4 \\ -3/4 & 1 \end{pmatrix}$. Without having computed the off-diagonal terms, we would expect $\sigma_x = \sqrt{1/2}$, $\sigma_y = 1$. (Black arrows.) However, by moving along a principal axis (red arrows) we find $\sigma_{\eta_1} = 0.65$, $\sigma_{\eta_{21}} = 1.29$. The real uncertainties of x and y , with covariance accounted for, are therefore $\sigma_x = 0.83$, $\sigma_y = 1.18$.

However, the existence of off-diagonal terms change the landscape of χ^2. Specifically, they tend to shear the contours, as in Figure 13.7. This corresponds to the notion that two different parameters, when varied, partially compensate each other, so one can move farther from the minimum without changing χ^2 significantly. Of interest, then, are the *principal axes* of parameter space in which one can move away from the minimum without any other direction being able to reduce χ^2.

These axes are, of course, just the eigenvectors of $\mathbf{M}$. By construction, $\mathbf{M}$ is diagonal, so we are guaranteed that the eigenvectors are orthogonal. Call these (normalized) eigenvectors $\{\hat{\eta}_i\}$. From the singular value decomposition it is clear that

$$\sigma_{\eta_i} = 1/\sqrt{E_i} \tag{13.61}$$

where E_i is the i-th eigenvalue of $\mathbf{M}$ corresponding to $\hat{\eta}_i$. We can write the basis of $\vec{a}$, $\{\hat{i}\}$ in terms of $\{\hat{\eta}_i\}$

$$\hat{i} = \sum_{j=1}^{k} (\hat{\eta}_j)_i \, \hat{\eta}_j \tag{13.62}$$

and use standard propagation of errors to derive the error bars on $\vec{a}$:

$$\begin{aligned}\sigma_{a_i} &= \sqrt{\sum_{j=1}^{k} (\hat{\eta}_j)_i^2 \, \sigma_{\eta_j}^2} \\ &= \sqrt{\sum_{j=1}^{k} \frac{1}{E_i} (\hat{\eta}_j)_i^2}\end{aligned} \tag{13.63}$$

In practice, the real computational obstacle lies in estimating the covariance matrix. As in the previous section, we vary each parameter by a small amount $\epsilon_i = 0.01 a_i$. Doing the diagonal elements first

$$\begin{aligned}\mathbf{M}_{ii} &\simeq \frac{1}{2} \left\{ \frac{\frac{\chi^2(\vec{a}+\vec{\epsilon}_i)-\chi^2(\vec{a})}{\epsilon_i} - \frac{\chi^2(\vec{a})-\chi^2(\vec{a}-\vec{\epsilon}_i)}{\epsilon_i}}{\epsilon_i} \right\} \\ &= \frac{1}{2\epsilon_i^2} \sum_{m=0}^{1} \chi^2(\vec{a} + (-1)^m \vec{\epsilon}_i) - \chi^2(\vec{a})\end{aligned} \tag{13.64}$$

with $\vec{a}$ evaluated at $\vec{a}_{best}$. Similarly, for the off-diagonal elements

$$\begin{aligned}\mathbf{M}_{ij} &\simeq \frac{1}{2} \left\{ \frac{\frac{\chi^2(\vec{a}+\vec{\epsilon}_i+\vec{\epsilon}_j)-\chi^2(\vec{a}+\vec{\epsilon}_i-\vec{\epsilon}_j)}{2\epsilon_j} - \frac{\chi^2(\vec{a}-\vec{\epsilon}_i+\vec{\epsilon}_j)-\chi^2(\vec{a}-\vec{\epsilon}_i-\vec{\epsilon}_j)}{2\epsilon_j}}{2\epsilon_i} \right\} \\ &= \frac{1}{8\epsilon_i\epsilon_j} \sum_{m,n=0}^{1} (-1)^{m+n} \chi^2(\vec{a} + (-1)^m \vec{\epsilon}_i + (-1)^n \vec{\epsilon}_j)\end{aligned} \tag{13.65}$$

Since $\mathbf{M}$ is symmetric, we only need to compute half of the off-diagonal elements explicitly. Nonetheless, for a 9×9 matrix, the full simulation must be run (and the χ^2 computed) a total of $1 + 9 \cdot 2 + 36 \cdot 4 = 163$ times. Fortunately, this calculation needs to be done only once, after one is sure that the global minimum of χ^2 has been found.

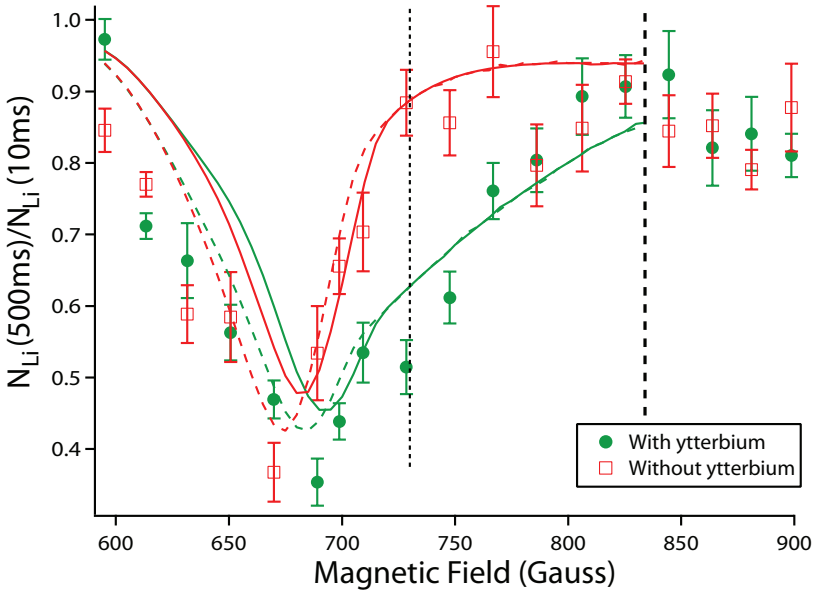

Figure 13.8: Magnetic field scan data, with theoretical model superimposed. Several stochastic parameters were used to account for artifacts arising from the magnetic field ramp to the target field. Solid lines represent a straightforward scaling model, whereas the dashed lines include a finite-temperature correction to the scattering length.

13.6 Rate Coefficient Scaling Laws

Of course, the L-coefficients that govern the dynamics of these systems depend on the scattering properties, and the bound-state wavefunction. It has been theoretically hypothesized that all of these coefficients scale nicely as powers of a_{Li}. L_3 was worked out in 2005 by Petrov *et al.* [110]; the others were computed by various grups, and can be found compiled by D'Incao *et al.* [111]

$$L_3 \propto a^6 \tag{13.66}$$
$$L_3' \propto a^4 \tag{13.67}$$
$$L_2 \propto a^{-3.33} \tag{13.68}$$
$$L_2' \propto a^{-1} \tag{13.69}$$
$$L_{3D}' \propto a^2 \tag{13.70}$$

The last of these, L_{3D}' describes the Li+Li+Yb process described in section 13.4.7. The Yb-only 3-body process in the same section is, of course, independent of the Li scattering length. Its value is estimated by Takasu *et al.* [13].

From the outset, one of the goals of our study was to experimentally investigate these

scaling laws. To this end, we revisited the initial data set, taken at a range of magnetic fields. (Figure 13.2) Using the rate coefficient values extracted at 710G and the theoretical scaling laws above, the simulation was repeated at a range of magnetic fields, and the appropriate ratio of atom numbers at 500ms and 10ms was computed for each field. The resulting theory curve was found to be in good qualitative agreement with the experimental data. To further improve the accuracy of the model, two modifications were made to the simulation input parameters. The first modification was to include a heuristic decline in initial atom number, and corresponding rise in initial temperature, across the loss feature. This corresponds to experimental observations of field-dependent initial conditions, which we attributed to chemical processes occurring in the $\sim$ 20ms during which the magnetic field was ramped toward the target value.

The second alteration was to slightly increase the value of L_3 at lower magnetic fields. This was done to account for a "saturation" effect that we believed to be present in the 710G data. The theoretical scaling laws were computed assuming a low-temperature limit in which the scattering length is energy independent. However, at temperatures where $ka \sim 1$ for typical particle momenta k the collisional cross-section is attenuated by a factor $(1 + k^2a^2)$, corresponding to an apparent attenuation $\sqrt{1 + k^2a^2}$ in the scattering length. By correcting for this behavior, using experimentally measured temperatures, we saw a small downward shift in the simulation data in the region where L_3 is the loss-limiting coefficient, which brought the simulation into excellent agreement with our data.

Although the accuracy of this study is not sufficient to actually measure the appropriate value of the scaling exponents, it gives good reason to believe that the theoretical values are of good accuracy. It has been our intention to return to this topic, and perform more involved dynamical measurements, similar to Figure 13.3, at a range of magnetic fields. In this way, we could extract the rate coefficient values for many different scattering lengths, and thus compute an experimental value of each exponent. At the time of writing, this experiment is still in the planning stages.

14 Manipulating Spatial Overlap

This section provides details of the fourth experimental publication of our lab,[112] which is provided in Appendix D.

After the publication of the double-degeneracy paper, it was deemed that it would be a good idea to write up a review article about our apparatus, for the benefit of the many other research groups who are starting up two-species experiments, and also for our own benefit

of collecting several years' worth of information about the machine. This writeup was taken to be a low priority, and thus it took over a year before the paper really got underway. In the end, its creation was facilitated by the desire to conduct a more extensive study on gravitational sag, and ways to combat the corresponding spatial overlap issues, and this goal seemed to be highly compatible with a broader discussion of our trapping apparatus.

The majority of this paper contains technical information that is also available elsewhere in this thesis,[112] and which does not require repetition. Instead, I will focus on the final section of the paper, which is centered around our studies of species-selective in-trap manipulation scheme.

14.1 Species-selective control

As had become apparent in the analysis work for each of our previous papers, gravitational effects play a major role in our experiment. Gravity modifies the effective trap depth seen by Ytterbium, affects evaporation rates, and also leads to relative displacement of lithium and ytterbium in the trap. Although some of these effects may be unwanted, external forces can also be utilized to perform new types of experiments. For instance, by applying a magnetic gradient one might use ytterbium as a spatially controlled probe of a degenerate gas or superfluid of lithium. Such gradients may also be used to achieve highly degenerate Fermi gases, by "skimming" the Fermi surface. Finally, and perhaps most importantly for our experiments, magnetic gradients may be utilized to maintain spatial overlap of lithium and ytterbium, even at low trap depths where ytterbium sag would otherwise separate the clouds entirely.

The goal of our paper was to focus on a quantitative study of in-trap displacement induced by gravity. Furthermore, using a magnetic gradient that would affect only lithium, we wished to demonstrate that the cloud separation that becomes apparent at low trap depths could be compensated by forcing a displacement of lithium equal to the gravitational sag of ytterbium.

14.2 The magic B-prime

To perfectly compensate for gravitational sag, a finely tuned magnetic gradient, or "magic B'" is required. The magic gradient turns out to be independent of the trap depth, or any details of the shape of the trapping potential. Consider first a one-dimensional gravitationally tilted potential experienced by ytterbium,

$$U_{Yb}(z) = \alpha_{Yb} I(z) - m_{Yb} g z \tag{14.1}$$

where α_{Yb} is the polarizability of ytterbium, and $I(z)$ is the intensity profile of the trapping beam.

When confined in the same trap, lithium, due to its higher polarizability, feels a stronger trapping potential, but a much weaker gravitational gradient. By adding an additional magnetic gradient, however, we achieve a trapping potential

$$U_{Li}(z) = \alpha_{Li} I(z) - m_{Li} g z - \mu B' z \tag{14.2}$$

where μ is the magnetic moment of the lithium atoms, and is a function of the bias field applied. If we choose B' such that

$$m_{Li} g z + \mu B' z = \frac{\alpha_{Li}}{\alpha_{Yb}} m_{Yb} g z \tag{14.3}$$

equation (14.2) can be rewritten

$$\begin{aligned} U_{Li}(z) &= \frac{\alpha_{Li}}{\alpha_{Yb}} \left(\alpha_{Yb} I(z) - m_{Yb} g z \right) && (14.4) \\ &= \frac{\alpha_{Li}}{\alpha_{Yb}} U_{Yb}(z) && (14.5) \end{aligned}$$

In other words, the lithium potential is identical to the ytterbium potential, up to an overall multiplicative factor α_{Li}/α_{Yb}. This necessarily implies that a local minimum of one potential is also a local minimum of the other, and our equal-displacement condition is thus fulfilled. Rewriting equation (14.3), we find the magic B-prime.

$$B'_{magic} = \frac{\alpha_{Li}}{\alpha_{Yb}} \frac{m_{Yb} g}{\mu} \left(1 + \frac{m_{Li}}{m_{Yb}} \frac{\alpha_{Yb}}{\alpha_{Li}} \right) \tag{14.6}$$

The second term in the brackets is a small correction ($\sim 1/60$) for to the effect of gravity on lithium.

The polarizability ratio $\alpha_{Li}/\alpha_{Yb} = 2.26$ may obtained from table 4.1 and equation (4.13). If we furthermore assume a sufficiently large bias field that $\mu \simeq \mu_B$, we get a magic B-prime

$$B'_{magic} = 68.2\text{G/cm} \tag{14.7}$$

14.3 Calibrations

In order to study the in-trap effects of magnetic gradients, we had to carefully calibrate both our understanding of the trap and the strength of the magnetic fields we were producing.

14.3.1 ODT power

First of all, we needed to know the trap depth as a function of the control voltage V_{contr} that we were applying. During this experiment, the control voltage operated a feedback system, which used a photodiode to monitor the ODT power. The feedback mechanism then ensured that the voltage from the photodiode, $V_{PD} = V_{contr}$.

One of the two ODT beams terminates in a high-intensity power meter, which was used to calibrate the photodiode signal, thus giving P_2/V_{contr}. By disconnecting the feedback mechanism, ramping the power to max, and using the $\lambda/2$ waveplate before the ODT beam splitter to send all the power to the power meter, we found $(P_1 + P_2)/P_2$. From this, we had $(P_1 + P_2)/V_{contr}$, which we could further convert to trap depth using the relation

$$U_0 = \alpha \frac{2(P_1 + P_2)}{\pi w_0^2} \tag{14.8}$$

However, before doing this we had to properly measure the beam waist.

14.3.2 Computing the beam waist

The beam waist was first estimated using the ytterbium sag data we had collected.

The dimensionless sag parameter $\xi = s/w_0$ may be numerically computed from the transcendental equation (8.15). Conveniently, it is a function of only one independent parameter, $u_0 = U_0/(mgw_0)$, which depends linearly on the ODT laser power. Here, w_0 is the waist of the trapping beam, and U_0 is the "nominal" trap depth in absence of gravity. (I.e. the AC stark shift at the beam center.) A numerical function of ξ vs u_0 may be computed and compared to the data. $\xi(u_0)$ is plotted in Figure 8.7b.

Figure 14.1 shows the sag data obtained by evaporating ytterbium to a variety of trap depths, set by V_{contr}. From this data we were able to extract an independent measurement of the trap depth and beam waist, using the fit function

$$\begin{aligned} y &= y_0 + s(U_0) \\ &= y_0 + w_0 \times \xi(V_{contr}/V_0) \end{aligned} \tag{14.9}$$

There are three unconstrained parameters here: y_0, V_0, and w_0. The parameter y_0 is the asymptotic position of the atoms at very high trap depths, whereas V_0 is the voltage that yields $u_0 = 1$.

Due to the definition of ξ, the waist may be extracted directly from one of the fit parameters. However, when this was attempted, it was found that the error bars returned by the

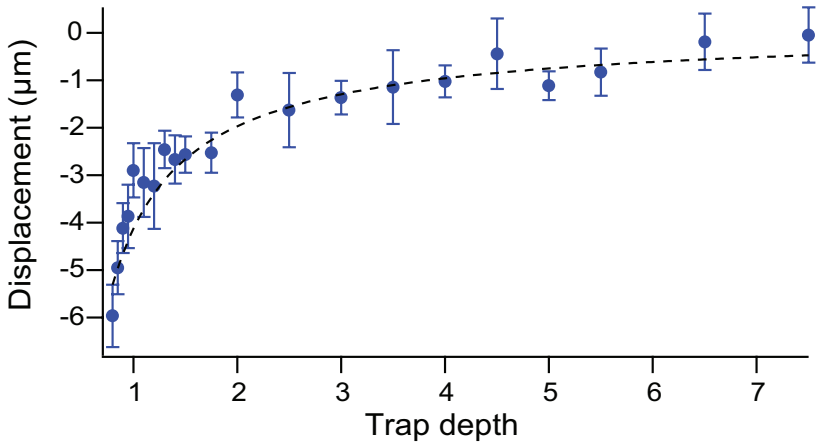

Figure 14.1: Ytterbium sag data for a range of trap depths. The x-axis is the analog control voltage V_{contr}, which is proportional to the trap depth. The dashed line is a best-fit of the model function $y(V_{contr}) = y_0 + w_0 \times \xi(V_{contr}/V_0)$, with V_0 constrained by equation (14.12).

fit were huge! The problem here is that over most of the data range we find $\xi(u_0) \simeq 1/(4u_0)$. On this region the fit function is overdetermined, with w_0 and V_0 exhibiting very strong covariance.

The solution to this problem was to somehow constrain these two parameters to one another. This could be done by plugging the definition of u_0 into that of V_0.

$$V_0 = mgw_0 \frac{V_{contr}}{U_0} \tag{14.10}$$

In the above equation, the partial derivative has been replaced with a simple fraction, as the feedback system ensured that nominal trap depth was proportional to the control voltage. Using the definition of U_0 from section 8.1,

$$U_0 = \alpha_{Yb} \frac{2P_1}{\pi w_0^2} + \alpha_{Yb} \frac{2P_2}{\pi w_0^2} \tag{14.11}$$

(where P_1, P_2 are the powers in the first and second ODT beam) we can rewrite the above as

$$V_0 = mgw_0 V_{contr} \frac{\pi w_0^2}{2(P_1 + P_2)} \tag{14.12}$$

Using the power calibration data from the previous section, we found

$$\frac{w_0^3}{V_0} = (44\mu m)^3/V \tag{14.13}$$

Plugging this relationship into the fit function, we got rid of the covariance problem

entirely, and found $w_0 = 33.9\mu m$.

This value was significantly higher than the expected 26μm that we measured for the double-degeneracy paper. (Granted, that measurement was over a year old, but no modifications had been made to ODT alignment since then.) To control this value, a second calculation was carried out, using trap frequency measurement data. By combining equations (8.6) and (14.8), we get the relation

$$\omega_y = \frac{8\alpha_{Yb}}{m\pi}\frac{(P_1 + P_2)}{w_x w_y^3} \tag{14.14}$$

which yields $(w_x w_y^3)^{1/4} = 29.5\mu m$. Again, the number is higher than expected, but the deviation is less than in the sag measurement. It is likely that this deviation is due to imperfect crossing of the ODT beams. Subtle alignment issues like these are notoriously hard to measure or correct, and the systematic error of $\sim 10\%$ was accepted as unreasonable to improve upon.

14.3.3 Magnetic fields

Next, the strength of the magnetic gradient had to be calibrated.[12] This was done by releasing lithium atoms from the trap with a strong magnetic gradient present. After release, the atoms would accelerate at a rate

$$a = \frac{\mu B'}{m_{Li}} \tag{14.15}$$

which we could measure by imaging the atoms after various fall times. Surprisingly, we discovered a significant ambient gradient of 13G/cm, even when the MOT coils were shut off. This was attributed to a slight imperfection in the flatness of the bias coil field profile. During the measurement the bias coils were held at 528G – the value used for high-field imaging. The gradient value given in Table 6.1 was calculated based on this assumption.

In order to calibrate the acceleration measurement, the experiment was carried out once more with ytterbium, which of course accelerates at a field-independent rate of 9.8m/s^2. Finally, small discrepancies of the imaging magnification between the two species was controlled for by allowing them to thermalize in the trap for ~ 10s, and measuring their temperatures.

[12] Technically, the magic B-prime formula also depends on the bias field strength through the magnetic moment μ. However, this parameter is very close to μ_B for the range of bias fields in which we operate, so careful bias calibration was not required for this study.

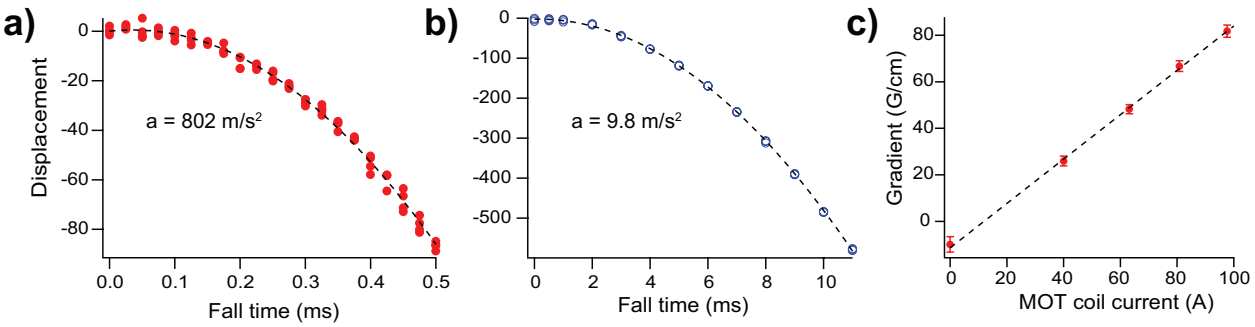

Figure 14.2: Calibration of the MOT coil magnetic gradient. a) Lithium atoms are released from the trap with a strong gradient present, and their position is fit to a quadratic function. From the magnitude of acceleration, the force $F = \mu B'$ is calculated. b) The acceleration of lithium atoms is calibrated to that of ytterbium atoms falling under gravity. c) Lithium acceleration plotted vs MOT coil current. A linear fit reveals a (negative) ambient gradient, even at zero current.

14.3.4 Axial sag

Finally, corrections had to be made to account for small deviations of the trap alignment from the horizontal plane, and of the magnetic gradient from vertical. Since the sag scales as $1/\omega_y^2$, even a small force projection along the long axis of the trap could cause axial sag, which would show up as a false signal. By imaging the atoms after a very short time of flight, we were able to estimate the angle of the long axis, as projected on the camera. By measuring both the horizontal and vertical sag (in the camera orientation) we were able to subtract off the axial sag with a simple linear transformation. This correction proved to be $\sim 10\%$.

14.4 Li-Yb separation data

Figure 14.3 shows the separation of the center of mass of the lithium and ytterbium clouds as a function of trap depth, for three different magnetic fields: -13G/cm, 35G/cm, and 64G/cm. The latter is very close to the magic B-prime; the small deviation is due to a mistake in the calibration at the time when data was taken. Nonetheless, it is clear that the separation due to gravitational sag is entirely suppressed, to within experimental uncertainties. The solid lines in the figure are based on the $\xi(u_0)$ model, and contain no free parameters.

It is evident that the numerical model over-estimates the separation somewhat at the lowest trap depths. This deviation is consistent with the notion of a slight misalignment in the ODT crossing, which leads to an artificially large beam waist being used by the model.

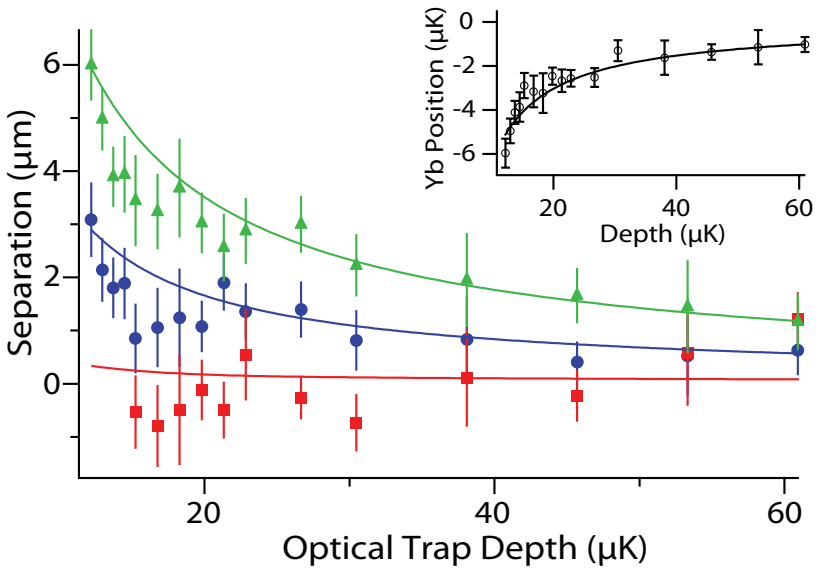

Figure 14.3: Center-of-mass separation of Li and Yb for various magnetic gradients: -13G/cm, (green triangles) 35G/cm, (blue circles) and 64G/cm (red squares). The solid lines are theoretical predictions with no free parameters, based on the Yb sag data in section 14.3.2.

15 Interactions with Metastable Ytterbium

This section provides details of the fifth experimental publication of our lab, which at the time of writing is being prepared for publication.

After completing the Feshbach molecule paper, it was clear that the machine was not yet optimized for producing large superfluids of lithium. Instead of investing time and effort making dedicated improvements to the machine for this purpose, we decided to make a move toward the other long-term goal of the lab: creating LiYb molecules. Experimental apparatuses such as ours have a way of maturing over many years, and the superfluid studies could most likely be revisited at a later time, under more favorable conditions.

Some of the experimental pathways toward molecules have been described in chapter 3. Although direct 1-photon photoassociation is possible in quantum gases with sufficiently high phase space density, the resulting distribution of rovibrational levels is very hard to transfer to the absolute ground state. A much more elegant approach is to magnetoassociate the constituent atoms into a single vibrational level, using a Feshbach resonance, and subsequently use multi-photon transfers to reach more deeply bound levels.

This, of course, poses a problem for researchers working with alkali-spin-singlet systems, in which no broad Feshbach resonances exist. (Narrow resonances of a few mG have been predicted,[88] but not yet observed, and would be highly impractical to use for magnetoas-

sociation.) One way of overcoming this problem is to excite the spin-singlet component into a metastable, spin-triplet state (^3P_J). Two electronic spin-doublets, $^2\Sigma$-$^4\Sigma$ and $^2\Pi$-$^4\Pi$, then appear in the heteronuclear system, which could be utilized to form interspecies magnetic Feshbach resonances. Anisotropic-interaction-induced resonances have already been demonstrated in mixtures involving metastable atoms.[113, 93]

Fortunately for us, Ytterbium has two accessible metastable states, which have been studied extensively.[95, 114, 115, 116] Of these, we chose the $^3P_2$ state for our experiment, and developed a set of laser systems, as described in chapter 9, for production and interrogation of these states.

Our first paper on Yb*, which is awaiting publication at the time of writing, describes some of our early studies of this system, including optical trapping of Yb* at 1064nm, and the interactions of Yb* with itself and lithium.

15.1 Measurement of AC stark shifts

As discussed in section 4.6.2, the Zeeman sublevels of Yb* have very different polarizabilities, due to the varying availability of Stark-coupled states. Figure 4.6 shows theoretical estimates of the AC stark shifts of each of the sublevels, provided by our theory collaborator, Svetlana Kotochigova. It is our hope that our measurements can be used to test and fine-tune these predictions.

The stark shift of our trap was measured in two ways. The first of these was through accurate measurements of trap frequencies of each of the magnetic states. The trap frequencies are given by equation (8.6), where $U_0 = \alpha I_{max}$, and the waists w_x, w_y and peak intensity I_{max} are independent of the state interrogated. Thus, there exists a simple scaling law $\omega_{Yb^*}/\omega_{Yb} = \sqrt{U_{Yb^*}/U_{Yb}}$, and by comparing the measured frequencies for each substate of Yb* to that for ground state ytterbium, the absolute polarizabilities could be backed out from the known value for ground state ytterbium.

Figure 15.1a shows the data from the trap frequency measurement, performed by direct observation of in-trap breathing oscillations. The measurement was performed for the $m_J = 0, -1, -2$ substates, and also for ground state ytterbium. The $m_J = 0, -2$ substates were prepared from a pure sample of $m_J = -1$, using RF transfer. As anticipated from the theoretical calculations, the breathing frequency of $m_J = -1$ was close to that of the ground state, whereas that for $m_J = -2$ was significantly smaller. Parametric heating measurements were also performed. These yielded consistent numbers, but with lower accuracy and precision.

The second method used was to measure the RF transfer resonance at various trap depths,

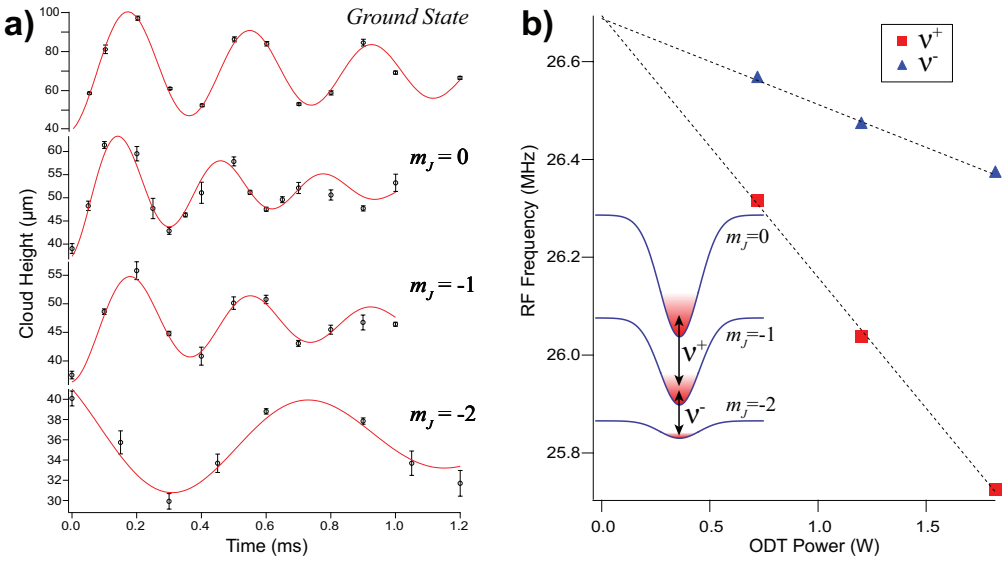

Figure 15.1: Measurement of Yb* polarizability. a) Radial breathing mode oscillations of Yb* in a single-beam ODT. The measured frequencies are compared to the corresponding value of 2.7kHz for ground state Yb, and the trap depth ratio is thus extracted. b) Differential trap depths, measured with RF spectroscopy at 12G. From the slopes, we may calculate the relative AC stark shift between neighboring substates.

at a bias field of 12G. Again starting with a pure sample of $m_J = -1$, we scanned the RF frequency near each transfer resonance, and measured the fraction of atoms transfered to a neighboring state using the Stern-Gerlach technique described in section 9.3.2. Under the influence of both a magnetic bias and a Gaussian ODT beam, the energy levels of the various states are given by

$$E_J = g_J m_J \mu_B B - \alpha_{m_J} \frac{2P}{\pi w_x w_y} \tag{15.1}$$

where P is the laser power. Rather than measuring the absolute stark shift, the RF spectroscopy technique gives us the separation of adjacent energy levels:

$$h\nu^{\pm}_{RF} = g_J \mu_B B - (\alpha_{m_J \pm 1} - \alpha_{m_J}) \frac{2P}{\pi w_x w_y} \tag{15.2}$$

As discussed in chapter 8, measurement of ODT beam waists have a significant margin of error. We rewrite the above equation in terms of the trap depth for ground state ytterbium at a given ODT power P_0.

$$U_0 = \alpha_{^1S_0} \frac{2P_0}{\pi w_x w_y} \tag{15.3}$$

This trap depth was measured by measuring the atom number and temperature of a

	Theory	Trap Frequencies	RF Spectroscopy
$m_J = 0$	1.49	1.38	
$m_J = \pm 1$	1.16	1.01	
$m_J = \pm 2$	0.18	0.20	
$\|0\rangle \rightarrow \|\pm 1\rangle$	0.33		0.22
$\|\pm 1\rangle \rightarrow \|\pm 2\rangle$	0.98		0.69

Table 15.1: Predicted and measured stark shifts of Yb* at 1064nm. Numbers are in units of the ground state polarizability $\alpha_{^1S_0}$.

sample of ytterbium in the ODT after various hold times, and fitting the data to a numerical evaporation model.[90] We thus estimated a trap depth of 100μK at a laser power of 2.8W.

$$h\nu_{RF}^{\pm} = g_J \mu_B B - \frac{(\alpha_{m_J \pm 1} - \alpha_{m_J})}{\alpha_{^1S_0}} U_0 \frac{P}{P_0} \tag{15.4}$$

By measuring the slope of the $\nu_{RF}^{\pm}$ resonances versus laser power, we thus estimated the differential polarizability of the two neighboring pairs of energy levels.

Although RF spectroscopy may yield very high accuracy under the right conditions, we consider this technique to be less accurate than the trap frequency measurement method. This is due to multiple unquantified systematics, including errors in trap depth estimates, calibration errors in the ODT power meter, and asymmetric temperature broadening.

Our measurements are summarized in table 15.1, along with the theoretical estimates. We find that our RF spectroscopy measurements differ significantly from the theoretical estimates, whereas the trap frequency measurements are consistent with theory to within $\sim 15\%$, whereas our statistical uncertainty is $\lesssim 1\%$. Additional systematic uncertainties of several percent may arise from finite-temperature effects, in which more energetic atoms sample anharmonic regions of the trap.

15.2 Measurement of Yb* inelastics

The second quantitative component to the Yb* paper involved a measurement of the inelastic interaction strenghts involving Yb*. Although this metastable state has a radiative lifetime of several seconds, decay to lower-lying electronic states may also be stimulated through collisions with other atoms.[95] In such events, some or all of the binding energy is likely to be released as kinetic energy, which ejects the collision partners from the trap.

To measure the inelastic coefficients, we performed a series of measurements of the in-trap dynamics of Yb*. The measurements were performed with pure samples of $m_J = -1$ at two different magnetic fields, 11G and 94G, and were repeated with and without lithium present.

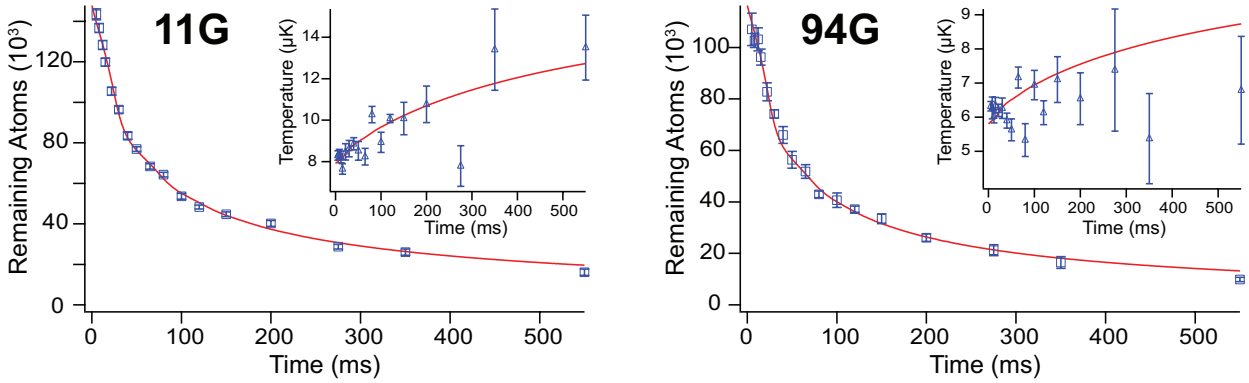

Figure 15.2: Population dynamics of Yb* in the $m_J = -1$ state. Measurements are performed at two magnetic fields. Insets show the temperature evolution, and solid lines are best-fits to a theoretical model.

The analysis for this component bore many resemblances to that for the Feshbach molecule paper, which also revolved around studying population dynamics in the presence of various inelastic channels. The chief difference here was that there was no molecule component or chemical equilibrium to worry about, (i.e. no q-factor that required careful analysis) and the experiment was performed at very high $\eta = U_0/k_BT$, where evaporation is negligible. For this reason, the analysis was done using the same software and procedures as the molecule analysis, with the appropriate modifications made to incorporate only the effects of interest.

15.2.1 Dynamics in a pure Yb* sample

With Ytterbium alone, we found decay lifetimes of $\approx$ 100ms for our densities and temperatures. As shown in Figure 15.2, the numerical model returned quantitatively good fits to the data, and we were able to back out inelastic coefficients of $(1.18 \pm 0.02) \times 10^{-11}\text{cm}^3/\text{s}$ at 11G, and $(1.09 \pm 0.03) \times 10^{-11}\text{cm}^3/\text{s}$ at 94G. Although these numbers are similar, there is no reason to expect them to be identical, since the Yb* system contains coupled channels that lead to magnetic field-dependent scattering behavior.

From the simulation we also estimated an upper-bound on the elastic cross-section of Yb* collisions, $\sigma_{Yb^*} \leq 8\pi(50a_0)^2$. If the scattering length were larger, the temperature would be significantly lowered by evaporation effects.

15.2.2 Dynamics in a mixture with Li

With the incorporation of lithium, purified to its hyperfine ground state, we noticed some very interesting effects. The first of these was a greatly reduced in-trap lifetime of ytterbium.

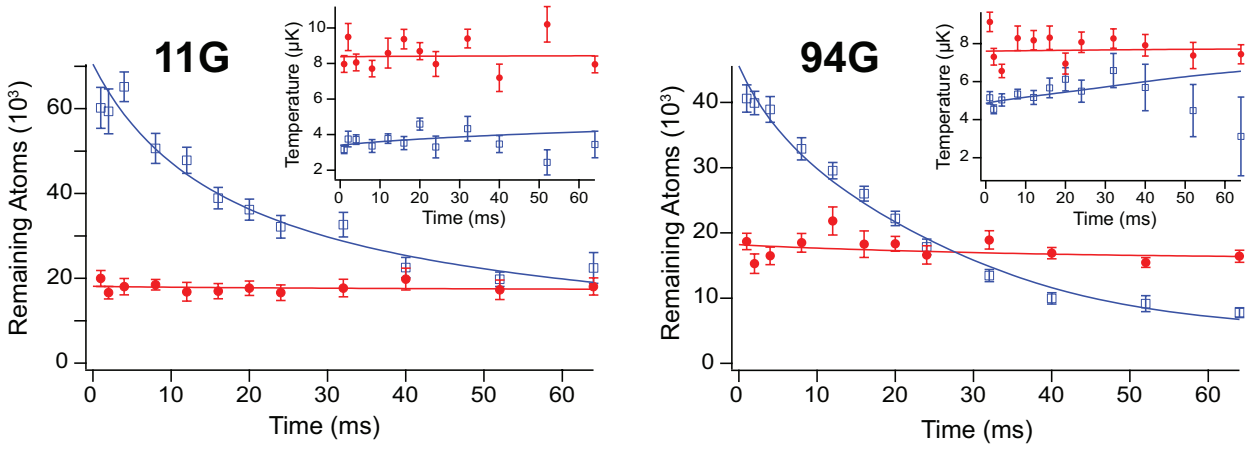

Figure 15.3: Population dynamics of simultaneously trapped Yb* $m_J = -1$ and Li in its absolute ground state. Insets show the temperature evolution, and solid lines are best-fits to a theoretical model.

Comparing the horizontal axis on Figures 15.2 and 15.3 reveals a lifetime reduction by almost an order of magnitude. This is partly due to the lower temperature of ytterbium in these data sets, (which owes to improved transfer laser stability during this data run) but perhaps also due to the presence of lithium. The lower initial atom numbers are partly due to optically induced interspecies inelastics during transfer, which we observed but did not attempt to study systematically.

When the Yb*-Yb* inelastic coefficients were constrained to their values from the Yb* only data, the numerical model yielded qualitatively inaccurate fits, suggesting that lithium was introducing some sort of loss mechanism in the system. However, the mixture data also exhibited a remarkable stability of lithium. Indeed, as can be seen in Figure 15.3, the lithium loss was almost undetectably small on the time scale of the Yb* lifetime. This was confusing to us, not least because it implied that interspecies inelastics could not account for the additional loss of Yb*: if the elevated Yb* decay rates were due to inelastic collisions with lithium, one would expect a reduction of the lithium number equal to the "surplus" Yb* losses.

Another possible explanation for the discrepancy is that the inelastic strength is a function of temperature, beyond the overlap density dependence $n_{LiYb^*} \propto T^{-3/2}$, which was accounted for by the simulation.

There were, furthermore, other strange features of these data sets. For one, the enhancement in Yb 2-body inelastics was nearly five times as great in the 94G data as at 11G, suggesting that the unknown loss mechanism was much stronger at this field. On the other hand, the axial breathing of the Yb* cloud, which at 94G was similar to the single-species data, was completely missing at 11G, suggesting that some other effect was somehow present

there to damp out the breathing oscillations. The two data sets were collected back-to-back, so there was no reason to believe that the experimental conditions had changed significantly between them. The collective effort of everyone working on the experiment did not suffice to think of a physical mechanism that could account for these effects, and the best we could do was to run the simulation with only those physical effects that we understood, and record the apparent Yb*-Yb* inelastic strength. The values obtained were $(2.5 \pm 0.2) \times 10^{-11}\text{cm}^3/\text{s}$ and $(7.8 \pm 0.5) \times 10^{-11}\text{cm}^3/\text{s}$ for 11G and 94G, respectively, whereas the Li-Yb* inelastic coefficients were less than $1 \times 10^{-11}\text{cm}^3/\text{s}$, with similar error bars. In the 11G data the coefficient was consistent with zero.

15.2.3 Axial breathing modes

Although the numerical model for this paper was overall a lot simpler than that for the molecule paper, there was one new effect that we had to take into account. The experimental procedure (outlined in section 9.3) called for a ramp-up of the single-beam optical trap after transfer to the $^3P_2$ state. This was done to mitigate effects of evaporation during the measurement, which are very challenging to model at low values of η. However, in order to avoid large atom losses during the ramp, it had to be performed very rapidly, in $\sim$ 1ms. For the radial oscillation modes, this was within the adiabatic condition $\partial(1/\omega)/\partial t \ll 1$ for the radial modes, for which $1/\omega \sim 0.2$ms, but was highly non-adiabatic for the axial mode, which exhibited a breathing period of 50ms. This, paired with the recoil energy deposited by the counterpropagating transfer beams, led to significant breathing oscillations. These oscillations could be readily observed by monitoring the apparent width of the atomic cloud on the absorption images. Similar effects have been observed in molecule formation experiments.[117, 118]

From the absorption images, the axial extent of the cloud was measured for each hold time. For this estimate, both the angle of the imaging axis to the ODT axis and the time-of-flight expansion of the cloud had to be taken into account. This $1/e$ width was then compared to the equilibrium size, $\sqrt{2k_BT/m\omega_z^2}$, where the axial trap frequency ω_z had previously been measured for ground-state ytterbium, to extract a dimensionless correction factor to the mean density of the atoms.

The breathing oscillations were found to be strongly damped, and were undetectable beyond 100ms, which corresponds to 2 full oscillations. Of interest to us was the physical nature of this damping. The damping could be due to collisions between atoms, or due to trap anharmonicities. In the former case the energy of the breathing motion is distributed across all 6 degrees of freedom of the trap, and the temperatures measured from radial time-of-flight expansion would yield good estimates of the axial width. In the latter case the

breathing energy is contained in the two axial degrees of freedom, resulting in an apparent axial tempertaure that is higher than the radial one. The energy in the axial mode and a given radial mode are then

$$E_{ax,f} = \frac{\langle p_i^2 \rangle}{2m} + \frac{1}{2} m\omega_f^2 \langle x_i^2 \rangle = \frac{1}{2}\left(1 + \frac{\omega_f^2}{\omega_i^2}\right) E_{ax,i} \tag{15.5}$$

$$E_{rad,f} = \frac{\omega_f}{\omega_i} E_{rad,i} \tag{15.6}$$

Here, the subscripts $i(f)$ refer to the initial(final) state of the ramp. It is assumed that the phase space distribution does not change appreciably during the ramp. The form of $E_{rad,f}$ follows from the adiabatic therorem. Using the above equations, we may derive an effective axial temperature

$$T_{ax} = \frac{1 + r^2}{2r} T_{rad} \tag{15.7}$$

where $r = \omega_f/\omega_i$. In our experiment, $r = 2.3$, which leads to an axial width that is greater than predicted by a factor of 1.2. In the other case, where damping is dominated by elastic collisions, we would expect a factor of 1.

In addition to the recompression effect, there is additional breathing energy due to the energy deposited, primarily in the axial mode, by the transfer beams. The figure of 1.2 is therefore a lower bound on the expected temperature discrepancy. In fact, we found that the axial width, after breathing had subsided, was 1.6 times greater than expected. Further data sets with ground-state ytterbium, which experiences rapid collisional damping under similar conditions, yielded an apparent elongation of 1.2, suggesting that the large axial widths of Yb* could be partially, but not entirely, due to imaging artifacts. The figure of 1.6, which was consistent across all four data sets, strongly suggested that the damping was due to trap anharmonicities. For this reason, a correction factor was applied to the numerical model to reduce the mean density by an appropriate amount.

Part IV

Conclusions and Outlook

This thesis reported on the construction of an experimental apparatus for trapping and studying ultracold quantum gases of 6-lithium and various isotopes of ytterbium. Aside from the technical details of the experiment, initial studies of interactions between the two species were discussed. These early scientific results have been presented in three main papers (of which one is yet unpublished at the time of writing), which explored interspecies interactions under three distinctive sets of conditions.[97, 105] In addition, two papers were published for the purpose of discussing technical features and capabilities of our experiment.[103, 112]

The experimental apparatus was modeled after similar machines at MIT and Berkeley, and its initial construction was completed over the course of three years, after which we were able to co-trap the two species and cool them toward degeneracy, using a sympathetic cooling scheme that utilizes the different electronic structure of the two species. Within the next year, we were able to achieve simultaneous quantum degeneracy in both the Bose-Fermi ^{174}Yb-^{6}Li and the Fermi-Fermi ^{173}Yb-^{6}Li systems, and had begun to explore the ^{6}Li Feshbach resonance. More recently, we have moved toward developing tools for studying ytterbium in the metastable $(6s6p)^3P_2$ state (Yb*).

Currently, our group is working toward synthesizing paramagnetic, polar LiYb molecules. The early studies of Yb* were the first step in this direction, as we believe that interspecies Feshbach resonances in the Li-Yb* system are a viable tool for bonding the constituent atoms, by magnetoassociation, potentially followed by multi-photon transfers toward lower-lying electronic and/or vibrational states.

At the time of writing, three further developments are in their early stages. The first of these is a systematic search for interspecies Feshbach resonances. Early attempts at finding these scattering resonances were confounded by sub-optimal technical capabilities, and poor understanding of the field-independent inelastic processes in the system. Over the course of studying these background inelastics, we have also made significant technical improvements, and are now in excellent shape to resume the Feshbach search.

The second project is to establish one-photon photoassociation capabilities, using the ytterbium $^1S_0$-$^3P_1$ intercombination line. This will give us a second path toward LiYb molecules, and also enable PA spectroscopy for determining the vibrational structure of these molecules. Currently we have a dedicated laser for this purpose, the tuning range of which is believed to be sufficient for us to detect several vibrational levels of the excited LiYb molecule.

The third project is the implementation of a 3-D optical lattice. Such a lattice will be crucial for studies involving polar molecules, for achieving efficient photoassociation, which depends on good spatial overlap of the constituent wavefunctions, and for achieving recoil-free transfer to Yb*. We have chosen an optical wavelength close to that of our optical dipole trap, which has favorable characteristics for lithium and ytterbium (in both the ground and metastable states), and is also believed to trap the LiYb molecule. This optical lattice is already under construction and will be an important tool in our experiment, for the aforementioned reasons and many others.

Beyond these goals, it is my hope that the experiment will develop the technical capabilities to create and detect superfluidity in ^{6}Li. This would open up a whole new set of interesting experimental studies of the BEC-BCS crossover, in which ytterbium would serve as a magnetically inert, massive ballistic probe. Such an ultracold three-component mixture would also be one starting point for studies of Efimov-like physics in highly mass-mismatched systems, if interspecies scattering resonances were found to exist within the broad ^{6}Li resonance. Other interspecies resonances at lower fields would then provide opportunities for studying few-body physics across a range of coupling configurations.

The study of ultracold polar molecules is still in its infancy, but has the promise of a rich experimental and theoretical field, with important applications toward condensed-matter and high-energy physics, and quantum computation. No doubt, as this fascinating field continues to develop, its landscape will continue to change and expand.

Appendix A

Sympathetic Cooling in an Optically Trapped Mixture of Alkali and Spin-Singlet Atoms

This appendix includes the following paper [97]: V. V. Ivanov, A. Khramov, A. H. Hansen, W. H. Dowd, F. Munchow, A. O. Jamison, and S. Gupta. Sympathetic cooling in an optically trapped mixture of alkali and spinsinglet atoms. *Phys. Rev. Lett.*, 106:153201, 2011.

Sympathetic Cooling in an Optically Trapped Mixture of Alkali and Spin-Singlet Atoms

Vladyslav V. Ivanov, Alexander Khramov, Anders H. Hansen, William H. Dowd, Frank Münchow, Alan O. Jamison, and Subhadeep Gupta

Department of Physics, University of Washington, Seattle, Washington 98195, USA

(Received 26 January 2011; published 11 April 2011)

We report on the realization of a stable mixture of ultracold lithium and ytterbium atoms confined in a far-off-resonance optical dipole trap. We observe sympathetic cooling of ^{6}Li by ^{174}Yb and extract the s-wave scattering length magnitude $|a_{^6\mathrm{Li}\text{-}^{174}\mathrm{Yb}}| = (13 \pm 3)a_0$ from the rate of interspecies thermalization. Using forced evaporative cooling of ^{174}Yb, we achieve reduction of the ^{6}Li temperature to below the Fermi temperature, purely through interspecies sympathetic cooling.

DOI: 10.1103/PhysRevLett.106.153201 PACS numbers: 34.20.Cf, 34.50.Cx, 05.30.Fk, 37.10.De

Ultracold mixtures composed of different atomic species [1–6] offer unique opportunities for probing few- and many-body physics. These include studies of Efimov states with mass-mismatched collision partners [7,8], impurity probes of superfluid properties [6,9], and mass imbalanced regimes of interactions and pairing in Fermi gases [10–12]. Further, the components of the mixture can be linked through field-induced scattering resonances to produce heteronuclear molecules [13–15], which are expected to be valuable tools for the study of dipolar quantum matter, quantum information science, and tests of fundamental physics [16]. An essential requirement for all of these ultracold mixture studies is an understanding of the ground state scattering properties. Favorable collisional properties are needed for mixture production and stability, while knowledge of the underlying potentials allow identification of regimes of tunable interactions.

In this Letter, we report on successful simultaneous optical trapping and measurements of scattering properties for a mixture of alkali ^{6}Li and spin-singlet ^{174}Yb. We observe collisional stability in this mixture and determine the magnitude of the previously unknown ^{6}Li-^{174}Yb s-wave scattering length from the time scale of interspecies thermalization [3,4,17]. Furthermore, we sympathetically cool ^{6}Li to below its Fermi temperature by forced evaporative cooling of ^{174}Yb. Unlike the case for bialkali mixtures [2,3], our method of sympathetic cooling an alkali by a spin-singlet atom has the advantage of being immune to inelastic spin changing collisions.

While studies of ultracold molecule formation from two-species mixtures are dominated by alkali + alkali combinations, molecules created from alkali + spin-singlet mixtures offer the additional advantage of possessing an unpaired electron spin to form a paramagnetic ground state. This is a feature of considerable interest for several proposed applications including quantum simulations of lattice spin models [18], topological quantum computing, and sensitive measurements of the electron electric dipole moment [19]. Prior to this work a dual-species Li-Yb magneto-optical trap (MOT) was demonstrated [20], but with densities too low to observe interspecies effects. First results for alkali + spin-singlet mixtures have been reported for the Rb + Yb combination. These include photoassociation in a dual-species MOT [21], and observations of sympathetic cooling [22] and spatial separation [23] in a combined optical and magnetic trap.

In addition to the pursuit of heteronuclear paramagnetic LiYb molecules, our system forms a starting point for studies of the ^{6}Li Fermi superfluid [24] using Yb as an impurity probe. Furthermore, tunable interspecies interactions may be induced between Li and Yb through magnetic [25] or optical [26] Feshbach resonances. Together with the straightforward availability of fermionic Yb isotopes, this will allow future explorations of few-body collision physics in the highly mass-mismatched regime [7,8] and fermionic interactions and pairing in mass imbalanced mixtures [11,12].

Our dual-species experimental setup consists of ^{174}Yb and ^{6}Li MOTs which are loaded from separate atomic beams, each emerging from a single-species oven and slowed by a single-species Zeeman slower. All laser cooling and absorption imaging of ^{6}Li is performed on the $^2S_{1/2} \rightarrow {}^2P_{3/2}$ line (wavelength $\lambda = 671$ nm, linewidth $\Gamma/2\pi = 6$ MHz). For ^{174}Yb, we use the $^1S_0 \rightarrow {}^1P_1$ line ($\lambda = 399$ nm, $\Gamma/2\pi = 29$ MHz) for Zeeman slowing and absorption imaging, and the $^1S_0 \rightarrow {}^3P_1$ line ($\lambda = 556$ nm, $\Gamma/2\pi = 182$ kHz) for the MOT. The optical dipole trap (ODT) is derived from the linearly polarized output of a 1064 nm fiber laser (IPG Photonics YLR-100-1064-LP) and is operated either in single or crossed beam geometry. The trap depth is controlled by an acousto-optic modulator.

To mitigate the strong inelastic losses in simultaneous two-species MOTs and to allow for different optimum MOT magnetic field gradients [27], we employ a sequential cooling and trapping strategy [see Fig. 1(a)] in which first Yb and then Li is laser cooled and transferred to the ODT. The laser cooling sequence for each species consists of a loading phase with large intensities and detunings of the cooling beams, and a compression phase where these intensities and detunings are reduced and the MOT

 © 2011 American Physical Society

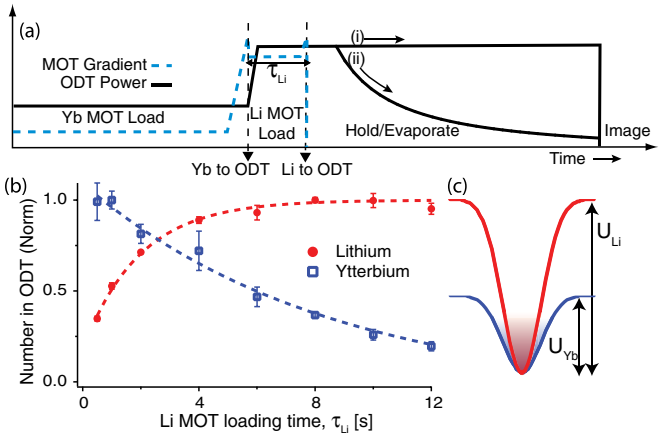

FIG. 1 (color online). Simultaneous optical trapping of ^{6}Li and ^{174}Yb. (a) shows the typical experimental sequence where the laser cooling and ODT loading are performed sequentially for the two species. In addition to the standard procedures for single-species operation, the magnetic field gradients and the initial optical trap depths are adjusted for each species to optimize number and temperature. After both species are in the ODT, either (i) the power is held constant to study interspecies thermalization, or (ii) the power is ramped down to perform forced evaporative cooling. Finally, the optical trap is switched off and the remaining atoms detected with resonant absorption imaging. As displayed in (b), varying the Li MOT loading time τ_{Li} allows us to control the initial ratio of the two species in the optical trap. The peak atom numbers correspond to $N_{\mathrm{Yb(Li)}} = 11(4) \times 10^5$, for trap depth $U_{\mathrm{Yb(Li)}} = 0.5(1.1)$ mK. The dashed lines are exponential fits. The Yb decay time is substantially shorter than the background lifetime because of a partial overlap with the ^{6}Li MOT during τ_{Li}. (c) Optical trapping potentials for Li and Yb for a given ODT power. The shading depicts the distributions at the same temperature.

gradient increased. The compressed Yb MOT contains $\gtrsim 2 \times 10^6$ atoms at a temperature of $\lesssim 30$ μK. The compressed Li MOT contains $\gtrsim 10^8$ atoms at $\lesssim 400$ μK, and is optically pumped into the lower $F = 1/2$ hyperfine state. Each species is transferred to the ODT by using magnetic bias fields to overlap the MOT with the ODT center and then switching off the laser cooling beams. During the Li laser cooling phase, Yb atoms trapped in the ODT are insensitive to the magnetic field manipulations used for the Li MOT. After all cooling beams are switched off, the ODT contains a mixture of Yb and Li atoms [see Fig. 1(b)]. While all the ^{174}Yb atoms are in the single $^1S_0$ ground state, the ^{6}Li atoms are distributed equally between the two $F = 1/2$ Zeeman ground states.

For our ODT wavelength, the relative trap depths and frequencies for the two species are $U_{\mathrm{Li}}/U_{\mathrm{Yb}} = 2.2$ and $\omega_{\mathrm{Li}}/\omega_{\mathrm{Yb}} = \sqrt{\frac{(U_{\mathrm{Li}}/m_{\mathrm{Li}})}{(U_{\mathrm{Yb}}/m_{\mathrm{Yb}})}} = 8$. The relative linear size in the harmonic regime is $x_{\mathrm{Li}}/x_{\mathrm{Yb}} = \sqrt{\frac{(T_{\mathrm{Li}}/U_{\mathrm{Li}})}{(T_{\mathrm{Yb}}/U_{\mathrm{Yb}})}} = 0.7$ for equal temperatures [see Fig. 1(c)]. The parameters are thus well suited for sympathetic cooling of lithium by ytterbium.

To monitor atom number and temperature, we quickly switch off the trap and perform resonant absorption imaging of both species for each experimental iteration. Each species is imaged onto a different part of the same CCD camera with independently adjustable ballistic expansion times. The trapping potential is characterized through measurements of trap frequencies by exciting dipole and breathing oscillations, as well as by parametric heating. The ODT is kept on all the time except during imaging.

We first describe our thermalization measurements, which allow us to determine the magnitude of the interspecies s-wave scattering length. For these measurements, we use a single beam ODT with $1/e^2$ intensity-radius (waist) of 30 μm. Yb is transferred from the MOT into an ODT of calculated depth $U_{\mathrm{Yb}} = 220$ μK (laser power 11 W), after which the depth is increased adiabatically in 0.2 s to $U_{\mathrm{Yb}} = 500$ μK (25 W) while the Li MOT is loaded (see Fig. 1). After $\simeq 0.5$ s MOT loading, Li is transferred into the ODT ($U_{\mathrm{Li}} = 1.1$ mK). We make our thermalization measurements at this point, where the measured trapping frequencies for Yb are $2\pi \times 1600$ Hz radially and $2\pi \times 13$ Hz axially. The initial number, temperature, and peak density of Yb (Li) atoms are $N_{\mathrm{Yb(Li)}} = 1.1 \times 10^6 (1.4 \times 10^5)$, $T_{\mathrm{Yb(Li)}} = 35(110)$ μK, and $n_{0,\mathrm{Yb(Li)}} = 1.1 \times 10^{13} (8.4 \times 10^{11})$ cm^{-3}. All the thermalization measurements are performed at near-zero magnetic field.

We observe the number and temperature evolution of the two atomic species either in separate single-species experiments, or together when in thermal contact with each other. The measured background single-species $1/e$ lifetimes are >30 s for both Li and Yb. The Yb temperature evolution is independent of the presence or absence of Li, equilibrating quickly and staying at 35 μK throughout the measurement. When Yb is not loaded, the two-spin state Li mixture behaves like an ideal gas in the optical trap and remains at its initial temperature of $\simeq 100$ μK without observable changes. This is due to a lack of intrastate collisions from Pauli blocking and a lack of interstate collisions from the negligible zero-field scattering cross section [28]. When both species are loaded, the hotter Li cloud equilibrates to the temperature of the Yb cloud (see Fig. 2). The lack of change in the Yb temperature is mainly due to the large number ratio $N_{\mathrm{Yb}}/N_{\mathrm{Li}}$ [29]. We also observe no change in the Li lifetime from contact with Yb, indicative of negligible inelastic interactions between the two species at these experimental parameters. In similar studies at various loading parameters, we observe additional losses in the Yb number only. We interpret this to be a result of a "sympathetic evaporation" effect [17] where during the thermalization process, Li which is confined by a deeper trap, transfers energy through elastic collisions to Yb, and subsequently ejects it from its shallower confinement [see Fig. 1(c)]. Indeed for larger fractional presence of Li, this effect becomes more pronounced and leads to a substantially reduced lifetime for the Yb cloud.

We analyze the thermalization measurements shown in Fig. 2 by assuming that the elastic interactions are purely s wave in nature. We are justified in this assumption because our measured temperatures ($\lesssim 110\ \mu$K) are much smaller than the p-wave threshold given by $\frac{2}{\sqrt{C_6}} \times (\frac{\hbar^2 l(l+1)}{6\mu})^{3/2} \simeq 2.5$ mK, where μ is the reduced mass and using the C_6 coefficient for LiYb calculated in [30]. The thermalization rate $\gamma_{\rm th}$ which characterizes the instantaneous variation of the temperature difference $\Delta T = T_{\rm Li} - T_{\rm Yb}$, can then be connected to the s-wave scattering cross section $\sigma_{\rm LiYb}$ through the relation

$$-\frac{1}{\Delta T}\frac{d(\Delta T)}{dt} = \gamma_{\rm th} = \frac{\xi}{\alpha}\bar{n}\sigma_{\rm LiYb}\bar{v}. \quad (1)$$

Here $\alpha = 2.7$ is the average number of collisions needed for thermalization for equal mass partners, $\xi = \frac{4m_{\rm Li}m_{\rm Yb}}{(m_{\rm Li}+m_{\rm Yb})^2} = 0.13$ is the correction factor for nonequal mass collisions [17], $\bar{v} = \sqrt{\frac{8k_B}{\pi}(\frac{T_{\rm Li}}{m_{\rm Li}} + \frac{T_{\rm Yb}}{m_{\rm Yb}})}$ is the mean relative velocity, $\bar{n} = (\frac{1}{N_{\rm Li}} + \frac{1}{N_{\rm Yb}})\int n_{\rm Li}n_{\rm Yb}d^3r$ is the overlap density, and n, N, and T are the density, number, and temperature of the two species. Since $\bar{v}$ and $\bar{n}$ change with the Li temperature, we use a numerical procedure to model the thermalization process. For a particular value of s-wave scattering length a, we iterate Eq. (1) with a short time step. We also include an energy dependence [31] to the s-wave cross section $\sigma_{\rm LiYb} = \frac{4\pi a^2}{[1-(1/2)k^2r_e a]^2 + k^2a^2}$, where $\hbar k$ is the relative momentum and r_e is the effective range evaluated from C_6 and a. By varying a, we obtain a best fit (see Fig. 2) and infer $|a_{^6\text{Li}\text{-}^{174}\text{Yb}}| = (13 \pm 3)a_0$. The quoted error in our measurement stems mainly from a systematic uncertainty in our trap frequencies ($\pm$ 20%), which limits our knowledge of absolute densities. Variations in $\sigma_{\rm LiYb}$ from the energy dependent terms are insignificant in comparison.

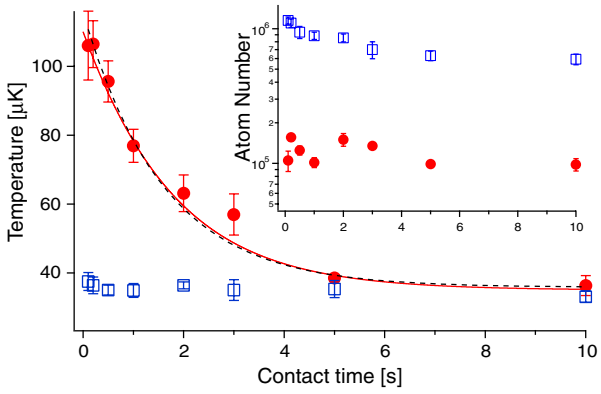

FIG. 2 (color online). Sympathetic cooling of ^{6}Li (red solid circles) by thermalization with a cold ^{174}Yb bath (blue open squares). The temperatures equilibrate with an exponential time constant of (1.7 $\pm$ 0.2) s (black dashed line). The red solid line is the result of a numerical model (see text). The inset shows the numbers of the two species which are almost an order of magnitude apart.

Since ^{174}Yb is spinless, we expect that $a_{^6\text{Li}\text{-}^{174}\text{Yb}}$ is the same for all hyperfine ground states of ^{6}Li. By using state selective imaging at magnetic fields near 500 G, we have verified that the two participating ^{6}Li $F = 1/2$ Zeeman states maintain equal population and temperature at an intermediate point during sympathetic cooling.

Since several potential applications of the Li-Yb mixture are at conditions near or below quantum degeneracy, we also assess methods of increasing the phase space density in the mixture. In single-species ^{6}Li experiments in our apparatus, up to $N_{\rm Li} = 2 \times 10^6$ can be loaded into a high power crossed beam ODT. With subsequent forced evaporation at $B \simeq 330$ G, where the interstate scattering length is $-280a_0$, we are able to enter the Fermi degenerate regime ($T_{\rm Li}/T_F \lesssim 0.6$) with total number $N_{\rm Li} = 1.5 \times 10^5$. Applying this approach to the Li-Yb mixture, however, leads to reduced initial $N_{\rm Yb}$ [see Fig. 1(b)] and shorter Yb lifetime from the sympathetic evaporation effect. We therefore restrict ourselves to keeping the initial ratio $N_{\rm Yb}/N_{\rm Li}$ large.

We now describe our measurements of sympathetic cooling of ^{6}Li in contact with ^{174}Yb which is undergoing forced evaporative cooling through a continuous lowering of the trap depth. In order to boost the collision rate, the single beam ODT for the thermalization measurement is modified to a crossed beam geometry by adding a second laser beam which intersects the first at a shallow angle of about 10°, and has the same power, orthogonal polarization, and a larger waist of 50 μm. After loading the atoms, we reduce the power in the optical trap following an approximately exponential shape. Figure 3 shows the number and temperature evolution during such an evaporation ramp at near-zero magnetic field.

We observe that Yb decays quickly with an exponential time constant of 4.3 s, while the longer decay constant of 24 s for Li is comparable with the vacuum limited lifetime. This implies that Yb loss is primarily from trap depth reduction while Li loss is primarily from background processes, as desired for efficient sympathetic cooling. During the cooling process, the Li phase space density increases by about 3 orders of magnitude as the gas is brought below the Fermi temperature, to $T_{\rm Li} = 1.2\ \mu$K with $T_{\rm Li}/T_F \simeq 0.7$. At this point $T_{\rm Yb} = 650$ nK, a factor of 4 above the critical temperature for Bose condensation. We are prevented from further sympathetic cooling by the rapidly increasing interspecies thermalization time from the lowered densities and lowered overlap from unequal gravitational sag. We are currently improving our cooling scheme by implementing more tightly focused ODT beams. Substantial improvements are also expected from the introduction of a magnetic field gradient [32] to allow manipulation of the Li trap depth and position, without affecting Yb.

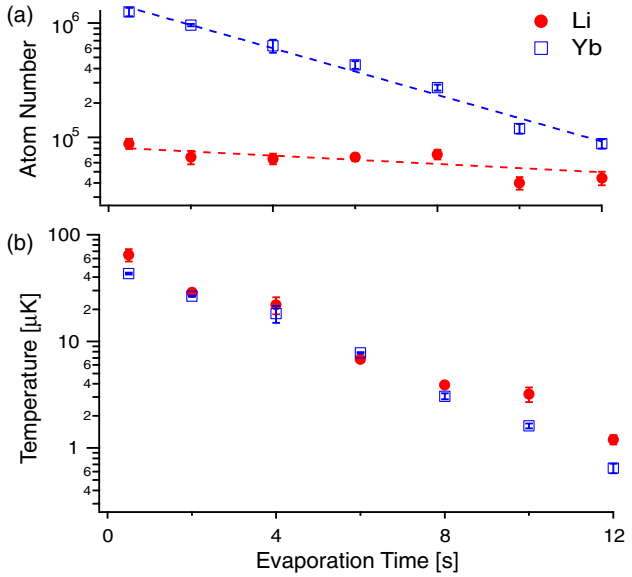

FIG. 3 (color online). Sympathetic cooling of lithium by forced evaporative cooling of ytterbium. (a) Number and (b) temperature evolution for ^{6}Li (solid circles) and ^{174}Yb (open squares) as the power in the crossed optical dipole trap is reduced by a factor of 28 over 12 s, corresponding to an approximately exponential ramp with a time constant of 2.9 s.

Our results establish a stable ultracold alkali + spin singlet mixture and also constitute the first instance of sympathetic cooling of a second atomic species by a spin-singlet atom. Future work includes studies of molecular levels by one- and two-photon photoassociation spectroscopies and searches for magnetically and optically induced Feshbach resonances [25,26], important steps towards production of paramagnetic polar molecules of LiYb. Improving our sympathetic cooling arrangement with magnetic gradients and tighter beams will allow us to reach double quantum degeneracy with various combinations of Li and Yb isotopes, including Fermi-Fermi degenerate mixtures with high mass imbalance. Yb atoms inside a degenerate Li cloud can also serve as an impurity to study superfluidity [33], and for thermometry of a deeply degenerate Fermi gas [6].

We thank W. Willcockson, J. K. Smith, R. Weh, W. English, and N. Maloney, for major technical contributions during the early stages of the experiment, E. N. Fortson for valuable discussions, and A. Görlitz and D. M. Stamper-Kurn for helpful comments. This work was supported by the National Science Foundation, the Alfred P. Sloan Foundation, UW Royalty Research Fund, and NIST. A. K. acknowledges support from the NSERC and F. M. from the DAAD.

[1] G. Modugno *et al.*, Science **294**, 1320 (2001).
[2] Z. Hadzibabic *et al.*, Phys. Rev. Lett. **88**, 160401 (2002).
[3] C. Silber *et al.*, Phys. Rev. Lett. **95**, 170408 (2005).
[4] S. Aubin *et al.*, Nature Phys. **2**, 384 (2006).
[5] M. Taglieber *et al.*, Phys. Rev. Lett. **100**, 010401 (2008).
[6] F. Spiegelhalder *et al.*, Phys. Rev. Lett. **103**, 223203 (2009).
[7] J. P. D'Incao and B. D. Esry, Phys. Rev. A **73**, 030702(R) (2006).
[8] B. Marcelis *et al.*, Phys. Rev. A **77**, 032707 (2008).
[9] E. Vernier *et al.*, Phys. Rev. A **83**, 033619 (2011).
[10] M. Iskin, Phys. Rev. A **78**, 021604(R) (2008).
[11] A. Gezerlis *et al.*, Phys. Rev. Lett. **103**, 060403 (2009).
[12] A. Trenkwalder *et al.*, Phys. Rev. Lett. **106**, 115304 (2011).
[13] J. M. Sage *et al.*, Phys. Rev. Lett. **94**, 203001 (2005).
[14] J. Deiglmayr *et al.*, Phys. Rev. Lett. **101**, 133004 (2008).
[15] K.-K. Ni *et al.*, Science **322**, 231 (2008).
[16] L. D. Carr *et al.*, New J. Phys. **11**, 055049 (2009).
[17] M. Mudrich *et al.*, Phys. Rev. Lett. **88**, 253001 (2002).
[18] A. Micheli *et al.*, Nature Phys. **2**, 341 (2006).
[19] J. J. Hudson *et al.*, Phys. Rev. Lett. **89**, 023003 (2002).
[20] M. Okano *et al.*, Appl. Phys. B **98**, 691 (2009).
[21] N. Nemitz *et al.*, Phys. Rev. A **79**, 061403(R) (2009).
[22] S. Tassy *et al.*, J. Phys. B **43**, 205309 (2010).
[23] F. Baumer *et al.* (to be published).
[24] M. W. Zwierlein *et al.*, Nature (London) **435**, 1047 (2005).
[25] P. S. Zuchowski, J. Aldegunde, and J. M. Hutson, Phys. Rev. Lett. **105**, 153201 (2010).
[26] R. Ciurylo, E. Tiesinga, and P. S. Julienne, Phys. Rev. A **71**, 030701(R) (2005).
[27] We observe significant reduction of Yb MOT number when operating simultaneous Li and Yb MOTs. The optimum MOT gradient for each species is related to the natural linewidth of the cooling transition and for our specific conditions differs empirically by a factor of 7.
[28] M. Houbiers *et al.*, Phys. Rev. A **57**, R1497 (1998).
[29] In the limit of no atom loss, the final temperature after thermalization is defined through the initial parameters as $\frac{N_{\mathrm{Yb}}T_{\mathrm{Yb}}+N_{\mathrm{Li}}T_{\mathrm{Li}}}{N_{\mathrm{Yb}}+N_{\mathrm{Li}}} = 43\ \mu$K in our case. This value is reduced by evaporative cooling. Assuming the calculated trap depths given in the text, numerical simulations indicate a Yb temperature rise of $\leq 5\ \mu$K, comparable to the statistical error bars in our measurement.
[30] P. Zhang, H. R. Sadeghpour, and A. Dalgarno, J. Chem. Phys. **133**, 044306 (2010).
[31] V. V. Flambaum, G. F. Gribakin, and C. Harabati, Phys. Rev. A **59**, 1998 (1999).
[32] C.-L. Hung *et al.*, Phys. Rev. A **78**, 011604(R) (2008).
[33] While the Li cloud is smaller than an equal temperature Yb cloud in the Boltzmann regime, because of Fermi pressure the opposite is true for $T/T_F \lesssim 0.27$ in the unitary regime of strong ^{6}Li interactions.

Appendix B

Quantum degenerate mixture of ytterbium and lithium atoms

This appendix includes the following paper [103]: A. H. Hansen, A. Khramov, W. H. Dowd, A. O. Jamison, V. V. Ivanov, and S. Gupta. Quantum degenerate mixture of ytterbium and lithium atoms. *Phys. Rev. A*, 84:011606(R), 2011.

PHYSICAL REVIEW A **84**, 011606(R) (2011)

Quantum degenerate mixture of ytterbium and lithium atoms

Anders H. Hansen, Alexander Khramov, William H. Dowd, Alan O. Jamison, Vladyslav V. Ivanov, and Subhadeep Gupta
Department of Physics, University of Washington, Seattle, Washington 98195, USA
(Received 27 May 2011; published 22 July 2011)

We have produced a quantum degenerate mixture of fermionic alkali-metal ^{6}Li and bosonic spin-singlet ^{174}Yb gases. This was achieved using sympathetic cooling of lithium atoms by evaporatively cooled ytterbium atoms in a far-off-resonant optical dipole trap. We observe the coexistence of Bose-condensed ($T/T_c \simeq 0.8$) ^{174}Yb with 2.3×10^4 atoms and Fermi degenerate ($T/T_F \simeq 0.3$) ^{6}Li with 1.2×10^4 atoms. Quasipure Bose-Einstein condensates of up to 3×10^4 ^{174}Yb atoms can be produced in single-species experiments. Our results mark a significant step toward studies of few- and many-body physics with mixtures of alkali-metal and alkaline-earth-metal-like atoms, and for the production of paramagnetic polar molecules in the quantum regime. Our methods also establish a convenient scheme for producing quantum degenerate ytterbium atoms in a 1064 nm optical dipole trap.

DOI: 10.1103/PhysRevA.84.011606 PACS number(s): 67.85.Pq, 37.10.De, 05.30.Fk, 67.10.Db

Quantum degenerate elemental mixtures can be used to study a variety of few- and many-body phenomena and form the starting point for creating quantum degenerate dipolar molecules. While bi-alkali-metal quantum mixtures [1–6] have been produced and studied for about a decade, mixtures of alkali-metal and electron spin-singlet atoms are a more recent development [7–11]. By exploiting the difference in mass of the components, the lithium-ytterbium quantum degenerate mixture may be used to investigate a range of interesting scientific directions including new Efimov states [12,13], impurity probes of the Fermi superfluid [6], and mass imbalanced Cooper pairs [14–16]. Furthermore, unlike the bi-alkali-metal case, mixtures of alkali-metal and alkaline-earth-metal-like atoms can lead to the realization of paramagnetic polar molecules by combining the atoms through field-induced scattering resonances, followed by multiphoton transfer processes to the ground state [17–19]. Such molecules hold great promise for quantum simulation and topological quantum computing applications [20]. They may also be good candidates for sensitive tests of fundamental symmetries, particularly if one of the constituents is a heavy atom, such as Yb [21].

In this paper, we report on simultaneous quantum degeneracy in a mixture of alkali-metal and alkaline-earth-metal-like atoms. In earlier work [11], we reported on collisional stability and sympathetic cooling in the ^{6}Li-^{174}Yb system, together with a measurement of the interspecies s-wave scattering length magnitude. Here we establish a convenient method to produce Bose-Einstein condensates (BECs) of ^{174}Yb. This allows the sympathetic cooling of ^{6}Li to well below its Fermi temperature and the achievement of simultaneous quantum degeneracy in the two species.

The cooling of various isotopes of ytterbium to quantum degeneracy has been pioneered by the group of Y. Takahashi in Kyoto [22–24]. In these studies, the optical dipole trap (ODT) was implemented at the wavelength 532 nm. While suitable for confining ytterbium which has a strong transition at 399 nm, this choice of wavelength will not confine common alkali-metal atoms due to their strong transitions occurring at wavelengths greater than 532 nm. For our ODT, we use 1064 nm light arranged in a straightforward horizontal geometry, and demonstrate efficient evaporative cooling of ^{174}Yb to BEC. This establishes a simple setup for studies with quantum degenerate ytterbium gases, particularly in the context of dual-species experiments.

Our experimental setup (see Fig. 1) is similar to what has been described previously [11]. Briefly, we sequentially load ^{174}Yb and then ^{6}Li from respective magneto-optical traps (MOTs) into the same ODT. We then perform forced evaporative cooling of ^{174}Yb by lowering the power in the ODT. This leads to quantum degeneracy in either single or dual-species experiments. Two improvements to our earlier setup which are crucial for this work are the use of higher power in the Yb Zeeman-slowing beam resulting in larger MOT numbers, and the implementation of a tighter ODT geometry [25] leading to more efficient evaporative cooling.

The ODT is derived from a 1064 nm linearly polarized fiber laser, operated at a power of 45 W. In order to control the trap depth, the output of the laser is sent through an acousto-optic modulator. The first-order output is split into two equal parts with orthogonal linear polarizations which then propagate horizontally toward the atoms. Each beam is focused to a (measured) waist of 26 μm and the foci are overlapped at an angle of 20 degrees. The trapping potential is characterized through measurements of trap frequencies by parametric heating. The relative trap depths and frequencies for the two species are $U_{\mathrm{Li}}/U_{\mathrm{Yb}} = 2.2$ and $\omega_{\mathrm{Li}}/\omega_{\mathrm{Yb}} = 8.1$. To monitor atom number and temperature, we quickly switch off the ODT and perform resonant absorption imaging of both species.

In single-species experiments with ^{174}Yb, we load 1.5×10^7 atoms in a MOT in 40 s from a Zeeman-slowed atomic beam. We use 100 mW power in the 399 nm ($^1S_0 \rightarrow {}^1P_1$) slowing beam and a total of 12 mW power in the 556 nm ($^1S_0 \rightarrow {}^3P_1$) MOT beams, operated in retroreflection configuration. A transient cooling and compression scheme then produces an atomic cloud at a temperature of 20 μK containing $\simeq 6 \times 10^6$ atoms.

About 1×10^6 atoms in the $^1S_0$ state are then loaded into the ODT where the background $1/e$ lifetime is 40 s. The initial ODT power at the atoms is 9 W per beam, corresponding to a trap depth of 430 μK. The power is then reduced by a

 ©2011 American Physical Society

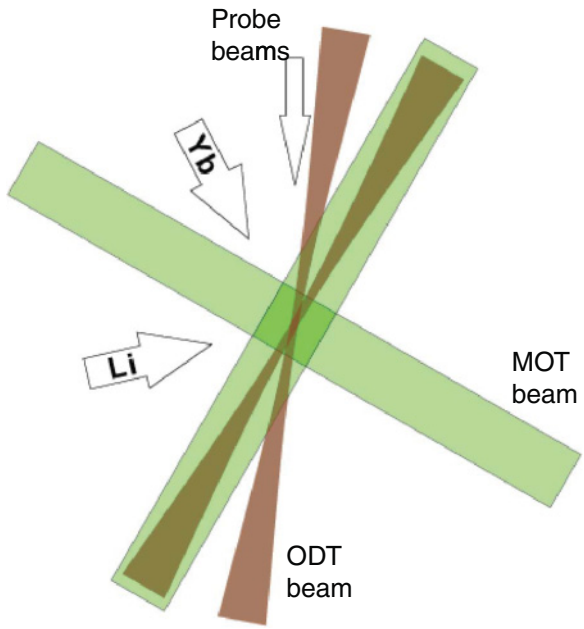

FIG. 1. (Color online) Experimental arrangement (top view) for producing simultaneous quantum degeneracy in lithium and ytterbium. Zeeman-slowed atomic beams of each species propagate along separate axes toward the MOT. The horizontal ODT beams (brown) are crossed at the MOT region at an angle of 20°. MOT beams (green) for both species are overlapped and arranged in a retroreflection configuration. Beams for the vertical MOT axis and Zeeman slowing are omitted from the figure for clarity.

factor of 100 over a time scale of 14 s, utilizing two stages of approximately exponential shape. The first stage lasts for 5 s with a time constant of 1.5 s. The second stage lasts for the remainder of the evaporation period and has a time constant of 3.6 s.

We observe efficient evaporative cooling with this arrangement [see Fig. 2(a)]. The critical temperature for Bose-Einstein condensation is achieved after evaporating for $\simeq$12.5 s. At this point the atom number is $N_{\mathrm{Yb}} = 7 \times 10^4$ and the temperature is $T_{\mathrm{Yb}} = 170$ nK. By fitting to the data prior to condensation, we extract an evaporation efficiency parameter $-d[\ln(\rho_{\mathrm{Yb}})]/d[\ln(N_{\mathrm{Yb}})] = 3.4(4)$ where ρ_{Yb} is the phase space density. Nearly pure condensates of up to 3×10^4 atoms can be prepared by continuing the evaporation process [see Fig. 2(b)].

For two-species experiments, we add to the optically trapped ^{174}Yb an equal mixture of the two $F = 1/2$ Zeeman states of ^{6}Li with an adjustable total number. After 1 s of interspecies thermalization at constant trap depth, we perform sympathetic cooling of ^{6}Li by ^{174}Yb at near-zero magnetic field by using the same evaporation ramp as described above. Sympathetic cooling works well in this mixture as described in our earlier work [11] where we reported an interspecies s-wave scattering length magnitude of $|a_{^6\mathrm{Li}\text{-}^{174}\mathrm{Yb}}| = (13 \pm 3)a_0$. The ^{6}Li number remains nearly constant due to its greater trap depth. After approximately 14 s of evaporation we observe simultaneous quantum degeneracy in the two species (see Fig. 3). At this point the geometric mean trap frequencies are $\bar{\omega}_{\mathrm{Yb(Li)}} = 2\pi \times 90$ (740) Hz, atom numbers

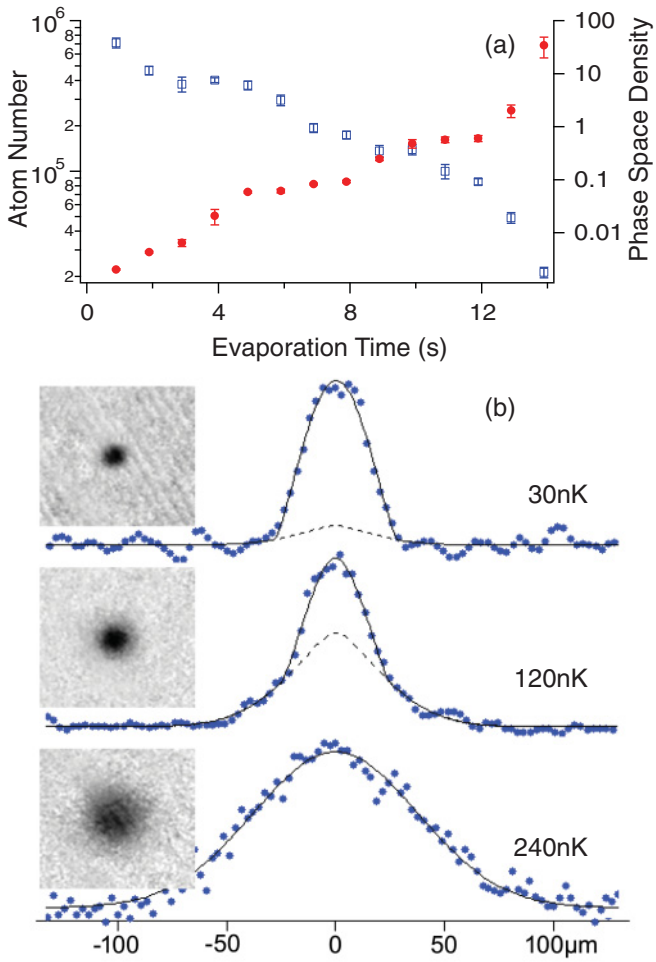

FIG. 2. (Color online) Evaporative cooling of ^{174}Yb to Bose-Einstein condensation in the crossed 1064 nm ODT. Panel (a) shows the evolution of ^{174}Yb number (open squares) and phase space density (filled circles) for a single-species experiment. BEC is achieved after about 12.5 s. Panel (b) shows absorption images and the corresponding atomic density profiles (vertical cross sections of these images) for three different final trap depths, showing the formation of the BEC. The solid line in each plot is a bimodal fit to the distribution with the dashed line showing the thermal component of the fit. The free expansion time after turning off the trap is 8 ms for each image. The total atom numbers and temperatures are 8.0, 5.6, and 2.1×10^4 and 240, 120, and 30 nK, respectively.

are $N_{\mathrm{Yb(Li)}} = 2.3\ (1.2) \times 10^4$, and temperatures are $T_{\mathrm{Yb(Li)}} = 100 \pm 10\ (320 \pm 36)$ nK. Here, N_{Li} is the total lithium atom number distributed equally between the two spin states. T_{Yb} is estimated from the fraction of condensed atoms. T_{Li} is a weighted average of three methods: a best-fit to the shape of the distribution using a Thomas-Fermi model with the fugacity as an independent parameter, and two Fermi-Dirac distribution fits to singly and doubly integrated density profiles.

The difference in temperature between the two species is largely attributable to the relative center-of-mass displacement at the end of the evaporation ramp arising from gravitational sag. Assuming perfect overlap, the estimated interspecies thermalization time at this stage is $\simeq$1 s, which is reasonably short. However, the separation of the two clouds due to unequal

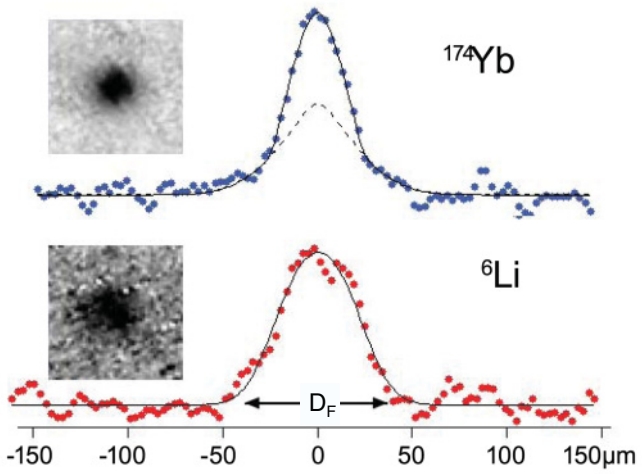

FIG. 3. (Color online) Quantum degenerate mixture of ^{174}Yb and ^{6}Li. The absorption images and density profiles correspond to the same experimental iteration with 14 s of evaporation. The free-expansion times are 8 ms for Yb and 0.7 ms for Li. Here $N_{\mathrm{Yb}} = 2.3 \times 10^4$ and $T_{\mathrm{Yb}} = 100$ nK, corresponding to $T_{\mathrm{Yb}}/T_{\mathrm{C,Yb}} = 0.8$, while $N_{\mathrm{Li}} = 1.2 \times 10^4$ and $T_{\mathrm{Li}} = 320$ nK, corresponding to $T_{\mathrm{Li}}/T_{\mathrm{F,Li}} = 0.3$. For ^{174}Yb, the solid line is a bimodal fit with the dashed line showing the thermal component of the fit. For ^{6}Li, the solid line is a Thomas-Fermi fit. The extent of the momentum-space Fermi diameter D_F, corresponding to the Fermi energy, is also indicated in the figure. The image was taken at near-zero magnetic field and includes both spin components.

effects of gravity is 5.1 μm while the lithium in-trap Fermi radius is 5.8 μm in the vertical direction. A numerical model of the cooling process incorporating this effect predicts a $1/e$ reduction of the interspecies collision rate due to separation when $T_{\mathrm{Yb}} \simeq 300$ nK, suggesting that sympathetic cooling does indeed become inefficient toward the end of evaporation.

Our results establish a new quantum system comprised of simultaneously degenerate one- and two-electron atomic gases. We also demonstrate a new method for achieving Bose-Einstein condensation of ^{174}Yb using a straightforward horizontal optical trapping arrangement with 1064 nm laser beams. Our setup could also be suitable for combining Yb with other alkalis such as Cs and Rb, since the trap depth and relative sizes would be amenable for sympathetic cooling by ytterbium. Further improvements to our cooling scheme include independent control over the powers in the two ODT beams and an additional magnetic field gradient to improve spatial overlap of the two species.

Extending our method to incorporate alternate ytterbium isotopes (such as the fermion ^{173}Yb [23]) appears realistic. This would then realize Fermi degenerate mixtures with a large mass ratio. Finally, our results represent a significant milestone toward the production of quantum gases of paramagnetic polar molecules. Theoretical work on the LiYb molecule has already been initiated by several groups [26–28]. Future experimental work on our system includes photoassociative spectroscopies and searches for Feshbach resonances [29] in this mixture, which are key steps toward forming the molecule.

Note added. Recently, we became aware of similar work [30] in which quantum degenerate mixtures of ^{6}Li-^{174}Yb and ^{6}Li-^{173}Yb were obtained.

This work was supported by the National Science Foundation, the Alfred P. Sloan Foundation, and NIST. A. K. acknowledges support from the NSERC.

[1] G. Modugno, G. Ferrari, G. Roati, R. Brecha, A. Simoni, and M. Inguscio, Science **294**, 1320 (2001).
[2] Z. Hadzibabic, C. A. Stan, K. Dieckmann, S. Gupta, M. W. Zwierlein, A. Görlitz, and W. Ketterle, Phys. Rev. Lett. **88**, 160401 (2002).
[3] C. Silber, S. Gunther, C. Marzok, B. Deh, P. W. Courteille, and C. Zimmermann, Phys. Rev. Lett. **95**, 170408 (2005).
[4] S. Aubin, S. Myrskog, M. H. T. Extavour, L. J. LeBlanc, D. McKay, A. Stummer, and J. Thywissen, Nature Phys. **2**, 384 (2006).
[5] M. Taglieber, A. C. Voigt, T. Aoki, T. W. Hänsch, and K. Dieckmann, Phys. Rev. Lett. **100**, 010401 (2008).
[6] F. M. Spiegelhalder, A. Trenkwalder, D. Naik, G. Hendl, F. Schreck, and R. Grimm, Phys. Rev. Lett. **103**, 223203 (2009).
[7] N. Nemitz, F. Baumer, F. Münchow, S. Tassy, and A. Görlitz, Phys Rev A **79**, 061403(R) (2009).
[8] S. Tassy, N. Nemitz, F. Baumer, C. Höhl, A. Batar, and A. Görlitz, J. Phys. B **43**, 205309 (2010).
[9] M. Okano, H. Hara, M. Muramatsu, K. Doi, S. Uetake, Y. Takasu, and Y. Takahashi, Appl Phys B **98**, 691 (2010).
[10] F. Baumer, F. Münchow, A. Görlitz, S. Maxwell, P. Julienne, and E. Tiesinga, Phys. Rev. A **83**, 040702 (2011).
[11] V. V. Ivanov, A. Khramov, A. H. Hansen, W. H. Dowd, F. Münchow, A. O. Jamison, and S. Gupta, Phys. Rev. Lett. **106**, 153201 (2011).
[12] J. P. D'Incao and B. D. Esry, Phys. Rev. A **73**, 030702 (2006).
[13] B. Marcelis, S. J. J. M. F. Kokkelmans, G. V. Shlyapnikov, and D. S. Petrov, Phys. Rev. A **77**, 032707 (2008).
[14] M. Iskin, Phys. Rev. A **78**, 021604 (2008).
[15] A. Gezerlis, S. Gandolfi, K. E. Schmidt, and J. Carlson, Phys. Rev. Lett. **103**, 060403 (2009).
[16] A. Trenkwalder, C. Kohstall, M. Zaccanti, D. Naik, A. I. Sidorov, F. Schreck, and R. Grimm, Phys. Rev. Lett. **106**, 115304 (2011).
[17] J. M. Sage, S. Sainis, T. Bergeman, and D. DeMille, Phys. Rev. Lett. **94**, 203001 (2005).
[18] J. Deiglmayr, A. Grochola, M. Repp, K. Mortlbauer, C. Gluck, J. Lange, O. Dulieu, R. Wester, and M. Weidemuller, Phys. Rev. Lett. **101**, 133004 (2008).
[19] K.-K. Ni, S. Ospelkaus, M. H. G. de Miranda, A. Peer, B. Neyenhuis, J. J. Zirbel, S. Kotochigova, P. S. Julienne, D. S. Jin, and J. Ye, Science **322**, 231 (2008).
[20] A. Micheli, G. K. Brennen, and P. Zoller, Nature Phys. **2**, 341 (2006).

[21] J. J. Hudson, B. E. Sauer, M. R. Tarbutt, and E. A. Hinds, Phys. Rev. Lett. **89**, 023003 (2002).

[22] Y. Takasu, K. Maki, K. Komori, T. Takano, K. Honda, M. Kumakura, T. Yabuzaki, and Y. Takahashi, Phys. Rev. Lett. **91**, 040404 (2003).

[23] T. Fukuhara, Y. Takasu, M. Kumakura, and Y. Takahashi, Phys. Rev. Lett. **98**, 030401 (2007).

[24] T. Fukuhara, S. Sugawa, Y. Takasu, and Y. Takahashi, Phys. Rev. A **79**, 021601 (2009).

[25] Compared to our earlier work, the power in the slowing beam is about three times larger. For the same ODT laser power, the mean trap frequency is also about three times larger.

[26] P. Zhang, H. R. Sadeghpour, and A. Dalgarno, J. Chem. Phys. **133**, 044306 (2010).

[27] G. Gopakumar, M. Abe, B. P. Das, M. Hada, and K. Hirao, J. Chem. Phys. **133**, 124317 (2010).

[28] Svetlana Kotochigova and Roman Krems (private communication).

[29] P. S. Zuchowski, J. Aldegunde, and J. Hutson, Phys. Rev. Lett. **105**, 153201 (2010).

[30] H. Hara, Y. Takasu, Y. Yamaoka, J. M. Doyle, and Y. Takahashi, Phys. Rev. Lett. **106**, 205304 (2011).

Appendix C

Dynamics of Feshbach molecules in an ultracold three-component mixture

This appendix includes the following paper [105]: A. Y. Khramov, A. H. Hansen, A. O. Jamison, W. H. Dowd, and S. Gupta. Dynamics of feshbach molecules in an ultracold three-component mixture. *Phys. Rev. A*, 86:032705, 2012.

Dynamics of Feshbach molecules in an ultracold three-component mixture

Alexander Y. Khramov, Anders H. Hansen, Alan O. Jamison, William H. Dowd, and Subhadeep Gupta
Department of Physics, University of Washington, Seattle, Washington 98195, USA
(Received 7 July 2012; published 10 September 2012)

We present investigations of the formation rate and collisional stability of lithium Feshbach molecules in an ultracold three-component mixture composed of two resonantly interacting fermionic ^{6}Li spin states and bosonic ^{174}Yb. We observe long molecule lifetimes (>100 ms) even in the presence of a large ytterbium bath and extract reaction rate coefficients of the system. We find good collisional stability of the mixture in the unitary regime, opening new possibilities for studies and probes of strongly interacting quantum gases in contact with a bath species.

DOI: 10.1103/PhysRevA.86.032705 PACS number(s): 34.50.Lf, 05.30.Fk

Magnetic Feshbach resonances allow precise control of collisional properties, making them a key tool in ultracold atom systems. They have been used extensively to study ultracold molecules, as well as few- and many-body physics [1]. Two-component Fermi gases near a Feshbach resonance provide excellent opportunities to study strongly interacting quantum systems [2]. This is possible due to the remarkable collisional stability of the atom-molecule mixture on the positive scattering length side of the resonance [3,4], attributed largely to Fermi statistics [5,6]. Extending the system to three-component mixtures in which only two are resonantly interacting [7] offers the exciting possibility of modifying or probing pairing dynamics by selective control of the third component. A third component may also be used as a coolant bath for exothermic molecule-formation processes, provided that inelastic processes with the bath are negligible. In the context of many-body physics, a third nonresonant component can be useful as a microscopic probe of superfluid properties [7,8], as a stable bath for studies of nonequilibrium phenomena [9], or for accurate thermometry of deeply degenerate fermions [10].

Collisional stability of Feshbach molecules in the absence of Fermi statistics becomes a crucial question for multicomponent mixtures [7,11,12]. A recent theoretical analysis of such mixtures suggests a possibility for enhanced molecule formation rates with good collisional stability [11]. Enhanced atom loss has been observed near a ^{6}Li p-wave resonance in the presence of a ^{87}Rb bath [13], while a small sample of the probe species ^{40}K has been found to be stable within a larger strongly interacting ^{6}Li sample [7].

In this paper, we investigate a mixture composed of two resonantly interacting spin states of fermionic ^{6}Li immersed in a large sample of bosonic ^{174}Yb atoms. While the Li interstate interactions are arbitrarily tunable by means of an s-wave Feshbach resonance at 834 G [14], the interspecies interactions between Li and Yb are constant and small [15]. We study the formation and evolution of Feshbach molecules in a bath of a second atomic species. In the unitary regime, we observe good collisional stability of the mixture with elastic interactions dominating over inelastic losses. We extract the reaction rate constants from a classical rate equations model of the system.

Our experimental procedure has been described in earlier work [16]. Briefly, 3×10^6 atoms of ^{174}Yb in the $^1S_0$ state and up to 4×10^4 atoms of ^{6}Li, distributed equally between the two $^2S_{1/2}$, $F = \frac{1}{2}$ states (denoted Li$|1\rangle$, Li$|2\rangle$), are loaded from magneto-optical traps into a crossed-beam optical dipole trap. We then perform forced evaporative cooling on Yb to a final trap depth $U_{\mathrm{Yb}}(U_{\mathrm{Li}}) = 15(55)\,\mu$K, with mean trap frequency $\bar{\omega}_{\mathrm{Yb}}\,(\bar{\omega}_{\mathrm{Li}}) = 2\pi \times 0.30\,(2.4)$ kHz [17], during which Li is cooled sympathetically by Yb. Following evaporation, the mixture is held at a constant trap depth to allow interspecies thermalization. With a time constant of 1 s, the system acquires a common temperature $T_{\mathrm{Yb}} = T_{\mathrm{Li}} = 2\ \mu$K with atom number $N_{\mathrm{Yb}}\,(N_{\mathrm{Li}}) = 2 \times 10^5\,(3 \times 10^4)$. This corresponds to $T_{\mathrm{Li}}/T_F \simeq 0.4$ and $T_{\mathrm{Yb}}/T_C \simeq 2.5$, where T_F is the Li Fermi temperature and T_C is the Yb Bose-Einstein condensation temperature [18].

After this initial preparation, we ramp up the magnetic field to a desired value and observe the system after a variable hold time. For fields in the vicinity of the Feshbach resonance, there is a field-dependent number loss and heating for the Li cloud during the 20 ms ramp time, resulting in T_{Li} rising to as high as 4.5 μK. At this point, the density-weighted average density $\langle n_{\mathrm{Yb}}\rangle$ ($\langle n_{\mathrm{Li}}\rangle$) is 2.6 (0.35) $\times\ 10^{13}\,\mathrm{cm}^{-3}$. For interrogation in the absence of the bath, Yb is removed from the trap with a 1 ms light pulse resonant with the $^1S_0 \rightarrow {}^1P_1$ transition [19]. Atom number and temperature are monitored using absorption imaging for both species after switching off the magnetic field.

We first present our results on atom-loss spectroscopy near the Feshbach resonance (see Fig. 1). The atom-loss maximum obtained in the absence of Yb has been observed previously [14] and can be explained as a result of the formation and subsequent decay of shallow lithium Feshbach dimers [3,4,20–22] which form only on the positive a side of the resonance. Here a denotes the Li$|1\rangle$-Li$|2\rangle$ scattering length. In the presence of the Yb bath, the loss feature is shifted and broadened. We interpret the behavior of the mixture in terms of five chemical processes:

$$\mathrm{Li}|1\rangle + \mathrm{Li}|2\rangle + \mathrm{Li} \rightleftharpoons \mathrm{Li}_2^s + \mathrm{Li} \quad (+\epsilon_B) \quad \text{(I)}$$
$$\mathrm{Li}_2^s + \mathrm{Li} \rightarrow \mathrm{Li}_2^d + \mathrm{Li} \quad (+\epsilon_D) \quad \text{(II)}$$
$$\mathrm{Li}|1\rangle + \mathrm{Li}|2\rangle + \mathrm{Yb} \rightleftharpoons \mathrm{Li}_2^s + \mathrm{Yb} \quad (+\epsilon_B) \quad \text{(III)}$$
$$\mathrm{Li}_2^s + \mathrm{Yb} \rightarrow \mathrm{Li}_2^d + \mathrm{Yb} \quad (+\epsilon_D) \quad \text{(IV)}$$
$$\mathrm{Li}|1\rangle + \mathrm{Li}|2\rangle + \mathrm{Yb} \rightarrow \mathrm{Li}_2^d + \mathrm{Yb} \quad (+\epsilon_D) \quad \text{(V)}$$

Forward process (I) corresponds to a three-body collision event which produces a shallow Feshbach dimer (denoted Li_2^s) accompanied by the release of the dimer binding energy $\epsilon_B = \frac{\hbar^2}{2m_{\mathrm{Li}}a^2}$. Li denotes a ^{6}Li atom in either of the two spin states. Process (II) corresponds to two-body loss to a deeply bound dimer (denoted Li_2^d) with binding energy ϵ_D. Processes

 ©2012 American Physical Society

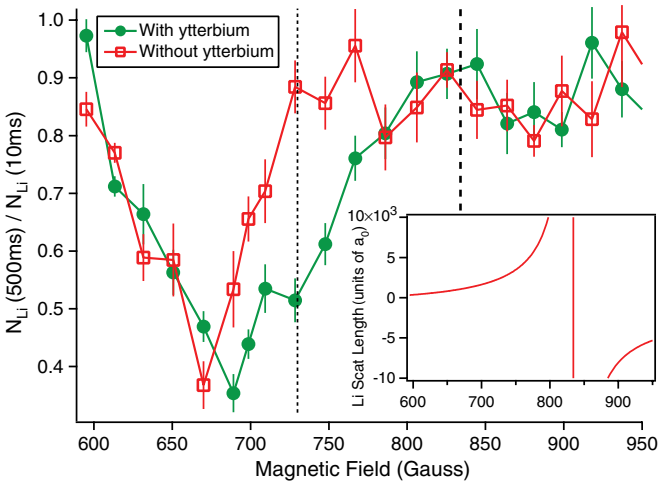

FIG. 1. (Color online) Li atom-loss spectroscopy in the presence (filled circles) and absence (open squares) of a Yb bath near the ^{6}Li 834 G Feshbach resonance (inset). We plot the number of Li atoms after 500 ms of evolution normalized to that at 10 ms. The thick dashed line indicates the resonance center and the thin dashed line indicates the magnetic field at which $\epsilon_B = k_B T_{\rm Li}$ for the initial conditions.

(III) and (IV) are similar to (I) and (II) with the spectator atom being Yb rather than Li [23]. Process (V) corresponds to direct three-body loss to a deeply bound molecule. Processes (II), (IV), and (V) always result in particle loss from the trap since $\epsilon_D \gg U_{\rm Li}$. Vibrational relaxation due to collisions between Li_2^s Feshbach molecules may contribute at the lowest fields, but it has a negligible rate for the fields at which we perform our analysis [3,22]. We have experimentally checked that direct three-body loss processes to deeply bound states involving three Li atoms as well as those involving one Li atom and two Yb atoms are negligible for this work [24]. Three-body losses involving Yb atoms alone have a small effect [25] and are taken into account in our analysis.

In the absence of Yb, only processes (I) and (II) contribute. If we neglect loss process (II), the atom-molecule mixture approaches an equilibrium, characterized by an equality of the forward and reverse rates and an equilibrium molecule fraction $\frac{2N_m}{N_{\rm Li}+2N_m} = (1 + \frac{e^{-\epsilon_B/k_BT}}{\phi_{\rm Li}})^{-1}$, where N_m is the molecule number and $\phi_{\rm Li}$ is the phase space density for each spin component in the ground state of the trap [20–22]. The time scale for achieving equilibrium depends on the three-body rate constant L_3 for process (I), which scales with the scattering length as a^6, whereas rate constant L_2 for process (II) scales as $a^{-3.3}$ [26,27]. The shape of the loss spectrum can thus be qualitatively explained by noting that the dimer formation rate increases with magnetic field while the equilibrium dimer fraction and the molecule decay rate decrease. The large rate for process (I) at high fields close to resonance ensures an equilibrium molecule fraction at all times. Broadly speaking, the rate-limiting step determining the system evolution is the molecule formation rate at low fields and the decay rate at high fields. The trap depth also affects the loss spectrum shape, since it determines the magnetic field range over which the formed shallow dimers remain trapped.

In the presence of Yb, the additional dimer formation (III), dimer decay (IV), and three-body loss (V) processes

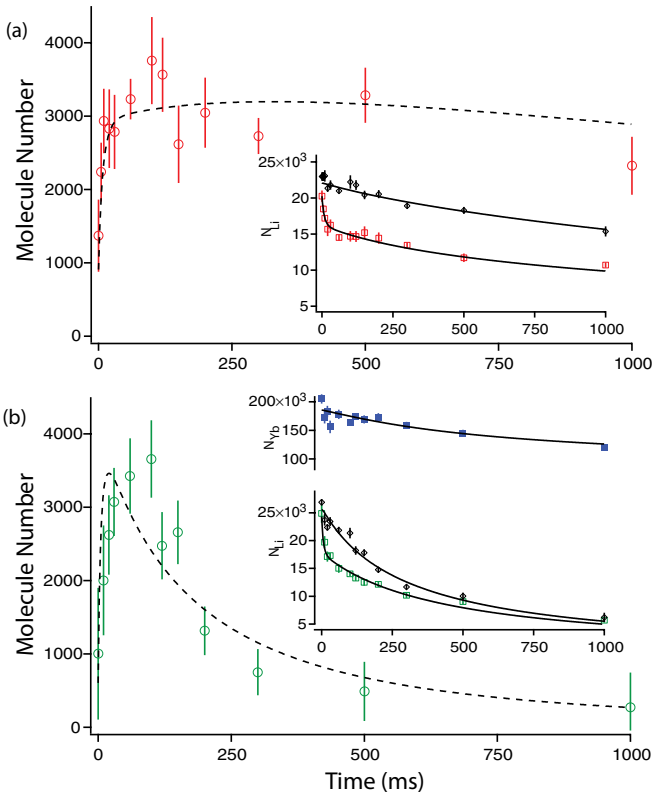

FIG. 2. (Color online) Evolution of Li Feshbach molecule number at 709 G without (a) and with (b) a Yb bath. The numbers are obtained by comparing Li atom numbers (insets) ramped across resonance (diamonds) or not (open squares) as described in the text. The lower inset also shows the Yb number (filled squares). The curves are fits with a rate equations-based model.

contribute. The observed loss spectrum is broadened on the higher field side, suggesting that for our parameters, processes (IV) and/or (V) play an important role while process (III) does not. The rate constants L_3', L_2', and L_3^d for processes (III), (IV) and (V), have theoretical scalings a^4, a^{-1}, and a^2, respectively [11,26]. Overall, we see two regimes of behavior—a lossy one where molecule formation is energetically favored ($\epsilon_B > k_B T_{\rm Li}$) and a stable one closer to resonance ($\epsilon_B < k_B T_{\rm Li}$). The criterion $\epsilon_B = k_B T$ separating these two regimes is equivalent to $ka = 1$, where $\frac{\hbar^2 k^2}{2m_{\rm Li}} = k_B T_{\rm Li}$, i.e., the unitary criterion.

To expand upon this qualitative picture, we study the time evolution of the three-component mixture at representative magnetic fields in the above two regimes. We are then able to extract quantitative information for the above processes from a rate-equations model of the system.

Figure 2 shows the Li atom and molecule number evolution at 709 G ($\epsilon_B = k_B \times 8.3\,\mu$K), a field value where modifications due to the Yb bath are apparent in Fig. 1. The number of Feshbach molecules at a particular field is determined by using a procedure similar to earlier works [3,4]. After variable evolution time, we ramp the magnetic field with a speed of 40 G/ms either up to 950 G, which dissociates the molecules back into atoms that remain in the trap, or to 506 G, which does not. We then rapidly switch off the magnetic field and image the atomic cloud. The molecule number is obtained from the number difference in the two images (see the insets in Fig. 2).

We see that the presence of Yb alters the molecule decay rate while the formation rate is unchanged. The Feshbach molecules appear to coexist for a long time (>100 ms) with the Yb bath, even in the absence of Pauli blocking [11]. We adapt the recent rate-equations analysis of Feshbach losses in a Fermi-Fermi mixture [22] to incorporate a third component, temperature evolution, and trap inhomogeneity. $T_{\rm Li}/T_F > 0.5$ is satisfied throughout the measurement range, allowing a classical treatment of the Li cloud. We model the density evolutions due to processes (I)–(V) using

$$\dot{n}_m = R_m + R'_m - L_2 n_m n_{\rm Li} - L'_2 n_m n_{\rm Yb}, \tag{1}$$

$$\dot{n}_{\rm Li} = -2R_m - 2R'_m - L_2 n_m n_{\rm Li} - 2L_3^d n_{\rm Li}^2 n_{\rm Yb}, \tag{2}$$

$$\dot{n}_{\rm Yb} = -L'_2 n_m n_{\rm Yb} - L_3^d n_{\rm Li}^2 n_{\rm Yb}. \tag{3}$$

Here n_m, $n_{\rm Li}$, and $n_{\rm Yb}$ are the densities of shallow dimers $\rm Li_2^s$, Li atoms, and Yb atoms, respectively. $R_m\,(R'_m) = \frac{3}{4}L_3\,(L'_3) n_{\rm Li}^2 n_{\rm Li\,(Yb)} - q\,L_3\,(L'_3) n_m n_{\rm Li\,(Yb)}$ is the net rate for molecule production via process (I) [(III)]. We determine q through the constraints on the molecule fraction at equilibrium $[R_m\,(R'_m) = 0]$. We obtain an upper bound for L_3^d by observations at large negative a (described below) which indicates a negligible effect for the data in Fig. 2, allowing us to set $L_3^d = 0$ for the analysis at 709 G.

The time evolutions of $T_{\rm Li}$ and $T_{\rm Yb}$ are modeled considering the energy deposition from processes (I) and (III) as well as heating from the density-dependent loss processes (II), (IV), and (V) [28]. In addition, our model also takes into account the effects of evaporative cooling [29], interspecies thermalization [15], one-body losses from background gas collisions, and Yb three-body losses [25,28]. The Li scattering length at 709 G is $a = 1860a_0$, ensuring rapid thermalization (<1 ms) in the lithium atom–Feshbach molecule mixture [26]. This allows the assumption of equal temperature $T_{\rm Li}$ for lithium atoms and Feshbach molecules. The heating from molecule formation at 709 G dominates over interspecies thermalization, maintaining $T_{\rm Li} \simeq 4.5\ \mu$K and $T_{\rm Yb} \simeq 2\ \mu$K, as observed in both the experiment and the model.

The best-fit rate coefficients extracted from the atom data (shown in the insets) are $L_3 = (1.4 \pm 0.3) \times 10^{-24}$ cm^6/s, $L_2 = (1.3 \pm 0.3) \times 10^{-13}$ cm^3/s, and $L'_2 = (2.3 \pm 0.2) \times 10^{-13}$ cm^3/s. L'_3 is consistent with 0. All reported uncertainties are statistical. The L_3 value is consistent with that obtained in Ref. [3] after accounting for the slight differences in experimental parameters. Using $L'_2\langle n_{\rm Yb}\rangle$ as a measure of the dimer decay rate, we get 170 ms as the lifetime of a Li Feshbach molecule in the Yb bath.

We now turn to the unitary regime, where we choose 810 G ($ka = +6$, $\epsilon_B = k_B \times 0.11\ \mu$K) as our representative field to study the mixture properties. It is difficult to reliably observe the molecule number using our earlier method in this regime, so we only monitor the atoms (see Fig. 3). Starting with an interspecies temperature differential as before, we observe a fast drop in $T_{\rm Li}$ in the presence of Yb and clear evidence of interspecies thermalization. The Li number in the three-component mixture exhibits a long $1/e$ lifetime of 2 s, far larger than at 709 G. However, this is still an order of magnitude shorter than that obtained in the absence of

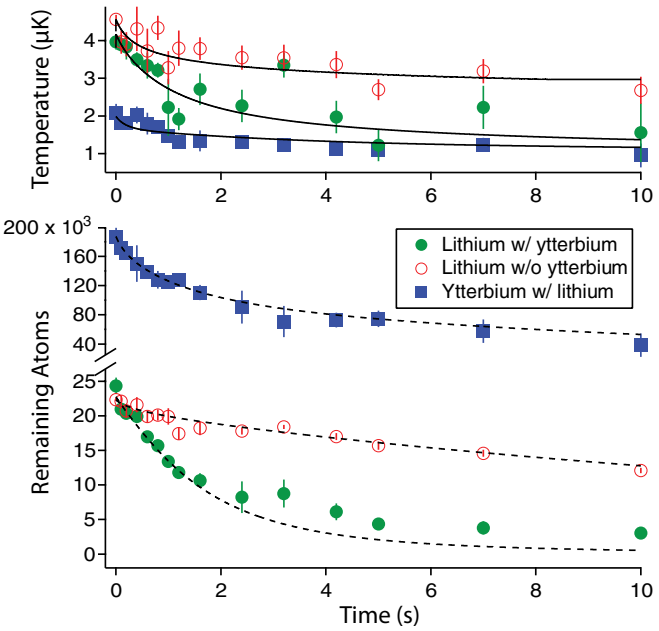

FIG. 3. (Color online) The evolution of temperature and number at 810 G for the Li atomic cloud with Yb (filled circles) and without (empty circles) and also for Yb in the presence of Li (filled squares). The curves are fits with a rate equations-based model.

Yb. The interpretation of the decay is not straightforward as both two-body [process (IV)] and three-body [process (V)] inelastic loss can contribute [7,30]. The large rate for process (I) in this regime ensures equilibrium molecule fraction at all times. By fitting to data taken at 935 G, where $ka = -2$ and process (V) is expected to be the dominant inelastic loss, we obtain $L_3^d = (4.3 \pm 0.3) \times 10^{-28}$ cm^6/s. This sets a lower bound for L_3^d at 810 G. We fit the first 2.5 s of data in Fig. 3 after fixing L'_2 to its value scaled from 709 G and find $L_3^d = (9.5 \pm 0.5) \times 10^{-28}$ cm^6/s at 810 G. The slight disagreement in Li atom number at long times may be due to a small (<10%) inequality in our spin mixture composition, which the model does not take into account.

The qualitative features of both spectra in Fig. 1 can be theoretically reproduced by using field-dependent reaction coefficients scaled from our measured values at 709 and 810 G. However, a full quantitative comparison will need to take into account the theoretical deviations from scaling behavior in the unitary regime as well as experimental variations in the initial temperature, and is open to future investigation.

By extending the forced evaporative cooling step, lower temperature mixtures can be produced where bosonic ^{174}Yb shrinks to a size smaller than the Fermi diameter of the ^{6}Li cloud. Such experiments at 834 G yield $T_{\rm Li}/T_F \simeq 0.25$ with $N_{\rm Yb} = N_{\rm Li} = 2.5 \times 10^4$. Here, the estimated volume of the Yb sample is $\simeq 0.3$ of the Li sample volume, compared to 3.3 in the classical regime. The mixture is thus also capable of achieving the opposite regime of a second species being immersed inside a strongly interacting quantum degenerate Fermi gas, similar to earlier studies in the K-Li mixture [7].

Our experiments with the Yb-Li mixture near a Feshbach resonance demonstrate the effects of an additional species on chemical reaction rates in the micro-Kelvin regime. We

observe a long lifetime for Feshbach molecules, even in the absence of Pauli blocking. Our demonstrated stability of the mixture near the unitary regime of the resonance opens various possibilities of studying strongly interacting fermions immersed in a bath species or being interrogated by a small probe species. Future experimental opportunities include realizations of nonequilibrium states and studies of superfluid properties, for instance by controlled relative motion between the two species. Finally, our results constitute an advance in the manipulation of ultracold mixtures of alkali-metal and alkaline-earth-metal-like atoms [16,31,32]. These mixtures may be used to produce quantum gases of paramagnetic polar molecules, which are promising for diverse applications such as quantum simulation of lattice spin models [33], tests of fundamental symmetries [34], and probes of time variations in fundamental constants [35].

We thank Ben Plotkin-Swing for experimental assistance, and J. P. D'Incao, T. -L. Ho, and M. W. Zwierlein for helpful discussions. We gratefully acknowledge support from the National Science Foundation and the Air Force Office of Scientific Research. A.Y.K. thanks the NSERC.

[1] C. Chin, R. Grimm, P. S. Julienne, and E. Tiesinga, Rev. Mod. Phys. **82**, 1225 (2010).
[2] S. Giorgini, L. P. Pitaevskii, and S. Stringari, Rev. Mod. Phys. **80**, 1215 (2008).
[3] S. Jochim, M. Bartenstein, A. Altmeyer, G. Hendl, C. Chin, J. H. Denschlag, and R. Grimm, Phys. Rev. Lett. **91**, 240402 (2003).
[4] J. Cubizolles, T. Bourdel, S. J. J. M. F. Kokkelmans, and C. Salomon, Phys. Rev. Lett. **91**, 240401 (2003).
[5] B. D. Esry, C. H. Greene, and H. Suno, Phys. Rev. A **65**, 010705(R) (2001).
[6] D. S. Petrov, C. Salomon, and G. V. Shlyapnikov, Phys. Rev. Lett. **93**, 090404 (2004).
[7] F. M. Spiegelhalder, A. Trenkwalder, D. Naik, G. Hendl, F. Schreck, and R. Grimm, Phys. Rev. Lett. **103**, 223203 (2009).
[8] K. Targonska and K. Sacha, Phys. Rev. A **82**, 033601 (2010).
[9] A. Robertson and V. M. Galitski, Phys. Rev. A **80**, 063609 (2009).
[10] S. Nascimbène, N. Navon, K. J. Jiang, F. Chevy, and C. Salomon, Nature (London) **463**, 1057 (2010).
[11] J. P. D'Incao and B. D. Esry, Phys. Rev. Lett. **100**, 163201 (2008).
[12] J. J. Zirbel, K.-K. Ni, S. Ospelkaus, J. P. D'Incao, C. E. Wieman, J. Ye, and D. S. Jin, Phys. Rev. Lett. **100**, 143201 (2008).
[13] B. Deh, C. Marzok, C. Zimmermann, and P. W. Courteille, Phys. Rev. A **77**, 010701(R) (2008).
[14] K. Dieckmann, C. A. Stan, S. Gupta, Z. Hadzibabic, C. H. Schunck, and W. Ketterle, Phys. Rev. Lett. **89**, 203201 (2002).
[15] V. V. Ivanov, A. Khramov, A. H. Hansen, W. H. Dowd, F. Münchow, A. O. Jamison, and S. Gupta, Phys. Rev. Lett. **106**, 153201 (2011).
[16] A. H. Hansen, A. Khramov, W. H. Dowd, A. O. Jamison, V. V. Ivanov, and S. Gupta, Phys. Rev. A **84**, 011606(R) (2011).
[17] The optical trap wavelength = 1064 nm, initial power = 10 W per beam, waist = 26 μm, crossing angle = 20°. During the evaporative cooling step, the power is reduced by a factor of 16 over 3 s. At the highest optical trap powers, $\bar{\omega}_{\mathrm{Yb}}/\bar{\omega}_{\mathrm{Li}} = 0.12$ and $U_{\mathrm{Yb}}/U_{\mathrm{Li}} = 0.45$. At the lower final power, gravity reduces the effective trap depth of the heavier component more, but has a negligible effect on the frequency ratio.
[18] By continuing the forced evaporation to lower trap depths, we can produce pure Yb BECs with $>2 \times 10^5$ atoms in single-species experiments and deeply Fermi degenerate gases $T_{\mathrm{Li}}/T_F \simeq 0.1$ in two-species experiments.
[19] This step is carried out either immediately before or after the field ramp, with no discernible difference in lithium number or temperature between the two.
[20] C. Chin and R. Grimm, Phys. Rev. A **69**, 033612 (2004).
[21] S. J. J. M. F. Kokkelmans, G. V. Shlyapnikov, and C. Salomon, Phys. Rev. A **69**, 031602(R) (2004).
[22] S. Zhang and T.-L. Ho, New J. Phys. **13**, 055003 (2011).
[23] Since we observe and model process (IV) by its loss signature, we cannot distinguish it from the analogous process resulting in a deeply bound LiYb molecule, $\mathrm{Li}_2^s + \mathrm{Yb} \rightarrow \mathrm{LiYb} + \mathrm{Li}\ (+\epsilon_{\mathrm{D}})$. Thus L_2' is the combined rate constant for both processes.
[24] We obtain an upper limit on the rate of processes involving one Li atom and two Yb atoms from lifetime measurements in mixtures of one spin state of Li with Yb at a magnetic field near the Li-Li Feshbach resonance. We obtain an upper limit on the rate of direct three body decay of Li from lifetime measurements of the Li spin mixture in the absence of Yb, on the negative a side of the resonance.
[25] Y. Takasu, K. Maki, K. Komori, T. Takano, K. Honda, M. Kumakura, T. Yabuzaki, and Y. Takahashi, Phys. Rev. Lett. **91**, 040404 (2003).
[26] D. S. Petrov, Phys. Rev. A **67**, 010703(R) (2003).
[27] J. P. D'Incao and B. D. Esry, Phys. Rev. Lett. **94**, 213201 (2005).
[28] T. Weber, J. Herbig, M. Mark, H.-C. Nägerl, and R. Grimm, Phys. Rev. Lett. **91**, 123201 (2003).
[29] K. M. O'Hara, M. E. Gehm, S. R. Granade, and J. E. Thomas, Phys. Rev. A **64**, 051403(R) (2001).
[30] X. Du, Y. Zhang, and J. E. Thomas, Phys. Rev. Lett. **102**, 250402 (2009).
[31] H. Hara, Y. Takasu, Y. Yamaoka, J. M. Doyle, and Y. Takahashi, Phys. Rev. Lett. **106**, 205304 (2011).
[32] F. Baumer, F. Münchow, A. Görlitz, S. E. Maxwell, P. S. Julienne, and E. Tiesinga, Phys. Rev. A **83**, 040702(R) (2011).
[33] A. Micheli, G. K. Brennen, and P. Zoller, Nat. Phys. **2**, 341 (2006).
[34] J. J. Hudson, D. M. Kara, I. J. Smallman, B. E. Sauer, M. R. Tarbutt, and E. A. Hinds, Nature (London) **473**, 493 (2011).
[35] M. Kajita, G. Gopakumar, M. Abe, and M. Hada, Phys. Rev. A **84**, 022507 (2011).

Appendix D

Production of quantum-degenerate mixtures of ytterbium and lithium with controllable interspecies overlap

This appendix includes the following paper [112]: A. H. Hansen, A. Y. Khramov, W. H. Dowd, A. O. Jamison, B. Plotkin-Swing, R. J. Roy, and S. Gupta. Production of quantum-degenerate mixtures of ytterbium and lithium with controllable interspecies overlap. *Phys. Rev. A*, 87:013615, 2012.

Production of quantum-degenerate mixtures of ytterbium and lithium with controllable interspecies overlap

Anders H. Hansen, Alexander Y. Khramov, William H. Dowd, Alan O. Jamison, Benjamin Plotkin-Swing, Richard J. Roy, and Subhadeep Gupta

Department of Physics, University of Washington, Seattle, Washington 98195, USA

(Received 12 November 2012; published 16 January 2013)

Quantum-degenerate mixtures of one-electron and two-electron atoms form the starting point for studying few- and many-body physics of mass-imbalanced pairs as well as the production of paramagnetic polar molecules. We recently reported the achievement of dual-species quantum degeneracy of a mixture of lithium and ytterbium atoms. Here we present details of the key experimental steps for the all-optical preparation of these mixtures. Further, we demonstrate the use of the magnetic field gradient tool to compensate for the differential gravitational sag of the two species and control their spatial overlap.

DOI: 10.1103/PhysRevA.87.013615 PACS number(s): 67.85.Pq, 37.10.De, 34.20.−b, 05.30.Fk

I. INTRODUCTION

Elemental quantum mixtures provide a path toward ultracold diatomic polar molecules [1]. Utilizing a second, distinguishable atomic species, such mixtures may also allow for impurity probing of quantum phenomena in an ultracold gas. Interspecies Feshbach resonances can enable studies of few- and many-body phenomena in mass-imbalanced systems. There has been great progress in the development of ultracold bi-alkali-metal gases, motivated by applications towards sympathetic cooling of Fermi gases [2], studies of strongly interacting mass-mismatched systems [3], and production of ultracold polar molecules [4].

Extending the choice of mixture components to include other parts of the periodic table, new scientific opportunities arise. For instance, the ground state of the diatomic molecule might now have a magnetic moment, leading to *paramagnetic* polar molecules. This has been a key motivation for our pursuit of the lithium-ytterbium combination.

The $^2\Sigma$ ground state of the YbLi molecule makes it a candidate system for simulating lattice spin models with applications in topological quantum computation [5]. Additionally, the Yb-Li mixture possesses a very large mass ratio, and a range of isotopic combinations with Bose and Fermi statistics. Tunable interactions between the components can lead to the creation of novel Efimov states [6]. When confined in an optical lattice, a heavy-light fermion mixture can realize the binary alloy model [7], with applications in simulating exotic condensed matter phases (e.g., studies of pattern formation [8,9]).

In previous work, we assessed the collisional stability of the Yb-Li mixture in weakly interacting regimes, and explored the strengths of various inelastic channels in a three-component mixture with one resonantly interacting pair. In this paper we describe the experimental details of our setup, stressing the areas that have required development beyond typical single-species experiments. We report on the production of large-number Bose- and Fermi-degenerate ytterbium gases and assess the cooling limits of the Yb-Li mixture from interspecies interactions. Finally we report the demonstration of interspecies spatial overlap control over a large temperature range, using a magnetic field gradient.

The remainder of this paper is organized as follows. In Sec. II we describe the salient features of our trapping apparatus. Section III discusses our atom manipulation and cooling techniques. In Sec. IV we summarize the performance of our system for the production of degenerate Yb-Li mixtures in different interaction regimes. Section V describes our interspecies spatial-overlap control scheme. Finally, in Sec. VI we present our conclusions and outlook.

II. TRAPPING APPARATUS

Our trapping apparatus uses standard techniques for single-species experiments, applied to two independent atomic sources, as pictured in Fig. 1. Yb and Li beams emerge from separate effusion ovens, and are directed towards the common "main" chamber through individually optimized Zeeman slower sections. The long slower tubes [lengths 93 cm (Li) and 40 cm (Yb), inner diameter 18 mm] also provide differential pumping. An additional stage of differential pumping is provided by a short tube (length 11 cm, inner diameter 5 mm) separating each oven assembly from an independently pumped "intermediate" chamber. We maintain the vacuum in each subchamber with ion pumps, and augment the main chamber vacuum with a titanium sublimation pump. During standard operation, the pressures are approximately $P_{\text{Li oven}} \simeq 3 \times 10^{-8}$ Torr, $P_{\text{Yb oven}} \simeq 1 \times 10^{-7}$ Torr, and $P_{\text{main}} < 1 \times 10^{-10}$ Torr, as measured by ion gauges. Each beamline is equipped with a gate valve, positioned between the oven and intermediate chambers. This allows us to perform single-species experiments, even when the other oven is being serviced.

A. Lithium and ytterbium ovens

The effusion ovens each consist of a vertically oriented "cup," connected via a 90° elbow to a nozzle: a 4-mm-diameter aperture in the Conflat (CF) assembly. We stabilize the Yb (Li) cup temperatures to 400 (375) °C during operation. The nozzles are stabilized at 450 °C permanently to prevent deposition and congestion. The areas between each nozzle and gate valve contain mechanical beam shutters mounted on rotary feedthroughs to control the atom flow to the main chamber, and a copper cold plate (−7 °C) to collect the atomic flux not directed towards the main chamber.

All heated oven parts are of type-316 stainless steel, while the rest of the vacuum apparatus is type-304 stainless steel.

 ©2013 American Physical Society

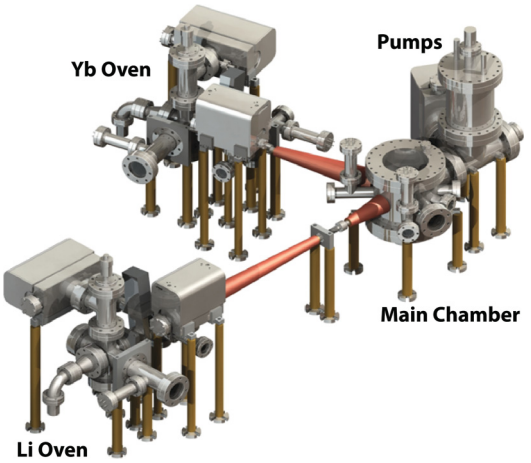

FIG. 1. (Color online) Schematic figure of dual-species apparatus. Ytterbium and lithium are prepared in separate ovens and slowed in individually optimized Zeeman slowers. Each oven is separated from the main chamber by two stages of differential pumping and an independently pumped intermediate chamber. The central part of each intermediate chamber (hidden from view) is a 2.75 in. six-way cross.

For the heated sections of the lithium oven we use nickel CF gaskets, which are more resilient than copper in high-temperature environments in the presence of lithium [10]. We have found, however, that nickel gaskets in the presence of hot Yb vapor undergo corrosive chemical reactions, which compromise the integrity of the vacuum after several months of operation. We now use copper gaskets in the ytterbium oven, which have been trouble-free for two years.

B. Main chamber

Our main chamber has a cylindrical geometry with ten viewports for optical access (Fig. 2). The top and bottom are sealed off by 10 in. CF flanges, into which custom-made re-entrant "buckets" for the electromagnets are recessed. Each bucket also has a 2.75 in. viewport for vertical MOT beams.

We keep the sapphire entry viewports for the Yb (Li) Zeeman slowing laser beams at a permanent 200 (250) °C; otherwise, metallic deposition is clearly evident. All other viewports are BK7 glass antireflection coated at the wavelengths for laser cooling and optical trapping of the two species.

Our experimental setup employs two pairs of electromagnetic coils, shown in Fig. 2. We apply antiparallel currents to the inner pair to generate the quadrupole field for the magneto-optical traps (MOTs), while the outer pair, arranged in parallel (Helmholtz) configuration, provide bias fields to access Feshbach resonances.

The MOT coils produce a vertical gradient of 1.0 G/cm/A, while the bias coils produce 4.2 G/A. We can electronically switch the MOT coils to parallel configuration, in which they yield 2.4 G/A . This allows for larger bias fields and improves the speed of magnetic field ramps.

Each coil is wound from hollow, square copper tubing (outer dimension 1/8 in., inner dimension 1/16 in.). A bias-field upper bound of 1000 G is set by the flow rate of the cooling water through the electromagnets at 100 psi building pressure.

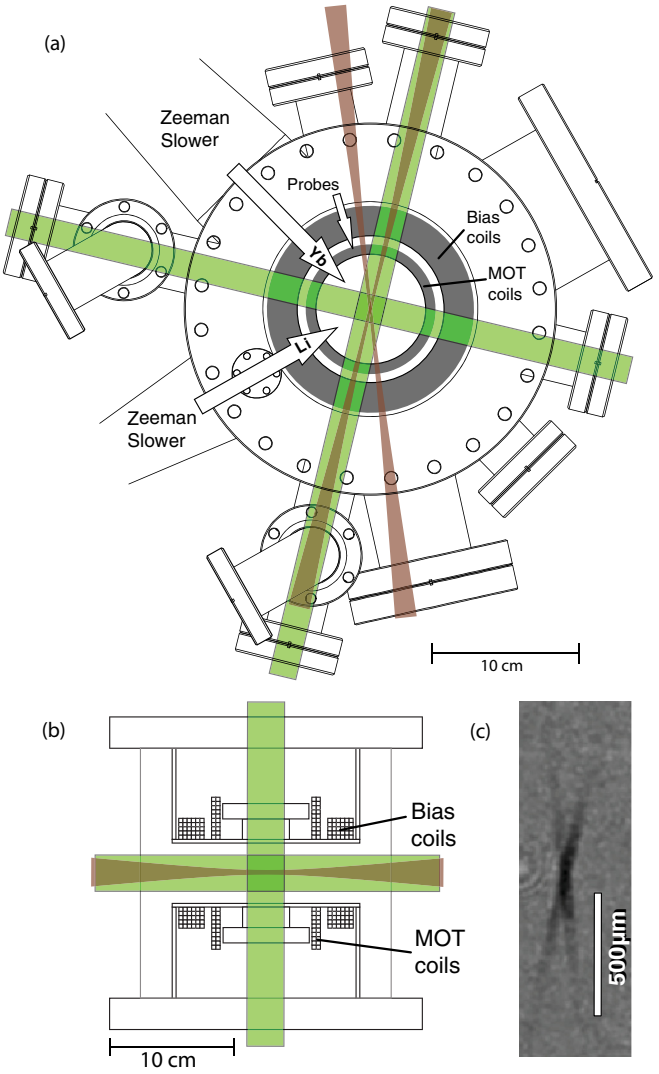

FIG. 2. (Color online) (a) Top view of main chamber, showing the configuration of magneto-optical trap (MOT) beams (green), optical dipole trap (ODT) beams (brown), magnetic coils (gray), and orientation of Yb and Li atomic beams and probe beams (arrows). Vertical MOT beams, vertical probe beams, slowing laser beams, and compensation coils are omitted for clarity. (b) Side view of main chamber, showing vertical and horizontal MOT beams, ODT beams, and recessed buckets with magnetic coils. (c) Sample in-trap absorption image of Yb atoms taken along the vertical axis, immediately after transfer to the ODT. The density distribution clearly shows the crossed-beam geometry. Upon further cooling, the atoms collect in the central crossing point of the two beams.

In order to reach higher fields (up to 1700 G), we employ a booster pump that raises the water pressure to 400 psi.

III. DUAL-SPECIES COOLING AND TRAPPING

We use three laser systems for slowing and laser cooling of lithium and ytterbium: one for ^{6}Li, addressing the $^2S_{1/2} \rightarrow {}^2P_{3/2}$ ($D2$) transition at 671 nm, and two for Yb, addressing the $^1S_0 \rightarrow {}^1P_1$ transition at 399 nm and $^1S_0 \rightarrow {}^3P_1$ (intercombination) transition at 556 nm (Fig. 3). We use acousto-optical modulators (AOMs) to provide all the required

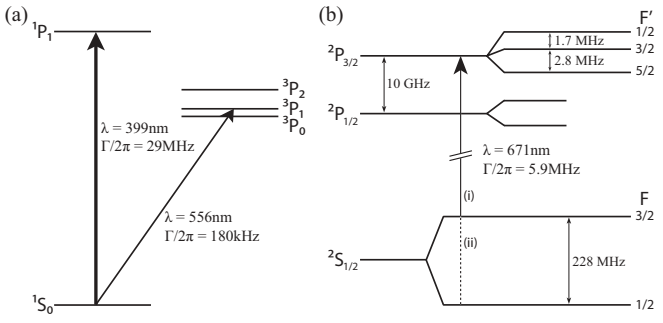

FIG. 3. Relevant energy levels for laser cooling of (a) ^{174}Yb and (b) ^{6}Li. Transitions used for trapping and cooling (see text) are indicated with arrows. In ^{173}Yb, only the excited states acquire hyperfine structure and the cooling lasers are tuned to the appropriate cycling transitions. To address lithium, we require separate frequency components for the cooling (i) and repumping (ii) transitions. The hyperfine splitting of the $^2P_{3/2}$ state is not resolved.

frequency shifts needed for slowing, trapping, repumping, and probing of the atoms.

We derive the 671 nm light from a commercial laser system (Toptica TA100), consisting of an external-cavity diode laser (ECDL) and a tapered amplifier (TA) system. We frequency-stabilize the laser using saturated absorption spectroscopy in a home-built vapor cell, with a lithium sample heated to 420 °C.

We derive the 399 nm light, used for slowing and imaging of Yb, from another commercial system (Toptica TA-SHG pro), consisting of an ECDL at 798 nm, a TA, and a second-harmonic generation (SHG) cavity. We frequency-stabilize this laser using saturated absorption spectroscopy in a commercial hollow-cathode lamp (Hamamatsu Laser Galvatron L2783).

We derive the 556 nm light, used for the Yb MOT, from another commercial system (Toptica FL-SHG pro), consisting of an ECDL, a fiber amplifier, and an SHG cavity. Since the linewidths of the blue and green transitions are different by more than two orders of magnitude, the two lasers require very different Yb column densities for spectroscopy. We frequency-stabilize this laser using saturated absorption spectroscopy in a home-built vapor cell with an ytterbium sample heated to 420 °C. In our setup, to reduce deposition on the cell viewports, we independently heat the viewport flanges while keeping the regions between the atomic sample and the glass at a lower temperature. We have also found it useful to reduce the diameter of the outermost section of the Yb cell on either end to reduce conduction.

A. Zeeman slowers

Each MOT loads from a separate Zeeman-slowed atomic beam. The solenoids for the Zeeman slowers are wound from the same copper wire as the MOT and bias coils. The Li slower uses a "spin-flip" configuration, consisting of a 60-cm-long decreasing-field section followed by a 15-cm-long increasing-field section. We operate each component at 30 A, yielding a net magnetic field variation $|\Delta\mathbf{B}|$ of 980 G. The atoms are slowed by a 40 mW laser beam, 732 MHz red-detuned from the $D2$ transition for the $F = \frac{3}{2}$ state. We derive the slower beam from an injection-locked diode laser. By adding a second injection beam 228 MHz blue-detuned from the first, we obtain light for repumping from the $F = \frac{1}{2}$ ground state within the slower.

The Yb slower consists of a single 40-cm-long increasing-field stage, operated at 15 A to yield $|\Delta\mathbf{B}| = 240$ G. The slowing beam has a power of 100 mW, and a red-detuning of 365 MHz from the $^1S_0 \rightarrow {}^1P_1$ transition.

Compensation coils, mounted opposite to each slower on the main chamber, cancel magnetic fringe fields at the position of the trapped atoms. Together with the vertical bias coils, the slower coils also serve as tools to move the center of the MOT quadrupole along all spatial axes, essential for relative positioning of the traps, as discussed below.

B. Magneto-optical traps

For magneto-optical trapping of the two species we use a standard single-species setup with retroreflected MOT beams [11], modified to accommodate a second atomic species. We combine the beams for the two species using a dichroic mirror, and divide the combined beam into three beams using broadband polarizing beam splitters. The polarizations are controlled by single-wavelength half-wave plates and dual-wavelength quarter-wave plates (Foctek).

Several factors have to be considered in determining the optimum parameters for dual-species laser cooling. Due to the difference in linewidth of the Li $D2$ and Yb intercombination lines (factor of 32) the two MOTs are optimized at very different magnetic gradients (see Table I). Furthermore, the optimal duration of the transitional cooling step (compression) before loading into the ODT differs greatly for the two species. Finally, the two species experience significant losses through inelastic collisions when the magneto-optical traps are spatially overlapped.

We find that the best performance in our setup is achieved using a sequential loading scheme, as described in [12], with typical parameters as listed in Table I. To summarize, we load Yb alone for 10–30 s, depending on experimental requirements. During this time, the detuning of the trapping light is modulated with an amplitude of 20 linewidths, at a frequency of 50 kHz, to increase the phase-space volume of the trapping region. We then compress Yb in 200 ms, and transfer it to the ODT. We subsequently optimize the

TABLE I. Typical experimental parameters for loading of ^{6}Li, ^{174}Yb, and ^{173}Yb: laser intensity I and red-detuning δ, and magnetic axial (vertical) field gradient B'. Two sets of numbers are provided for each isotope, reflecting the parameters for MOT loading and for the end point of compression (see the text) before transfer to the ODT. I refers to the total laser intensity in all three retroreflected beams; the total optical intensity at the atoms is twice the listed value. Γ and $I_{\rm sat}$ for Yb refer to the properties of the intercombination transition.

		^{6}Li $F = 3/2$	^{6}Li $F = 1/2$	^{174}Yb	^{173}Yb
Load	I	$60I_{\rm sat}$	$55I_{\rm sat}$	$750I_{\rm sat}$	$750I_{\rm sat}$
	δ	6Γ	3.5Γ	$(55 \pm 20)\Gamma$	$(40 \pm 20)\Gamma$
	B'	20 G/cm		3 G/cm	3 G/cm
Final	I	$0.07I_{\rm sat}$	$0.08I_{\rm sat}$	$0.8I_{\rm sat}$	$2I_{\rm sat}$
	δ	1.5Γ	3Γ	2Γ	4Γ
	B'	60 G/cm		18 G/cm	25 G/cm

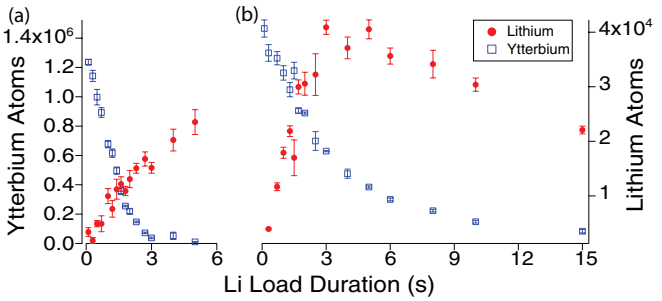

FIG. 4. (Color online) Number of trapped atoms, after a variable Li load time and 1 s hold in the ODT at fixed depth. (a) [(b)] shows results with a vertical bias field of 0 (2) G, corresponding to a 1 mm center-of-mass displacement of the Li MOT. In the favorably displaced case (b), Li numbers are optimized at a finite load time; at longer load times sympathetic cooling becomes inefficient due to low Yb numbers. Each error bar represents statistical fluctuations of four experimental iterations.

quadrupole field for lithium, load the Li MOT for 0.5–4 s (depending on experimental requirements), compress in 50 ms, and transfer to the ODT. A short (100 μs) pulse of light resonant with the Li $F = \frac{3}{2}$ $D2$ transition optically pumps the Li atoms into the ground $F = \frac{1}{2}$ state.

The positioning of the Li MOT during load is crucial for large dual-species samples as can be seen in Fig. 4. The large losses for suboptimal positioning can be interpreted as a consequence of elastic collisions that heat Yb through contact with the Li MOT, and also of inelastic collisions of ground-state Yb with electronically excited Li atoms in which both constituents are lost. The latter process also impedes the rate at which the Li MOT loads, as can be observed in Fig. 4.

We mitigate this effect by applying a bias field during the Li load, which spatially offsets the MOT from the ODT. With a vertical bias field of 2 G the lifetime of Yb atoms is quadrupled. Although this lifetime is less than the vacuum-limited lifetime of ∼45 s, this still leads to simultaneous confinement of 10^6 Yb atoms and 10^5 Li atoms in the ODT, immediately after switching off all the laser cooling beams.

Due to the greater abundance of Yb in the ODT, as well as its lower MOT temperature, Yb acts as a coolant for Li. At zero bias field we observe that, in the absence of Yb, most of the Li atoms spill from the trap during the first 1 s after transfer from the MOT. With a large bath of Yb present, these losses are mitigated, as the Li atoms thermalize with the bath.

C. Optical dipole trap

We derive our ODT from an ytterbium fiber laser (IPG Photonics YLR-100-LP) that can provide up to 100 W laser power at 1064 nm. During standard operation, we run the laser at 40 W. We send the laser output through an AOM and split the first-order output into two components of equal power and orthogonal polarization. Each component is focused to a waist of ≈26 μm and crossed at a 20° angle at the atoms. As shown in Fig. 2, both beams are horizontally aligned through the chamber. This configuration provides a straightforward geometry for our crossed ODT.

We perform evaporative cooling by controlling the efficiency of the ODT AOM. The geometry of the trap is thus preserved during evaporation, and trap frequencies may be interpolated between measurements at various depths [13].

D. Evaporative and sympathetic cooling strategies

For a given intensity of the 1064 nm ODT beam, the optical potential for Li is greater than that for Yb by a factor of about 2. Thus, at the same temperature, Yb will evaporate from the trap significantly faster than Li. For this reason, and because the Li (linear) size is smaller by a factor of 0.7 at equal temperature, the most practical cooling strategy involves sympathetically cooling Li in a bath of Yb. We thus optimize the initial conditions to a larger proportion ($\geqslant$90%) of trapped Yb, and set the rate of evaporative cooling to match the interspecies thermalization time, which is of order 1 s throughout. This method works well even in the regime of quantum degeneracy, since the condensation temperature for Yb is an order of magnitude lower than the Li Fermi temperature (for equal Li and Yb numbers). A more detailed discussion of this scheme can be found in [14].

We believe that this method of cooling will readily transfer to other alkali metal + spin-singlet systems, where some performance aspects may be even better than in Yb-Li. The number of interspecies collisions necessary for thermalization between particles of masses m_1 and m_2 is of order $2.7/\xi$, where the dimensionless parameter $1/\xi = (m_1 + m_2)^2/4m_1m_2$ [15]. For ^{6}Li and ^{174}Yb, $2.7/\xi = 21$, which is relatively large. Furthermore, since Li cannot be laser cooled to such low temperatures as Yb, a considerable amount of Yb is lost through evaporation during initial thermalization. Both of these effects will be less severe with other alkali-metal atoms such as Na, K, Rb, and Cs. We also note that a similar mismatch of trap depth in a 1064 nm ODT will exist and a similar immunity to two-body inelastic losses is expected, both advantageous for sympathetic cooling with Yb [16].

E. Simultaneous dual-species imaging

We simultaneously probe the collocated, optically trapped clouds of Li and Yb using absorption imaging. The imaging beams are overlapped before they enter the vacuum chamber, using a broadband polarizing beam splitter. The beams are split after they emerge from the vacuum chamber using dichroic mirrors, and the cloud images are projected onto two different regions of the CCD camera chip. Absorption images for both clouds are obtained for each experimental iteration.

IV. Yb-Li QUANTUM MIXTURES

Our quantum mixture preparation relies on the direct evaporative cooling of Yb which then cools the co-trapped Li sympathetically, as described in Sec. III D. Cooling in the absence of an external magnetic field leads to weakly interacting Bose-Fermi mixtures. By applying external magnetic fields, strongly interacting regimes may then be accessed through available Feshbach resonances. In this section, we first report our current system performance for producing quantum-degenerate gases of single-species Yb isotopes. We then present the production of weakly interacting Yb-Li mixtures through sympathetic cooling. Finally we briefly discuss regimes of strong interactions in Yb-Li mixtures.

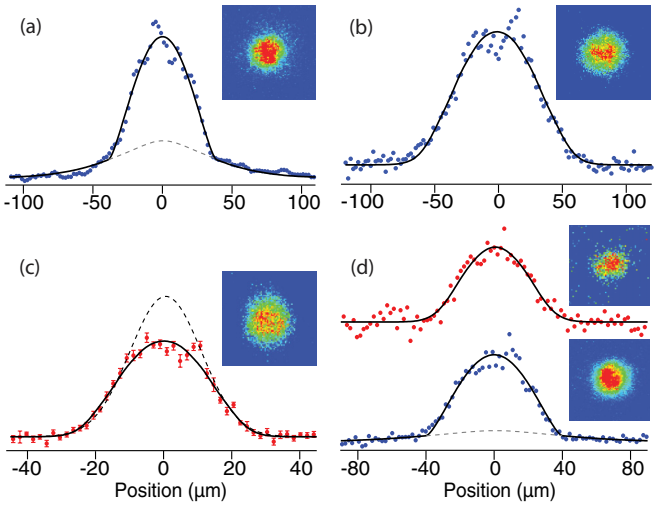

FIG. 5. (Color online) Density cross sections of lithium and ytterbium from absorption images (insets) of degenerate gases. (a) Quantum-degenerate gas of ^{174}Yb atoms with 2.5×10^5 atoms in the condensate imaged at a time of flight (TOF)12 ms. (b) Degenerate Fermi gas of 1×10^5 ^{173}Yb atoms with $T/T_F = 0.3$ and TOF 5 ms. (c) Degenerate Fermi gas of 1.6×10^4 ^{6}Li atoms with $T/T_F \approx 0.06$ and TOF 0.4 ms. (d) Simultaneous quantum degeneracy of ^{6}Li and ^{174}Yb with 2×10^4 (3×10^4) atoms of Li (Yb). $T/T_F \approx 0.2$ for Li and TOF 0.5 (10) ms. Solid lines are least-square fits to local-density-approximation models for Bose and Fermi gases, while dashed lines are classical fits to the wings of the distributions.

A. Quantum-degenerate ytterbium

Our current apparatus has several new features beyond what was reported in [14]. Our Yb laser cooling procedure now employs greater power and frequency sweep range in the MOT beams during load (see Sec. III). The optical trap now features electronic stabilization of depth and adjustable volume through a time-averaged potential generated by frequency modulation of the ODT AOM [18]. This "painting" of the potential increases the volume of the loading trap and allows a much larger load of Yb. Optimization of both loading and evaporation is obtained by continuously reducing the volume and the depth of the trap during evaporative cooling. Loading from 7×10^7 laser-cooled atoms at a temperature of $\simeq 20$ μK, we achieve an optical trap load of up to 5×10^6 atoms and ^{174}Yb condensate numbers of 3×10^5 [Fig. 5(a)]. Applied to fermionic ^{173}Yb, we can achieve up to 1.2×10^5 [Fig. 5(b)] atoms in a mixture of the six spin states at $\frac{T}{T_F} = 0.3$. By reducing the loading and evaporative cooling sequence times, we can improve the repetition rate of Yb condensate production to 10 s, with (5×10^4)-atom Bose-Einstein condensates (BECs). Fast experimental repetition rates are crucial to precision measurements with BECs, which depend on large statistical data samples [19].

B. Weakly interacting quantum-degenerate Yb-Li mixture

For dual-species experiments in which Li is co-trapped and sympathetically cooled by Yb, the time-averaging option is not used as the accompanying reduction in trap depth is too great to efficiently load Li into the optical trap. As noted earlier, the larger polarizability of Li makes Yb a suitable sympathetic coolant. At the lowest temperatures, the large mass difference affects the standard procedure in two significant ways—the degeneracy temperatures for equal numbers are different by an order of magnitude, and the differential gravity-induced trap modification is relatively large.

By controlling the final depth of the evaporation ramp, we achieve simultaneous degeneracy, with similar atom numbers (few $\times 10^4$) of each species. The quantum-degenerate Yb-Li mixture at zero external magnetic field [Fig. 5(d)] is weakly interacting with interspecies scattering length of magnitude $13a_0$ [12,14,20]. In our system, $N_{\rm Li} \approx N_{\rm Yb}$ when the condensation temperature T_C is achieved. By this stage of the cooling the volume of the Li Fermi gas (constrained by Fermi degeneracy) is larger than that of the coolant Yb bosons. The reduction in size and heat capacity of the coolant, and the differential gravitational sag are all effects which can reduce the sympathetic cooling efficiency [14]. Further, we might expect a reduction in condensate number in the presence of Li, due to collisions between energetic Li atoms near the Fermi velocity $v_F \simeq 5$ cm/s and the Yb BEC (peak condensate speed of sound $v_c \simeq 1$ mm/s), which may explain the condensate number reduction reported in [20].

In spite of the aforementioned issues, sympathetic cooling can produce deeply degenerate Fermi gases in our apparatus. By sacrificing all of the coolant Yb through evaporation, temperatures below $0.1T_F$ can be achieved [Fig. 5(c)]. By keeping a small amount of Yb in the trap, we establish a system in which Yb may act as an impurity probe of the ^{6}Li degenerate Fermi gas.

C. Yb-Li mixtures in strongly interacting regimes

Two different regimes of strong interactions in the Yb-Li system are of current scientific interest. The first one is a three-component system of Yb and two resonantly interacting Li spin states, a regime recently explored experimentally by Khramov *et al.* [21]. Here studies of strongly interacting Fermi gases using Yb as a dissipative bath or an impurity probe may be carried out. While the strong interactions induce inelastic loss processes at unitarity, which are unobservable in the weakly interacting regime, the interspecies elastic processes still dominate and we have observed temperatures as low as $0.25T_F$.

The other strongly interacting regime of current interest is a Feshbach resonance between Yb and Li atoms. Theoretical calculations by Brue and Hutson [22], predict narrow magnetically induced Feshbach resonances between ^{173}Yb and ^{6}Li. These have not yet been experimentally observed.

A fundamental limiting factor in preserving interspecies contact in degenerate Yb-Li mixtures is the differential gravitational sag of the two species at low trap depths. In our trap, the Yb atoms, due to their greater mass and weaker optical confinement, become significantly displaced from the Li atoms at temperatures near 300 nK, compromising the efficiency of sympathetic cooling and generally the study of any interspecies interaction effects. A technique for circumventing this limitation is discussed in the following section.

V. CONTROL OF INTERSPECIES SPATIAL OVERLAP

Differences in internal properties between components of an ultracold mixture can result in a differential response to external fields. This sometimes leads to unwanted effects such as the differential vertical displacement due to gravity experienced in mixtures with unequal mass constituents. For the weak optical potentials needed to achieve the highest phase-space densities, this "gravitational sag" leads to reduced spatial overlap and reduced interspecies interactions. The differential gravitational sag is an important limiting factor for the molecule formation efficiency in the K-Rb mixture [23], where the mass ratio is 2.2. In the case of the Yb-Li mixture, where the mass ratio is 29, this effect is even more significant, leading to a nearly complete decoupling of the two species at the lowest temperatures [14]. Here we demonstrate that this differential gravitational sag can be mitigated by the use of a magnetic field gradient which exerts a force on only the lithium component.

In principle, one may use external magnetic fields to achieve independent control of any two atomic species. For instance, in alkali-metal atoms with half-integer nuclear spin there will exist states with magnetic projection $m_F = 0$ in the direction of the magnetic field, allowing one species to be made insensitive to magnetic gradients. However, this insensitivity does not extend to the high magnetic fields often required in experiments (e.g., to address Feshbach resonances) due to hyperfine decoupling. Furthermore, mixtures of high-field- and low-field-seeking atoms are prone to inelastic, internal state-changing collisions, which lead to trap losses.

Mixtures of alkali-metal and alkaline-earth-metal atoms avoid these limitations as the ground-state magnetic moment of the alkaline-earth-metal species is zero or nearly zero for all external fields. Furthermore, in isotopes with zero nuclear moment, spin-exchange collisions are suppressed entirely. This feature has been used to overlap clouds of magnetically trapped rubidium atoms with optically trapped ytterbium atoms [24]. Here we report on manipulating the relative displacement of two species that are confined in the same optical trapping potential, and over a large temperature range down to <1 μK.

When atoms in a trap are subjected to a uniform force $F = mg$, the center of mass is displaced by an amount $\Delta z = g/\omega^2$, where ω is the vertical trapping frequency. Due to differences in mass and polarizability, the trap frequencies for Li and Yb differ by a factor of 8, leading to substantial differential gravitational sag at low trap depths.

We demonstrate control of interspecies spatial overlap by applying a magnetic gradient which acts as a "pseudogravitational" force on Li only. We first prepare a mixture of ^{6}Li in its two lowest-energy states and the single ground state of ^{174}Yb at a particular optical trap depth. For experimental simplicity, we ramp the bias field to 530 G, where the two Li spin states have equal magnetic moments $1\mu_B$ and negligible interaction strength. We then turn on our MOT coils to add a magnetic quadrupole field to the vertical bias field, thereby creating a magnetic force in the direction of the bias field. Our system is capable of producing vertical gradients up to 170 G/cm; however, a more modest gradient of 65 G/cm is sufficient to make the atom clouds concentric.

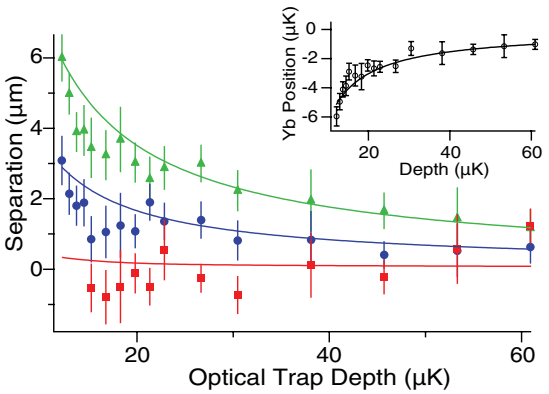

FIG. 6. (Color online) Relative displacement of centers of mass of Li and Yb clouds, versus optical trap depth for Yb atoms, at various magnetic gradients: -13 G/cm (filled triangles), 35 G/cm (filled circles), and 64 G/cm (filled squares). Each data point gives the average center-of-mass position of between 7 and 12 absorption images of lithium, subtracted from the average of 11 ytterbium images. The inset shows the displacement of Yb from the ODT beam center. The solid lines are results of a numerical model.

Figure 6 shows the separation of the cloud centers as a function of optical potential for different magnetic gradients. The gradient strength was determined by releasing the Li atoms and imaging them after a variable time to measure the acceleration $\mu_B B'/m_{\mathrm{Li}} + g$. The analysis also identified and corrected for slight ($<1^\circ$) deviations of the long trap axis from horizontal and the magnetic bias from vertical.

The lowest Yb optical trap depth for the data in Fig. 6 is 12 μK. Due to gravity, this corresponds to an effective trap depth of 4 μK, which goes to zero at an optical trap depth of 6 μK. We observe the onset of BEC at 15 μK optical depth when loading Yb alone.

At the lowest depths, the in-trap $1/e$ height of the ytterbium cloud is approximately 2 μm, whereas the Li cloud size is near the Fermi radius of 6 μm. Thus, in the absence of a magnetic gradient, the spatial overlap of the two clouds is critically reduced at trap depths below 20 μK.

Also shown in Fig. 6 is a set of theoretical curves of relative displacement, derived from a simple numerical model assuming a Gaussian trap profile. The only variable parameter in the model is the ODT (vertical) beam waist, which agrees at the 10% level with measurements of trap frequency via parametric excitation. We find reasonably good agreement between this model and the experimental data, although the calculation slightly overestimates the degree of sag at the lowest trap depths. One plausible explanation for this is a small vertical misalignment of the ODT beams, leading to a deviation from a Gaussian profile.

A side effect of this technique is that the applied gradient, while shifting the center of the trap, also effectively lowers the trap depth. Thus, for deeply degenerate Fermi clouds where the initial trap depth is close to the Fermi temperature, the "tilted" potential leads to spilling of Li atoms near the Fermi energy. This effect appears as a gradient-dependent Li number loss at

the lowest depths (when $T \lesssim 0.1T_F$) in our experiment and has been utilized elsewhere to measure interaction strength in Fermi gases [25] and to accelerate evaporative cooling in Bose gases [26].

We also note that the field inhomogeneity introduced by the magnetic gradient can limit its usefulness in experiments that require extremely homogeneous magnetic fields. For instance, a gradient of 65 G/cm corresponds to a magnetic field variation of tens of milligauss across the sample, much larger than the theoretical width of the predicted magnetic Feshbach resonances between ^{173}Yb and ^{6}Li [22].

Species-selective control of atomic samples has also been demonstrated using only optical fields. Bichromatic optical traps exploiting the different ac Stark shifts of atoms have been demonstrated [24]. Our technique has the advantage of requiring no additional lasers or sensitive alignment of optics. The effect is achieved entirely with existing hardware, operating under typical conditions.

In addition to the application described above, the magnetic gradient technique enables experiments involving the use of one atomic species as a local probe of the other. In the ^{6}Li-^{174}Yb system, the Yb acts as a "bath" at temperatures above degeneracy, where its cloud is much larger than that of Li. At low temperatures, Yb can act as a "probe," since the Yb cloud is much smaller than the Li Fermi radius [21]. Under the latter conditions, Yb can be a useful probe for studying the local properties of a Fermi gas in the weakly interacting as well as in the superfluid regime.

Beyond spatial control, one can also use magnetic gradients to achieve selective control of the momentum of the magnetically sensitive species, by changing the gradient nonadiabatically. Such velocity-control techniques may be useful for a range of studies, such as measures of viscosity and tests of superfluidity.

VI. CONCLUSIONS AND OUTLOOK

We have presented a detailed description of our apparatus to produce stable quantum mixtures of lithium and ytterbium atoms. We have also demonstrated a method of controlling the spatial overlap of the two species, general to combinations of magnetic and nonmagnetic atoms. When prepared near the ^{6}Li Feshbach resonance, bosonic Yb can act as a microscopic probe of the strongly interacting lithium Fermi gas. Other future applications of the mixture include the study of condensed matter models in an optical lattice, such as the binary-alloy model.

An interspecies Feshbach resonance between lithium and ytterbium will allow the exploration of three-body Efimov states with large mass mismatch, and potential studies of the many-body physics of mass-imbalanced pairs. While such resonances have not yet been observed, they may show up in the near future in experiments with the ground-state mixture, or by using Yb in an excited metastable state (such as $^{3}P_2$) [27]. An additional possibility is an interspecies optical Feshbach resonance [28]. Finally, the quantum-degenerate mixture of lithium and ytterbium provides the starting point for the production of quantum gases of paramagnetic polar molecules of YbLi. Such ultracold molecules are of general interest from the perspective of quantum simulation [5], quantum information [29], tests of fundamental symmetries [30], and probes of time variations of physical constants [31].

ACKNOWLEDGMENTS

We thank Lee Willcockson and Ryan Weh for major technical contributions during the early stages of the experiment. This work was supported by the National Science Foundation, the Air Force Office of Scientific Research, the Alfred P. Sloan Foundation, the UW Royalty Research Fund, and NIST.

[1] L. D. Carr, D. DeMille, R. V. Krems, and J. Ye, New J. Phys. **11**, 055049 (2009).
[2] Z. Hadzibabic, C. A. Stan, K. Dieckmann, S. Gupta, M. W. Zwierlein, A. Görlitz, and W. Ketterle, Phys. Rev. Lett. **88**, 160401 (2002).
[3] C. Kohstall, M. Zaccanti, M. Jag, A. Trenkwalder, P. Massignan, G. M. Bruun, F. Schreck, and R. Grimm, Nature (London) **485**, 615 (2012).
[4] K.-K. Ni, S. Ospelkaus, M. H. G. de Miranda, A. Peer, B. Neyenhuis, J. J. Zirbel, S. Kotochigova, P. S. Julienne, D. S. Jin, and J. Ye, Science **322**, 231 (2008).
[5] A. Micheli, G. K. Brennen, and P. Zoller, Nat. Phys. **2**, 341 (2006).
[6] E. Braaten and H. W. Hammer, Phys. Rep. **428**, 259 (2006).
[7] C. Ates and K. Ziegler, Phys. Rev. A **71**, 063610 (2005).
[8] M. M. Maska, R. Lemanski, J. K. Freericks, and C. J. Williams, Phys. Rev. Lett. **101**, 060404 (2008).
[9] M. M. Maska, R. Lemanski, C. J. Williams, and J. K. Freericks, Phys. Rev. A **83**, 063631 (2011).
[10] C. A. Stan and W. Ketterle, Rev. Sci. Instrum. **76**, 063113 (2005).
[11] H. J. Metcalf and P. Van der Straten, *Laser Cooling and Trapping* (Springer, Berlin, 1999).
[12] V. V. Ivanov, A. Khramov, A. H. Hansen, W. H. Dowd, F. Münchow, A. O. Jamison, and S. Gupta, Phys. Rev. Lett. **106**, 153201 (2011).
[13] At the highest laser powers (>50 W), however, we have observed thermal lensing effects in various optical components in the ODT path.
[14] A. H. Hansen, A. Khramov, W. H. Dowd, A. O. Jamison, V. V. Ivanov, and S. Gupta, Phys. Rev. A **84**, 011606(R) (2011).
[15] A. Mosk, S. Kraft, M. Mudrich, K. Singer, W. Wohlleben, R. Grimm, and M. Weidemüller, Appl. Phys. B: Lasers Opt. **73**, 791 (2001).
[16] Three-body losses may then be the dominant loss mechanism, as in the ^{174}Yb-^{87}Rb mixture [17].
[17] F. Baumer, F. Münchow, A. Görlitz, S. E. Maxwell, P. S. Julienne, and E. Tiesinga, Phys. Rev. A **83**, 040702(R) (2011).
[18] K. Henderson, C. Ryu, C. MacCormick, and M. Boshier, New J. Phys. **11**, 043030 (2009).
[19] A. O. Jamison, J. N. Kutz, and S. Gupta, Phys. Rev. A **84**, 043643 (2011).

[20] H. Hara, Y. Takasu, Y. Yamaoka, J. M. Doyle, and Y. Takahashi, Phys. Rev. Lett. **106**, 205304 (2011).
[21] A. Y. Khramov, A. H. Hansen, A. O. Jamison, W. H. Dowd, and S. Gupta, Phys. Rev. A **86**, 032705 (2012).
[22] D. A. Brue and J. M. Hutson, Phys. Rev. Lett. **108**, 043201 (2012).
[23] J. J. Zirbel, K.-K. Ni, S. Ospelkaus, J. P. D'Incao, C. E. Wieman, J. Ye, and D. S. Jin, Phys. Rev. Lett. **100**, 143201 (2008).
[24] S. Tassy, N. Nemitz, F. Baumer, C. Höhl, A. Batar, and A. Görlitz, J. Phys. B **43**, 205309 (2010).
[25] S. Jochim, M. Barternstein, A. Altmeyer, G. Hendl, S. Riedl, C. Chin, J. Hecker Deschlag, and R. Grimm, Science **302**, 2101 (2003).
[26] C.-L. Hung, X. Zhang, N. Gemelke, and C. Chin, Phys. Rev. A **78**, 011604(R) (2008).
[27] S. Kato, S. Sugawa, K. Shibata, R. Yamamoto, and Y. Takahashi, arXiv:1210.2483.
[28] S. Blatt, T. L. Nicholson, B. J. Bloom, J. R. Williams, J. W. Thomsen, P. S. Julienne, and J. Ye, Phys. Rev. Lett. **107**, 073202 (2011).
[29] D. DeMille, Phys. Rev. Lett. **88**, 067901 (2002).
[30] J. J. Hudson, D. M. Kara, I. J. Smallman, B. E. Sauer, M. R. Tarbutt, and E. A. Hinds, Nature (London) **473**, 493 (2011).
[31] M. Kajita, G. Gopakumar, M. Abe, and M. Hada, Phys. Rev. A **84**, 022507 (2011).

References

[1] C. B. Schaffer. *Interaction of Femtosecond Laser Pulses with Transparent Materials.* PhD thesis, Harvard University, 2001.

[2] M. H. Anderson, J. R. Ensher, M. R. Matthews, C. E. Wieman, and E. A. Cornell. Observation of Bose-Einstein condensation in a dilute atomic vapor. *Science*, 269:198, 1995.

[3] K. B. Davis, M.-O. Mewes, M. R. Andrews, N. J. van Druten, D. S. Durfee, D. M. Kurn, and W. Ketterle. Bose-Einstein condensation in a gas of sodium atoms. *Phys. Rev. Lett.*, 75:(22):3969, 1995.

[4] B. DeMarco and Jin. D. S. Onset of Fermi degeneracy in a trapped atomic gas. *Science*, 285:1703, 1999.

[5] F. Schreck, L. Khaykovich, K. L. Corwin, G. Ferrari, T. Bourdel, J. Cubizolles, and C. Salomon. Quasipure Bose-Einstein condensate immersed in a Fermi sea. *Phys. Rev. Lett*, 87:080403, 2001.

[6] M. W. Zwierlein, C. H. Schunck, A. Schirotzek, and W. Ketterle. Vortices and superfluidity in a strongly interacting Fermi gas. *Nature*, 435:1047, 2005.

[7] M. W. Zwierlein, A. Schirotzek, C. H. Schunck, and W. Ketterle. Fermionic superfluidity with imbalanced spin populations. *Science*, 311:492, 2006.

[8] M. Greiner, C. A. Regal, and D. S. Jin. Emergence of a molecular Bose-Einstein condensate from a Fermi gas. *Nature*, 426:537, 2003.

[9] M. Bartenstein, A. Altmeyer, S. Riedl, S. Jochim, C. Chin, J. Heckler Denschlag, and R. Grimm. Crossover from a molecular Bose-Einstein condensate to a degenerate Fermi gas. *Phys. Rev. Lett*, 92:120401, 2004.

[10] C. C. Bradley, C. A. Sackett, and R. G. Hulet. Bose-Einstein condensation of lithium: Observation of limited condensate number. *Phys. Rev. Lett.*, 78:985, 1997.

[11] D. G. Fried, T. C. Killian, L. Willmann, D. Landhuis, S. C. Moss, D. Kleppner, and T. J. Greytak. Bose-Einstein condensation of atomic hydrogen. *Phys. Rev. Lett.*, 81:3811, 1998.

[12] T. Weber, J. Herbig, M. Mark, H.-C. Nagerl, and R. Grimm. Bose-Einstein condensation of cesium. *Science*, 299:232, 2003.

[13] Y. Takasu, K. Maki, K. Komori, T. Takano, K. Honda, M. Kumakura, T. Yabuzaki, and Y. Takahashi. Spin-singlet Bose-Einstein condensation of two-electron atoms. *Phys. Rev. Lett.*, 91:040404, 2003.

[14] A. Robert, O. Sirjean, A. Browaeys, J. Poupard, S. Nowak, D. Boiron, C. I. Westbrook, and A. Aspect. A Bose-Einstein condensate of metastable atoms. *Science*, 292:461, 2001.

[15] S. Kraft, F. Vogt, O. Appel, F. Riehle, and U. Sterr. Bose-Einstein condensation of alkaline earth atoms: ^{40}Ca. *Phys. Rev. Lett.*, 103:130401, 2009.

[16] S. Stellmer, M. K. Tey, B. Huang, R. Grimm, and F. Schreck. Bose-Einstein condensation of strontium. *Phys. Rev. Lett.*, 103(200401), 2009.

[17] A. Griesmaier, J. Werner, S. Hensler, J. Stuhler, and T. Pfau. Bose-Einstein condensation of chromium. *Phys. Rev. Lett.*, 94:160401, 2005.

[18] M. Lu, N. Q. Burdick, S. H. Yourn, and B. L. Lev. Strongly dipolar Bose-Einstein condensate of dysprosium. *Phys. Rev. Lett.*, 107:190401, 2011.

[19] K. Aikawa, A. Frisch, M. Mark, S. Baier, A. Rietzler, R. Grimm, and F. Ferlaino. Bose-Einstein condensation of erbium. *Phys. Rev. Lett.*, 108:210401, 2012.

[20] E. S. Shuman, J.F. Barry, and D. DeMille. Laser cooling of a diatomic molecule. *Nature*, 467:820, 2010.

[21] C. A. Regal, C. Ticknor, J. L. Bohn, and D. S. Jin. Creation of ultracold molecules from a Fermi gas of atoms. *Nature*, 424:47, 2003.

[22] K. E. Strecker, G. B. Partridge, and R. G. Hulet. Conversion of an atomic Fermi gas to a long-lived molecular Bose gas. *Phys. Rev. Lett.*, 91(080406), 2003.

[23] K.-K. Ni, S. Ospelkaus, M. H. G. de Miranda, A. Peer, B. Neyenhuis, J. J. Zirbel, S. Kotochigova, P. S. Julienne, D. S. Jin, and J. Ye. A high phase-space-density gas of polar molecules. *Science*, 322:231, 2008.

[24] J. Deiglmayr, A. Grochola, M. Repp, K. Mortlbauer, C. Gluck, J. Lange, O. Dulieu, R. Wester, and M. Weidemuller. Formation of ultracold polar molecules in the rovibrational ground state. *Phys. Rev. Lett.*, 101:133004, 2008.

[25] D. E. Miller, J. K. Chin, C. A. Stan, Y. Liu, W. Setiawan, C. Sanner, and W. Ketterle. Critical velocity for superfluid flow across the BEC-BCS crossover. *Phys. Rev. Lett.*, 99:070402, 2007.

[26] E. A. Hinds. Testing time reversal symmetry using molecules. *Phys. Scr.*, T70:34, 1997.

[27] W. Ketterle, D. S. Durfee, and D. M. Stamper-Kurn. Making, probing and understanding Bose-Einstein condensates. In *Proceedings of the International School of Physics "Enrico Fermi"*, volume CXL.

[28] W. Ketterle and M. W. Zwierlein. Making, probing and understanding ultracold Fermi gases. In *Ultracold Fermi Gases, Proceedings of the International School of Physics "Enrico Fermi"*, volume CLXIV.

[29] S. Giorgini, L. P. Pitaevskii, and S. Stringari. Theory of ultracold atomic Fermi gases. *Rev. Mod. Phys.*, 80:1215, 2008.

[30] F. Dalfovo, S. Giorgini, L. P. Pitaevskii, and S. Stringari. Theory of Bose-Einstein condensation in trapped gases. *Rev. Mod. Phys.*, 71:463, 1999.

[31] J. Herbig, T. Kraemer, M. Mark, T. Weber, C. Chin, H.-C. Nagerl, and R. Grimm. Preparation of a pure molecular quantum gas. *Science*, 301:1510, 2003.

[32] C. A. R. Sa de Melo, M. Randeria, and J. R. Engelbrecht. Crossover from BCS to Bose superconductivity: Transition temperature and time-dependent Ginzburg-Landau theory. *Phys. Rev. Lett.*, 71:3202, 1993.

[33] A. Bulgac, J. E. Drut, and P. Magierski. Quantum Monte Carlo simulations of the BCS-BEC crossover at finite temperature. *Phys. Rev. A*, 78:023625, 2008.

[34] E. Burovski, E. Kozik, N. Prokof'ev, B. Svistunov, and M. Troyer. Critical temperature curve in BEC-BCS crossover. *Phys. Rev. Lett.*, 101:090402, 2008.

[35] M. J. H. Ku, A. T. Sommer, L. W. Cheuk, and M. W. Zwierlein. Revealing the superfluid lambda transition in the universal thermodynamics of a unitary Fermi gas. *Science*, 335:563, 2012.

[36] A. Perali, P. Pieri, G. C. Stringari, and C. Castellani. Pseudogap and spectral function from superconducting fluctuations to the bosonic limit. *Phys. Rev. B*, 66:024510, 2002.

[37] J. P. Gaebler, J. T. Stewart, T. E. Drake, D. S. Jin, A. Perali, P. Pieri, and G. C. Strinati. Observation of pseudogap behaviour in a strongly interacting Fermi gas. *Nature Physics*, 6:569, 2010.

[38] G. P. Partridge, W. Li, R. I. Kamar, Y. Liao, and R. G. Hulet. Pairing and phase separation in a polarized Fermi gas. *Science*, 311:503, 2006.

[39] E. Braaten and H. W. Hammer. Universality in few-body systems with large scattering length. *Phys Rep*, 428:259, 2006.

[40] E. R. Hudson, J. R. Bochinski, H. J. Lewandowski, B. C. Sawyer, and J. Ye. Efficient Stark deceleration of cold polar molecules. *Eur. Phys. J. D*, 31:351, 2004.

[41] M. Zeppenfield, B. G. U. Englert, R. Glöckner, A. Prehn, M. Mielenz, C. Sommer, L. D. van Buuren, M. Motsch, and G. Rempe. Sisyphus cooling of electrically trapped polyatomic molecules. *Nature*, 491:570, 2012.

[42] B. K. Stuhl, M. T. Hummon, M. Yeo, G. Quéméner, J. L. Bohn, and J. Ye. Evaporative cooling of the dipolar hydroxyl radical. *Nature*, 492:396, 2012.

[43] L. D. Carr, D. DeMille, R. V. Krems, and J. Ye. Cold and ultracold molecules: science, technology, and applications. *New J. Phys.*, 11:055049, 2009.

[44] T. V. Tscherbul and R. V. Krems. Quantum theory of chemical reactions in the presence of electromagnetic fields. *J. Chem. Phys.*, 129:034112, 2008.

[45] H. Lefebvre-Brion and R. W. Field. *Perturbations in the Spectra of Diatomic Molecules.* Academic Press, 1986.

[46] G. Herzberg. *Molecular Spectra and Molecular Structure.* D. Van Nostrand Co Inc, 1950.

[47] J. A. King, J. K. Webb, M. T. Murphy, and R. F. Carsell. Stringent null constraint on cosmological evolution of the proton-to-electron mass ratio. *Phys. Rev. Lett.*, 101:251304, 2008.

[48] M. T. Murphy, V. V. Flambaum, S. Muller, and C. Henkel. Strong limit on a variable proton-to-electron mass ratio from molecules in the distant universe. *Science*, 320:1611, 2013.

[49] B. K. Stuhl, B. C. Sawyer, D. Wang, and J. Ye. Magneto-optical trap for polar molecules. *Phys. Rev. Lett.*, 101(243002), 2008.

[50] K. M. Jones, E. Tiesinga, P. D. Lett, and P. S. Julienne. Ultracold photoassociation spectroscopy: Long-range molecules and atomic scattering. *Rev. Mod. Phys.*, 78:483, 2006.

[51] S. Tojo, M. Kitagawa, K. Enomoto, Y. Kao, Y. Takasu, M. Kumakura, and Y. Takahashi. High-resolution photoassociation spectroscopy of ultracold ytterbium atoms by using the intercombination transition. *Phys. Rev. Lett.*, 96:153201, 2006.

[52] E. R. I. Abraham, N. W. M. Ritchie, W. I. McAlexander, and R. G. Hulet. Photoassociative spectroscopy of long-range states of ultracold $^6Li_2$ and $^7Li_2$. *J. Chem. Phys.*, 103:7773, 1995.

[53] C. Haimberger. *Photoassociation of ultracold NaCs.* PhD thesis, University of Rochester, 2010.

[54] F. K. Fatemi, K. M. Jones, and P. D. Lett. Observation of optically induced Feshbach resonances in collisions of cold atoms. *Phys. Rev. Lett.*, 85:4462, 2000.

[55] K. Enomoto, K. Kasa, M. Kitagawa, and Y. Takahashi. Optical Feshbach resonance using the intercombination transition. *Phys. Rev. Lett.*, 101:203201, 2008.

[56] S. Blatt, T. L. Nicholson, B. J. Bloom, J. R. Williams, J. W. Thomsen, P. S. Julienne, and J. Ye. Measurement of optical Feshbach resonances in an ideal gas. *Phys. Rev. Lett.*, 107:073202, 2011.

[57] M. Yan, B. J. DeSalvo, B. Ramachandhran, H. Pu, and T. C. Killian. Controlling condensate collapse and expansion with and optical Feshbach resonance. *Phys. Rev. Lett.*, 110:123201, 2013.

[58] J. Deiglmayr, M. Repp, O. Dulieu, R. Wester, and M. Weidemuller. Population redistribution in optically trapped polar molecules. *Eur. Phys. J. D*, 65:99, 2011.

[59] J. M. Sage, S. Sainis, T. Bergeman, and D. DeMille. Optical production of ultracold polar molecules. *Phys. Rev. Lett.*, 94:203001, 2005.

[60] C. Chin and R. Grimm. Thermal equilibrium and efficient evaporation of an ultracold atom-molecule mixture. *Phys. Rev. A*, 69:033612, 2004.

[61] C. Chin, R. Grimm, P. S. Julienne, and E. Tiesinga. Feshbach resonances in ultracold gases. *Rev. Mod. Phys.*, 82:1225, 2010.

[62] E. A. Donley, N. R. Claussen, S. T. Thompson, and C. E. Wieman. Atom-molecule coherence in a Bose-Einstein condensate. *Nature*, 417:529, 2002.

[63] J. Cubizolles, T. Bourdel, S. J. J. M. F. Kokkelmans, G. V. Schlyapnikov, and C. Salomon. Production of long-lived ultracold Li_2 molecules from a Fermi gas. *Phys. Rev. Lett.*, 91:240401, 2003.

[64] K. Xu, T. Mukaiyama, J. R. Abo-Shaeer, J. K. Chin, D. E. Miller, and W. Ketterle. Formation of quantum-degenerate sodium molecules. *Phys. Rev. Lett.*, 91:210402, 2003.

[65] J. J. Zirbel, K.-K. Ni, S. Ospelkaus, T. L. Nicholson, M. L. Olsen, P. S. Julienne, C. E. Wieman, J. Ye, and D. S. Jin. Heteronuclear molecules in an optical dipole trap. *Phys. Rev. A*, 78:013416, 2008.

[66] F.M. Spiegelhalder, A. Trenkwalder, D. Naik, G. Kerner, E. Wille, G. Hendl, F. Schreck, and R. Grimm. All-optical production of a degenerate mixture of ^{6}Li and ^{40}K and creation of heteronuclear molecules. *Phys. Rev. A*, 81:043637, 2010.

[67] M.-S. Heo, T. T. Wang, C. A. Christensen, T. M. Rvachov, D. A. Cotta, J.-H. Choi, Y.-R. Lee, and W. Ketterle. Formation of ultracold fermionic NaLi Feshbach molecules. *Phys. Rev. A*, 86:021602(R), 2012.

[68] C.-H. Wu, J. W. Park, P. Ahmadi, S. Will, and M. W. Zwierlein. Ultracold Fermionic Feshbach molecules of ^{23}Na^{40}K. *New J. Phys.*, 11:055049, 2009.

[69] T. Takekoshi, M. Debatin, R. Rameshan, F. Ferlaino, R. Grimm, H.-C. Nagerl, C. Ruth Le Sueur, J. M. Hutson, P. S. Julienne, S. Kotochigova, and E. Tiemann. Towards the production of ultracold ground-state RbCs molecules: Feshbach resonances, weakly bound states, and the coupled-channel model. *Phys. Rev. A*, 85:032506, 2012.

[70] B. Marzok, B. Deh, C. Zimmermann, and Ph. W. Courteille. Feshbach resonances in an ultracold ^{7}Li and ^{87}Rb mixture. *Phys. Rev. A*, 79:012717, 2009.

[71] M. Repp, R. Pires, J. Ulmanis, R. Heck, E. D. Kuhnle, and M. Weidemuller. Observation of interspecies ^{6}Li-^{133}Cs Feshbach resonances. *Phys. Rev. A*, 87:010701(R), 2013.

[72] J. P. D'Incao and B. D. Esry. Suppression of molecular decay in ultracold gases without Fermi statistics. *Phys. Rev. Lett.*, 100:163201, 2008.

[73] D. Jaksch, V. Venturi, J. I. Cirac, C. J. Williams, and P. Zoller. Creation of a molecular condensate by dynamically melting a mott insulator. *Phys. Rev. Lett.*, 89:040402, 2002.

[74] E. Wille, F. M. Spiegelhalder, G. Kerner, D. Naik, A. Trenkwalder, G. Hendl, F. Schreck, R. Grimm, T. G. Tiecke, J. T. M. Walraven, S. J. J. M. F. Kokkelmans, E. Tiesinga, and P. S. Julienne. Exploring an ultracold Fermi-Fermi mixture: Interspecies Feshbach resonances and scattering properties of ^{6}Li and ^{40}K. *Phys. Rev. Lett.*, 100:053201, 2008.

[75] J. G. Danzl, E. Haller, M. Gustavsson, M. J. Mark, R. Hart, N. Bouloufa, O. Dulieu, H. Ritsch, and H.-C. Nagerl. Quantum gas of deeply bound ground state molecules. *Science*, 321:1062, 2008.

[76] A. Micheli, G. K. Brennen, and P. Zoller. A toolbox for lattice-spin models with polar molecules. *Nature Physics*, 2:341, 2006.

[77] L. E. Sadler, J. M. Higbie, S. R. Leslie, M. Vengalattore, and D. M. Stamper-Kurn. Spontaneous symmetry breaking in a quenched ferromagnetic spinor Bose-Einstein condensate. *Nature*, 443:312, 2006.

[78] K.-K. Ni, S. Ospelkaus, D. Wang, G. Quéméner, M. H. G. Neyenhuis, B. de Miranda, J. L. Bohn, J. Ye, and D. S. Jin. Dipolar collisions of polar molecules in the quantum regime. *Nature*, 464:1324, 2010.

[79] B. Yan, S. A. Moses, B. Gadway, J. P. Covey, K. R. A. Hazzard, A. M. Rey, Jin. D. S., and Ye. J. Realizing a lattice spin model with polar molecules. *arXiv:1305.5598*, 2013.

[80] M. E. Gehm. *Preparation of an optically trapped degenerate Fermi gas of ^{6}Li: Finding the route to degeneracy.* PhD thesis, Duke University, 2003.

[81] W. M. Haynes. *Handbook of Chemistry and Physics.* CRC Press, 94th edition, 2013-2014.

[82] J. Lekavich. Basics of acousto-optic devices. *Lasers and Applications*, page 59, Apr 1986.

[83] H. J. Metcalf and P. Van der Straten. *Laser Cooling and Trapping.* Springer, 1999.

[84] W. Ketterle, K. B. Davis, M. A. Joffe, A. Martin, and D. E. Pritchard. High densities of cold atoms in a dark spontaneous-force optical trap. *Phys. Rev. Lett.*, 70:2253, 1993.

[85] S. Tassy, N. Nemitz, F. Baumer, C. Höhl, A. Batar, and A. Görlitz. Sympathetic cooling in a mixture of diamagnetic and paramagnetic atoms. *J. Phys. B*, 43:205309, 2010.

[86] S. G. Porsev, Y. G. Rakhlina, and M. G. Kozlov. Electric-dipole amplitudes, lifetimes, and polarizabilities of the low-lying levels of atomic ytterbium. *Phys. Rev. A*, 60:2781, 1999.

[87] K. Pandey, K. D. Rathod, S. B. Pal, and V. Natarajan. Magnetic trapping of Yb in the metastable $^3P_2$ state. *Phys. Rev. A*, 81:033424, 2010.

[88] D.A. Brue and J.M. Hutson. Magnetically tunable Feshbach resonances in ultracold Li-Yb mixtures. *Phys. Rev. Lett.*, 108:043201, 2012.

[89] Z. Hadzibabic, C. A. Stan, K. Dieckmann, S. Gupta, M. W. Zwierlein, A. Görlitz, and W. Ketterle. Two-species mixture of quantum degenerate Bose and Fermi gases. *Phys. Rev. Lett.*, 88:160401, 2002.

[90] K. M. O'Hara and J. E. Thomas. Scaling laws for evaporative cooling in time-dependent optical traps. *Phys. Rev. A.*, 64:051403(R), 2001.

[91] C-L Hung, X. Zhang, N. Gemelke, and C. Chin. Accelerating evaporative cooling of atoms into Bose-Einstein condensation in optical traps. *Phys. Rev. A*, 78:011604(R), 2008.

[92] S. Inouye, J. Goldwin, M. L. Olsen, C. Ticknor, J. L. Bohn, and D. S. Jin. Observation of heteronuclear Feshbach resonances in a mixture of bosons and fermions. *Phys. Rev. Lett.*, 93:183201, 2004.

[93] S. Kato, S. Sugawa, K. Shibata, R. Yamamoto, and Y. Takahashi. Control of resonant interaction between electronic ground and excited states. *Phys. Rev. Lett.*, 110:173201, 2013.

[94] A. Y. Khramov. *Experiments in the Ultracold Lithium-Ytterbium System.* PhD thesis, University of Washington, 2013.

[95] A. Yamaguchi, S. Uetake, D. Hashimoto, J. M. Doyle, and Y. Takahashi. Inelastic collisions in optically trapped ultracold metastable ytterbium. *Phys. Rev. Lett.*, 101:233002, 2008.

[96] A. Keshet. *A Next-Generation Apparatus for Lithium Optical Lattice Experiments.* PhD thesis, Massachusetts Institute of Technology, 2012.

[97] V. V. Ivanov, A. Khramov, A. H. Hansen, W. H. Dowd, F. Münchow, A. O. Jamison, and S. Gupta. Sympathetic cooling in an optically trapped mixture of alkali and spin-singlet atoms. *Phys. Rev. Lett.*, 106:153201, 2011.

[98] Kenneth M. O'Hara. *Optical Trapping and Evaporative Cooling of Fermionic Atoms.* PhD thesis, Duke University, 2000.

[99] C. R. Monroe, E. A. Cornell, C. A. Sackett, C. J. Myatt, and C. E. Wieman. Measurement of Cs-Cs elastic scattering at T =30 μK. *Phys. Rev. Lett.*, 70:414, 1993.

[100] M. Arndt, M. Ben Dahan, D. Guery-Odelin, M. W. Reynoldes, and J. Dalibard. Observation of a zero-energy resonance in Cs-Cs collisions. *Phys. Rev. Lett.*, 79:625, 1997.

[101] A. Mosk, S. Kraft, M. Mudrich, K. Singer, W. Wohlleben, R. Grimm, and M. Weidemüller. Mixture of ultracold lithium and cesium atoms in an optical dipole trap. *Appl. Phys. B*, 73:791, 2001.

[102] F. Baumer, F. Münchow, A. Görlitz, S.E. Maxwell, P.S. Julienne, and E. Tiesinga. Spatial separation in a thermal mixture of ultracold ^{174}Yb and ^{87}Rb atoms. *Phys. Rev. A.*, 83:040702(R), 2011.

[103] A. H. Hansen, A. Khramov, W. H. Dowd, A. O. Jamison, V. V. Ivanov, and S. Gupta. Quantum degenerate mixture of ytterbium and lithium atoms. *Phys. Rev. A.*, 84:011606(R), 2011.

[104] H. Hara, Y. Takasu, Y. Yamaoka, J.M. Doyle, and Y. Takahashi. Quantum degenerate mixtures of alkali and alkaline-earth-like atoms. *Phys. Rev. Lett.*, 106:205304, 2011.

[105] A. Y. Khramov, A. H. Hansen, A. O. Jamison, W. H. Dowd, and S. Gupta. Dynamics of Feshbach molecules in an ultracold three-component mixture. *Phys. Rev. A*, 86:032705, 2012.

[106] S. Jochim, M. Barternstein, A. Altmeyer, G. Hendl, C. Chin, J. Hecker Deschlag, and R. Grimm. Pure gas of optically trapped molecules created from fermionic atoms. *Phys. Rev. Lett.*, 91:240402, 2003.

[107] D. S. Petrov, C. Salomon, and G. V. Shlyapnikov. Weakly bound dimers of fermionic atoms. *Phys. Rev. Lett.*, 93:090404, 2004.

[108] S. Zhang and T.-L. Ho. Atom loss maximum in ultra-cold Fermi gases. *New J. Phys.*, 13:055003, 2011.

[109] T. Weber and R. Grimm. Three-body recombination at large scattering lengths in an ultracold atomic gas. *Phys. Rev. Lett.*, 91:123201, 2003.

[110] D. S. Petrov, C. Salomon, and G. V. Shlyapnikov. Scattering properties of weakly bound dimers of fermionic atoms. *Phys. Rev. A*, 71:012708, 2005.

[111] J. P. D'Incao and B. D. Esry. Scattering length scaling laws for ultracold three-body collisions. *Phys. Rev. Lett.*, 94:213201, 2005.

[112] A. H. Hansen, A. Y. Khramov, W. H. Dowd, A. O. Jamison, B. Plotkin-Swing, R. J. Roy, and S. Gupta. Production of quantum-degenerate mixtures of ytterbium and lithium with controllable interspecies overlap. *Phys. Rev. A.*, 87:013615, 2012.

[113] A. Petrov, E. Tiesinga, and S. Kotochigova. Anisotropy-induced Feshbach resonances in a quantum dipolar gas of highly magnetic atoms. *Phys. Rev. Lett.*, 109:103002, 2012.

[114] T. Hong, C. Cramer, E. Cook, W. Nagourney, and E. N. Fortson. Observation of the $^1S_0$-$^3P_0$ transition in atomic ytterbium for optical clocks and qubit arrays. *Opt. Lett.*, 30:2644, 2005.

[115] C. W. Hoyt, Z. W. Barber, C. W. Oates, T. M. Fortier, S. A. Diddams, and L. Hollberg. Observation and absolute frequency measurements of the $^1S_0$-$^3P_0$ optical clock transition in neutral ytterbium. *Phys. Rev. Lett.*, 95:083003, 2005.

[116] A. Yamaguchi. *Metastable State of Ultracold and Quantum Degenerate Ytterbium Atoms: High-Resolution Spectroscopy and Cold Collisions.* PhD thesis, Kyoto University, 2007.

[117] T. Mukaiyama, J. R. Abo-Schaeer, K. Xu, J. K. Chin, and W. Ketterle. Dissociation and decay of ultracold sodium molecules. *Phys. Rev. Lett.*, 92:180402, 2004.

[118] Y. Inada, M. Horikoshi, S. Nakajima, M. Kuwata-Gonokami, M. Ueda, and T. Mukaiyama. Collisional properties of p-wave Feshbach molecules. *Phys. Rev. Lett.*, 101:100401, 2008.